Versatile Hydrodynamic Modelling of Global Ocean Tides and their Derived Variables for Geodesy and Paleo Sea Level Reconstruction

Dissertation

zur Erlangung des Doktorgrades
der Naturwissenschaften
vorgelegt von

Roman Lucas Sulzbach

am Fachbereich Geowissenschaften der Freien Universität Berlin,
angefertigt am Deutschen GeoForschungsZentrum GFZ, Potsdam.

Berlin, 2023

Erstgutachter:	Prof. Dr. Maik Thomas
Zweitgutachter:	Prof. Dr. Michael Schindelegger

Datum der Einreichung:	02.06.2023
Datum der Disputation:	15.11.2023

Abstract

Many geoscientific measurements exhibit significant variability induced by ocean tides that can, if uncorrected, degrade the quality of observations. Thus, tidal variability is usually reduced on the observation level with the help of background models.
The barotropic ocean tide model TiME has been refined to improve this correction process. Major upgrades include updating the bathymetric data, improving the energy dissipation mechanisms, and including the effect of self-attraction of the ocean water and its loading on the solid Earth. These refinements allowed reducing the open ocean root-mean-square deviation from geodetic data by over 70% for the main lunar M_2 tide, corresponding to an accuracy on the 80%-level with respect to the mean signal. The model operates independently of empirical satellite altimetry data, so this high relative accuracy also extends to partial tides with minor amplitude, where altimetry-constrained models are less accurate. TiME's forcing module was augmented by degree-3 spherical harmonic functions and barometric and wind stress acceleration induced by the atmosphere, which enabled the simulation of additional tidal subgroups at the same accuracy level. For degree-3 tides, it could be shown that their gravimetric fingerprints on the level of only $100\frac{\mathrm{pm}}{\mathrm{s}^2}$ can be identified in superconducting gravimeters and agree with the modelling results. This level is close to the threshold of gravimetric detectability and emphasizes TiME's accuracy for the smallest tidal signals.
As a result of these simulations, the TiME22 ocean tide atlas, which comprises 57 partial ocean tides, has been compiled and is provided in Stokes coefficients for terrestrial and satellite gravimetric applications. Many minor ocean tides from this collection are not included in data-constrained ocean tide atlases. Therefore, they are usually only linearly estimated or completely neglected for gravimetric applications. It is shown for several cases that TiME22 minor tide solutions can improve the accuracy of the tidal correction for geodetic techniques, including satellite and terrestrial gravimetry. More precisely, the model validation conducted within this thesis recommends the utilization of hybrid tidal atlases comprised of altimetry data-constrained ocean tide models for large-signal tides and unconstrained solutions, such as TiME22, for minor tides. The results confirm that purely hydrodynamic ocean tide models can reliably predict tidal variability in cases where empirical data is so sparse or of such low precision that tidal solutions cannot be adequately constrained.
This line of argumentation extends to paleo-ocean tides, where direct observations are impossible, and information can only be extracted by archeological or geological sea-level markers. Within this thesis, TiME is employed to predict paleo tide levels, which indicate the possible height deviation of sea-level markers from the mean sea level at that time. Tidal levels are simulated with dense temporal sampling since the Last Glacial Maximum. The predicted levels (*e.g.*, the mean high water) compare well to available observations and other paleo tidal simulations and represent the first data set with truly-global coverage that allows for interpretation of paleo sea level data.

Kurzfassung

Viele geowissenschaftliche Messungen weisen erhebliche gezeitenbedingte Schwankungen auf, die, wenn sie nicht korrigiert werden, die Qualität der Beobachtungen beeinträchtigen können. Daher wird die Gezeitenvariabilität in der Regel auf der Beobachtungsebene mit Hilfe von Hintergrundmodellen korrigiert.
Das barotrope Gezeitenmodell TiME wurde weiterentwickelt, um diesen Korrekturprozess zu verbessern. Die wichtigsten Verbesserungen beinhalten verfeinerte Energiedissipationsmechanismen, die Aktualisierung der Bathymetrie und die Einbeziehung des Effekts der Selbstanziehung des Ozeans und dessen Auflast auf die feste Erde. Durch diese Neuerungen war es möglich, die mittlere quadratische Abweichung der gezeiteninduzierten Meeresspiegelanomalie im offenen Ozean von geodätischen Daten um über 70% für die wichtigste Mondgezeit M_2 zu verringern. Dies entspricht einer Genauigkeit von 80% in Bezug auf das mittlere Gezeitensignal. Das Modell arbeitet unabhängig von empirischen Satellitenaltimetriedaten, so dass sich diese hohe relative Genauigkeit auch auf partielle Gezeiten mit geringerer Amplitude erstreckt. Das Antriebsmodul von TiME wurde durch Grad-3 Kugelflächenfunktionen und atmosphärisch induzierte Beschleunigungen ergänzt. Dadurch ist die Simulation von zusätzlichen Partialtiden mit konstanter relativer Genauigkeit möglich. Für Grad-3 Gezeiten konnte gezeigt werden, dass ihre gravimetrischen Signaturen mit einer Amplitude von nur $100\,\frac{\mathrm{pm}}{\mathrm{s}^2}$ in supraleitenden Gravimetern identifiziert werden können und mit den Modellierungsergebnissen übereinstimmen. Dieses Signallevel liegt nahe an der Schwelle der gravimetrischen Nachweisbarkeit und stellt die Genauigkeit von TiME für die kleinsten Gezeitensignale heraus.
Als Ergebnis dieser Simulationen wurde der TiME22 Gezeitenatlas erstellt, der 57 Partialtiden enthält. Dieser Atlas enthält viele kleinere Ozeangezeiten, die in datengestützten Ozeangezeitenatlanten nicht enthalten sind. Es wird für mehrere Fälle gezeigt, dass TiME22-Lösungen für kleinere Gezeiten die Gezeitenkorrektur geodätischer Prozesse, einschließlich Satelliten- und terrestrischer Gravimetrie, verbessern können. Insgesamt bestätigen die Ergebnisse, dass rein hydrodynamische Gezeitenmodelle die Gezeitenvariabilität in Fällen zuverlässig vorhersagen können, in denen Beobachtungen so rar oder von so geringer Genauigkeit sind, dass keine präzise empirische Vorhersage möglich ist.
Diese Argumentation erstreckt sich auch auf die Gezeiten im Paläo-Ozean, wo direkte Beobachtungen unmöglich sind und Informationen nur durch archäologische oder geologische Meeresspiegelmarker gewonnen werden können. TiME wird im Rahmen dieser Arbeit zur Vorhersage von Paläo-Gezeitenpegeln eingesetzt, die die Höhenabweichung von Meeresspiegelmarkern vom damaligen mittleren Meeresspiegel angeben. Die Gezeitenpegel wurden in engem zeitlichen Raster seit dem letzten glazialen Maximum simuliert. Die Ergebnisse stimmen gut mit den verfügbaren Beobachtungen und anderen Paläo-Gezeitensimulationen überein und liefern den ersten derartigen Datensatz mit globaler Abdeckung. Dieser ermöglicht die Interpretation von Meeresspiegelmarkern und kann für Paläo-Meeresspiegelstudien verwendet werden.

Résumé

De nombreuses mesures géoscientifiques révèlent une variabilité significative induite par les marées océaniques qui, si elle n'est pas corrigée, peut dégrader la qualité des observations. Ainsi, la variabilité des marées est généralement corrigée au niveau de l'observation à l'aide de modèles numériques.
Le modèle de marée océanique barotrope TiME a été affiné pour améliorer ce processus de correction. Les principales améliorations portent sur les mécanismes de dissipation de l'énergie, la mise à jour des données bathymétriques et la prise en compte de l'effet d'auto-attraction de l'eau de mer et de sa chargement sur la Terre solide. Ces améliorations ont permis de réduire l'écart quadratique moyen en haute mer par rapport aux données géodésiques de plus de 70% pour la marée lunaire principale, ce qui correspond à une précision de 80% par rapport au signal moyen. Le modèle fonctionne indépendamment des données altimétriques empiriques des satellites, de sorte que cette grande précision relative s'étend également aux marées partielles de faible amplitude. Le module de forçage de TiME a été complété par des fonctions harmoniques sphériques de degré 3 et des accélérations barométriques et éoliennes induites par l'atmosphère, ce qui a permis de simuler des sous-groupes de marées supplémentaires au même niveau de précision. Pour les marées de degré 3, on a pu montrer que leurs empreintes gravimétriques à $100\frac{\mathrm{pm}}{s^2}$ près peuvent être identifiées dans des gravimètres supraconducteurs et qu'elles sont en accord avec les résultats de la modélisation. Ce résultat est proche du seuil de détectabilité gravimétrique et favorise la précision de TiME pour les signaux de marée les plus faibles.
Ces simulations ont permis de compiler l'atlas des marées océaniques TiME22, qui comprend 57 marées océaniques partielles. Nous montrons pour plusieurs cas que les solutions de marée mineure de TiME22 peuvent améliorer la précision des processus géodésiques, y compris la gravimétrie satellitaire et terrestre. Les résultats confirment que les modèles purement hydrodynamiques de marée océanique peuvent prédire de manière fiable la variabilité de la marée dans les cas où les données empiriques sont si rares ou si peu précises que les solutions de marée ne peuvent pas être contraintes de manière adéquate.
Cette argumentation s'applique également aux paléo-marées océaniques, où les observations directes sont impossibles et où l'information ne peut être extraite que par des marqueurs archéologiques ou géologiques du niveau de la mer. Dans le cadre de cette thèse TiME est utilisé pour prédire les niveaux de marée paléo, qui indiquent l'écart de hauteur possible des marqueurs du niveau de la mer par rapport au niveau moyen de la mer de cette époque. Les niveaux de marée sont simulés en continu depuis le Dernier Maximum Glaciaire. Les résultats correspondent bien aux observations disponibles et à d'autres études et fournissent le premier ensemble de données avec une couverture véritablement mondiale. Celui-ci permet d'interpréter les marqueurs du niveau de la mer et peut être utilisé pour des études paléo du niveau de la mer.

Contents

1
Introduction

How are tides distinguished from other planetary phenomena? The words that are used to describe the phenomenon in different languages hint at its fundamental characteristics. For example, *tide* and the German equivalent *Gezeit* originate from the word *time* (German: *Zeit*) and point to the strictly periodic nature of tidal phenomena (Cartwright, 1999). On the other hand, the French counterpart *marrée* (Italian and Spanish: *marea*) stems from *mer*, meaning sea, and reflects that tides were first observed in the ocean. However, the modern definition of tidal phenomena is not restricted to oceans. Still, it signifies small, periodic disturbances over the entire Earth system (*i.e.*, the geosphere[1], hydrosphere, magnetosphere, and atmosphere) excited by forces originating from celestial bodies, especially Sun and Moon[2] (Simon, 2007). Therefore, tidal periodicities are determined by the ephemeris[3] of the solar system, which is the primary characteristic distinguishing them from non-tidal phenomena (*e.g.*, the general circulation of ocean and atmosphere).

The observation of tides in the oceans is straightforward as their effects, *e.g.*, the changing water level, are evident to the naked eye of a coastal observer. Also, they are relatively easy to quantify through tide gauge measurements, which in their basic form can be realized by a vertical leveling staff attached to the sea floor. Moreover, a basic understanding of local ocean tidal regimes was of core importance for coastal communities, as the apparent diurnal or semidiurnal frequency of ocean tides imposes a natural rhythm onto everyday coastal life. This necessity explains the early formation of the first ideas about ocean tides in prehistoric civilizations and the close etymological relation to the word for the sea in many languages. Since then, tidal research has sustained its significance in science but repeatedly shifted its foci (*e.g.*, Cartwright, 1999).

[1] Within this thesis, the term is used to describe the entity of the solid Earth - from the Earth's surface to the Core.

[2] This definition allows for the inclusion of periodically exerted solar radiation as the origin of tides.

[3] The word *ephemeris* (pl. *ephemerides*; from Latin: diary) describes the knowledge of the trajectory of natural astronomical bodies or artificial satellites in the sky over time.

1.1 Tides of the Earth System

Observation of tidal movements in the atmosphere and solid Earth, but also in the deep ocean, is more complicated than for the rise and fall of ocean waters at the coast due to the absence of horizontal discontinuities of the observed media. More advanced instrumentation was needed to detect these phenomena. For example, the detection of tidal periodicity in the air pressure in the 18th century benefited from the invention of the mercury barometer roughly 100 years earlier (*e.g.*, Cartwright, 1997). Analogously, detecting tidal signatures in the Earth's magnetic field, primarily induced by ionospheric currents due to the atmospheric tides but also induced by the flow of conducting ocean water through the ambient magnetic field, required precise magnetic field measurements (*e.g.*, Gauss, 1877; Schuster, 1908; Longuet-Higgins, 1949).
Furthermore, the tides of the solid Earth (further called Earth tides) were even harder to observe. Hence, scientists anticipated their existence before they could be established empirically. The high interest in Earth tides hints at two aspects of tides in general. First, the observation of tidal oscillations can be used to study large-scale Earth system properties that are otherwise hard or impossible to assess (in this case, the solid Earth's rigidity). Second, various tidal phenomena in the Earth's subsystems are generally not independent. Especially Earth and ocean tides are intimately interlaced. Thus, the first investigation of the Earth tides and the Earth's rigidity was based on the observations of long-period (fortnightly and longer) ocean tides (Darwin, 1907), as the back-action of the solid Earth reduces their amplitude by about 30%. Later, Earth tides could be detected with more direct approaches, *e.g.*, by measuring their induced tilt and strain, horizontal and vertical displacements, and gravity variations (*e.g.*, Melchior, 1981; Zürn, 1997a).
This thesis deals with the tides of the world ocean. Nevertheless, the latter example of solid Earth tides impacting ocean tidal dynamics implies that tidal models must consider interactions between different terrestrial subsystems to arrive at a sound understanding of the involved phenomena. Another example of coupled tidal processes is the excitation of Earth and ocean tides due to atmospheric pressure loading, thus entangling tides in the atmosphere, hydrosphere, and geosphere. On the other hand, ocean tidal dynamics (OTD) also impacts the atmosphere (*e.g.*, Renault and Marchesiello, 2022) and, most notably, the solid Earth, forming a strong feedback loop to OTD itself (Henderschott, 1972; Ray, 1998a).
Subsequently, signatures of ocean tides are not limited to the world oceans. Ocean tides induce periodic variations in atmospheric pressure, displace the Earth's crust vertically and horizontally, and alter the gravity field. Due to the all-encompassing presence of ocean tide signatures over the Earth system, many geodetic observing systems are impacted by OTD, which, in many cases, explains large parts of the observed signal variability.

1.2 Ocean Tide Signatures in Geodetic Measurements

Ocean tides induce periodic sea surface height (SSH) disturbances, denoted ζ, accompanied by ocean currents, characterized by their velocity, denoted $\mathbf{v}$, and their associated transport, *i.e.*, depth-integrated velocity, $\mathbf{V}$. These variables will be labeled as *primary observables* in the following, as they are the dynamic core variables of the prognostic partial differential equations (PDEs) that govern OTD. Within this thesis, they are dis-

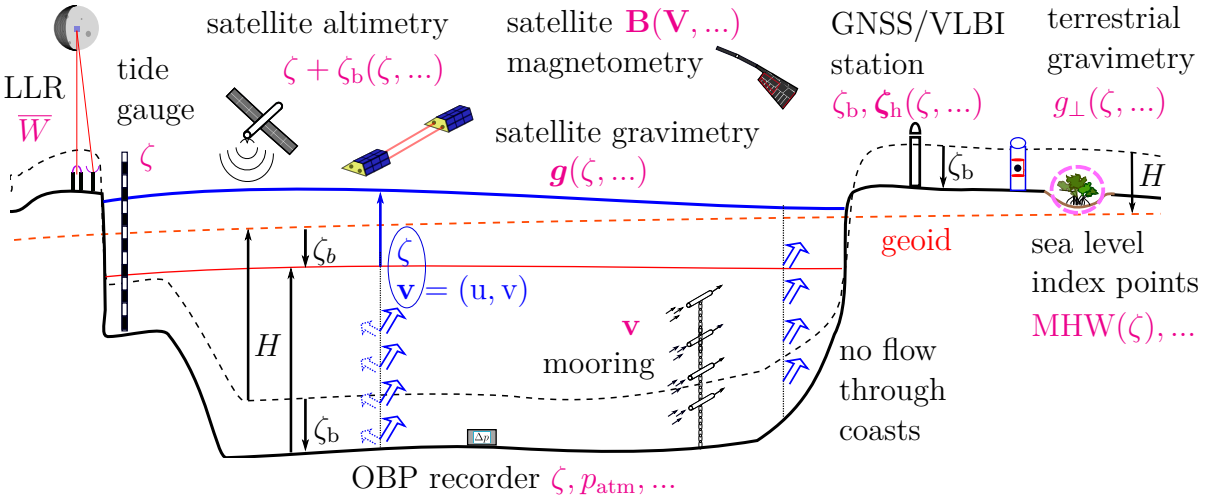

Figure 1.1: Definition of the prognostic ocean state variables of the tidal equations, ζ and $\mathbf{v}$ (blue), the geoid (red, dashed) and the surface loading displaced mean sea level (red, solid), the undisturbed topography, denoted H (black, dashed), and the ocean loading displaced topography (black, solid). Within, ζ_b signifies vertical ocean loading displacement of the Earth's crust. Additionally, several instrumentation techniques sensitive to ocean tidal signatures are illustrated, with the sensitive quantity noted in magenta (cf. Table 1.1). All listed abbreviations and symbols are introduced within this chapter.

tinguished from *secondary observables* derived from primary observables via diagnostic equations (cf. Table 1.1). Consider Figures 1.1 and 1.2 for the following discussion, illustrating geodetic techniques sensitive to OTD-derived observables.

Two instrumentation techniques are commonly used to investigate the primary observables. First, moored current meters can measure ocean tidal currents (*e.g.*, Luyten and Stommel, 1991). They usually sample the ocean current at different depths and allow investigation of the vertical profile of the current (*e.g.*, Gould and McKee, 1973). On the other hand, observations of the sea surface height by tide gauge (TG) measurements are much less costly and, therefore, routinely performed in most harbors, spanning a dense observation network over the globe, which is a powerful tool to investigate OTD (*e.g.*, TICON-3, Hart-Davis et al., 2022). A weakness of this type of observation is its restricted coverage of the ocean surface to inshore areas. They concentrate on the continental coasts, with only a few stations in the open ocean at small islands (cf. Figure 1.2). Naturally, tidal researchers were interested in closing the data gap in the open ocean. As the measurement of tidal sea surface elevations in the deep ocean required a more advanced measurement technique, it took until the 1960s to obtain reliable estimates by ocean bottom pressure (OBP) recorders (*e.g.*, Filloux, 1970; Ray, 2013). OBP records are invaluable in broadening the empirical data basis for tidal research. On the other hand, OBP recorders are also sensitive to atmospheric pressure variations (*i.e.*, atmospheric tides), which complicates evaluation for some tidal frequencies. Moreover, OBP recorders are expensive and only sparsely deployed in the open ocean.

Another extraordinarily successful approach in detecting open ocean tides is the operation of satellite altimeters. Especially the altimetry missions Topex/Poseidon (T/P) and their

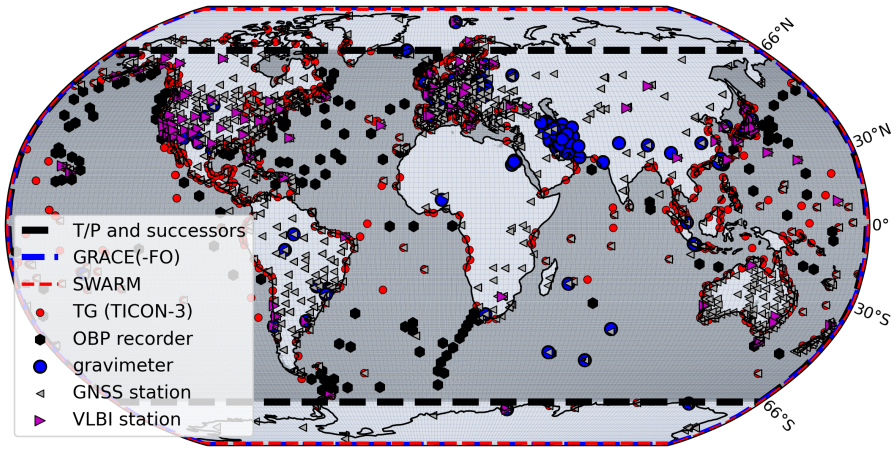

Figure 1.2: Terrestrial geodetic observation systems sensitive to ocean tide-induced signals, including TG stations, OBP recorders (Ray, 2013), GNSS and VLBI stations used as ITRF2020 geodetic markers, as well as terrestrial gravimeters from IGETS (and more locations, see full text). The Earth surface coverage by the satellite missions SWARM, GRACE(-FO), and the altimetry mission T/P and its successors is also indicated

successors (*e.g.*, Fu et al., 1994; Schrama and Ray, 1994; Fu and Cazenave, 2000) led to a revolution in ocean tidal research by providing a robust and spatially continuous data basis for open ocean tidal dynamics. With some years of satellite altimetry data available, it was possible to produce data-constrained tidal atlases (*e.g.*, Andersen, 1995; Ray, 1999) that nowadays are accurate to the centimeter level in the open ocean and somewhat less accurate in coastal areas (cf. Stammer et al., 2014 for an overview).

Precisely speaking, satellite altimetry does not directly observe the sea surface anomaly ζ but the geocentric tide, *i.e.*, the combination of $\zeta + \zeta_\mathrm{b}$, where ζ_b is the deformation of the solid Earth in the vertical direction by the ocean load[4]. This process is known as ocean tidal loading and can be observed with space geodetic techniques, for example, VLBI (Very-Long-Baseline Interferometry, *e.g.*, Schuh and Moehlmann, 1989; Scherneck, 1991), or GNSS[5] (Global Navigation Satellite System, *e.g.*, Bos et al., 2015). As sea surface loads represent large-scale mass anomalies, ocean tides also produce a fingerprint in the Earth's gravity field, $\boldsymbol{g}$, that is detectable by terrestrial gravimetry (vertical surface gravity $g_\perp$, *e.g.*, Boy et al., 2003, 2004, 2006, cf. IGETS database Boy et al., 2020) and satellite gravimetry, most notably the Gravity Recovery and Climate Experiment (GRACE) and GRACE Follow-on (GRACE-FO) (*e.g.*, Wiese et al., 2016; Tapley et al., 2019). The global distribution of the described techniques is visualized in Figure 1.2 and achieves a near-global coverage, emphasizing the ubiquitous presence of OTD-induced signals.

Variables related to ocean tidal loading are secondary observables in the sense that they are derived from the interaction of primary variables (here ζ) with other subsystems of the

[4]There is also a horizontal deformation component $\boldsymbol{\zeta}_\mathrm{h}$ with impact on geodetic measurements.

[5]The GNSS station locations shown in Figure 1.2 were obtained from `https://itrf.ign.fr/en/solutions/itrf2020`, while the gravimeter coordinates originate from `http://loading.u-strasbg.fr/surface_gravity.php`.

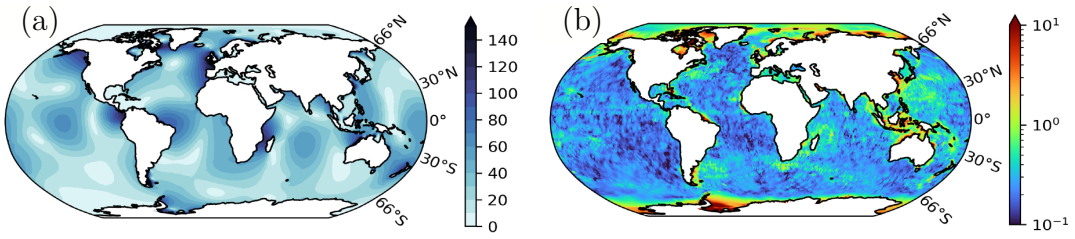

Figure 1.3: Mean amplitude (a) and standard deviation (b) for the main lunar tide (M_2) for an ensemble of 5 satellite altimetry data-constrained models (Abrykosov et al., 2021). The logarithmic scale highlights the polar-dominated uncertainty structure. The scale of both plots is in cm.

Earth via diagnostic equations. In the same way, ocean tide-induced magnetic fields, denoted $\boldsymbol{B}$, are secondary variables. They can be measured with terrestrial magnetometers or satellite missions such as CHAMP (*e.g.*, Tyler et al., 2003) or SWARM (*e.g.*, Friis-Christensen et al., 2006) and originate from the interaction of tidal currents with the magnetosphere.

As a last example, it is remarked that ocean tides also have a notable impact on the Earth's rotation by periodically modifiying its momentum budget and inertia tensor (*e.g.*, Weis, 2006). Therefore, secondary tidal signatures are also present in the Earth's angular velocity $\boldsymbol{\Omega}_e$ and the length of day (LOD). One way to observe them is with space geodetic techniques. Further, refined gravity and optical clock measurements (*e.g.*, by approaches based on quantum technology, cf. Puetzfeld and Lämmerzahl, 2019) might enable the observation of gravity field components described by relativistic geodesy, *e.g.*, the *gravitomagnetic field*, which contains signatures of the Earth rotation (Hackmann and Lämmerzahl, 2014).

1.3 Relevance of Primary and Secondary Observables

Observation systems that directly measure primary observables (*e.g.*, TG stations, OBP recorders, and satellite altimetry) are usually employed to extract localized, empirical estimates of OTD. These empirical estimates are then used to validate ocean tide models (*e.g.*, Ray, 2013) or serve as observational constraints resulting in data-constrained ocean tide atlases (*e.g.*, Lyard et al., 2021; Hart-Davis et al., 2021b; Egbert and Erofeeva, 2002). Using empirical data constraints is an important distinction for classifying ocean tidal models. One distinguishes between unconstrained (exclusively based on the laws of tidal hydrodynamics) models and data-constrained models that employ observations for correction or via data assimilation. As mentioned, modern data-constrained ocean tide models achieve excellent accuracy (Stammer et al., 2014).

At the same time, a typical disadvantage of satellite altimetry data-constrained models is their reliance on data quality and availability. While data availability is typically very good at latitudes smaller than 66° corresponding to the orbit inclination of Topex/Poseidon, polar areas can be less consistently observed. Therefore, the uncertainty for those models is highest in polar regions, where yet large ocean tide amplitudes

Table 1.1: Primary (prognostic) and secondary (diagnostic) observables of OTD that are considered or mentioned within this thesis. Additionally, possible observation systems and several sensitive quantities for diagnostic observables are listed.

Primary observables

Quantity	Symbol		Observation by
SSH anomaly	ζ		TG, OBP, altimetry, ...
Tidal flow velocity	$\mathbf{v}$		Moored current meter, ...
Tidal transport	$\mathbf{V}= \int_0^H \mathbf{v} dh$		Barotropic: $\mathbf{V}= H\mathbf{v}$
Secondary observables		Derived from	
Gravity field	$g_\perp, \boldsymbol{g}$	ζ, SE-structure, ...	Terr. & sat. gravimetry
Surface displacement	ζ_b, $\boldsymbol{\zeta}_\mathrm{h}$	ζ, SE-structure, ...	GNSS, VLBI, SLR, ...
Tidal mean dissipation	$\overline{W}$	ζ, $\mathbf{v}$, ephemeris, ...	LLR, SLR, hist. eclipses, ...
Ocean tide levels	MHW, ...	ζ	TG, altimetry, SLIPs, ...
Magnetic field	$\boldsymbol{B}$	$\mathbf{V}$, OC-salinity, ...	Terr. & sat. magnetometers
Earth Rotation	$\boldsymbol{\Omega}_\mathbf{e}$, ...	ζ, SE-inertia, ...	VLBI, rel. gravimetry, ...

SE=solid Earth, OC=ocean

are present (cf. Figure 1.3).
On the other hand, the observation of secondary observables (*e.g.*, GNSS stations, gravimetric, or magnetic observations) offers two options if their spatiotemporal resolution is sufficiently high. Either the measurement can be inverted to yield primary observables (*e.g.*, Boy et al., 2003), or prior knowledge of presumed primary variables can be used to study properties of the Earth system (*e.g.*, Darwin, 1908; Petereit et al., 2019; Huang et al., 2022; Arnoso et al., 2023).

However, the spatiotemporal coverage of many observation systems is insufficient to extract tidal signals coherently. Depending on the noise level (Munk and Hasselmann, 1964) and the observation systematic, tidal oscillations are often unidentifiable and alias into the observed signal. A famous example is the spatiotemporal aliasing of ocean tidal signals into GRACE-(FO) solutions, which are known to significantly limit the observation resolution and quality (Flechtner et al., 2016; Ray et al., 2003; Han et al., 2004). Thus, modelers usually subtract independently modeled ocean tide signals on the observation equation level. This correction step is essential and requires the availability of accurate global ocean tide models that can predict the secondary tidal observables at a sufficiently high accuracy.
Figures 1.2 and 1.3 illustrate the weak point that arises from relying solely on modern satellite data-constrained models. On the one hand, terrestrial geodetic observations are performed over the entire globe and require precise knowledge of global OTD. Contrariwise, altimetry data is not available with a constant high accuracy everywhere and for the whole tidal spectrum. Limited by the signal-to-noise ratio (SNR) of the observations, tidal solutions of small amplitude are often not included in tidal atlases, both in the spatial domain (*i.e.*, polar and near-costal areas) and the spectral domain (for so-called *minor* ocean tides). In these cases, data-unconstrained tidal models can provide valuable constraints for improving tidal corrections.

This argumentation also applies to paleotidal dynamics, where direct observation of primary observables is impossible, and only imprecise secondary observations can be considered. One aspect of paleo-ocean tides, which was at the center of ocean tidal research for quite a long time, is the evolution of the global mean dissipation rate by ocean tides, denoted $\overline{W}$ (Cartwright, 1999). Implications of the temporal dynamics of $\overline{W}$ are widespread. They include the long-term development of the Earth-Moon-Sun system (*e.g.*, Daher et al., 2021; Farhat et al., 2022) and the changes in the thermohaline circulation (*e.g.*, Schmittner et al., 2015) with a substantial impact on global climates.
Another aspect is the evolution of ocean tide levels, which define the conditions under which geological and biological sea-level index points (SLIPs) are deposited. Ocean tide levels are classified by reference heights like the Mean High Water (MHW) or Mean Low Water (MLW), structuring the apparent tidal regime around the local mean sea level. SLIPs represent observations of the local mean sea and ocean tide levels, which can be seen as a secondary observable of OTD, depending on ζ (cf. Table 1.1). The apparent tidal regime systematically affects the interpretation of SLIPs and, thus, the reconstruction of the paleo mean sea level and its uncertainty, the so-called indicative range. As tidal levels changed by several meters over time (*e.g.*, Wilmes et al., 2019), reliable paleo tide models are essential for coherently reconstructing the sea level history (*e.g.*, Horton et al., 2013).
While geodetic measurements precisely constrain the present-day tidal dynamics and dissipations rates (*e.g.*, Lunar Laser Ranging, LLR, *e.g.*, Dickey et al., 1994, cf. Figure 1.1, or Satellite Laser Ranging, SLR), this is impossible for paleo tides.
Thus, the availability of versatile, accurate, data-unconstrained ocean tide models, adaptable to a wide range of (paleo) conditions, is an important tool for paleo studies of the Earth system.

1.4 Objectives and Outline of this Thesis

Ocean tide variability is a ubiquitous feature of modern space geodetic measurements, which allows data-constrained ocean tide atlases to reach impressive accuracy. At the same time, it poses the need for independent tidal background models to correct the obtained time series on the observation level.
This statement forms the basis of our research hypothesis: Eventually, the quality of the applied tidal correction limits the accuracy of geodetic products and the understanding of the Earth system in general. It is thus required to improve the quality of ocean tidal atlases, especially in sparsely observed geographical regions, for insufficiently-constrained partial tides and past epochs inaccessible from precise modern geodetic methods.
Based on this assumption, three main objectives for this thesis are formulated:

(O1) Development of an accurate ocean tide model which can resolve a large spectrum of partial tides on a truly-global domain

(O2) Accurate prediction of formerly unmodeled minor tides, which will contribute to tidal corrections of improved quality, especially for satellite gravimetry

(O3) Precise simulation of paleotidal dynamics between the Last Glacial Maximum (21,000 years ago) and the present-day and extraction of secondary observables for sea level reconstruction with dense temporal sampling

O1 forms the foundation for O2 and O3, which in turn define constraints for implementing O1. The principal framework on which the model must operate is set by the sparsity and relatively low quality of observations available for minor tides and the complicated accessibility of paleotidal fingerprints. Hence, the model must be independent of empirical observations, *i.e.*, data-unconstrained. To enable accurate tidal simulations, the model should thus transcribe a solid understanding of ocean tide physics, which is the only way to produce credible and plausible modelling results if validation data is sparse or absent. Special emphasis will be put on the representation of tidal energy dissipation mechanisms, the interaction of ocean tides with solid Earth tides, and the representation of bathymetry, which are all known to be critical aspects for high model accuracy (*e.g.*, Arbic et al., 2009; Schindelegger et al., 2018; Barton et al., 2022). Further, O2 and O3 pose the need for a high versatility of the model because they require high flexibility of the boundary conditions under which the model has to operate, both for astronomical forces and oceanographic conditions.

Setting the stage for this thesis and O1, the modern understanding of OTD is reviewed in Chapter 2. The detailed discussion of the tidal spectrum further allows us to denominate four groups of partial tides, which are of particular interest to be addressed in the frame of O2. Based on the introduced fundamentals of ocean tide theory, Chapter 3 discusses their numerical implementation into the ocean tide model TiME.

The model validation utilizing geodetic data for major tides follows in Chapter 4. Further, this chapter discusses the performance of TiME in polar regions and in simulating the first tidal subgroup introduced in Chapter 2. In Chapter 5, the discussion advances towards O2, focussing on the subgroup of degree-3 tides. In the final part of this chapter, additional simulations of minor tides are presented, which together comprise the TiME22 atlas. This data set is further used to provide secondary observables (gravity and displacements), which can be used to perform tidal corrections.

Eventually, an approach to O3 is presented in Chapter 6. The discussion focuses on two aspects of paleo OTD: First, the temporal development of tidal dissipation, which has implications on ocean stratification and circulation (Munk and Wunsch, 1998; Wilmes et al., 2019), and second, tidal levels as secondary observables. A résumé of this thesis is provided in the final Chapter 7.

2
Global Ocean Tidal Dynamics

Deriving the equations governing the dynamics of the global ocean tides is an exercise that some of the most influential scientists have set forth. The first formulation of the tide-raising forces and the respective *Tide-Generating Potential* (TGP) is counted as a major achievement of Sir Isaac Newton. It can be seen as the first essential step towards deriving said equations. Knowledge of the TGP allows for the concept of equilibrium tides, associated with Newton and Daniel Bernoulli (cf. Cartwright, 1999, and references therein).
However, the second indispensable component is the principles of hydrodynamics, which describe the dynamics of the oceans themselves. Both components were first combined into a set of PDEs by the French scientist Pierre-Simon de Laplace, henceforth known as *Laplace Tidal Equations* (LTE) (Laplace et al., 1798). While the LTE have been proven to depict the characteristics of ocean tides correctly, they possess a well-arranged and minimalistic form that employs several assumptions and approximations. Thus, the reproduction of this established set of equations from more general principles with a detailed and precise description of the applied assumptions was conducted by scientists in the 19th century (*e.g.*, Hough, 1897) and 20th century (*e.g.*, Pekeris, 1974; Schwiderski, 1980), which is briefly reproduced in the following.
Due to the huge horizontal length scale of the world oceans, their hydrodynamic tidal flow must be considered turbulent. Thus, a modern approach to deriving the equations that govern ocean tidal dynamics should start with the general, nonlinear *Navier-Stokes Equations* (NSE) of a viscous, incompressible fluid (*e.g.*, Schlichting and Gersten, 2017) that express the conservation of momentum and mass in the oceans. The derivation leads to equations for the turbulent 'mean' motion by a formal time-averaging procedure applied to the NSE (*e.g.*, Schwiderski, 1980). In addition, several approximations that have been carefully tested to be robust for ocean tidal dynamics are applied. They include:

- The assumption of the Earth to be a perfect sphere with radius $R_\mathrm{e} = 6371$ km[1]
- Elastic response of the solid Earth to body forces and surface forces

[1]The presented numerical values are not essential for the derivation of the PDEs but later considered for tidal modelling.

- Steady Earth rotation with angular velocity $\Omega_\mathrm{e} = \frac{2\pi}{1\mathrm{d}}$ (d is 1 sidereal day)
- Incompressibility and homogenous density $\rho_\mathrm{sw} = 1024\frac{\mathrm{kg}}{\mathrm{m}^3}$ of the seawater
- Smallness of tidal variations compared to other relevant scales
- The assumption $H \ll R_\mathrm{e}$ for bathymetric depth H and Earth radius R_e

Especially the latter two points are strong approximations that allow the formulation of ocean tidal dynamics in a single-layer ocean while fulfilling the hydrostatic pressure assumption, *i.e.*, in the form of *Shallow-Water Equations* (SWE). In this description, the ocean state at a given location is completely defined by the depth-averaged flow velocity $\mathbf{v} = (\mathrm{u}, \mathrm{v})$ (u and v point in the direction of the local orthogonal coordinate system, later identified with east and north) and the local sea surface anomaly ζ (cf. Figure 1.1). Altogether, the nonlinear, inhomogeneous PDEs

$$\begin{matrix}(\mathbf{v}\cdot\nabla)\,\mathbf{v} \\ \boldsymbol{\nabla}\cdot(\zeta\ \mathbf{v})\end{matrix} + \underbrace{\begin{cases}\partial_\mathrm{t}\mathbf{v} + \mathbf{f}\times\mathbf{v} &= -g_0\boldsymbol{\nabla}\{\zeta - \zeta_\mathrm{eq} - \zeta_\mathrm{SAL}\}^\mathrm{seqt} \\ \partial_\mathrm{t}\zeta + \boldsymbol{\nabla}\cdot(H\ \mathbf{v}) &= 0\end{cases}}_{\mathrm{LTE}} \quad -\mathbb{D}\mathbf{v} + \mathbf{a}_\mathrm{atm} \tag{2.1}$$

are retained, which describe the temporal evolution of ζ and $\mathbf{v}$ comprised in an ocean state vector $\boldsymbol{\zeta}(\mathbf{x}, t) = (\mathbf{v}, \zeta) \in \mathbb{R}^3$ within this thesis. The spatial coordinates are later identified with $\mathbf{x} = (\phi, \lambda)$, being latitude and longitude. Here, the second equation describes the law of mass conservation for a barotropic flow over the undisturbed bathymetry $H(\mathbf{x})$, with ∂_t being the partial derivative in time and $\boldsymbol{\nabla}$ designating the horizontal nabla operator. The first vectorial equation expresses the law of momentum conservation for a geofluid on the rotating sphere, where $\mathbf{f} = 2\Omega_\mathrm{e}\sin\phi\ \mathbf{e}_\mathrm{vert}$ is the vertical Coriolis vector, and $g_0 = 9.80665\frac{\mathrm{m}}{\mathrm{s}^2}$ is the surface gravity. On the right-hand side, the equation is balanced by gradient forces of the sea surface anomaly (pressure gradient), the Tide-Raising Potential, given by $V_\mathrm{tid} = g_0\zeta_\mathrm{eq}$, the Self-attraction and Loading potential, $V_\mathrm{SAL} = g_0\zeta_\mathrm{SAL}$, and accelerations exerted by the atmosphere, $\mathbf{a}_\mathrm{atm}$. While the part of Equations (2.1) in curly brackets indicates the original form of the LTE, several additional terms are considered in the equations.

This chapter is structured in such way that the individual contributions to Equations (2.1) are consecutively discussed in the following sections forming an extensive overview of OTD. First, gravitational, atmospheric, and secondary tide-generating forces are discussed in Sections 2.1.1 to 2.1.3. Suppose the ocean bottom pressure gradient entirely balances these gradient forces. In that case, the definition of the equilibrium tide is obtained (cf. Section 2.1.4), which is indicated above by setting the gradient of the curly brackets, labeled *seqt*, equal to zero.

Transitioning to Laplace's dynamical theory of ocean tides (Section 2.2), the problem of understanding and describing frictional processes, here expressed in the general form $-\mathbb{D}\mathbf{v}$, became the key challenge for tidal modelers and is discussed in Section 2.2.1. Further, the rigorous derivation from the NSE adds the nonlinear effects of wave drift and advection to the PDE (left-hand side of Equations 2.1). Together with nonlinear frictional terms, they hamper the validity of the superposition principle for OTD. While linearization of Equations 2.1 grants in-depth insight into the characteristics of ocean tide physics (Section 2.2.2), the more general, nonlinear form (Section 2.2.3) is necessary to understand OTD in all aspects. The chapter closes by discussing the relationship between primary (prognostic) to secondary (diagnostic) tidal observables.

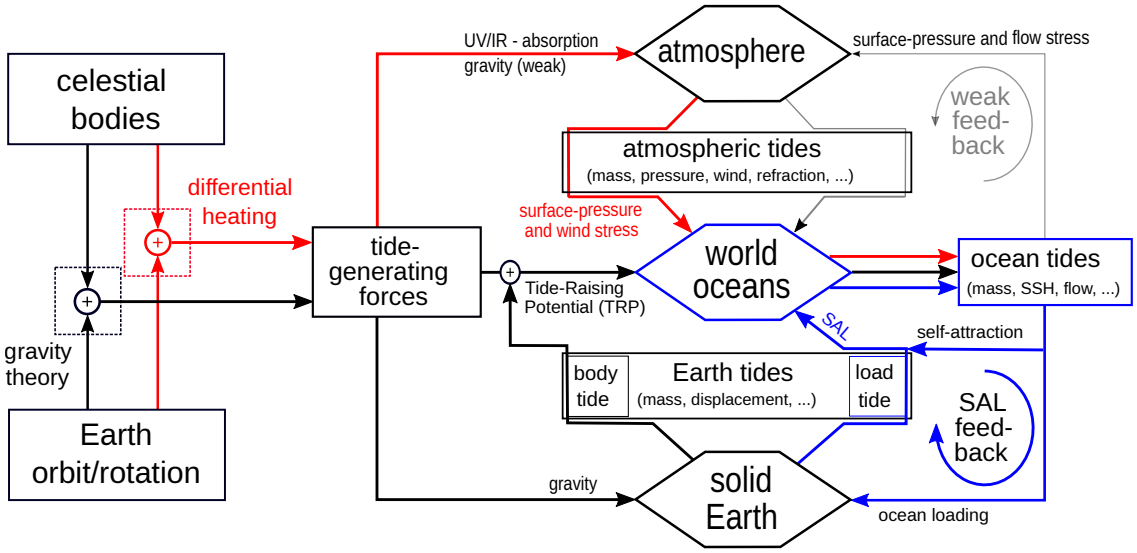

Figure 2.1: Primary excitation mechanisms of tides in the solid Earth, atmosphere, and world oceans. Effects of radiational origin are marked in red, effects of gravitational origin in black, and the oceanic Self-attraction and Loading (SAL) feedback appears in blue. This chart is designed to display interactions for understanding OTD and does not give a comprehensive overview of all tidal phenomena on Earth. Inspired by Agnew (2012).

2.1 Tide-Generating Forces

Chapter 1 introduced a rather general definition of the word tide: a minor periodic disturbance of the Earth system related to the ephemeris of celestial bodies. This general viewpoint is necessary to examine OTD, as the interaction between tides in the Earth's subsystems is crucial for its correct description. Thus in this section, the tide-generating forces that drive the dynamics of the ocean tides are introduced under consideration of interactions between individual tidal phenomena in the geosphere. The following discussion relates to Figure 2.1.

Under the influence of the Earth's rotation and the evolution of the solar system, tide-generating forces originate from the time-variable gravitational acceleration exerted by celestial bodies, mainly the Sun and the Moon, onto Earth. Gravitational forces impact all subsystems of the Earth, with a substantial effect on the solid Earth, inducing so-called *body tides*. The body tidal response is virtually in-phase with its generating forces and influences OTD by a linear modification of the TGP. This fact allows for the concept of the *Tide-Raising Potential* (TRP) as the primary generator of ocean tides (Section 2.1.1). On the other hand, atmospheric tides are dominantly excited by the absorption of solar radiation, which induces periodic tidal winds and pressure variations that interact with the ocean. Suchlike evoked ocean tides are called *radiational tides* in recognition of their root origin in solar radiation. The respective exciting forces are discussed in Section 2.1.2. Both introduced excitation mechanisms of OTD originate from external forces mediated by gravity, the solid Earth, and the atmosphere. Vice versa, ocean tides excite tidal oscillations in the solid Earth by surface loading (the *load tide*) and in the atmosphere by barometric forcing at the atmosphere-ocean boundary. On the other hand, this induces

secondary potentials that depend self-consistently on the OTD itself and are discussed in Section 2.1.3. This section concludes with a presentation of the concept of the equilibrium tide.

2.1.1 Tide-Raising Potential

The following discussion relates to the black (gravitational) excitation pathway of Figure 2.1. The gravitational TGP, denoted V_{grav}, at a location $\mathbf{x}$ is composed of the individual potentials exerted by massive objects (celestial bodies) with masses M^j_{ext} at time variable positions $\mathbf{x}_j(t)$ (cf. Figure 2.2). Following the Newtonian law for gravitation, the total potential reads

$$V_{\text{grav}}(\mathbf{x},t) = \sum_j \frac{GM^j_{\text{ext}}}{|\mathbf{x}_j(t)-\mathbf{x}|} = \sum_j \frac{GM^j_{\text{ext}}}{|\mathbf{x}_j(t)|} \frac{1}{\sqrt{1+\left(\frac{R_{\text{e}}}{|\mathbf{x}_j(t)|}\right)^2 - 2\frac{R_{\text{e}}}{|\mathbf{x}_j(t)|}\cos\alpha^{\text{ext}}_j(\mathbf{x}_j(t),\mathbf{x})}} \ . \tag{2.2}$$

Here, G is the universal gravitational constant, and we assume a rotating, Earth-fixed reference system, *i.e.*, $\mathbf{x}$ is constant while $\mathbf{x}_j(t)$ changes with time. In the second step, the trigonometric cosine rule was exercised onto the expression in the denominator, where $|\mathbf{x}_j(t)|$ is the distance between Earth's gravitational center and the external mass, and α^{ext}_j is the angle between the $\mathbf{x}$ and $\mathbf{x}_j(t)$ (Agnew, 2007).
Expression (2.2) is transformed by developing spatial dependencies into real-valued, fully-normalized spherical harmonic functions $Y_{lm}(\phi,\lambda)$, where ϕ and λ are the geographical latitude and longitude, and l and m are the degree and order of Y_{lm}, respectively. They are defined by

$$Y_{l,m\geq 0}(\phi,\lambda) \equiv \overline{P}_{lm}(\sin\phi)\cos(m\lambda) \quad \text{and} \quad Y_{l,m<0}(\phi,\lambda) \equiv \overline{P}_{l|m|}(\sin\phi)\sin(m\lambda) \ , \tag{2.3}$$

where $\overline{P}_{lm}(\sin\phi)$ are fully-normalized, associated Legendre Polynomials[2] (cf. Appendix A). Further, temporal dependencies are developed into the harmonic constituents of the ephemeris of the solar system, and degrees $l = 0, 1$ are discarded as they do not induce tidal forces. Considering this, one obtains

$$V_{\text{grav}}(\phi,\lambda,t) = \sum_{l=2}^{\infty}\sum_{m=0}^{l} \overline{P}_{lm}(\sin\phi) \sum_i \left(C^{lm}_i \cos(m\lambda + \chi'_i[t]) + S^{lm}_i \sin(m\lambda + \chi'_i[t]) \right) \ . \tag{2.4}$$

This is the typical notation for the harmonic development of the TGP, where C^{lm}_i and S^{lm}_i are the temporal harmonic coefficients for a constituent labeled i, and $\chi'_i(t)$ is the time-dependent phase of said constituent (*e.g.*, Hartmann and Wenzel, 1994, 1995b).
For ocean tide modelling, the effective TRP differs from the TGP, as the linear (in-phase) back-action of the solid Earth body tides on the ocean is included by multiplication with the frequency-dependent factor $a^{\text{b}}_l(\omega_i)$.
The reason for this frequency dependence takes its foundation in the solid Earth response to the TGP that possesses a significant resonance in the diurnal frequency band, the near-diurnal free wobble (NDFW) (*e.g.*, Zürn, 1997b), with observed resonance frequency

[2]The $\sqrt{}$-expression in Equation (2.2) can be directly developed into a series of Legendre Polynomials $P_l(\sin\phi)$.

Table 2.1: Love number taken from Spiridonov (2018) for the diurnal partial tide spectrum (degree 2) and for semidiurnal and terdiurnal partial tides of degree l=2 (d2) and degree l=3 (d3). Coupling with Earth's NDFW-resonance renders Love numbers in the diurnal band frequency-dependent. Strong deviations from d2 are indicated in **bold**.

tide	$2Q_1$	Q_1	ρ_1	O_1	P_1	K_1	Ψ_1	ϕ_1	OO_1	**d2**	**d3**
h_l^{b}	0.602	0.601	0.601	0.600	0.578	0.519	1.079	0.666	0.606	0.606	0.290
k_l^{b}	0.296	0.296	0.296	0.296	0.284	0.255	0.536	0.329	0.299	0.299	0.091
a_l^{b}	0.694	0.695	0.695	0.696	0.706	**0.736**	**0.457**	0.663	0.693	0.693	**0.801**

$f_{NDFW}^{-1} \approx (1 - 430^{-1})$d (Wahr and Sasao, 1980; Wahr, 1981; Rosat, S. and Lambert, S. B., 2009), that is related to the Earth's Free Core Nutation (FCN). The factor $a_l^{\mathrm{b}}(\omega_i) = 1 + k_l^{\mathrm{b}}(\omega_i) - h_l^{\mathrm{b}}(\omega_i)$ is a combination of Love numbers (Love, 1909) that encrypts the back-action of elastic body tides on oceanic tides. The NDFW-resonance significantly impacts tides in the K_1 tidal group, compare Table 2.1 (Ray, 2017).
In summary, the TRP can be noted as

$$V_{\mathrm{tid}}(\phi, \lambda, t) = \sum_{l=2}^{\infty} \sum_{m=0}^{l} \sum_{i} a_l^{\mathrm{b}}(\omega_i)\ A_i\ Y_{lm}(\phi, \lambda + \frac{\chi_i(t)}{m})\ , \tag{2.5}$$

with[3] $A_i = \sqrt{(C_i^{lm})^2 + (S_i^{lm})^2}$. The time-dependent phase argument

$$\chi_i(t) = \sum_{j}^{7} q_j^i\ D_j^{\mathrm{astro}}(t) = q_1^i \tau + q_2^i s + q_3^i h + q_4^i p + q_5^i N' + q_6^i p_s + q_7^i \frac{\pi}{2} \tag{2.6}$$

is given following Doodson (1921) and Pugh and Woodworth (2014b). This notation depends on six astronomical arguments that progress quasi-linearly in time, *i.e.*, with nonlinear deviations on the scale of millennia (*e.g.*, Simon, 2007). The respective partial tide frequency can be obtained by $\omega_i = \partial_t \chi_i(t)|_{J2000}$, where J2000 signifies the currently used standard epoch (Julian date: 2451545.0 TT [Terrestrial Time]).
Here, $\tau(t)$ is the mean lunar time (period: T_τ = 24h 50m 28.3s =1 lunar day), $s(t)$ is the mean longitude of the Moon (T_s = 27.3216 d), $h(t)$ is the mean longitude of the Sun (T_h = 365.2422 d), $p(t)$ is the mean longitude of the lunar perigee (T_{p} = 8.847 yr), $N'(t)$ is the negative of the longitude of the Moon's mean ascending node ($T_{N'}$ = 18.613 yr) on the ecliptic, and $p_s(t)$ is the mean longitude of the solar perigee (T_{p_s} = 20941 yr) (Agnew, 2007). These arguments are multiplied with the integer values, q_1^i to q_6^i, characteristic of each tidal constituent and define the phase progression. Within, the frequency band of the tide is determined by q_1^i, which is always identical to the spherical harmonic order m. The presented temporal harmonic decomposition of the TRP into a series of constituents allows an undisturbed view of its spectral composition. Individual constituents are called *partial tides* and are referred to by the multipliers q_1 to q_6 that are usually presented in the form of *Doodson codes* that are noted as '$q_1(5{+}q_2)(5{+}q_3)\boldsymbol{.}(5{+}q_4)(5{+}q_5)(5{+}q_6)$'.
Doodson designed this notation to be handy and robust, as for all but the lowest amplitude

[3]The indices l, m are dropped in the following, as the index i unambiguously defines the tidal constituent.

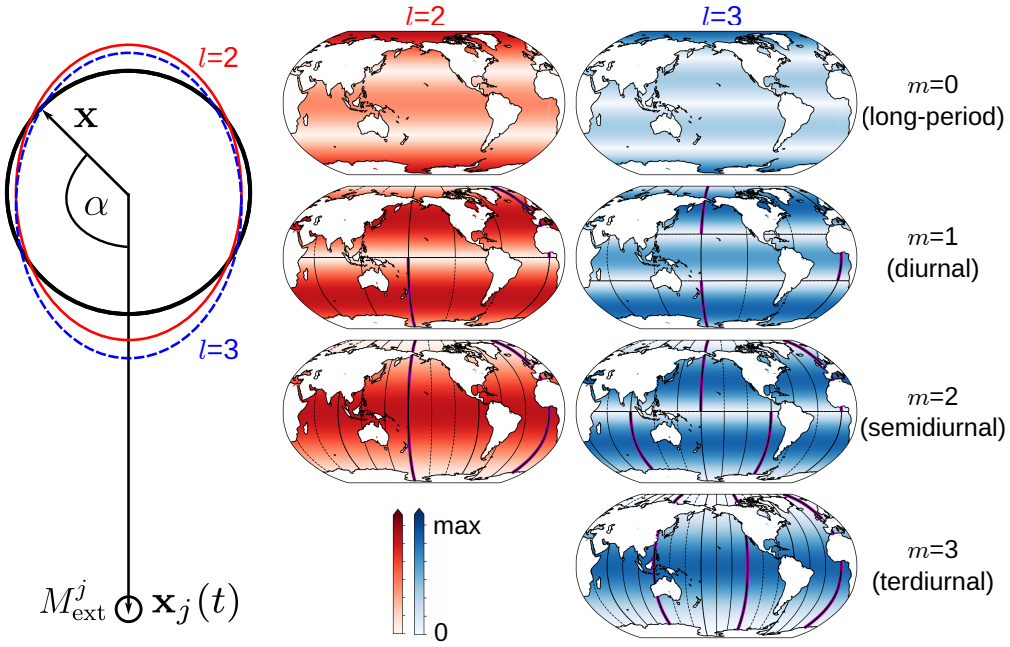

Figure 2.2: The TGP exerted by an external mass M^j_{ext}, denoted V^j_{grav}, for maximum spherical harmonic degrees $l = 2$ (red) and $l = 3$ (blue) at radius $|\mathbf{x}| = R_{\text{e}}$ (left). Temporal and spherical harmonic development of the TGP leads to the description of the TGP by tidal constituents that are proportional to the spherical harmonic functions Y_{lm} (right). The plots show the amplitude of the spherical harmonic functions $\sim \overline{P}_{lm}(\sin\phi)$ color coded for $l = 2$ (red) and $l = 3$ (blue). Overlain, the phase-shift with respect to Greenwich-zero $\phi^m_i + \lambda^{lm}_G$ (magenta) is plotted in increments of 60° (negative values are dashed).

partial tides $q_1 = 0, 1, 2, 3$ and $-5 < q_{2\ldots6} < 5$, which allows codes with throughout positive digits (no need to write down $\pm$, which can induce confusion). Further, the characteristic frequencies associated with each multiplier are chosen to be widely separated in frequency space. Hence, Doodson codes sort constituents effectively after their frequencies. Partial tides are assigned a *tidal species* referring to their first multiplier q_1, as it defines the character (long-period, diurnal, semidiurnal, ...). The first two multipliers define a *tidal group*, as tides with identical q_1 and q_2 only differ in frequency on the order of a few cycles per year (cpy).

For example, the principal semidiurnal lunar tide[4], M_2, is assigned the Doodson code 255.555, while the main solar semidiurnal tide, S_2, is referred to as 273.555. The employed notation allows the immediate insight that the frequency of S_2 is larger than that of M_2. The here ad-hoc introduced labels M_2 and S_2 are historic notations for the larger partial tides and implicitly refer to a defined Doodson code[5]. An overview of the tidal constituents with the largest amplitude is presented in Table E.1 alongside historical labels and Doodson codes.

[4] M_2 is the ocean tide with the strongest global mean signal. Therefore, it appears at the center of most discussions.

[5] The letters initially refer to 'fictional stars' on simplified orbits, which can be thought of as generating the respective tidal frequencies.

So far, the seventh argument, q_7, was spared from the discussion. This last multiplier only takes integer values that induce an additional phase shift in increments of $\frac{\pi}{2}$ and is referred to as the Doodson-Warburg phase convention (cf. Petit and Luzum, 2010). A detailed formula for tides up to degree $l = 3$ is given by[6]

$$q_7^{ilm} = 2\tan^{-1}\left(S_i^{lm}, C_i^{lm}\right)\pi^{-1} + 2\delta_{m0} + 2\delta_{m1}\delta_{l3} \ , \tag{2.7}$$

where the Kronecker-δ as the discrete formulation of the Dirac-δ-function was introduced. It is defined by $\delta_{nm} = \{1, \text{if n=m}; 0, \text{else}\}$.
We recall that $\chi_i(t) = \chi_i'(t) + q_7^{ilm}\frac{\pi}{2}$. While the first term of Equation (2.7) is just the phase of the partial TGP for $\chi'(t) = 0$ (cf. Equation 2.4), $\lambda_G^{lm} = -2\delta_{m0} - 2\delta_{m1}\delta_{l3}$ represents an additional phase shift that was historically introduced to ensure positive values of the partial TRP for $\lambda = 0$ (*The Greenwich-zero*) at the equator, or just north of the equator for $\chi'(t) = 0$. While this phase convention might appear to introduce unnecessary complications, it simplifies local comparisons of tidal regimes from different partial tides, as phases are measured with respect to a fixed phase of the TGP, which is an advantage to understanding ocean resonances.
Additionally, the alternate form for the individual partial TRPs (2.5)[7]

$$V_{\text{tid}}^{ilm}(\phi, \lambda, t) = a_l^{\text{b}}(\omega_i)\ A_i\ \left(Y_{lm}(\phi, \lambda)\ \cos\chi_i(t) - Y_{l-m}(\phi, \lambda)\ \sin\chi_i[t]\right)\ , \tag{2.8}$$

is presented, which separates the temporal and spatial variables. Further, the in-phase and quadrature components of the partial potential, $c_i^{lm}(\mathbf{x}) = a_l^{\text{b}}(\omega_i)A_iY_{lm}(\phi, \lambda)$ and $s_i^{lm}(\mathbf{x}) = -a_l^{\text{b}}(\omega_i)A_iY_{l-m}(\phi, \lambda)$ are introduced, as well as the amplitude $a_i^{lm}(\sin\phi) = a_l^{\text{b}}(\omega_i)A_i\overline{P}_{lm}(\sin\phi)$ and the phase shift $\phi_i^m(\lambda) = m\lambda$, which allows reformulating Equation (2.8) as

$$V_{\text{tid}}^{ilm}(\phi, \lambda, t) = a_i^{lm}(\sin\phi)\cos\left(\chi_i(t) - \phi_i^m[\lambda]\right) = c_i^{lm}(\mathbf{x})\cos\chi_i(t) + s_i^{lm}(\mathbf{x})\sin\chi_i(t)\ . \tag{2.9}$$

Equation (2.9) summarizes the complementary amplitude/phase vs. in-phase/quadrature notations used to describe tidal oscillations. While the in-phase/quadrature notation depicts real physical fields obtained at $\chi_i = 0$ and $\chi_i = \frac{\pi}{2}$, respectively, the amplitude/phase-notation facilitates the perception of large-scale oscillation patterns. It is used for representation within this thesis. Figure 2.2 shows the partial TRPs for different species (order m) and degrees l of the spherical harmonic functions, with the zero meridians in magenta colors. The following discussion refers to this figure.
The spherical harmonic development of the TRP (2.5) is typically truncated at a certain maximum degree l_{max}, as the magnitude of individual constituents decreases with $\left(\frac{R_e}{|\mathbf{x}_j|}\right)^{l-2}$, when compared to $l = 2$. Nonetheless, geodetic observations show that lunar contributions up to order $l = 3$ are evident for ocean tides (and even up to higher degrees for solid Earth tides). Therefore, the TRP up to $l_{max} = 3$ is considered within this thesis.
Equation (2.5) highlights that for m>0, the TRP is composed of a series of westwards propagating partial waves, with individual frequencies but spatial patterns that follow the spherical harmonic functions.
On the other hand, the long-period species (for $m = 0$) are zonally uniform, only exhibit-

[6] $\tan^{-1}$ has to be evaluated by means of the *atan2*-function that was first introduced in Fortran.
[7] The identity is easily obtained by considering $\cos(a + b) = \cos a\cos b - \sin a\sin b$.

ing gradients in the meridional direction. For a partial tide of a given degree l and order m, there is but one characteristic spatial pattern, *i.e.*, $\boldsymbol{\psi}_{lm} = \boldsymbol{\nabla} Y_{lm}$, in which barotropic (depth-independent) acceleration is applied to the water masses. As, for example, the previously mentioned gravitational partial tides M_2 and S_2 stem from the same species of degree-2 tides, they are forced with the same pattern. Differences in the ocean response will only arise from the sensitivity of OTD to the respective forcing frequencies.

2.1.2 Radiational Excitation

While studying tides in the atmosphere is an independent research field with a rich history and important implications for geosciences, it is only touched superficially within this thesis concerning its relevance for OTD. For deeper insight into the topic, it is referred to, *e.g.*, Schindelegger et al. (2023) and Chapman and Lindzen (1970).
It is primarily the periodically-modulated absorption of solar UV radiation by ozone and infrared radiation by water vapor that which excites atmospheric tides (Chapman and Lindzen, 1970; Dieminger et al., 1996). However, secondary excitation mechanisms that include gravitational forces (cf. the previous subsection) and interaction with the ocean and solid Earth tide induce atmospheric tidal dynamics. Especially the interaction with the ocean tide displaces the lower boundary of the atmospheric layer, induces tidal winds over broad shelf regions, and disturbs the atmosphere by secondary gravitational potentials (*e.g.*, Renault and Marchesiello, 2022; Platzman, 1991). These contributions are of high significance for the atmospheric lunar M_2 tide (*e.g.*, Schindelegger and Dobslaw, 2016; Schindelegger et al., 2023), as already noted by (Laplace et al., 1798).
Because the discussion focuses on the effects of atmospheric tides on the ocean, the atmospheric tides are assumed to be independent of OTD. Thus, the gray-colored feedback loop in Figure 2.1 is not self-consistently considered in contrast to fully-coupled atmosphere-ocean models (*e.g.*, Hollingsworth, 1971). Instead, accelerations of atmospheric origin are treated as invariant concerning OTD.
In general, atmospheric dynamics contain signatures with a broad frequency range. However, a significant part of the variability oscillates with tidal frequencies, especially in the tropics (Ray, 1998b). The dominant atmospheric variable excites tide-like signals in the ocean is the atmospheric surface pressure anomaly p_{atm}, which induces a barotropic, *i.e.*, depth-independent acceleration of the ocean. Thus, the forces exerted by atmospheric pressure variations are gradient forces to be derived from the respective potential $V_{\mathrm{p}} = -p_{\mathrm{atm}} \rho_{\mathrm{sw}}^{-1}$. Further, tidal winds periodically apply a wind stress acceleration $\boldsymbol{W}$ to the ocean surface. This acceleration is concentrated on the ocean surface, with weakened drag accelerations acting on deeper ocean layers and thus depth-dependent. Therefore, a barotropic response is not to be expected *ex-ante*. Even more, ocean mixing and excitation of internal ocean dynamics that cannot be resolved within the framework of the barotropic SWE are known to be driven by wind stress (*e.g.*, Pollmann, 2020).
Nonetheless, a reasonable parameterization can include the mean effect of wind stress excitation on the barotropic momentum balance in the SWE (2.1), which is done following Gill (1982), reading

$$\boldsymbol{a}_{\mathrm{atm}} = \boldsymbol{\nabla} \left(V_{\mathrm{p}} + V_{\mathrm{l}} + V_{\mathrm{o}} \right) + \mathbf{W} \ . \tag{2.10}$$

In addition to the atmospheric pressure potential and the wind stress accelerations, the secondary potentials V_{o} and V_{l} were added, which comprise two effects. First, the grav-

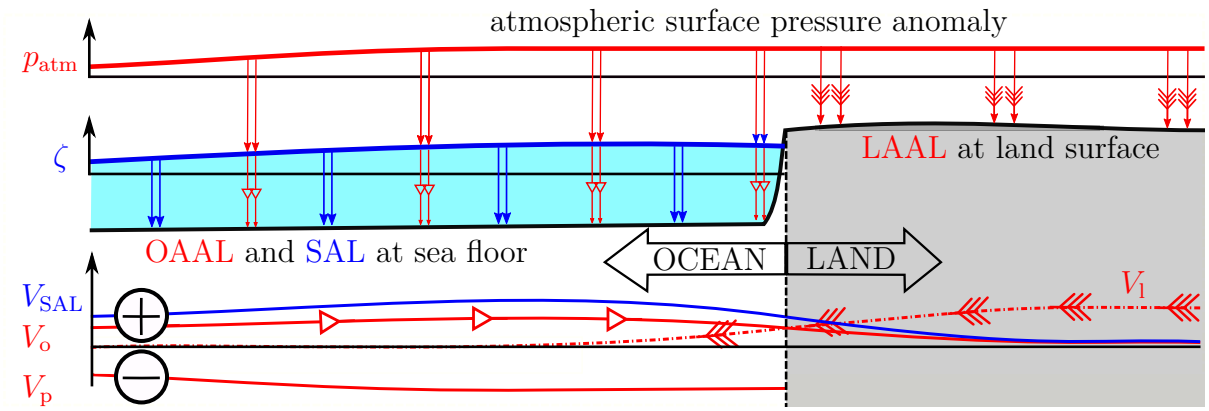

Figure 2.3: Primary and secondary barotropic potentials generated by the atmospheric surface pressure anomaly p_{atm} (red), acting on the ocean surface (V_{p}, $\ominus$), the seafloor by OAAL (V_{o}, triangle, $\oplus$), and the land surface by LAAL (V_{l}, arrow, $\oplus$). Further, the SAL potential induced by the sea surface anomaly ζ (blue) is depicted (V_{SAL}, $\oplus$). The signs $\oplus/\ominus$, signify whether a positive anomaly induces an attractive or repulsive potential.

itational potential that the atmosphere exerts on the ocean masses, *i.e.*, *atmospheric attraction*, and second, the gravitational potential induced due to the deformation of the solid Earth by *atmospheric loading*. Here, both effects are discriminated into a part that originates from atmospheric pressure on the ocean floor (denoted o) or the land-covered areas (denoted l) and consequently called ocean-bound/land-bound atmospheric attraction and loading (OAAL and LAAL, cf. Figure 2.3). The same effect arises from ocean bottom pressure anomalies $\delta p = g_0 \rho_{\mathrm{sw}} \zeta$ due to the propagation of ocean tidal waves and is called Self-attraction and Loading (SAL) (Farrell, 1972; Kuhlmann et al., 2011; Schindelegger et al., 2018), which will be discussed in the next section.
Atmospheric secondary potentials are calculated by

$$V_{l/o}(\mathbf{x}) = -\frac{3\rho_{\mathrm{sw}}}{\rho_{\mathrm{se}}} \sum_{l,|m|\leq l} \frac{\alpha_l}{2l+1} V_{\mathrm{l/o}}^{lm}\, Y_{lm}(\mathbf{x}) \;, \tag{2.11}$$

where $\rho_{\mathrm{se}} = 5510 \frac{\mathrm{kg}}{\mathrm{m}^3}$ is the mean density of the solid Earth, and $\sum_{l,|m|<l} V_{\mathrm{l/o}}^{lm} Y_{lm}(\mathbf{x})$ is the decomposition of $V_p M_{\mathrm{l/o}}$ into a set of real-valued spherical harmonic functions, with $M_{\mathrm{l/o}}$ being the mask comprising wet (for o), or dry (for l) grid cells. Here, and in the following, a spherical, non-rotating, elastic, and isotropic (SNREI) Earth (*e.g.*, Agnew, 2012) is assumed.
Factor $\alpha_l = 1 + k_l - h_l$ describes the effect per spherical harmonic degree l, where the direct gravitational attraction by the atmosphere is proportional to 1. Further, k_l and h_l are load Love numbers (LLNs, *e.g.*, Munk and MacDonald, 1960) that describe the loading potentials, that is, the gravity potential induced by the Earth's deformation and the Earth's surface deformation in its static gravity field, respectively. Depending on the selected solid Earth model, α_l converges to approximately $\alpha_\infty \approx 6.4$. Thus, the atmospheric loading components dominate the attraction aspect for large degrees.
While a positive atmospheric pressure anomaly leads to a repulsive, direct potential for

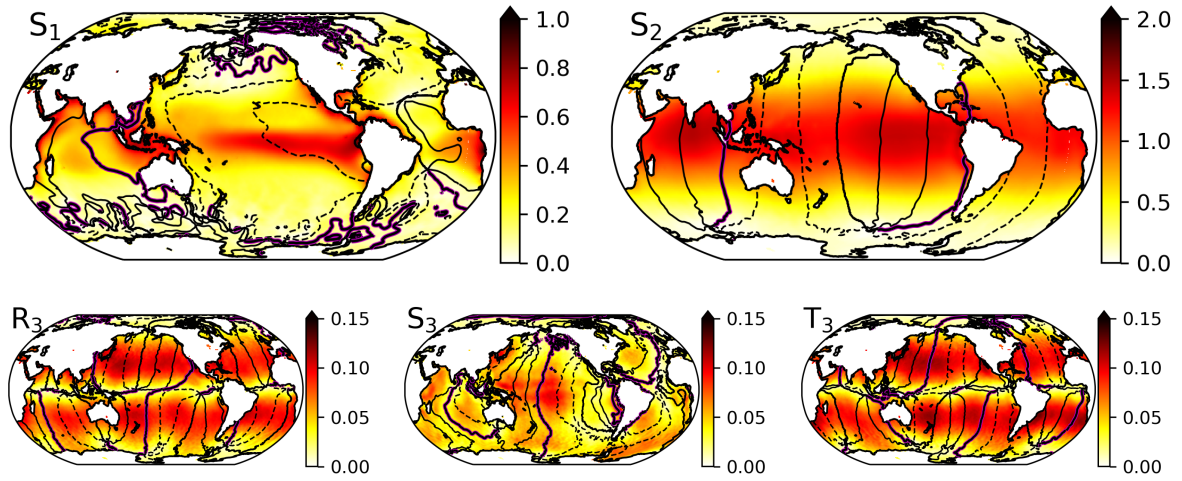

Figure 2.4: Amplitude a_i^{atm}/g_0 of the atmospheric surface pressure potential (in cm) for tides S_1 (top, left), S_2 (top, right), and the terdiurnal triplet (R_3-S_3-T_3, bottom), *i.e.*, tidal periods of 1, $\frac{1}{2}$, and $\frac{1}{3}$ solar days, respectively. The lines R_3 and T_3 are shifted by $\pm 1\mathrm{yr}^{-1}$ compared to the S_3 frequency and induce a seasonal modulation of the terdiurnal solar tide. Phase lags ϕ_i^{atm} are plotted in increments of 60° (magenta: $\phi = 0°$; dashed: $\phi < 0°$). Reproduced from Balidakis et al. (2022).

the ocean masses, the secondary potentials V_{o} and V_{l} exert attractive forces dominated by Y_{lm} of low degree l, as high degrees lead to smaller contributions in Equation (2.11). This long-wavelength character is visible as a smoothing of the respective secondary potentials (cf. Figure 2.3) and causes the potential V_{l} to be evanescent towards the ocean's interior[8].

An in-depth discussion of the four unique atmospheric excitation mechanisms (pressure forcing, LAAL, OAAL, and wind stress) for the S_1-tide can be found in Balidakis et al. (2022). They find that including secondary effects impacts the ocean tide simulations at the 10%-level of the ocean tide signal. A straightforward approach to estimate tidal atmospheric forcing potentials is to analyze long time series of the variables of interest (surface pressure and wind stress) for tidal frequency components, *i.e.*, conducting a *tidal analysis*. The method of tidal analysis has a potent advantage over analyzing the time series through a Fourier transform: The a-priori-knowledge of the tidal frequencies described by the Doodson-formalism (cf. Equation 2.6) reduces the unknown variables and allows the *Super-resolution of tides* (Munk and Hasselmann, 1964). Thus, when conducting a tidal analysis, the resolvability of 2 tidal constituents depends not only on their frequency difference δf and the time series length but also on the noise level and noise color of the time series. This often implies a better resolvability than predicted by the Rayleigh criterion.

Given the availability of multiple decades of high-accuracy atmospheric reanalysis products

[8]The same 'leakage-effect' of ocean-bound potentials into the continental interior is the reason for the detectability of ocean tides by terrestrial observation, *e.g.*, with GNSS-stations or gravimeters.

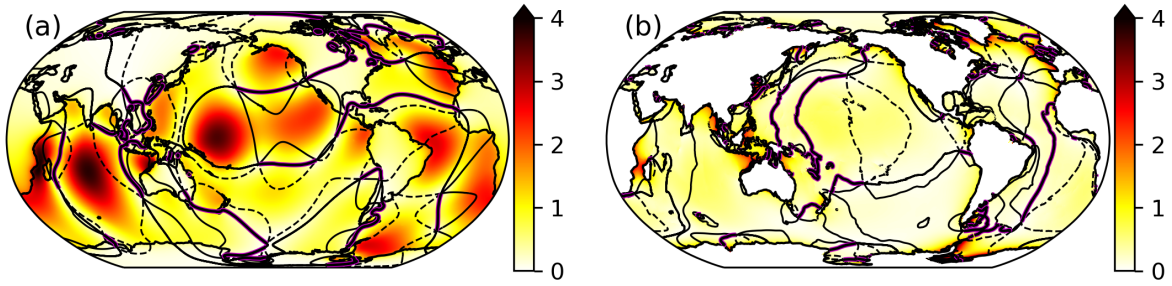

Figure 2.5: Equilibrium potential height $a_i^{\mathrm{SAL}}(\mathbf{x})$ of the SAL potential $\zeta_{\mathrm{SAL}} = a_i^{\mathrm{SAL}}(\mathbf{x}) \cos\left(\chi_i(t) - \phi_i^{\mathrm{SAL}}[\mathbf{x}]\right)$ in cm, constructed by spherical harmonic evaluation up to degree $l_{max} = 1024$ for the S_2-tide of the FES14 ocean tide atlas (a). The difference potential between (a) and the scalar-approximated SAL potential, $\zeta_{\mathrm{SAL}} = 0.1\zeta$ is presented in (b). Phase lags ϕ_i^{SAL} are plotted in increments of 60° (magenta: $\phi = 0°$; dashed: $\phi < 0°$).

(*e.g.*, ERA5: Hersbach et al., 2020), it is possible to extract harmonic constituents

$$V_{\mathrm{p}}(\mathbf{x}, t) = \sum_i a_i^{\mathrm{atm}}(\mathbf{x}) \cos\left(\chi_i(t) - \phi_i^{\mathrm{atm}}[\mathbf{x}]\right) = \sum_i c_i^{\mathrm{atm}}(\mathbf{x}) \cos\chi_i(t) + s_i^{\mathrm{atm}}(\mathbf{x}) \sin\chi_i(t) \ , \tag{2.12}$$

where $a_i^{\mathrm{atm}} = \sqrt{(c_i^{\mathrm{atm}})^2 + (s_i^{\mathrm{atm}})^2}$ is the amplitude, $\phi_i^{\mathrm{atm}}(\mathbf{x})$ is the phase lag, while $c_i^{\mathrm{atm}}(\mathbf{x})$ and $s_i^{\mathrm{atm}}(\mathbf{x})$ are the in-phase and quadrature components of the partial potential, respectively. This representation relates directly to Equation (2.9), with amplitude and phase-lags represented in Figure 2.4 after Balidakis et al. (2022), who identified 16 atmospheric partial tides with relevant effects on ocean tide excitation and satellite gravimetry. Within, the strongest pressure variations occur at the semidiurnal S_2-frequency ($T_{S_2} = 12$ h), showing a pattern that resembles the gravitational excitation proportional to $\overline{P}_{22}$ with minor deviations. More pronounced differences are obtained for the S_1 potential ($T_{S_1} = 24$ h), which is in contrast to its gravitational counterpart mainly of equatorial character. As the solar excitation has the shape of a smoothed box function (Schindelegger et al., 2023), semidiurnal, terdiurnal ($T_{S_3} = 8$ h), and also higher-frequency atmospheric tides generate overtones of the S_1 ocean tide.
This section is closed by comparing the ocean tide-generating forces originating from the atmosphere to the direct gravitational excitation, exemplarily for S_2. The maximum value for the S_2 gravitational equilibrium height (cf. Figure 2.2) is obtained at the equator and amounts to 7.8 cm. The maximum atmospheric potential is smaller than 2 cm (cf. Figure 2.4). Thus gravitational excitation dominates, while the atmospheric potential represents a significant correction (Arbic, 2005). On the other hand, the SAL potential introduced along the way in Figure 2.3 exhibits maximum equilibrium values of approximately 4 cm for S_2, thus representing a major modification of the exciting potential. Therefore, it is an essential process for OTD and the subject of the next section.

2.1.3 Secondary Forces: Self-Attraction and Loading

Already Pierre-Simon de Laplace was aware of the significance of the secondary gravit-

ational potential induced by the redistribution of ocean mass itself (Laplace et al., 1798). On the other hand, the theory of solid Earth tides that is essential to formulate the solid Earth response to variations of ocean bottom pressure needed to be further advanced. Thus, Laplace's formulation only expressed the gravitational self-attraction of ocean water. With the development of geoscientific disciplines in the 19th and 20th centuries, understanding of the phenomenon of solid Earth tides, which allows for the correct formulation of the TRP and the accurate prediction of long-period (equilibrium) tides, was accumulated (*e.g.*, Thomson, 1863; Lau and Schindelegger, 2023). At the same time, insight into the deformation of the solid Earth under surface loads grew persistently (Henderschott, 1972). The inauguration of the first automatic computers that could solve the LTE for realistic basin geometries enabled comparisons of modelling results to geodetic data. Thereby, it was recognized that this effect, called *ocean loading*, had a profound impact on OTD (Cartwright, 1999).
Today it is well established that the SAL potential height

$$\zeta_{\mathrm{SAL}}(\mathbf{x}) = \frac{3\rho_{\mathrm{sw}}}{\rho_{\mathrm{se}}} \sum_{l,|m|\leq l} \frac{\alpha_l}{2l+1}\, \zeta_{lm} Y_{lm}(\mathbf{x}) \;, \tag{2.13}$$

must be rigorously considered in order to render the most accurate depiction of ocean tide physics possible (Ray, 1998a). The formulation is structurally identical to Equation (2.11), where the atmospheric attraction and loading potential were introduced. Technically, the formulation considers the decomposition of the sea surface anomaly function into spherical harmonic functions (the eigenfunctions of the gravity field), *i.e.*, $\zeta(\mathbf{x}) = \sum_{l,|m|<l} \zeta_{lm} Y_{lm}(\mathbf{x})$. As for atmospheric attraction and loading, factor $\alpha_l = 1 + k_l - h_l$ is a combination of load Love numbers.
In contrast to the TGP introduced in Equation (2.2), series (2.13) cannot be terminated at a low spherical harmonic degree l_{max} without inducing significant errors for two reasons. First, individual contributions are only weakly dampened with $(2l+1)^{-1}$, and second, the degree-wise sea surface height elements ζ_{lm} possess relevant amplitudes at large degrees due to the scale of tidal oscillation systems and the occurrence of Gibb's Phenomenon at coastal margins.
The root cause for Gibb's phenomenon is the typically large ocean tide amplitude in coastal regions and the obvious absence of OTD on the land, which translates to a discontinuous ocean load function. However, discontinuities are known to be non-representable by (spherical) harmonic functions, retaining at least a 9% deviation in its vicinity regardless of the maximum degree l_{max}.
Conveniently, $\alpha_l/(2l+1)$ decreases with rising degree l, ensuring slow but steady convergence, thus counteracting *Gibbs Phenomenon* at coastal load discontinuities (Agnew, 2007; Hewitt and Hewitt, 1979).
The inclusion of Equation (2.13) converts the LTE into an integrodifferential equation, as the spherical harmonic coefficients

$$\zeta_{lm} = \int_O dA'\; \zeta(\mathbf{x}')\; Y_{lm}(\mathbf{x}') \tag{2.14}$$

have to be calculated at each time step (in contrast to the atmospheric attraction at loading) by solving respective global integrals over the entire ocean domain O. In other

words, SAL induces the interaction of OTD at an arbitrary location with each point on the globe, which renders the PDE non-local. In a numerical sense, the matrices describing OTD become non-sparse (even fully populated), drastically complicating their inversion. While numerical aspects of the LTE are discussed in the next chapter, the computational complications due to SAL potential are already pointed out here because they gave rise to the introduction of several approximations of Equation (2.13), which are still important for modern numerical models.

While the weighting of individual contributions in Equation (2.13) is performed with a factor depending on the spherical harmonic degree l, a straightforward approach is to introduce a general factor ϵ, which is independent of l, but chosen to approximate the function optimally. The potential height is then formulated as $\zeta_{\mathrm{SAL}} \approx \epsilon\zeta$ for typical values of $0.08 < \epsilon < 0.12$ (*e.g.*, Accad and Pekeris, 1978; Weis et al., 2008; Velay-Vitow et al., 2020). This approximation implicitly assumes a dominant spatial scale of tidal oscillation systems, which can be a powerful approximation for tides in basins of comparable depths. As ϵ is usually chosen to accurately depict tides in the deep ocean, the ϵ-approximation introduces larger errors in shallow shelf regions, where tidal waves have shorter wavelengths (cf. Figure 2.5b). Possible ways to improve the approach are to include depth or latitude-dependent parametrizations (*e.g.*, Ray, 1998a; Stepanov and Hughes, 2004; Müller, 2007).

A second feasible approach is to compute ζ_{SAL} from an external, reasonably accurate tidal solution prior to solving the PDEs (*e.g.*, Lyard et al., 2021; Blakely et al., 2022). This means treating SAL in the same way as the atmospheric excitation (Section 2.1.2). This only imposes the need to evaluate Equation (2.13) once per model run instead of once per time step. On the other hand, this approach heavily constrains the obtained ocean tide solution to the adapted SAL potential: The simulation results can not be considered independent of prior assumptions, a central requirement of O1. Figure 2.5 shows ζ_{SAL} computed from the satellite data-constrained ocean tide atlas FES14 for S_2, *i.e.*, an altimetry-constrained estimate, and the deviations to the ϵ-approximation also computed from FES.

To retain the independence of simulation results from prior assumptions, one can construct ζ_{SAL} from prior solutions of the employed model. This implies iteratively simulating sea surface height anomalies ζ, and SAL potential heights ζ_{SAL}, *i.e.*, self-consistently solving for ζ_{SAL} (*e.g.*, Ray, 1998a; Accad and Pekeris, 1978). As ζ and ζ_{SAL} depend linearly on each other, the solution is unique, and the procedure converges within a few iterations (Egbert et al., 2004).

While the described approximations work well within their inherent restrictions, the most exact approach remains to repeatedly recompute Equations (2.13) and (2.14). With recent software developments (*e.g.*, Schaeffer, 2013), this more comprehensive SAL approach became computationally feasible (Schindelegger et al., 2018) and will be discussed in more detail later.

2.1.4 Equilibrium Tides

The discussion of the individual tide-generating forces is concluded by introducing the previously mentioned equilibrium tide solutions. Except for the wind stress acceleration $\boldsymbol{W}$, which only faintly affects OTD (Ray and Egbert, 2004; Balidakis et al., 2022), all

excitation mechanisms in Equation (2.1) are gradient forces[9]. In the limit $\mathbf{v} \to 0$, the PDEs reduce to

$$\begin{aligned} g_0 \boldsymbol{\nabla} \left(\zeta_{\mathrm{seqt}} - \zeta_{\mathrm{SAL}} - \zeta_{\mathrm{eq}} - \zeta_{\mathrm{atm}} \right) &= 0 \ , \\ \text{and} \quad \int_O dA \ \zeta(t) &= 0 \ . \end{aligned} \tag{2.15}$$

Here, $\zeta_{\mathrm{atm}} = (V_{\mathrm{p}} + V_{\mathrm{l}} + V_{\mathrm{o}})/g_0$ is set. A solution is obtained by setting

$$\zeta_{\mathrm{seqt}}(\mathbf{x}, t) = \zeta_{\mathrm{eq}}(\mathbf{x}, t) + \zeta_{\mathrm{atm}}(\mathbf{x}, t) + \zeta_{\mathrm{SAL}}(\zeta_{\mathrm{seqt}}[\mathbf{x}, t]) + c_{\mathrm{m}}(t) \ . \tag{2.16}$$

The time-dependent but spatially-uniform parameter $c_{\mathrm{m}}(t)$ is called *Darwin's correction* and must be included to ensure mass conservation (*e.g.*, Marchuk and Kagan, 1983).
The integrodifferential character of SAL remains the major complication in evaluating Equation (2.16), as the solution ζ_{seqt} must be solved self-consistently with the induced SAL potential $\zeta_{\mathrm{SAL}}(\zeta_{\mathrm{seqt}})$. Therefore, the solution is called *Self-Consistent Equilibrium Tide* (SEQT). Finding the SEQT for a given potential is possible by iterative evaluation of Equation 2.16 under consideration of mass conservation.
Due to frictional forces in the ocean, the assumption $\mathbf{v} \to 0$ is reasonable if the tidal period is sufficiently long, allowing the described balance between generating potential and $\boldsymbol{\nabla}(g_0 \zeta_{\mathrm{seqt}})$ to adjust. The typical ocean response timescale to tidal forcing is in the order of hours to days (*e.g.*, Müller, 2007). Ocean tides are close to equilibrium for long-period tides with timescales on the order of weeks and longer. Hence, the SEQT description is often employed for those tides, especially for solar long-period tides ($\mathrm{S_{ta}}$, $\mathrm{S_{sa}}$, $\mathrm{S_a}$) and longer-periods (*e.g.*, Ω_1, cf. Table E.1). Following Equation (2.16), the SEQT is proportional to its generating potential with a minor modification by SAL. Therefore, gravitational SEQTs strongly resemble the patterns displayed in Figure 2.2. Significant deviations exist for the fortnightly tide $\mathrm{M_f}$, for which the ocean response exhibits deviations from equilibrium, presumably due to the excitation of ocean oscillations driven by the conservation of vorticity (Wunsch, 1967; Cartwright and Ray, 1990).
While the deviations observed for $\mathrm{M_f}$ point to the importance of dynamic effects in the ocean's response to tidal forcing, the equilibrium description breaks down in predicting the ocean response for diurnal, semidiurnal, and higher-frequency tides. Here the ocean response does not resemble the patterns of its generating potential (cf. Figure 2.2). Description by the dynamic theory, *i.e.*, for non-vanishing velocity $\mathbf{v}$, is required, which is reviewed in the following section.

2.2 Dynamical Ocean Tides

Since the dynamics of the ocean itself are not sufficiently considered in equilibrium tide theory, its predictions of diurnal and semidiurnal tidal species are rather imprecise. Laplace then recognized the absence of hydrodynamic principles, hence founding the LTE. In their original form, the LTE (cf. Equation 2.1) describe the acceleration of a shallow geofluid by tide-generating forces. Also, the LTE consider Coriolis accelera-

[9]Effectively, the wind stress can be decomposed into a curl-free (gradient) and a divergence-free (rotational) component employing a *Helmholtz decomposition*.

tion while ensuring the conservation of ocean mass in terms of the continuity equation. Analytical solutions of the LTE are only possible for simplified bathymetric functions (*e.g.*, water planets and cylindrical basins). While the realistic ocean depth and coastline are much more complicated, analytical solutions are invaluable to understanding the fundamental characteristics of tidal waves. Thus, the field of theoretical hydrodynamics has benefited from the work of many scientists, starting with Laplace himself, but also by William Thomson, known as Lord Kelvin (Thomson, 1879), Sir Horace Lamb, Sydney Samuel Hough, and many others (Cartwright, 1999). A short review of the theory of ocean normal modes as the result of a more analytical approach to OTD is presented in Section 2.2.2.
In their initial form, the LTE lack frictional forces, *i.e.*, forces that inherently remove mechanical energy from the hydrodynamic system. While friction is a realistic assumption for any natural system, it also has important implications for the stability of the LTE. Laplace further realized that due to friction, any information about the initial state vanishes from the system over a long time, *i.e.*, the periodically forced dynamics of the world oceans converge to the same periodicity as the forces that drive it. While this fact seems straightforward from a modern point of view, it is the basis for the procedure of harmonic tidal analysis. On the other hand, the correct formulation of dissipative terms of OTD is complicated and has been one of the main challenges for tidal scientists in the last two centuries. Section 2.2.1 discussed frictional forces, where nonlinear contributions are included. Together with other nonlinear terms retained when rigorously deriving the LTE, the dynamic theory of ocean tides is rendered weakly nonlinear, which causes the interaction of individual partial tides (Section 2.2.3).

2.2.1 Tidal Friction

It can be verified with the help of modern numerical ocean tide models that the realistic representation of tidal friction, and thus tidal dissipation rates, is critical to accurately reproduce geodetic observations of ocean tides (similar to the impact of SAL).
However, long before the advent of the first global ocean tide models, the historical interest in tidal dissipation rates was more strongly motivated due to its influence on the evolution of Earth-Moon-Sun system. Especially the lunar orbit is not only impacted by Newtonian orbital mechanics (Laplace, 1788), but also by tidal friction that transfers angular momentum from the Earth's rotation to the lunar orbit (*e.g.*, Darwin, 1908). Thus, ancient observations of eclipses and modern measurements of, *e.g.*, the length of the day and month and the lunar distance allow for estimating the system's long-term evolution (Cartwright, 1999).
While quantifying the orbital (non-tidal) influences on the Earth-Moon history was subject to intense scientific debates (Kushner, 1989), these estimates translate to the magnitude of tidal dissipation necessary to sustain the observed orbital evolution. The tidal dissipation estimates converged during the 20th century. Thus, the question of how and where the energy is dissipated came to the center of attention. The understanding of tidal friction and dissipation is one of the most persistent enigmas of ocean tide research as discussed, *e.g.*, successively by Jeffreys (1920), Munk (1968), and Munk (1997). In the following, the dominant dissipation mechanisms are introduced.

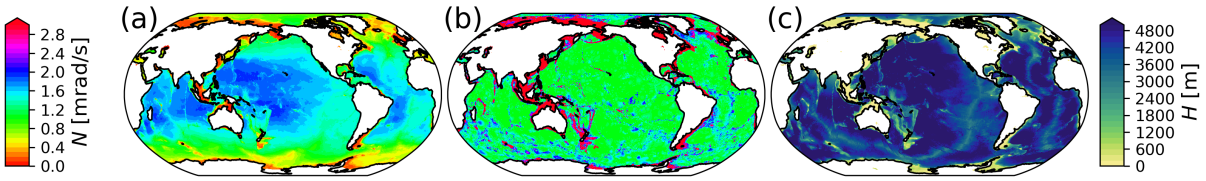

Figure 2.6: The mean buoyancy frequency $\overline{N}$ (a) and bottom buoyancy frequency N_b (b) represent a measure of the ocean stratification. Subplot (c) shows the bathymetric map constructed from the RTopo-2 data set (Schaffer et al., 2016).

Turbulent Bottom Friction A modern estimate for the mean ocean tidal dissipation carried out by the lunar M_2 tide is 2.45 TW (Egbert and Ray, 2000), excluding tidal dissipation in the solid Earth (Ray et al., 2001) and atmosphere, that is much smaller. Governed by the laws of hydrodynamics, tidal flow velocities are small, on the order of $1\frac{\mathrm{cm}}{\mathrm{s}}$, in the deep ocean, and large, on the order of $50 - 150\frac{\mathrm{cm}}{\mathrm{s}}$, in shallow seas. Thus, the frictional interaction of tidal flows with the sea floor was the first energy sink that was investigated. The first studies that considered linear frictional accelerations in the Irish Sea, an area with well-documented surface currents, resulted in estimated global dissipation estimates far smaller than the astronomically observed value (Street, 1917). The turbulent nature of the tidal flow over the ocean bottom is better described by a quadratic friction law that induces a braking acceleration of the form

$$\boldsymbol{a}_\mathrm{bf} = \frac{r}{H}|\mathbf{v}|\ \mathbf{v}\ , \tag{2.17}$$

and thus leads to dissipation densities that scale with $|\mathbf{v}|^3$, resulting in two orders of magnitude higher dissipation rates in shallow seas, *e.g.*, the Irish Sea (Taylor, 1920). Here r is the bottom friction coefficient.
The quadratic bottom friction law leads to the concentration of ocean tide dissipation in only a few shelf regions and amounts to approximately $\frac{2}{3}$ of the M_2 dissipation under present-day conditions. It has become a routinely employed parametrization of for global, barotropic ocean tide models.
On the other hand, the nonlinear dependence on the state variables u and v contradicts the superposition principle of individual solutions that only holds for linear PDEs (Section 2.2.3). With proper tuning of the friction coefficient r, linearized parametrizations can realistically reproduce OTD, and linear friction laws are routinely employed to study selected aspects of the ocean tide (Section 2.2.2). Despite the improvements in estimating global dissipation by bottom friction, it was not possible to satisfactorily close the tidal energy budget by exclusively considering this single effect.

Topographic Wave Drag Historically, ocean tidal energy dissipation was believed to be dominated by turbulent bottom friction in shallow waters, *i.e.*, by the process described in the preceding paragraph. However, the development of precise, data-constrained ocean tide models enabled by several years of ocean observation by satellite altimetry made it possible to spatially resolve the ocean tide energy budget. This analysis showed that a

significant fraction of energy dissipation (approximately 30 % for M_2, but only 12% for diurnal tides) was carried out in the deep ocean (Egbert and Ray, 2000, 2001, 2003). Although these inversion techniques can only track the area where dissipation happens and not the responsible hydrodynamic process, it was assumed that the generation of internal waves by tides, *i.e.*, internal tides, was the dominant contributor.
Internal waves are oscillations of a stratified fluid with only a minor imprint on the free surface (*e.g.*, Wunsch, 1975), which nevertheless can be detected with modern altimetric techniques (*e.g.*, Zhao et al., 2011; Zaron, 2017). Significant conversion of barotropic wave energy to internal tides is achieved at prominent bathymetric features. At these locations, the barotropic current is partially diverted into the vertical direction. which excites internal waves – a prominent example is, *e.g.*, the Hawaiian Ridge (Zaron and Egbert, 2006). The feedback to the barotropic flow is of dampening nature and therefore described as topographic wave drag. However, the exact representation of this effect in barotropic ocean tide models is impossible: A baroclinic, depth-resolving approach is required to allow for the propagation of internal waves (*e.g.*, Arbic et al., 2012). Hence, the preferred approach is to include the mean effect of this process on barotropic motion in terms of a parametrization.
A general, linear representation of this dampening acceleration is

$$\mathbf{a_{wd}} = -\frac{1}{H}\boldsymbol{\mathcal{C}} \cdot \mathbf{v} \ , \tag{2.18}$$

a second-order wave drag tensor, denoted $\boldsymbol{\mathcal{C}}$, with possible off-diagonal elements multiplied by the flow velocity. Multiple wave drag formulations have been developed and successfully implemented in ocean tide models (*e.g.*, Green and Nycander, 2013). These formulations are derived from different approaches. Several formulations are scalar, *i.e.*, not-requiring four tensor elements, and some include an independent tuning parameter.
A common feature of all parametrizations is their dependency on the Brunt–Väisälä frequency (or buoyancy frequency), denoted N, and the ocean bathymetry. Figure 2.6 illustrates that optimum conditions for wave drag dissipation are found in the deep ocean in the vicinity of ridges. For this thesis, calculations with data from the world ocean atlas for salinity (Zweng et al., 2018) and temperature (Locarnini et al., 2019).

Parameterized Horizontal Eddy-Viscosity Sensitivity studies with modern ocean tide models propose that the previously mentioned processes dominate the ocean tidal energy budget and are sufficient to accurately represent OTD at levels of $80-90\%$ in the open ocean. As ocean dynamics are known to be turbulent, most tidal models considered dissipation by parametrized horizontal turbulence, a free parameter often used to optimize the model's agreement with geodetic data sets (*e.g.*, Weis et al., 2008).
The central reason to include the so-called eddy-viscosity term is the numerical stability of the model, which sets a lower limit for this effect depending on the grid resolution (*e.g.*, Egbert et al., 2004; Schindelegger et al., 2018). It is possible to formulate the term in different ways. The simplest might be a relaxation proportional to $\Delta\mathbf{v}$. Here, the more involved formulation

$$\mathbf{a}_{\mathrm{ed}} = \hat{\mathbf{R}}\mathbf{v} = \frac{A_{\mathrm{h}}}{R_{\mathrm{e}}^2}\left(\frac{\partial_\lambda^2}{\cos\phi} + \partial_\phi^2 - \tan\phi\ \partial_\phi - (1+\tan^2\phi)\right)\begin{pmatrix}\mathrm{u}\\ \mathrm{v}\end{pmatrix} 2\tan\phi\ \partial_\lambda \begin{pmatrix}\mathrm{v}\\ \mathrm{u}\end{pmatrix} \ , \tag{2.19}$$

utilized by Weis et al. (2008), is employed. It can be argued that the specific structure is not crucial when the eddy-viscosity coefficient A_h is minimized.
However, the exact formulation of this term will be more critical if this effect carries out a larger amount of dissipation.

Turbulent Ice Friction While the tropical and mid-latitudes are effectively free of sea ice, the polar seas are covered by floating ice masses that vary in their extent seasonally and over longer time scales. Further, the ice cover is only partially landfast (glaciers and shelf ice). Sea ice is adrift, *i.e.*, it possesses a relative velocity with respect to solid Earth and ocean, a process that was famously used by historical (Nansen, 1897) and modern-day expeditions across the Arctic Ocean (Nicolaus et al., 2022).
In a similar way as the ocean currents dissipate energy while streaking over the ocean bottom (Equation 2.17), a frictional interaction with floating ice masses occurs. Further, one should replace the barotropic flow velocity $\mathbf{v}$ with the relative velocity between ice and ocean flow $\mathbf{v}_{\mathrm{rel}} = \mathbf{v}_{\mathrm{ice}} - \mathbf{v}$. Thus, the introduced acceleration reads

$$\mathbf{a}_{\mathrm{ice}} \;=\; \frac{r_{ice}\, f_{\mathrm{ice}}}{H}\, |\mathbf{v}_{\mathrm{rel}}|\; (\mathbf{v}_{\mathrm{ice}} \;-\; \mathbf{v}) \tag{2.20}$$

The most basic approach to parameterize this effect is assuming doubled bottom friction, $r_{\mathrm{ice}} = r$, in ice-covered regions (ice cover: $0 < f_{\mathrm{ice}} < 1$). It should be noted that Equation (2.20) does not only introduce a dissipative acceleration proportional to $-\mathbf{v}$ but also a residual acceleration proportional to $\mathbf{v}_{\mathrm{ice}}$.
While the impact of turbulent ice friction is small on a global scale, regional effects can be much more substantial, which will be of interest for paleo tides under glacial conditions. Further, the periodic variation of the ice cover, especially in the Arctic region, leads to seasonal variations in frictional forces. Seasonal variations are also known to affect other dissipative forces and lead to the modification of tidal constituents by seasonal modifier (also called satellite) lines (*e.g.*, Müller et al., 2014; Schindelegger et al., 2022). Here, energy is transferred to tidal frequencies, separated by 1 cpy from M_2.
The presented dissipation mechanisms will be revisited when introducing the ocean tide model in the next chapter. However, analytical solutions of the tidal PDEs are of interest to understand the mechanisms that control OTD. To fathom these principles, a linear approximation of Equations (2.1) is discussed in the following section.

2.2.2 Linearized Ocean Tidal Dynamics

Consider the linear set of equations (Müller, 2008; Zahel, 1980)

$$\partial_{\mathrm{t}}\mathbf{v} + \mathbf{f}\times\mathbf{v} + g_0\nabla\left(\zeta - \zeta_{\mathrm{SAL}}\right) + \mathbb{D}_{\mathrm{lin}}\mathbf{v} \;=\; \boldsymbol{F}^{\omega}\;, \tag{2.21}$$

$$\partial_{\mathrm{t}}\zeta + \boldsymbol{\nabla}\cdot(H\;\mathbf{v}) \;=\; 0\;, \tag{2.22}$$

where the linearized frictional accelerations discussed in the preceding chapter are comprised in the terms $-\hat{\mathbb{D}}_{\mathrm{lin}}\mathbf{v}$, while $\boldsymbol{F}^{\omega} = \boldsymbol{F}_0\; e^{i\omega t}$ comprises periodic external forces of frequency ω. As the PDE is linear in $\boldsymbol{\zeta} = (\zeta, \mathrm{u}, \mathrm{v})$, it is possible to derive free solutions (*i.e.*, for $\boldsymbol{F}^{\omega} = 0$), the *eigenmodes* of the system, denoted $\tilde{\boldsymbol{\zeta}}_k = \left(\tilde{\zeta}_k, \tilde{\mathrm{u}}_k, \tilde{\mathrm{v}}_k\right) \in \mathbb{C}^3$, by factorization of spatial and temporal dependencies as $\boldsymbol{\zeta}_k(\mathbf{x}, t) = \tilde{\boldsymbol{\zeta}}_k(\mathbf{x})\; e^{i\omega_k^{\mathrm{eig}} t}$, where $\omega_k^{\mathrm{eig}} \in \mathbb{C}$ is

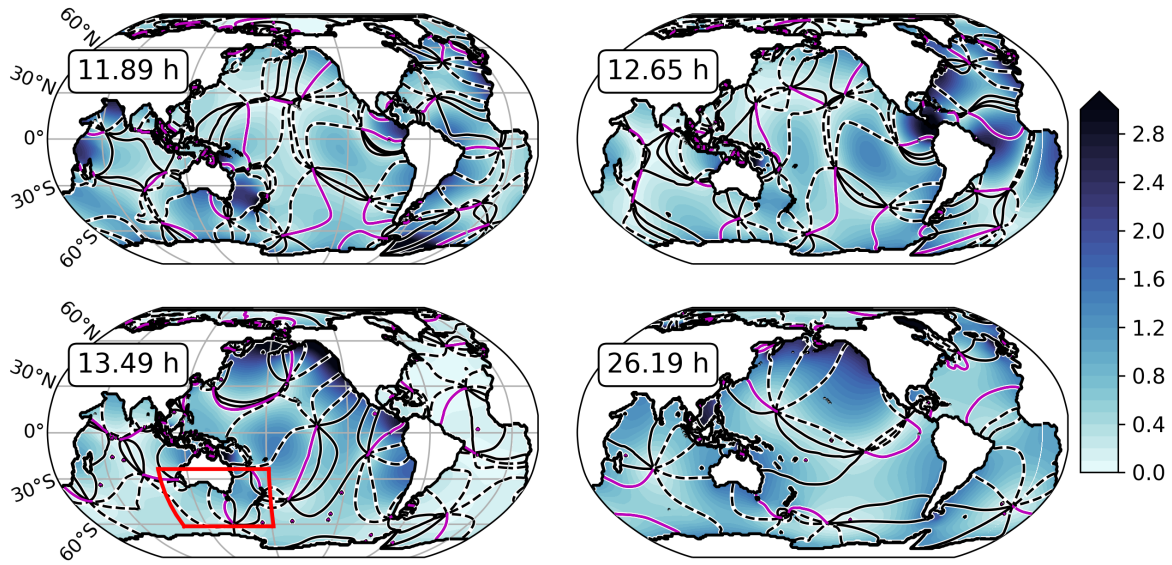

Figure 2.7: Selected ocean normal modes (SSH component $\tilde{\zeta}_k$), including three eigenmodes that are important for the synthesis of semidiurnal degree-2 tides (*e.g.*, M_2). The modes are labeled by their period lengths $T_k = \mathrm{Re}(2\pi[\omega_k^{\mathrm{eig}}]^{-1})$, where the ($T = 26.19$ h)-mode dominates the evolution of diurnal degree-2 tides (*e.g.*, K_1). Amplitudes are given in arbitrary units, with phase lags (*i.e.*, cotidal lines) are plotted in increments of 60° (magenta: $\phi_k^{\mathrm{eig}} = 0°$; dashed: $\phi_k^{\mathrm{eig}} < 0°$). The red frame indicates the region depicted in Figure 2.9, where tidal dynamics show the depicted Kelvin wave pattern.

the so-called *eigenfrequency* of the respective eigenmode. With the help of the eigenmodes of the adjoint problem $\tilde{\boldsymbol{\zeta}}_{\boldsymbol{k}}^{\boldsymbol{ad}}$, the temporal evolution of the forced system is a superposition of said eigenmodes, reading

$$\boldsymbol{\zeta}^{\omega}(\mathbf{x}, \omega t) = \mathrm{Re}\left(\sum_k \frac{1}{i(\omega_k^{\mathrm{eig}} - \omega)} \; < \boldsymbol{F}_0, \tilde{\boldsymbol{\zeta}}_{\boldsymbol{k}}^{\boldsymbol{ad}} > \; \tilde{\boldsymbol{\zeta}}_k(\mathbf{x}) \; e^{i\omega t} \right) , \tag{2.23}$$

where the summation is carried out over all eigenmodes, and $< \cdot, \cdot >$ is a suitable scalar product, *e.g.*, the global energy functional (Marchuk and Kagan, 1983). Equation (2.23) is used to illustrate the nature of OTD in the following.

Resonance The relative weights attributed to the individual eigenmodes are determined by two factors. The first is the *shape factor*, $C_k =< \boldsymbol{F}_0, \tilde{\boldsymbol{\zeta}}_{\boldsymbol{k}}^{\boldsymbol{ad}} >$, and the second is the *resonance depth*, $R_k(\omega) = -i(\omega_k^{\mathrm{eig}} - \omega)^{-1}$ (Müller, 2008; Marchuk and Kagan, 1983; Platzman, 1991). The shape factor is identical for all gravitational tides of a given degree and order as $\boldsymbol{F}_0 \sim \boldsymbol{\nabla} Y_{lm}$ (cf. Equation 2.8). Only the resonance depth depends on the frequency ω of the exciting acceleration. It is maximum for $\omega = \mathrm{Re}(\omega_k^{\mathrm{eig}})$, in which case $R_k = \mathrm{Im}(\omega_k^{\mathrm{eig}})^{-1}$ indicates that the system is on resonance.
The linearized equations allow one to precisely distinguish the description of tidal resonance from the respective eigenmodes, which are independent of the amplitude and frequency of the exciting force.

Ocean Normal Modes and Tidal Waves The eigenmodes of the world oceans are called *ocean normal modes* and, together with their eigenfrequencies ω_k^{eig}, define the response characteristics of the ocean to barotropic forcing.
Following Equation (2.21), these solutions crucially depend on a set of parameters of which some are constant (*e.g.*, g_0) or vary in a precisely known way (*e.g.*, $f[\phi]$). However, at least two parameters are strongly variable on a global scale: The parametrization of friction and the bathymetric function H (including coastlines that appear as no-flow boundary conditions). Especially the latter exerts a sensitive influence on the eigenmodes and the resonance frequencies of the ocean, being the controlling parameter of the shallow-water wave speed $c_{\text{sw}} = \sqrt{g_0\ H}$.
Due to the high variability of H, analytical solutions only exist for simplified ocean geometries, *e.g.*, water planets, cylindrical, or other symmetrical basins (*e.g.*, Pnueli and Pekeris, 1968; Thomson, 1879). Ocean normal modes are calculated with the help of numerical procedures (*e.g.*, Platzman, 1984a) and are presented in Figure 2.7 for the computation of Müller (2008). For the world oceans, several eigenmodes possess resonance frequencies ω_k^{eig} close to diurnal and semidiurnal ocean tide frequencies with relatively large scale factors C_k. Consequently, only a few eigenmodes dominate the tidal ocean response.
Generally, eigenmodes are grouped in Kelvin (gravity) and Rossby (vorticity) waves, depending on the physical principles that dominate their propagation. Concerning the later presented ocean tide solutions, we want to focus on the essential characteristics of normal modes. These include the occurrence of *amphidromic points* (points where the tidal amplitude $|\zeta|$ is zero) and the description by *cotidal lines* (connecting points that experience high water simultaneously). Cotidal lines converge towards amphidromic points (cf. Figure 2.7 and later figures). Thus, tidal surface waves encircle these points in the direction described by the succession of high waters. One should remember that ocean normal modes consist of tidal flow and elevation components. The relation of tidal flow to tidal elevation is briefly discussed in Section 2.3.

Linear Admittance Theory Due to the near-resonant nature of the ocean normal modes to tidal frequencies, the mean ocean response to tidal forcing is typically much stronger than predicted by equilibrium theory. A dimensionless measure for the ocean resonance strength can be constructed by dividing the first component (ζ-component) of Equation (2.23) by the amplitude of the partial tide generating potential $a_l^{\text{b}} A_i / g_0$, *i.e.*, normalizing the forcing strength to a unit value[10] $\boldsymbol{f}_0^{lm}$. The degree and order of the TRP were reapplied to the unit forcing to highlight their importance for the shape factor. The dimensionless, complex admittance function

$$Z_{lm}(\mathbf{x}, \omega_i) = g_0 \frac{\tilde{\zeta}^{\omega_i}(\mathbf{x})}{a_l^{\text{b}} A_i} = \sum_k \frac{1}{i(\omega_k^{\text{eig}} - \omega_i)} \ < \boldsymbol{f}_0^{lm}, \tilde{\boldsymbol{\zeta}}_{\boldsymbol{k}}^{\boldsymbol{ad}} > \ \tilde{\zeta}_k(\mathbf{x}) \ , \tag{2.24}$$

which can be evaluated for individual partial tides, labeled i, is obtained. The admittance function can be seen to yield a perfect description of barotropic ocean tide physics and predict the ocean response when forced at an arbitrary frequency, *e.g.*, for any selected

[10] Partial tides with significant radiational forcing should be treated individually, as their shape factors differ from purely gravitationally excited tides.

partial tide i, by evaluating

$$\zeta^{\omega_i}(\mathbf{x}, \omega_i t) = \mathrm{Re}\left(\frac{a_l^{\mathrm{b}} A_i}{g_0} Z_{lm}(\mathbf{x}, \omega_i) e^{i\omega_i t}\right) \ . \tag{2.25}$$

While Equation (2.24) motivates that Z_{lm} is a continuously-differentiable function in ω_i, with multiple resonances, it is a practical matter of fact that Z_{lm} varies only weakly within the width of the tidal bands $\delta\omega \approx 3\frac{^\circ}{\mathrm{h}}$.
This observation founds the basis for *tidal inference* (*e.g.*, Ray, 2017), for which the most prominent example is *linear admittance theory*. Here one assumes that Z_{lm} varies only linearly in a specific frequency range bounded by major-amplitude tides that can be precisely measured with geodetic techniques. The linear approximation is then employed to evaluate Z_{lm} for other partial tides that can be measured less precisely, typically minor tides. Linear admittance theory is, with some success, routinely applied to increase the number of partial tides provided by data-constrained tidal atlases (*e.g.*, Petit and Luzum, 2010).
On the other hand, there are cases where the theory is non-applicable. First, Z_{lm} is only a smooth function of frequency for tides with identical unit forcing $\mathbf{f}_0^{lm}$, *i.e.*, it is unsteady for tides originating from higher degree forcing (*e.g.*, $l = 3$) or radiational tides. Further, It is evident from Equation (2.24) that the linear approximation is not exact, especially close to resonance or for larger interpolation spans. Additionally, realistic OTD is (weakly) nonlinear, which results in a nonlinear generalization of Equation (2.24). In summary, the resonant nature of OTD that is best traceable within the linearized approximation motivates some aspects of linear admittance but shows the limits of its applicability.

Tidal Synthesis Equation (2.23) formulates the ocean response to forcing of a fixed frequency will be a superposition of independent ocean normal modes oscillating at the same frequency, *i.e.*, as a linear, frequency-dependent operator. This description implies that the ocean response to accelerations which are composed of a multitude of individual frequency components (*e.g.*, Platzman, 2002), can be described individually for each frequency without having to consider the interaction between individual components (superposition). While nonlinear operators in the PDE contradict this expectation, OTD is empirically observed to be close to linear, with small yet significant nonlinear corrections that will be discussed in more detail in the following section.

2.2.3 Nonlinear Ocean Tidal Dynamics and Tidal Spectrum

Drawing on the material the previous sections, the momentum conservation component of Equations (2.1) is reformulated, reading

$$\begin{aligned} \partial_{\mathrm{t}}\mathbf{v} + \mathbf{f}\times\mathbf{v} + (\mathbf{v}\cdot\nabla)\,\mathbf{v} &= -g_0\nabla\left(\zeta - \zeta_{\mathrm{SAL}}\right) - \mathbb{D}\mathbf{v} + \boldsymbol{F} \ , \\ \text{with} \quad \mathbb{D}\mathbf{v} &= \frac{r}{H}\,|\mathbf{v}|\mathbf{v} - \hat{\mathbf{R}}\mathbf{v} + \frac{1}{H}\boldsymbol{\mathcal{C}}\mathbf{v} + \frac{r_{\mathrm{ice}} f_{\mathrm{ice}}}{H}\,|\mathbf{v} - \mathbf{v}_{\mathrm{ice}}|\,\mathbf{v} \ , \\ \text{and} \quad \boldsymbol{F} &= \boldsymbol{\nabla}\left(V_{\mathrm{tid}} + V_p + V_{\mathrm{l}} + V_{\mathrm{o}}\right) + \mathbf{W} + \frac{r_{\mathrm{ice}} f_{\mathrm{ice}}}{H}\,|\mathbf{v} - \mathbf{v}_{\mathrm{ice}}|\,\mathbf{v}_{\mathrm{ice}} \ . \end{aligned} \tag{2.26}$$

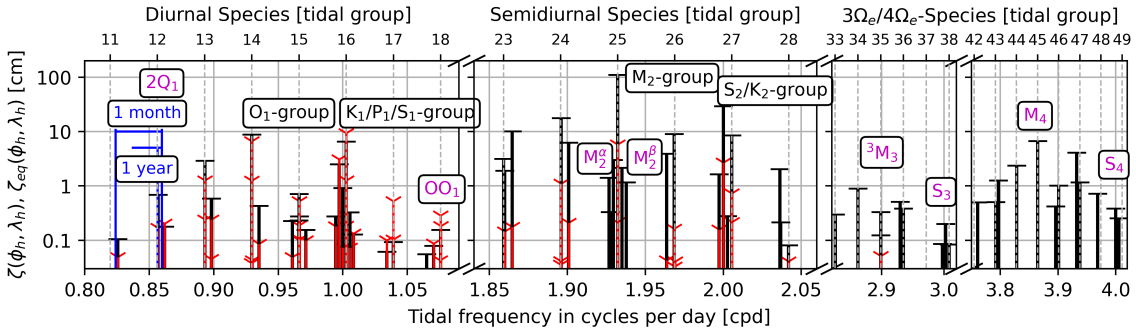

Figure 2.8: Tidal spectrum at the small offshore island of Helgoland (location: 'Binnenhafen', $\phi_h = 54.179°N$, $\lambda_h = 7.890°E$) presented for diurnal to 1/4-diurnal frequencies. The tidal sea surface height constituents are plotted in black, with the equilibrium tidal heights of the TGP added in red. The relation from black to red markers indicates insignificant resonance for diurnal and terdiurnal tides, strong resonance for semidiurnal tides, and significant shallow-water tides of terdiurnal and higher frequencies that do not have a notable counterpart in the TGP.

The equations are nonlinear in $\boldsymbol{\zeta}$. Turbulent ice friction, advection (*i.e.*, $[\mathbf{v} \cdot \nabla]\mathbf{v}$), wave drift (*i.e.*, $-\nabla \cdot [\zeta \mathbf{v}]$), and, most notably, turbulent bottom friction lead to the interaction of individual partial tides. Among other effects, these interactions trigger *second-harmonic generation* (*e.g.*, $\omega + \omega = 2\omega$), forming *overtides*, and sum-frequency generation (*e.g.*, $\omega_1 + \omega_2 = \omega_3$), forming *compound tides*. They are often summarized under the term *shallow-water tides*, as nonlinear effects are strongest in shallow-water areas, where the tidal velocity $\mathbf{v}$ is much higher, hence inducing more vital interaction.
Shallow-water tides are generated independently from external tide-generating forces and often do not possess a notable counterpart in the TRP (cf. Figure 2.8 for terdiurnal and higher frequencies). The TG in Figure 2.8 is placed in a shallow-water environment indicating that nonlinear tides can reach considerable amplitude (most notably 1/4-diurnal components, as M_4, the principal overtide of M_2). Nevertheless, they are not restricted to shallow seas but also propagate into the deep ocean. While the TRP for diurnal tides has even higher equilibrium values than for semidiurnal tides at this latitude, the ocean tide response is feeble. Insignificant diurnal tides also motivate the small amplitude of terdiurnal compound tides that originate from interaction between a diurnal and semidiurnal partial tide (*e.g.*, $K_1 + M_2 \rightarrow MK_3$).
Out of the example tidal spectrum in Figure 2.8, data-constrained ocean tide models only provide a reduced sample size, *e.g.*, 34 tides for FES14 (Lyard et al., 2021) or 17 tides for EOT20 (Hart-Davis et al., 2021b). Residual partial tides are estimated using the linear admittance theory (Section 2.2.2). We want to distinguish several partial tides where this approach is imprecise or non-applicable. For these partial tides, data-unconstrained solutions are beneficial and valuable. Thus, they will be targeted in this thesis. These groups include (cf. Figure 2.8):

- Degree-2 partial tides that are located at the edges of the tidal bands (*e.g.*, $2Q_1$ and OO_1) to reduce the extrapolation distance of the admittance function

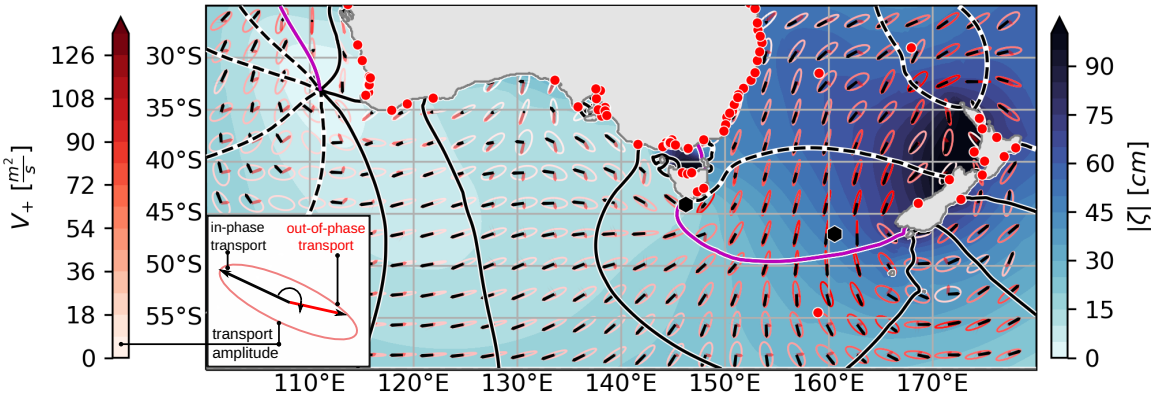

Figure 2.9: Ocean tidal dynamics evoked by the M_2 partial tide around New Zealand and South Australia taken from the FES14 tidal atlas. The tidal sea surface anomaly ζ is depicted in the amplitude-phase notation, where tidal phase lags ϕ_ζ (*i.e.*, cotidal lines) appear in increments of 60° (magenta: $\phi_\zeta = 0°$; dashed: $\phi_\zeta < 0°$). Tidal transports $\mathbf{V}$ are integrated as ellipses, where the color coding refers to the maximum tidal transport (*i.e.*, the semi-major axis V_+). Transport phase lags are plotted relative to ϕ_ζ, where black arrows symbolize the transport that is in-phase with the local sea surface anomaly, and red arrows refer to the out-of-phase component (for $\zeta[\mathbf{x}, t] = 0$). The plot is augmented by TG stations (red, ∘) and OBP recorders (black, ⬢) as in Figure 1.2.

- Degree-3 partial tides like ${}^3M_3$, where excitation functions follow spherical harmonic functions Y_{3m}, and cannot be related to major tides which are of degree-2
- Tides that are partially or entirely excited by atmospheric effects as S_1, S_2, and S_3 (*e.g.*, Balidakis et al., 2022) and thus possess unique excitation patterns and thereby shape factors C_k
- Nonlinear, shallow-water tides that are unrelated to external forcing potentials (*e.g.*, M_4, MK_3, or MS_4)
- Seasonal variation tides as $M_2^{\alpha,\beta}$, that originate from periodic variations in ice cover, ocean stratification (Müller et al., 2014), and other time-variable components of the PDE given in Equation (2.26)

This chapter is concluded by introducing partial ocean tide solutions in analogy to the partial potentials of Equation (2.8). Additionally, diagnostic equations that can be used to derive selected secondary observables are discussed.

2.3 Primary and Secondary Ocean Tide Observables

Tide-generating forces (Section 2.1) induce periodic disturbances in the world oceans. Equations (2.26) describe the underlying dynamics, including nonlinear contributions.

Thus, the tidal state of the world ocean, $\boldsymbol{\zeta} = (\zeta, \mathrm{u}, \mathrm{v})$, can be described by

$$\boldsymbol{\zeta}(\mathbf{x}, t) = \sum_{\text{all tides}} \boldsymbol{\zeta}^i_{\cos}(\mathbf{x}) \cos \chi_i(t) + \boldsymbol{\zeta}^i_{\sin}(\mathbf{x}) \sin \chi_i(t) = \sum_{\text{all tides}} |\boldsymbol{\zeta}_i|(\mathbf{x}) \cos\left(\chi_i(t) - \boldsymbol{\phi_i}[\mathbf{x}]\right) \ , \tag{2.27}$$

where $|\boldsymbol{\zeta}_i| = (|\zeta|, |\mathrm{u}|, |\mathrm{v}|)_i$ comprises SSH and flow amplitudes, and $\boldsymbol{\phi}_i = (\phi_\zeta, \phi_\mathrm{u}, \phi_\mathrm{v})_i$ is the corresponding phase vector (cf. Equation 2.9).
We refer to $\boldsymbol{\zeta}$ as primary ocean tide observables. The label 'all tides' in series (2.27), refers to all partial tide frequencies of the tide-generating forces and all frequencies originating from nonlinear tidal interaction, as described in the previous section. In principle, this is an indefinitely large number. However, only partial tides that induce significant signal variability are empirically resolvable. The vectors $\boldsymbol{\zeta}^i_{cos}$ and $\boldsymbol{\zeta}^i_{sin}$ are the in-phase and quadrature part of the individual partial tides equivalent to the amplitude/phase notation as in Equation (2.12), *i.e.*, $|\boldsymbol{\zeta}|_i$ and $\boldsymbol{\phi}_i$. For convenience, they are comprised in the complex vector field $\boldsymbol{\zeta}^i = \boldsymbol{\zeta}^i_{cos} + \mathrm{im}\, \boldsymbol{\zeta}^i_{sin}$, where $\mathrm{im} = \mathrm{i} = \sqrt{-1}$, is the imaginary unit. $\boldsymbol{\zeta}^i$ extensively defines the OTD evoked by a certain partial tide i[11].
OTD for each partial tide comprise oscillations of the sea surface anomaly ζ^i and the ocean flow, described by the velocity vector $\mathbf{v}^i$, or the transport vector $\mathbf{V}^i = H\mathbf{v}^i$. The relation of the tidal velocity to the tidal elevation is non-trivial[12]. While ζ^i is a scalar, $\mathbf{V}^i$ is a vector whose east and north components, U^i and V^i, both possess individual amplitudes and phases. Thus, the tidal transport vector generally changes its direction and absolute value, encircling a *tidal ellipse*. Consider the Appendix of Pugh and Woodworth (2014a) for a detailed description of the tidal ellipses.
This thesis focuses, above all, on tidal elevations ζ. To nonetheless get a picture of the relationship between tidal elevation and tidal transport, tidal ellipses for the M_2 partial tide are presented in Figure 2.9 for a designated region. The ellipses are augmented with vectors depicting the tidal flow's direction and relative strength. Black arrows indicate transport vectors in phase with the sea surface height anomaly, while out-of-phase transports are shown as red arrows. Ellipses dominated by black arrows point to progressing waveforms (*e.g.*, the Kelvin wave around New Zealand), which means that the tidal flow is at it's maximum at high and low water. In contrast, a dominant red arrow component points to a standing wave character (*e.g.*, in the Great Australian Bight), which means that the tidal flow is strongest in between ebb and flood. The rotational sense of the ellipse can be tracked by rotating the black arrow on the shortest way to the position of the red arrow.
In addition to the introduced primary observables, this thesis is concerned with the prediction of secondary observables of OTD (cf. Table 1.1). The discussion concentrates on signatures of ocean tidal loading and ocean tide levels, which are both derived from the tidal sea surface height displacement ζ^i. In the following, the diagnostic equations describing said secondary observables are introduced.

Ocean Tidal Loading Ocean partial tides periodically impose a load onto the solid Earth that is proportional to the induced sea surface height anomaly and expressed by $\rho_\mathrm{sw}\, g_0\, \zeta^i$. The imposed load induces a vertical displacement of the solid Earth's surface,

[11] In this thesis tides are labeled with i, ω, and ω_i, which implicitly refer to the same partial tide.
[12] It is possible to indirectly observe tidal transports by their induced magnetic field, which is another secondary observable (*e.g.*, Saynisch-Wagner et al., 2020).

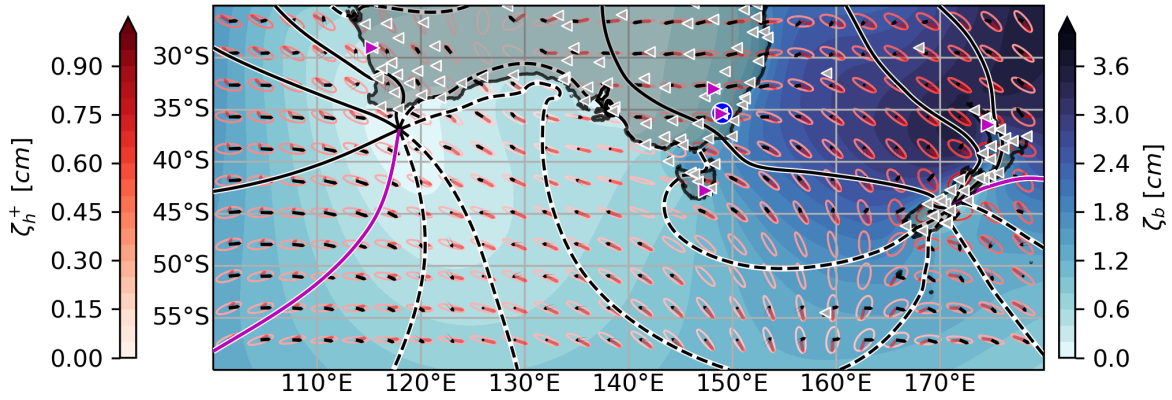

Figure 2.10: Ocean loading displacements evoked by the M_2 partial tide around New Zealand and South Australia taken from FES14. The vertical displacement ζ_b is depicted in the amplitude-phase notation, where tidal phase lags ϕ_b (*i.e.*, cotidal lines) appear in increments of 60° (magenta: $\phi_b = 0°$; dashed: $\phi_{M_2} < 0°$). Horizontal (east/north) displacements $\boldsymbol{\zeta}_\mathrm{h}$ are integrated as ellipses, where the color coding refers to the maximum horizontal displacement (*i.e.*, the semi-major axis ζ_h^+). Horizontal displacement phase lags are plotted relative to ϕ_b, where black arrows symbolize the displacement that is in-phase with the local vertical deformation, and red arrows refer to the out-of-phase component (for $\zeta_\mathrm{b}(\mathbf{x}, t) = 0$). The plot is augmented by GNSS (gray, ◁) and VLBI (magenta, ▷) stations and gravimeteric observatories (blue, ○) as in Figure 1.2.

denoted

$$\zeta_\mathrm{b}^i(\mathbf{x}) = \frac{3\rho_\mathrm{sw}}{\rho_\mathrm{se}} \sum_{l,|m|\leq l} \frac{h_l}{2l+1}\, \zeta_{lm}^i Y_{lm}(\mathbf{x}) \;. \tag{2.28}$$

Additionally, horizontal loading displacements are obtained by evaluating

$$\boldsymbol{\zeta}_\mathrm{h}^i(\mathbf{x}) = \frac{3\rho_\mathrm{sw}}{\rho_\mathrm{se}} \sum_{l,|m|\leq l} \frac{l_l}{2l+1}\, \zeta_{lm}^i \boldsymbol{\nabla} Y_{lm}(\mathbf{x}) \;. \tag{2.29}$$

Here l_l is the Shida number of degree l, which is used to describe horizontal displacements (*e.g.*, Agnew (1997)). These displacements are accompanied by gravity anomalies on the Earth's surface[13] (Merriam, 1980), reading

$$g_\perp(\mathbf{x}) = -g_0 \frac{3\rho_\mathrm{sw}}{\rho_\mathrm{se}} \sum_{l,|m|\leq l} \frac{l-(l+1)k_l+2h_l}{2l+1}\, \zeta_{lm} Y_{lm}(\mathbf{x}) \;, \tag{2.30}$$

and generally in the gravity potential at constant height z, reading

$$V[\zeta^i](\mathbf{x}, z) = \frac{3\rho_\mathrm{sw}}{\rho_\mathrm{se}} \sum_{l,|m|\leq l} \frac{1+k_l}{2l+1} \left(\frac{R_\mathrm{e}}{R_\mathrm{e}+z}\right)^{l+1} \zeta_{lm}^i Y_{lm}(\mathbf{x}) \;. \tag{2.31}$$

[13]This formulation ignores possible short-ranged Newtonian attraction components (cf. Voigt et al., 2023) from close-by water masses.

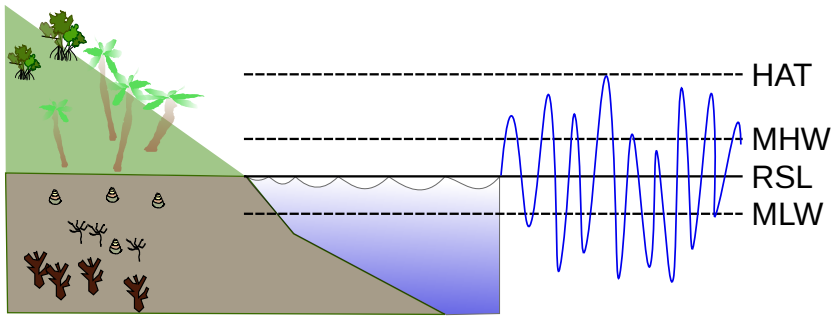

Figure 2.11: The tidal temporal variations of the sea level $\zeta(t)$ around the RSL define tidal marshes that are the basis for the occurrence of biological species, or geological tracers, which then can become SLIPs. The tidal marshes are limited by ocean tide levels, which are statistical measures of $\zeta(t)$.

These quantities are detectable with geodetic techniques described in Section 1.2. Like the SAL potential, these observables are expressed as a spherical harmonic series (*e.g.*, Agnew, 2012) of the tidal sea surface height anomaly ζ^i. We recall that $\zeta^i = \zeta^i_{\cos} + \mathrm{im}\,\zeta^i_{\sin} \in \mathbb{C}$. Hence, the discussed quantities follow was complex vectors of identical structure. Differences between the latter four equations reside in the combinations of the load Love and load Shida number h_l, k_l, and l_l that define the degree-wise weighting of spherical harmonic contributions. Like the SAL potential, contributions are dampened degree-wise by $(2l+1)^{-1}$, which leads to the dominance of long wavelengths.
Further, the definition of the tidally-induced gravity potential (Equation 2.31) shows that individual contributions to the potential are dampened depending on the evaluation height z and the spherical harmonic degree l. Therefore, information about the gravity field is usually stored in *Stokes Coefficients* for each base function Y_{lm} and $z = 0$ (*e.g.*, Chao, 2004; Heiskanen and Moritz, 1967), which allows a straightforward evaluation of $V[\zeta^i]$ at arbitrary heights.
The relation between ζ^i and the derived quantity ζ^i_b is depicted in Figs. 2.9 and 2.10, where the latter is obtained by inserting ζ^i into Equation (2.28). The oscillation systems are not identical, but ζ_b appears smoothed and shifted by approximately 180°, as positive loads lead to negative surface displacements. Further, the displacement field ζ_b extends to the inland, *i.e.*, load tide signatures appear in GNSS, VLBI, and gravimeter measurements.
The same convention is adapted to depict the horizontal tidal displacement vectors $\boldsymbol{\zeta}^i_\mathrm{h}$ with respect to the horizontal displacement ζ^i_b, that, in the same manner, describe elliptic orbits. On the other hand, the causal relation is fundamentally different, as the divergence of tidal transports $\boldsymbol{\nabla} \cdot \mathbf{V}^i$ induces temporal changes in ζ^i. At the same time, vertical and horizontal displacements are both derived from ζ^i. Consequently, $\boldsymbol{\zeta}^i_\mathrm{h}$ and $\mathbf{V}^i$, do not resemble each other, as was the case for ζ^i_b and ζ^i.

Ocean Tide Levels Further, the interpretation of sea-level index points (SLIPs) is in the focus of this thesis. SLIPs are related the local relative sea level RSL(t) under consideration of ocean tide levels.
For this, the approach is to derive statistical measures of the tidal sea surface height

dynamics, *i.e.*, the ζ-component of Equation (2.27)

$$\zeta(\mathbf{x}, t) = \mathrm{Re}\left(\sum_i \zeta^i(\mathbf{x})\, e^{i\,\chi_i(t)}\right) \ . \tag{2.32}$$

Ocean tide levels are derived from time series of sea surface height elevations. Levels of interest are, for example, the mean high water (MHW), and the mean low water (MLW), which are defined as the mean of all high (low) waters identified within the time series. Also, the highest astronomical tide (HAT), which is just the highest tidal elevation obtained over the whole time series, represents a reference tide level with respect to the RSL (cf. Figure 2.11).
Hence, in contrast to ocean tidal loading-derived observables, tidal levels (and marsh environments) are functions of the entire tidal spectrum and cannot be derived for individual partial tides. The derivation and interpretation of tidal levels will be specified more precisely within Chapter 6.
The mathematical equations that define other diagnostic observables of Table 1.1 are omitted, as they were not employed to study geodetic data within this thesis. Thus, the review of the theory of global ocean tides is closed, depicting all aspects that are needed to motivate the development of the employed ocean tide model and its applications in the following chapters.

3
Ocean Tide Modelling

In developing an ocean tide model to fulfill O1, the presented efforts are built on decade-long work to simulate global ocean tides in Hamburg, Germany. Starting from the fundamental work of W. Zahel (Zahel, 1977, 1978), unconstrained hydrodynamic models were used to quantify the contributions of ocean tides to Earth's rotation (Seiler, 1991), the evolution of tides since the Last Glacial Maximum and its consequences for oceanic torques acting on the solid Earth (Thomas and Sündermann, 1999), interactions among ocean tides and the general circulation (Thomas et al., 2001), and the identification of free barotropic normal modes in the world ocean under the influence of friction and sea-bottom deformations caused by surface loading (Zahel and Müller, 2005).
This Chapter is dedicated to describing the numerical ocean tide modeling conducted within this thesis. First, the ocean tide model TiME that is employed for this PhD thesis is introduced in Section 3.1. Subsequently, Section 3.2 discusses upgrades to the initial model configuration, intending to depict advanced tidal hydrodynamics as introduced in Chapter 2. Afterward, in Section 3.3, the numerical implementation of the novel characteristics into TiME is outlined, and its general mode of operation is discussed[1].

3.1 Tidal Model Forced by Ephemerides

The starting point is the Tidal Model forced by Ephemerides (TiME) as described by Weis (2006), which simulates global barotropic tidal dynamics by solving the nonlinear, inhomogeneous shallow-water equations (*e.g.*, Pekeris, 1974)

$$\begin{aligned} \partial_t \mathbf{v} + \mathbf{f} \times \mathbf{v} + (\mathbf{v} \cdot \nabla)\,\mathbf{v} &= -g_0 \nabla \left(\zeta - \zeta_{\mathrm{SAL}} - \zeta_{\mathrm{eq}}\right) - \frac{r}{H}\,|\mathbf{v}|\mathbf{v} + \hat{\mathbf{R}}\mathbf{v} \\ \partial_t \zeta &= -\boldsymbol{\nabla}\left([H+\zeta]\,\mathbf{v}\right)\ . \end{aligned} \tag{3.1}$$

determining $\boldsymbol{\zeta} = (\mathbf{v}, \zeta) = (\mathrm{u}, \mathrm{v}, \zeta) \in \mathbb{R}^3$. All elements of Equation (3.1) were introduced in the last chapter, while the equation itself is a reduced form of Equation (2.26).
Tidal dissipation (Section 2.2.1) is carried out by quadratic bottom friction and paramet-

[1] This chapter partially addresses contents that were originally published in Sulzbach et al. (2021a).

rized horizontal eddy viscosity $\hat{\mathbf{R}}\mathbf{v}$ (cf. Equation 2.19), while dissipation by wave drag or ice friction was not considered.
The principal forcing term $g_0\nabla\zeta_{\mathrm{eq}} = \nabla V_{\mathrm{tid}}$ is an individual partial tide excitation (restricted to degree-2), *i.e.*, V_{tid}^{ilm} (Equation 2.8). Alternatively, forcing by the full lunisolar tidal potential as quantified by the ephemerides of the Sun and the Moon (Bartels, 1957) could be invoked, which implies simultaneously forcing the model with all partial tide potentials at once.
Since TiME considers nonlinear accelerations, ephemeridic forcing enables interactions between individual partial tides. While forcing by atmospheric effects was not considered, the SAL potential was included in parameterized from, *i.e.*, setting $\zeta_{\mathrm{SAL}} = \epsilon\zeta$ (cf. Section 2.1.3). TiME solves Equations (3.1) on a regular longitude/latitude (λ/ϕ) grid at a resolution of $\frac{1}{12}^\circ$ employing a semi-implicit finite-difference algorithm as described by Backhaus (1982, 1985).
Since the smallest zonal grid cell size limits the time step size, the zonal resolution is reduced at two latitude circles towards the North pole and finalized by a spherical cap to avoid the polar coordinate singularity. Numerical experiments are based on global GEBCO (GEBCO Compilation Group, 2019) and ETOPO1 (Amante and Eakins, 2009) bathymetries. It is noteworthy that the bathymetric data set implicitly impacts the tidal wave propagation by defining the boundary conditions, which is the vanishing of tidal flow through the coastal margins.
In the following sections, upgrades to the described model configuration and their numerical implementation will be presented. Later, results from both model stages (initial and upgraded) will be compared.

3.2 Model Characteristics

First, the numerical domain that, in the configuration of Weis (2006), relies on a *pole cap* (a large grid cell) at the North Pole is discussed. While this implementation proved robust, it introduces numerical artifacts that are hard to quantify and limit the model's plausibility in the Arctic region. An updated numerical grid that does not necessitate the pole cap formulation (Section 3.2.1) is introduced to eliminate this source of uncertainty. This updated numerical grid has implications for the ocean tide model as a whole.
Therefore, Sections 3.2.2 to 3.2.7 summarize changes to the implementation of the Coriolis acceleration, the formulation of tidal dissipation, the TRP, and tide-generating forces by atmospheric effects and SAL with respect to the novel grid. Especially in Sections 3.2.3 to 3.2.5, model upgrades are on purpose discussed together with changes due to the new numerical grid, as both aspects cannot be distinctly separated. The model upgrades are introduced to improve the model accuracy, which is discussed in Chapter 4.

3.2.1 Numerical Domain: The Rotated-Pole Grid

The numerical core of TiME is based on a temporal finite-difference solver that operates on a regular (λ/ϕ)-grid on a spherical Earth of radius R_{e}, which is reintroduced later in Section 3.3. For numerical stability, the discretization is performed in a staggered scheme that evaluates the tidal flow velocities (u, v) spatially in between the evaluation points of the sea surface height anomaly ζ (Zahel, 1977).

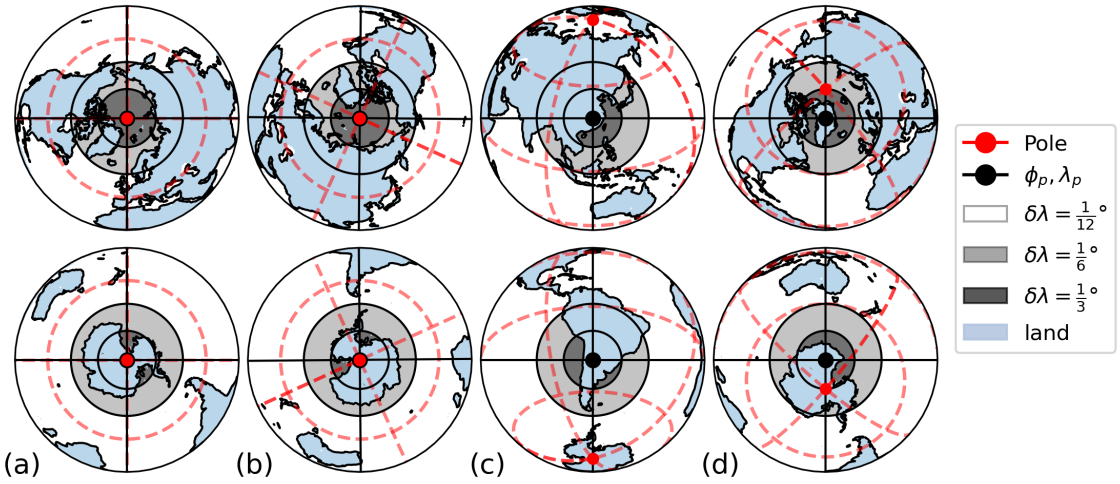

Figure 3.1: Selected numerical grid orientations (numerical poles: black circles) on the world map (geographical poles: red circles), for the Northern (top) and the Southern hemisphere (bottom). The geographical latitude circles $(0°, \pm 45°)$ are indicated (red, dashed), as well as the boundaries of the reduced resolution zones of the numerical grid (black, shaded) at $\pm 60°, \pm 75°$. The selected orientations of the rotated poles are $\phi_\mathrm{p}, \lambda_\mathrm{p} = (90°\mathrm{N}, 0°\mathrm{E})$ for grid *arc* (a), $(90°\mathrm{N}, 114.5°\mathrm{E})$ for (b), $(28.5°\mathrm{N}, 114.5°\mathrm{E})$ for grid *chi* (c) and $(75°\mathrm{N}, 40°\mathrm{W})$ for grid *gre* (d).

Due to Earth's curvature, the zonal distance between two meridian circles is latitude dependent, proportional to $\Delta\mathrm{x} = R_\mathrm{e}\delta\phi\cos\phi$, where $\delta\phi$ is the constant meridional resolution. The zonal resolution halves at $\phi = \pm 60°$ and also at $\phi = \pm 75°$, which implies a zonal resolution transition from $\Delta\mathrm{x} = \frac{1}{2}\delta\phi R_\mathrm{e}$ to $R_\mathrm{e}\delta\phi$ and from $\Delta\mathrm{x} = 0.52\ \delta\phi R_\mathrm{e}$ to $1.04\ \delta\phi R_\mathrm{e}$, respectively[2] (cf. Figure 3.3). Polewards of 75°, the zonal resolution increases further, which results in progressively asymmetrical grid cell boundaries in high latitudes.
While this asymmetrical shape is undesirable in itself, it further limits the model's time step size Δt, as the Courant–Friedrichs–Lewy (CFL) condition qualitatively limits the stability of the solver, *i.e.*, $\Delta t / \Delta x^\mathrm{min}\ c_\mathrm{sw} \leq C_\mathrm{max}$. Thus, keeping the minimum zonal distance Δx^min as large as possible is invaluable to allow larger time steps Δt. While pinching out half of the remaining meridians polewards of two fixed latitude circles allows quadrupling the time step size (formulation after Zahel, 1970), the zonal resolution converges to 0 while approaching the numerical singularity at the poles.
The geographical South Pole is land-covered (approximate dry radius $\Delta\phi_\mathrm{SP} = 5°$), so the numerical singularity was elegantly avoided. However, the North Pole is centered in the Arctic Ocean. This problem was treated in the implementation of Weis (2006) by a pole cap formulation, which is a large grid cell of radius $\Delta\phi_\mathrm{NP}$ that closes the numerical domain for the northernmost latitudes. Thus, effectively, the zonal resolution can be limited to $\Delta x^\mathrm{min} = 4\delta\phi\cos\left(\frac{\pi}{2} - \min[\Delta\phi_\mathrm{NP}, \Delta\phi_\mathrm{SP}]\right) R_\mathrm{e}$. The default resolution of TiME is $\delta\phi = \frac{1}{12}°$ (implying $\delta\lambda = \frac{1}{6}°$ and $\delta\lambda = \frac{1}{3}°$ in reduced resolution zones) and $\Delta\phi_\mathrm{NP} = 4°$, resulting in a minimum zonal increment of $\Delta x^\mathrm{min} = 2.59$ km, which is 28% of the meridional increment

[2]Originally, the formulation of Weis (2006) only existed for the Northern Hemisphere but was extended to the southern latitudes.

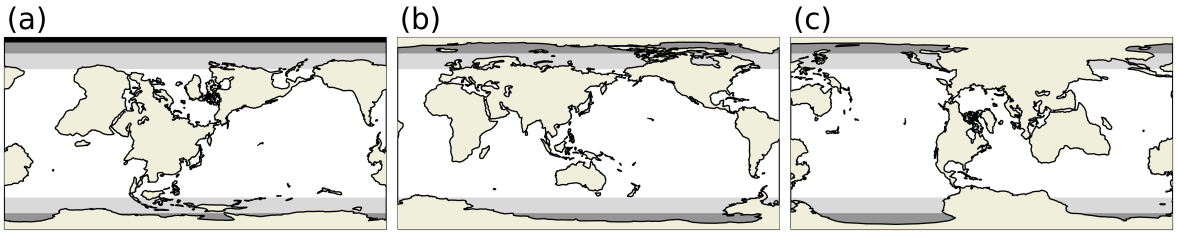

Figure 3.2: Selected numerical grids used for experiments with TiME, defined by their numerical North Pole position on the standard grid. The poles of grid (a), labeled *aus*, are positioned in Australia (dry pole) and the North Atlantic (wet pole) at $\phi_\mathrm{p}, \lambda_\mathrm{p}$= (24°N, 45°W). Subplot (b) shows grid *gre* with poles at (75°N, 40°W), and (c) introduces grid *chi* (28.5°N, 114.5°E). The polar reduced resolution zones are introduced as gray-shaded regions, as in Figure 3.1.

of 9.3 km. This numerical implementation is labeled as *arc* grid (cf. Figure 3.1a).
The occurrence of coordinate singularities in the numerical domain is a common challenge in Earth system modeling. Possible solutions include reformulation of the PDE, *e.g.*, on a spherical harmonic basis (*e.g.*, Stevens et al., 2013), unstructured numerical meshes (*e.g.*, Carrère and Lyard, 2003; Korn, 2017), or regular grids that position numerical poles outside of the computational domain (*e.g.*, by using a tripolar grid, *e.g.*, Jungclaus et al., 2013). The numerical core of TiME is kept largely unmodified and positions the numerical poles on land-covered antipodes. This modification does not impact the solving algorithm. Changes due to this *pole rotation* are confined to modifying physical effects depending on the geographical location.
Two pole orientations were selected to allow a minimum 'dry-radius' $\min(\Delta\phi_\mathrm{NP}, \Delta\phi_\mathrm{SP}) = 4°$ around the numerical pole, which is the maximum under present-day conditions. These are configurations with numerical poles in East Asia/South America (configuration *chi*, Figure 3.1c), and in Greenland/Antarctica (configuration *gre*, Figure 3.1d)[3]. The minimum dry radius determines the largest zonal resolution. Thus, the maximum time step is comparable to the standard configuration (*arc*). Additionally, another configuration is employed for testing purposes. This configuration (*aus*) positions the numerical pole cap in the North Atlantic (South Pole: Australia), *i.e.*, in a region with pronounced OTD, to estimate the impact of the pole cap formulation. The three numerical grids are presented in their unfolded form in Figure 3.2.

3.2.2 Coordinate Transform and Coriolis Acceleration

In principle, the pole rotation affects all components of PDEs (2.26) and (3.1), which exhibit an explicit coordinate dependence. We denote the initial geographical coordinate system as (λ, ϕ) and the new, rotated system as (λ', ϕ'), where the numerical poles of the rotated coordinate system $(\lambda'_\mathrm{p} = 0°, \phi'_\mathrm{p} = 90°)$ are positioned at the geographical coordinates $(\lambda_\mathrm{p}, \phi_\mathrm{p})$ on the unrotated grid. The two reference systems can be transferred to each other by successive rotations parameterized with Euler angles. Here, the right-

[3]A third configuration in South America/Kalimantan (*kal*) was considered but discarded it due to its reduced dry radius.

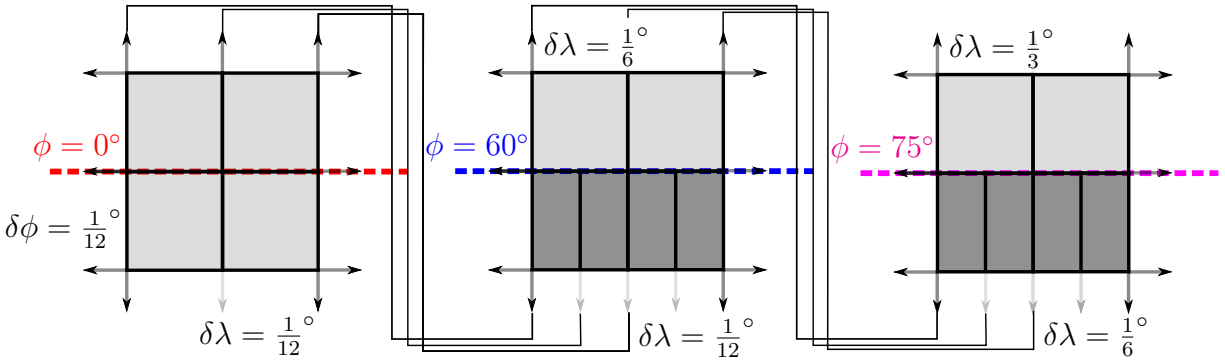

Figure 3.3: Convergence of the meridians on the Northern Hemisphere, and zonal resolution reduction ($\delta\lambda$) at $|\phi| = 60°$ (blue) and $|\phi| = 75°$ (magenta) of TiME's numerical domain. The depicted aspect ratio of the grid cells changes between approximately 1:1 (light gray) and 1:2 (dark gray) at the indicated latitude circles (cf. Figures 3.2 and 3.1).

handed coordinate system is chosen so that, in the unrotated system, the z-axis is the Earth rotation axis, and x and y point from the Earth center into the directions $\lambda_x = 0°, \phi_x = 0°$ and $\lambda_y = 90°, \phi_y = 0°$, respectively. The rotations are:

- First, a rotation around the z-axis (Earth axis) by angle $\alpha_e = \lambda_p$
- Second, a rotation around the new y-axis by angle $\beta_e = 90° - \phi_p$
- The third Euler angle is $\gamma_e = 0$.

Figures 3.1a-c illustrate the transformation from *arc* to *chi* by successive Euler rotations. Evaluating the rotation matrices results in the coordinate transformation

$$\begin{aligned} \sin\phi &= \cos\phi' \cos\phi_p \ \cos\lambda' + \sin\phi_p \sin\phi' \ , \\ \text{and} \quad \tan(\lambda - \lambda_p) &= \frac{\sin(\lambda')}{\sin\phi_p \cos\lambda' - \cos\phi_p \tan\phi'} \ , \end{aligned} \tag{3.2}$$

that specify the old coordinates in the new coordinate system depending on the location of the rotated poles. Equations (3.2) can be used to transfer scalar quantities of the PDE to the new coordinate system, which applies to the Coriolis factor $f(\phi) = 2\Omega_e \sin\phi$. As an example, Figure 3.4b displays the Coriolis factor of the rotated *chi* grid, where the maximum absolute value of $f(\phi)$ at the geographical poles is visible.
On the other hand, the transfer of vectors between both reference systems is more complicated due to the locally different definitions of north and east on both grids. In general, the reference directions of both coordinate systems, *i.e.*, $\boldsymbol{e}_N$ and $\boldsymbol{e}'_N$, are misaligned by a certain angle $\alpha = \boldsymbol{e}_N \cdot \boldsymbol{e}'_N$. The respective local unit vectors in both reference systems can be derived by differentiation of the coordinate vector $\boldsymbol{e}_r = (\cos\phi\cos\lambda, \cos\phi\sin\lambda, \sin\phi)$ after ϕ, ϕ' (north) and λ, λ' (east). Utilizing Equations (3.2), the rotation angle is given by

$$\tan\alpha = -\frac{\cos\phi' \ \cos\phi_p \ \sin\lambda'}{\cos\phi_p \ \sin\phi' \ \ cos\lambda' - \sin\phi_p \ \cos\phi'} \ . \tag{3.3}$$

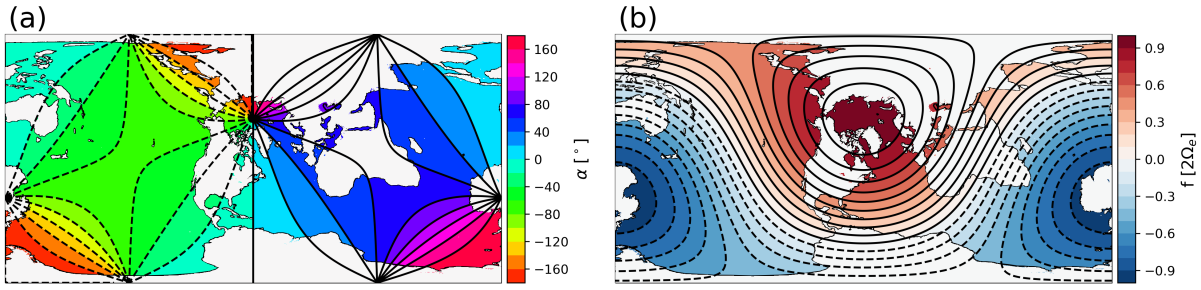

Figure 3.4: Rotation angle α, as obtained by evaluation of Equation (3.3) (a), and Coriolis-factor $f(\lambda', \phi')$ on rotated *chi* grid (b).

It is possible to invert this equation using the *atan2*-function, where the rotation angle α is marked in Figure 3.4a. When transferring vectorial quantities (as, for example, barotropic transports $\mathbf{V}$, or velocities $\mathbf{v}$) back from the rotated to the unrotated grid, it is necessary to reverse the misalignment by applying the rotation matrix

$$\boldsymbol{T}_\alpha = \begin{pmatrix} \cos\alpha & \sin\alpha \\ -\sin\alpha & \cos\alpha \end{pmatrix} , \tag{3.4}$$

in evaluating $\mathbf{v} = \boldsymbol{T}_\alpha \mathbf{v}'$. All quantities presented on standard grids within this thesis are obtained by first-order conservative remapping (*e.g.*, Jones, 1999) with the help of the Climate Data Operators software (CDO) (Schulzweida, 2022). Vectorial quantities (*e.g.*, transport ellipses as in Figure 2.9) are rectified by applying the rotation matrix (3.4). An example of the local rotation angle is attached to Figure 3.5c and 3.5f , which integrates the definitions of north and east on both grids. In the following sections, the impact of introducing the described rotated-pole grid on other aspects of the model is revisited.

3.2.3 Bathymetric Map

The most prominent component of the ocean tide model affected by the rotated-pole setup is the bathymetric function $H(\lambda, \phi)$. In the following, the discussion focuses on the selection and creation of the bathymetric map.
In its initial configuration, TiME employed GEBCO and ETOPO1 bathymetries. More recently, the high-resolution RTopo-2 data set (Schaffer et al., 2016) also became available (cf. Figure 2.6c). Based on GEBCO data, RTopo-2 uses additional data sources in polar latitudes to accurately represent sub-ice-shelf cavities. These areas are given consideration by computing the difference between the ice base and bedrock depth as bathymetric depth, *i.e.*, the free water column (cf. Schaffer et al., 2016, page 545). Compared to the original GEBCO data set, this modification implies a substantial extension of the ocean domain towards the south (the southernmost ocean point moves from approximately 78°S to 86°S). This extension is expected to strongly impact the tidal resonance strength, as the bathymetric function is known to exert substantial control over the ocean normal modes (Section 2.2.2) and OTD in general (Wilmes and Green, 2014; Arbic et al., 2009).
Since the resolution of TiME ($\frac{1}{12}^\circ$ = 5 arc minutes) is well below the resolution of the

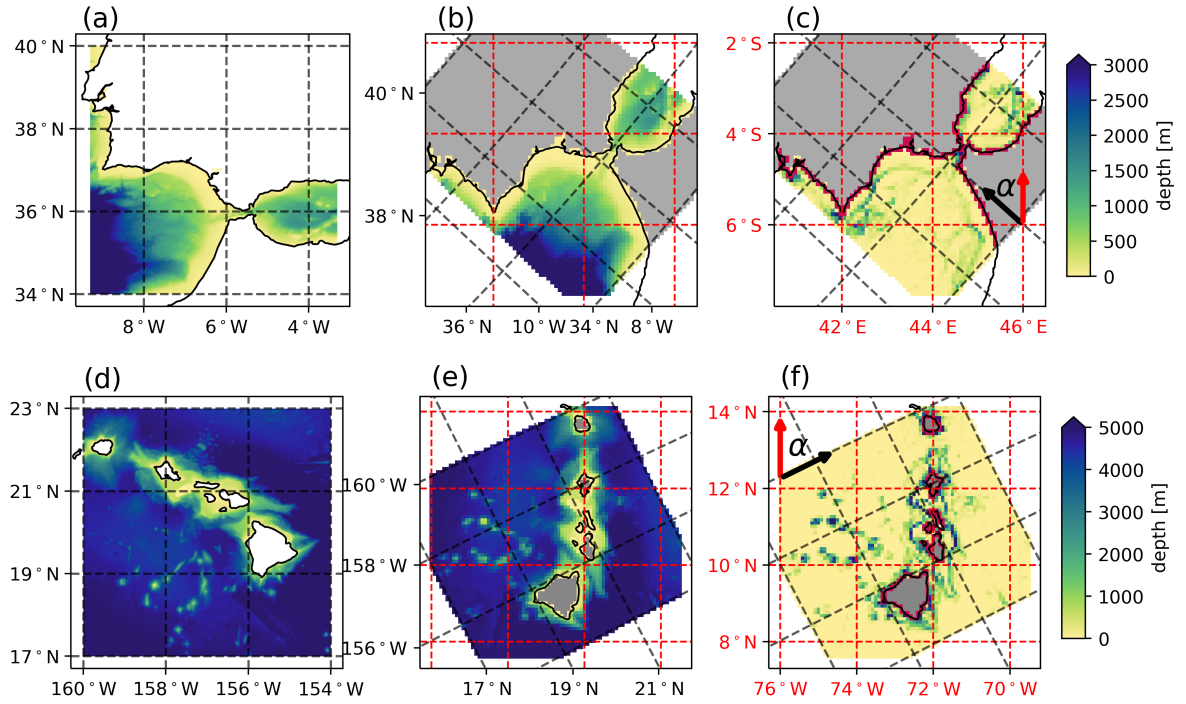

Figure 3.5: Derivation of the bathymetric map for two example locations: The Straight of Gibraltar (top) and the Hawaiian Archipelago (bottom). The high-resolution RTopo-2 bathymetry (a, d) is interpolated to the rotated grid *chi* at $\frac{1}{12}^\circ$ (b, e), employing the approach described in the text. Subplots (c, f) show the tenfold magnified differences induced by *inv-con* remapping with respect to *con* remapping. Differences in the ocean domain between both interpolation strategies are highlighted (magenta), and the rotation angle α (cf. Equation 3.3) is indicated. (Un)rotated coordinates appear in black (red).

RTopo-2 bathymetry (30 arc seconds), special attention is paid to how to perform the necessary resolution reduction.

The employed interpolation strategy is motivated by the perturbation theory of Equations (2.26) (cf. Appendix B). The interpolation algorithm is implemented using CDO. It creates the bathymetric map in the rotated-pole orientations (*arc*/*chi*/*gre*/*aus*). Within, the remapping was performed individually for 10×5 subdomains of the final bathymetric map to limit the necessary amount of memory. The algorithm mainly relies on the first-order conservative interpolation (*e.g.*, Jones, 1999) of inverse depth (*inv-con*), *i.e.*, $\frac{1}{H}$, which assigns the highest weights to the most shallow depths. Thus, this approach preserves ridges and seamounts.

As a secondary effect, inverse-conservative interpolation maximizes the land domain, *i.e.*, evaluating all grid cells as land, which contain at least one dry grid cell. This side effect is often undesirable, as it can induce the closing of straights (*e.g.*, the Straight of Gibraltar), which alters the character of the ocean domain unrealistically. Therefore, the algorithm relies on conservative interpolation of ocean depth H for grid cells on the boundary between land and ocean (*con*). As the depth $H = 0$ is assigned to dry grid cells, this approach maximizes the ocean domain and conserves the mean depth of the

respective grid cell, a property that is important for narrow straights. This approach thus aims at being 'ridge and straight conserving'. The subdomain-wise interpolation approach is illustrated in Figure 3.5, where the Straight-conserving character is presented on top (a-c). At the same time, an example of ridge conservation is shown below (d-f). When employing this algorithm, the final bathymetry should be tested for the correct representation of isthmuses that function as hydrodynamic barriers, *e.g.*, the Isthmus of Panama. Following this interpolation procedure, the minimum water depth is set to 15 m, while alternative minima of 10 or even 5 m have a negligibly small influence on tidal dynamics. In addition, the Caspian Sea Level (CSL) is subject to rapid climatic changes compared to the open ocean (Beni et al., 2013; Chen et al., 2017) and has been fixed to -26.5 m. The finally obtained bathymetric map is thus fit to simulate tides in the global world oceans, as well as in marginal seas and the world's largest endorheic basin, the Caspian Sea (*e.g.*, Medvedev et al., 2016, 2017).

3.2.4 Tide-Raising Potential

This section discusses the upgraded implementation of the TRP, which pursues two goals. First, the adaptation of the TRP to the rotated-pole grid and, second, the consideration of degree-3 spherical harmonic functions that allows the simulation of degree-3 tides.
In Section 2.1.1, the partial TRP (2.8) was derived in the form

$$V_{\mathrm{tid}}^{ilm}(\phi,\lambda,t) = a_l^b(\omega_i)\; A_i \left(Y_{lm}(\phi,\lambda)\cos\chi_i(t) - Y_{l-m}(\phi,\lambda)\sin\chi_i[t]\right) \;, \tag{3.5}$$

that allows separating spatial variables (ϕ,λ) from the temporal dependency encoded in the phase argument $\chi_i(t)$. It is aimed to rewrite $V_{\mathrm{tid}}^{ilm}(\phi,\lambda,t)$ as $V_{\mathrm{tid}}^{ilm}(\phi[\phi',\lambda'],\lambda[\phi',\lambda'],t)$ to represent the tide-raising forces on the rotated grid correctly. In principle, achieving this rotation by inverting Equations (3.2) is possible. However, an alternative approach is preferred because rotations must only be applied to spherical harmonic functions Y_{lm} and Y_{l-m}.
This approach employs *Wigner D-functions* that have their origin in the theory of representations of the three-dimensional rotation group, O(3), and the special unitary transformation group, SU(2) (Risbo, 1996). Their main applications are in the theory of angular momentum in quantum mechanics (*e.g.*, Varshalovich et al., 1988). Nevertheless, the possible field of applications is much broader. We refer to the latter two publications and references therein for an in-depth discussion of Wigner-D matrices and related topics. This thesis is concerned with the specialized application of rotating real-valued spherical harmonic functions with the help of D-functions and derived quantities, which is also necessary for several other geoscientific problems, *e.g.*, the perturbation of satellite orbits (*e.g.*, Gooding and Wagner, 2008).
When parameterizing the rotation as outlined in Section 3.2.2 by two non-zero Euler angles, the transformation reduces to

$$Y_{lm}(\phi,\lambda) = \sum_{\mu=-l}^{l} \boldsymbol{r}_{lm\mu}(\phi_{\mathrm{p}},\lambda_{\mathrm{p}})\; Y_{l\mu}(\phi',\lambda') \;. \tag{3.6}$$

Within, the tensor $\boldsymbol{r}_{lm\mu}(\phi_{\mathrm{p}},\lambda_{\mathrm{p}})$ encrypts the projection of the 'input' spherical harmonic function $Y_{lm}(\phi,\lambda)$, on the 'output' function $Y_{l\mu}(\phi',\lambda')$ in the rotated system (with its

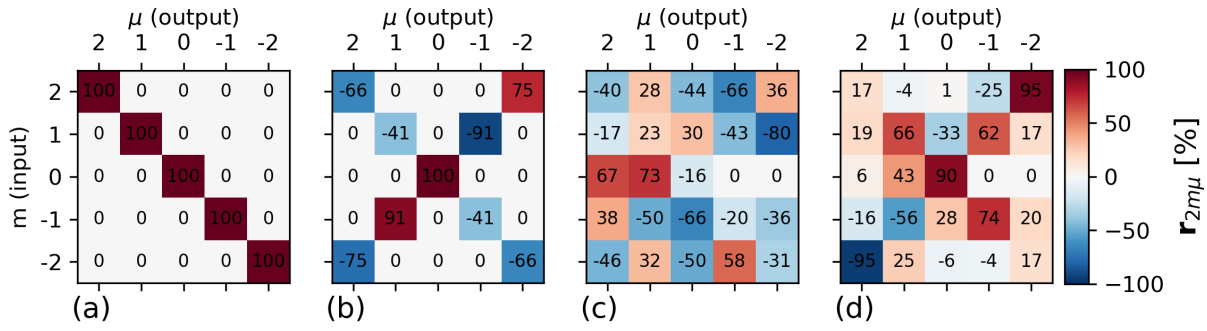

Figure 3.6: Rotation Matrices $\boldsymbol{r}_{2m\mu}$ that performs rotations of the degree-2 TRP for different pole locations: (a) the *arc* grid at $\phi_\mathrm{p}, \lambda_\mathrm{p} = (90°\mathrm{N}, 0°\mathrm{E})$, (b) the *arc* grid rotated in an east-west direction to $(90°\mathrm{N}, 114.5°\mathrm{E})$, (c) the *chi* grid at $(28.5°\mathrm{N}, 114.5°\mathrm{E})$, and (d) the *gre* grid at $(75°\mathrm{N}, 40°\mathrm{W})$.

North Pole located at $\phi_\mathrm{p}, \lambda_\mathrm{p}$). To obtain the entire transformation, projections within the indicated spherical harmonic degree l are added, which is $2l + 1$ contributions in total. While this approach allows quick rotations of spherical harmonic coefficients up to a high degree (Risbo, 1996), it also has the practical advantage that spherical harmonic functions of degrees 2 and 3 (as in the TRP) can be described by a 5×5 and a 7×7 matrix, respectively[4]. For example, $\boldsymbol{r}_{2m\mu}(\phi_\mathrm{p}, \lambda_\mathrm{p})$ is presented in Figure 3.6 for several grid configurations (identical to Figure 3.1).
The respective matrices have to be only calculated once per pole orientation. TiME employs the rotation algorithm provided by (Gooding and Wagner, 2010), which is applied to spherical functions of degree l. The astronomical Tide-Generating Potential is adapted from the HW95 tidal development of Hartmann and Wenzel (1994, 1995b).
Mathematically, tide-raising accelerations are proportional to $\boldsymbol{\nabla} Y_{lm}$. As the analytical differentiation of spherical harmonic functions is straightforward, accelerations are calculated directly on the staggered numerical grid by evaluating the differentiated versions of Y_{lm} in the east and north directions (cf. Appendix A).

3.2.5 Energy Dissipation

Out of the dissipative mechanisms introduced in Section 2.2.1, the initial TiME implementation did not include topographic wave drag and sea-ice friction. Therefore, they are included in the conducted upgrade. The latter has a minimal impact on the model performance, as quantified by geodetic data sets, but allows investigating the influence of glacial, paleoclimatic conditions on tidal dynamics. Paleo simulations are the subject of Chapter 6, where the ice friction parameterization is briefly introduced as modified bottom friction. As it is not significant for the TiME's core characteristics, the effect is ignored here, and focus is given to the newly implemented topographic wave drag parametrization, which has been shown to exert a critical influence on the model accuracy

[4]The vertical Coriolis vector $\boldsymbol{f}$ is proportional to $\sin\phi = P_{10}(\sin[\phi])$ and can be rotated with the procedure discussed in this Section, *i.e.*, employing the matrix $\boldsymbol{r}_{1m\mu}$.

(*e.g.*, Buijsman et al., 2015).
Barotropic parameterizations of baroclinic dissipative processes have been shown to accurately capture spatial dissipation patterns (*e.g.*, Green and Nycander, 2013; Buijsman et al., 2015). A parameterization introduced by Nycander (2005) is employed that is built on prior considerations of Bell (1975) and Llewellyn Smith and Young (2003). The wave drag formulation is described by the fully-populated second rank tensor

$$\boldsymbol{\mathcal{C}} = \frac{N_\mathrm{b}}{4\pi}\sqrt{1-\frac{f^2}{\omega^2}}\,\Theta_H(|f|-\omega)\begin{pmatrix} 2\,(\partial \mathrm{x}_1 H\;\partial \mathrm{x}_1 j) & \partial \mathrm{x}_1 H\;\partial \mathrm{x}_2 j + \partial \mathrm{x}_2 H\;\partial \mathrm{x}_1 j \\ \partial \mathrm{x}_1 H\;\partial \mathrm{x}_2 j + \partial \mathrm{x}_2 H\;\partial \mathrm{x}_1 j & 2\,(\partial \mathrm{x}_2 H\;\partial \mathrm{x}_2 j) \end{pmatrix} . \tag{3.7}$$

Here N_b is buoyancy frequency evaluated at the sea floor, and x_i are local orthogonal coordinates that we identify with east and north directions on the rotated-pole grids (λ' and ϕ'). Please note that the explicit dependence on ω renders $\boldsymbol{\mathcal{C}}$ non-local in time. Further, the tensor implicitly depends on the geographical latitude, encoded in $f = 2\Omega_\mathrm{e}\sin\phi$, and is set to zero polewards of the *critical latitude*, defined by $|f|-\omega = 0$. Within Equation (3.7) the Heaviside-Function $\Theta_\mathrm{H}(\omega)$, which is equal to 1 for $\omega > 0$, and 0 for $\omega \leq 0$, ensures the consideration of the critical latitude.
The function

$$\partial \mathrm{x}_i j(\mathbf{x}) = \int dA' g_\sigma(|\mathbf{x}-\mathbf{x}'|)\partial \mathrm{x}_i H(\mathbf{x}') \tag{3.8}$$

is calculated by a bathymetric convolution integral with the non-homogeneous Green's function $g_\sigma(r) = \frac{1}{\sigma}G_\sigma(\frac{r}{\sigma})$. Within, the kernel function $G_\sigma(r')$ is defined as

$$G_\sigma(r') = \frac{1}{r'} - \frac{\sqrt{\pi}}{2}e^{-r'^2/8}I_0(\frac{r'^2}{8}) \;, \tag{3.9}$$

where I_0, the modified Bessel function of the first kind, serves as a wave filter. The explicit space dependence of g_σ originates from the length scale $\sigma(\mathbf{x}) = 1.45\overline{N}H/(\pi\sqrt{\omega^2-f^2})$, which contains information about bathymetry $H(\mathbf{x})$, the depth-averaged buoyancy frequency $\overline{N}(\mathbf{x})$, and the tidal frequency ω. $\boldsymbol{\mathcal{C}}$ is calculated separately for each rotated grid, following the improved numerical scheme described by Green and Nycander (2013) at a resolution of 1/30°. It is then interpolated conservatively with CDO to the coarser 1/12°-resolution (also 1/6° and 1/3°) of TiME. The convolution integral (3.8) is truncated at $r = 5\sigma$ for each integration point to reduce the computational load.

This parameterization is rigorously inferred from linear wave theory, which allows deriving the tensor $\boldsymbol{\mathcal{C}}$ from the physical fields $H(\mathbf{x})$, $\overline{N}(\mathbf{x})$, and $N_\mathrm{b}(\mathbf{x})$ without the need to introduce a free 'tuning' parameter that has to be adapted to the ocean tide model (cf. Figure 2.6). This feature distinguishes the presented approach from several alternative formulations of $\boldsymbol{\mathcal{C}}$, which often implicitly simplify the kernel function G_σ to be proportional to the Dirac-δ-function. Provided adequate model tuning, the mentioned alternative formulations result in accurate ocean tide solutions. However, the here pursued formulation has the clear advantage of being directly applicable in situations where rigorous tuning is impossible (*e.g.*, for objective O3).
To derive the tensor for present-day conditions, depth-resolved hydrographic data from the World Ocean Atlas (WOA) for salinity (Zweng et al., 2018) and temperature (Locarnini et al., 2019) is used in combination with the TEOS-10 equation of state (McDougall and Barker, 2011) to compute a global map of the buoyancy-frequency $N(\phi, \lambda, z)$, where

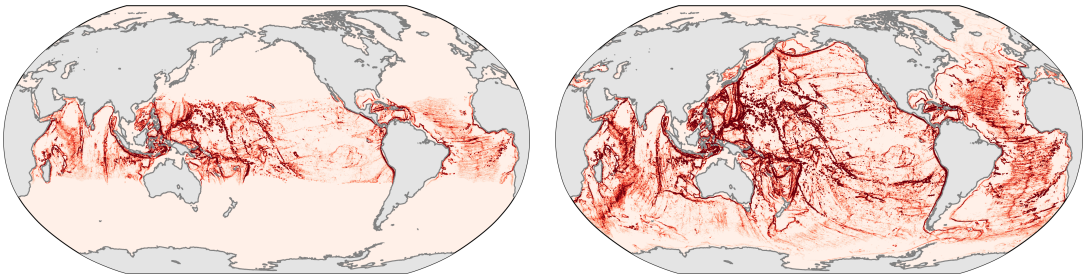

Figure 3.7: Amplitude of the diagonal tensor elements of $\boldsymbol{\mathcal{C}}$, *i.e.*, $\sqrt{\boldsymbol{\mathcal{C}}_{11}^2 + \boldsymbol{\mathcal{C}}_{22}^2}$, for diurnal tides (left) and semidiurnal tides (right). The plots are presented in arbitrary units to highlight the spatial structure of the strongly frequency-dependent dissipation process.

z is a depth coordinate (cf. Figure 2.6). The excitation of internal waves is a strongly frequency-dependent process that differs for diurnal ($\omega_\mathrm{d} = \Omega_\mathrm{e}$), semidiurnal ($\omega_\mathrm{sd} = \Omega_\mathrm{e}/2$), and terdiurnal ($\omega_\mathrm{td} = \Omega_\mathrm{e}/3$) tidal species resulting in different wave drag tensors for each species ($\boldsymbol{\mathcal{C}}_{\mathrm{d/sd/td}}$)[5]. The frequency-dependent character of $\boldsymbol{\mathcal{C}}$ is especially evident for diurnal tidal species, where the tensor is 0 polewards of the critical latitude $\pm 30°$, while for semidiurnal tides the tensor extends towards the poles (cf. Figure 3.7).
As Buijsman et al. (2015), we follow the approach introduced and developed by Nikurashin and Ferrari (2011); Melet et al. (2013). and Scott et al. (2011) to reduce potentially overestimated wave drag strength at supercritical slopes. To these means, the drag tensor is normalized at supercritical slopes to compensate for overestimated dissipation. Further, a cutoff depth of 150 m is introduced by assuming shallower seas to be well-mixed (*e.g.*, Schindelegger et al., 2018).
For the implementation in TiME, a tuning parameter for the wave drag tensor, κ_w is added, *i.e.*, $\boldsymbol{\mathcal{C}} \rightarrow \kappa_\mathrm{w}\boldsymbol{\mathcal{C}}$. While the formulation of the effect proposes $\kappa_\mathrm{w} = 100\%$, narrow-bounded variations of κ_w are allowed. Yet, several factors can influence the accuracy of the derived tensor. These include the precise numerical formulation (Nycander, 2005), the accuracy and resolution of the stratification and bathymetric data, and necessary approximations, *e.g.*, for supercritical slopes. As the uncertainties arising from these factors cannot be precisely quantified, deviations from $\kappa_\mathrm{w} = 1$ are possible. Therefore, they are considered to optimize the modelling agreement with geodetic data.

3.2.6 Self-Attraction and Loading

The linear parameterization of SAL, $\zeta_\mathrm{SAL} = \epsilon\zeta$, is often implemented as a computationally lightweight solution that can capture the mean effect for selected partial tides. A more elaborate approach is required for high-accuracy simulations (Ray, 1998a). Here, we follow an approach reintroduced by Schindelegger et al. (2018) that relies on truncated spherical harmonic analysis of the SAL potential, *i.e.*, constraining sum (2.13) to a certain

[5] As long-period tides are very close to the SEQT description, wave drag dissipation has an insignificant effect on them and is neglected.

maximum degree and order $l_{\max}$, *i.e.*,

$$\zeta_{\mathrm{SAL}}(\mathbf{x}) = \frac{3\rho_{\mathrm{sw}}}{\rho_{\mathrm{se}}} \sum_{l,|m|\leq l}^{l_{\max}} \frac{\alpha_l}{2l+1}\, \zeta_{lm} Y_{lm}(\mathbf{x}) \ . \tag{3.10}$$

For the computation, the constants $\rho_{\mathrm{sw}} = 1024\,\mathrm{kg\,m^{-3}}$ (mean density of seawater) and $\rho_{\mathrm{se}} = 5510\,\mathrm{kg\,m^{-3}}$ (mean density of the solid Earth) are assumed, while load Love numbers (LLNs) stem from Wang et al. (2012) (based on the Preliminary Reference Earth Model, short: PREM) with a correction to represent low degree LLNs in the frame of figure (Blewitt, 2003) for evaluation of α_l.
On the one hand, the numerical cost for the degree-wise algebraic evaluations in Equation (3.10) is negligibly small. On the other hand, the computational burden is shifted to repeated transformations between the spectral and the spatial domain for each time step. These transformations are efficiently handled with the highly optimized SHTns-package (Schaeffer, 2013). The high efficiency of this SAL implementation utilizing SHTns has rendered it a frequently used solution in ocean tide modelling (*e.g.*, Shihora et al., 2021; Barton et al., 2022; Brus et al., 2023).
The decisive parameter within this implementation is the maximum spherical harmonic degree $l_{\max}$, which defines the degree of approximation of this approach. We set $l_{\max} = 10...1024$ for later simulations to estimate the impact on the model's accuracy.

3.2.7 Atmospheric Forcing

TiME includes atmospheric forcing for 16 partial tides provided by Balidakis et al. (2022). The periodic pressure potential V_{p} for each atmospheric partial tide is first transformed to the rotated-pole grid using conservative interpolation with CDO. Then, the LAAL and OAAL potentials (Equation 2.11) are derived from V_{p} with the help of the SHTns package ($l_{\max} = 1024$, other parameters as for Equation 3.10).
Afterward, the atmospheric potentials V_{p}, V_{l}, and V_{o} are combined to calculate barotropic accelerations on the staggered grid employing finite differences. Similarly, wind stress accelerations $\boldsymbol{W}$ for each partial tide are transferred to the rotated-pole grid. Rectification of the respective vector direction employing matrix (3.4) is necessary before adding them to the accelerations induced by atmospheric surface pressure anomalies.

3.3 Numerical Solver

The equations of Seiler (1991) were reformulated after the numerical scheme of Backhaus (1985) by Weis (2006). The resulting semi-implicit numerical scheme has the general form

$$\begin{pmatrix} \mathrm{u} \\ \mathrm{v} \end{pmatrix}^{p+1} = \boldsymbol{R}_1 \cdot \begin{pmatrix} \mathrm{u} \\ \mathrm{v} \end{pmatrix}^{p} - g_0\, \boldsymbol{R}_2 \cdot \begin{pmatrix} \partial_{\mathrm{x}}\zeta \\ \partial_{\mathrm{y}}\zeta \end{pmatrix}^{p+\frac{1}{2}} + \Delta t \cdot \begin{pmatrix} X \\ Y \end{pmatrix} \ , \tag{3.11}$$

with the Coriolis rotation matrices R_1 and R_2, defined as

$$\boldsymbol{R}_1 = \begin{pmatrix} \alpha_{\mathrm{c}} & \beta_{\mathrm{c}} \\ -\beta_{\mathrm{c}} & \alpha_{\mathrm{c}} \end{pmatrix} \quad , \text{ and } \boldsymbol{R}_2 = \frac{1}{f} \begin{pmatrix} \beta_{\mathrm{c}} & \gamma_{\mathrm{c}} \\ -\gamma_{\mathrm{c}} & \beta_{\mathrm{c}} \end{pmatrix} \ . \tag{3.12}$$

Here, the temporal index p and $p+1$ refer to the former and following time step, t_p and t_{p+1}, respectively. The index $p+\frac{1}{2}$ signifies the intermediate time step of the semi-implicit solver. The rotation matrices $\boldsymbol{R}_{1,2}$ are populated by the expressions $\alpha_c = \cos(f\Delta t)$, $\beta_c = \sin(f\Delta t)$, and $\gamma_c = 1 - \alpha_c$, which result in improved stability of the numerical scheme (Weis, 2006). Further, $\Delta t = t_{p+1} - t_p$ is the time step size of the solver, and X and Y represent the residual terms, *i.e.*, accelerations, of Equations (3.1).
The semi-implicit algorithm is formulated as an iterative scheme (iteration index: n) by successive over-relaxation (SOR, *e.g.*, Press et al., 2007). The iterative equation for the sea surface height difference $\Delta\zeta_{ij} = \zeta_{ij}(t_{p+1}) - \zeta_{ij}(t_p)$, reads

$$(\Delta\zeta_{ij})^{n+1} = (1-\omega_r)(\Delta\zeta_{ij})^n + \frac{\omega_r}{1+c_5}\left(\sum_{k\in\oplus(ij)} c_k\ \Delta(\zeta_{ij,k})^{n+1} + B_{ij} + C_{ij}\right)\ , \qquad (3.13)$$

where $\oplus(ij)$ signifies all eight neighboring grid cells of (ij), running clockwise from the northwest in a 'compass stencil'. Further, ω_r is the scheme's relaxation parameter that controls the convergence speed. Weis (2006) selected $\omega_r = 1.3$ as an optimal value. The coefficients c_k, C_{ij}, and B_{ij} are explicitly evaluated functions of the ocean state (u, v), predicted by Equations (3.11). The SOR problem is formulated on a so-called 'chess-board-scheme', as the updated values $(\Delta\zeta_{ij})^{n+1}$ only depend on prior values of neighboring grid cells on the compass stencil.
The discretized sea surface elevation array (ζ_{ij}) is divided into four subgroups. Each subgroup contains all elements with a spacing[6] $\Delta i = \Delta j = 2$. Therefore, iterations all four subgroups are independent. Successive evaluation of Equation (3.13) within each subgroup results in updating the entire set of grid cells. This procedure is repeated iteratively until the residuum, $R_n = \sum_{ij} |(\Delta\zeta_{ij})^{n-1} - (\Delta\zeta_{ij})^n|$, drops below a certain threshold that is set to $R_{crit} = 10^{-7}$cm. A first guess to start the iteration scheme is linearly interpolated from the last two time steps, $(\Delta\zeta_{ij})^{n=0} = 2\Delta\zeta_{ij}(t_{p-1}) - \Delta\zeta_{ij}(t_{p-2})$. As partial tides typically have much longer periods than the time step size of the model, this linear prediction is close to the final result and, therefore, causes a significant reduction of the required number of iterations (Weis, 2006).
Additionally, the solver considers boundary conditions of two kinds. First, no-flow conditions are implemented at the coasts by enforcing orthogonal flow velocities to vanish (cf. Figure 1.2). Second, periodic boundary conditions are considered for the westernmost and easternmost grid cells. They are realized by extending the grid in the zonal direction by two recurring elements, which TiME synchronizes after each iteration of Equation (3.13). For the explicit formulation of the finite-difference algorithm, the boundary conditions to the reduced resolution zones, and the pole cap formulation, we refer to the Appendix of Weis (2006) and Backhaus (1985).

3.3.1 Introduction of the Rotated-Pole Grid

The numerical solver is virtually unaffected by the newly introduced rotated-pole grids. In most cases, the rotation is applied to physical fields before loading them into the model (bathymetry, atmospheric forcing, wave drag formulation, sea ice cover). The data

[6]The term 'chess-board scheme' is slightly misleading here, as the iteration scheme relies on four different subgroups of elements, whereas a chess-board has only two subgroups of fields, black and white.

Table 3.1: Overview of the data sets, algorithms, and the respective reference publications used by the updated ocean tide model TiME within this thesis.

Model component	Label	References
Bathymetric map	H	Schaffer et al. (2016)
Eddy viscosity scheme	$\hat{R}\mathbf{v}$	Weis (2006)
Love numbers (PREM)	k_l, l_l, h_l	Wang et al. (2012); Blewitt (2003)
	$h_l^{\mathrm{b}}, k_l^{\mathrm{b}}$	Spiridonov (2018)
Numerical solver	SOR	Backhaus (1982, 1985)
Ocean stratification	$N_{\mathrm{b}}, \overline{N}$	Zweng et al. (2018); Locarnini et al. (2019)
		McDougall and Barker (2011)
Pole rotation algorithm	$\boldsymbol{r}_{lm\mu}$, ...	Gooding and Wagner (2010); Risbo (1996)
Pole rotation transform	$\boldsymbol{T}_{\alpha}$, ...	Schulzweida (2022)
Atmospheric Excitation	V_{p}, W, ...	Balidakis et al. (2022); Gill (1982)
Tide-Generating Potential	V_{grav}	Hartmann and Wenzel (1994, 1995b)
Self-attraction and loading	ζ_{SAL}	Schaeffer (2013); Schindelegger et al. (2018)
Wave drag tensor	$\boldsymbol{\mathcal{C}}$	Nycander (2005); Green and Nycander (2013)

input/output of time was modernized to operate with NetCDF files (Unidata, 2012), which allows platform-independent handling and evaluation of employed data sets. Slight changes in the code must only be implemented for few mechanisms.
These changes comprise the rotation of the Coriolis acceleration by replacing $f(\phi)$ by $f(\lambda', \phi')$ (cf. Equation 3.2). Further, the spherical harmonic functions of degree-3 (cf. Appendix A) were added, as well as their spatial derivatives. TiME also employs the rotation routines of Gooding and Wagner (2010), which allows for evaluating Equation (3.6), for both degree-2 and degree-3 partial tides. To accommodate the influence of the NDFW-resonance on the TRP (Section 2.1.1), the last row of Table 2.1 is used to evaluate $\alpha_l^b(\omega_i)$. While α_l^b is constant for tides outside the diurnal spectrum of Table 2.1, modifications are also significant for degree-3 tides. With the updated implementation of the TRP, TiME can evaluate tide-raising forces for arbitrarily rotated-pole locations $\lambda_{\mathrm{p}}, \phi_{\mathrm{p}}$ and variable partial tides up to degree-3.
The most important consequence of the pole rotation is the closed land cover at the numerical poles. Thus, the no-flow boundary conditions within the TiME code form an impenetrable barrier around the poles, which isolates the pole cap from OTD. Therefore, the updated model no longer employs the pole cap formulation. Another change was made to the latitude circles at which resolution changes become effective. While they resided at $\pm 76.5°$ and $\pm 82.5°$ in the initial TiME version, they were moved to $\pm 60°$ and $\pm 75°$ in the updated setup. Weis (2006) found negligibly slight differences between simulations performed with both configurations. The latter was preferred because the aspect ratio of most grid cells is kept closer to 1 while reducing the overall computational load.

3.3.2 Implementation of Additional Accelerations

Another significant change to the model concentrates on the modification in the momentum balance Equation from (3.1) into (2.26) by introducing additional tide-generating

(atmospheric forcing, SAL acceleration) and dissipative (wave drag) accelerations. This was possible in the framework of the numerical solver by a simple expansion of the acceleration terms X and Y in Equation (3.11), which propagates to B_{ij} and C_{ij} in Equation (3.13).
In this manner, the solver explicitly considers accelerations induced by SAL, which read $g_0 \boldsymbol{\nabla}(\zeta_{\mathrm{SAL}})^p$ and are in sync with ζ^p (Figure 3.8, center). Therefore, the SHTns package (Schaeffer, 2013) was compiled with the TiME source code for repeated evaluation of Equations (3.10) and the spherical harmonic transformation (2.14). SHTns was configured with regular nodes and poles included, which rendered an intermediate, lightweight interpolation of the TiME grid necessary, as it is shifted by $\frac{1}{2}\delta\phi$ and did not include the poles. Additionally, atmospheric accelerations are evaluated for each time step. While wind stress accelerations are loaded directly into the model, accelerations induced by the combined atmospheric potential $V_{\mathrm{atm}} = V_{\mathrm{p}} + V_{\mathrm{l}} + V_{\mathrm{o}}$ are calculated within TiME by differentiation onto the staggered grid. Together, the updated TiME implementation allows the specification of arbitrary external barotropic accelerations in terms of a gradient potential (as for V_{atm}) or direct accelerations (as for $\boldsymbol{W}$). While this is initially tailored for atmospheric forcing, the functionality is by no means restricted to studying atmospheric tides. Other applications include, for example, investigating the ocean response to the partial TRP of degree-4 and higher or the impact of a laterally inhomogeneous Earth structure on SAL (Huang et al., 2021, 2022).
Similarly, the wave drag (Equation 2.18) enters the momentum equation by modifying expressions X and Y. On top, the wave drag accelerations are stored in the memory individually. This effect-wise storage is performed for all dissipative mechanisms (bottom friction, eddy viscosity, ice friction) and allows discrimination of individual energy sinks of the ocean tide energy balance.
In summary, the framework of the numerical solver remains unaltered by the conducted changes, which are combined in Table 3.1. On the other hand, the individual weights within the scheme are changed. As this could cause changes in the optimized numerical setup, we consider readjusting the parameters with respect to the choices of Weis (2006) in the following section.

3.3.3 Tidal Modelling Approach

The updated TiME model represents an implementation of the scheme in Figure 2.1. For simulations presented in this thesis, the model is run in *partial tide forcing mode*, *i.e.*, considering a single partial component of the TRP and atmospheric forcing (cf. Figure 3.8), whose phase $\chi_i(t)$ progresses with $\omega_i t$. The model is initialized in a zero-state, *i.e.*, $\boldsymbol{\zeta}(t_0 = 0) = \mathbf{0}$. Due to the action of frictional forces, the model dynamics converge towards

$$\begin{aligned} \boldsymbol{\zeta}(\mathbf{x}, t) &= \mathrm{Re}\Big(\sum_{n=0} \boldsymbol{\zeta}^{n\omega_i}(\mathbf{x})\, e^{\mathrm{i}n\chi_i(t)} \Big) \\ &= \boldsymbol{\zeta}^{\omega_i}_{\cos} \cos\chi_i(t) + \boldsymbol{\zeta}^{\omega_i}_{\sin} \sin\chi_i(t) + \Big(\boldsymbol{\zeta}^{\omega_i}_{\mathrm{const}} + \boldsymbol{\zeta}^{2\omega_i}_{\cos} \cos 2\chi_i(t) + \boldsymbol{\zeta}^{2\omega_i}_{\sin} \sin 2\chi_i(t) + ... \Big) \ , \end{aligned} \tag{3.14}$$

which is a small subset of the partial tides considered in Equation (2.27). Here, $\boldsymbol{\zeta}^{n\omega}(\mathbf{x}) \in \mathbb{C}^3$ describes the part of the field oscillating at frequency $n\omega$, comprised of *in-phase* $\boldsymbol{\zeta}^{n\omega}_{\cos}$ and *quadrature* component $\boldsymbol{\zeta}^{n\omega}_{\sin}$, as $\boldsymbol{\zeta}^{n\omega} = \boldsymbol{\zeta}^{n\omega}_{\cos} + \mathrm{im}\ \boldsymbol{\zeta}^{n\omega}_{\sin}$ (cf. Section 2.3). The following

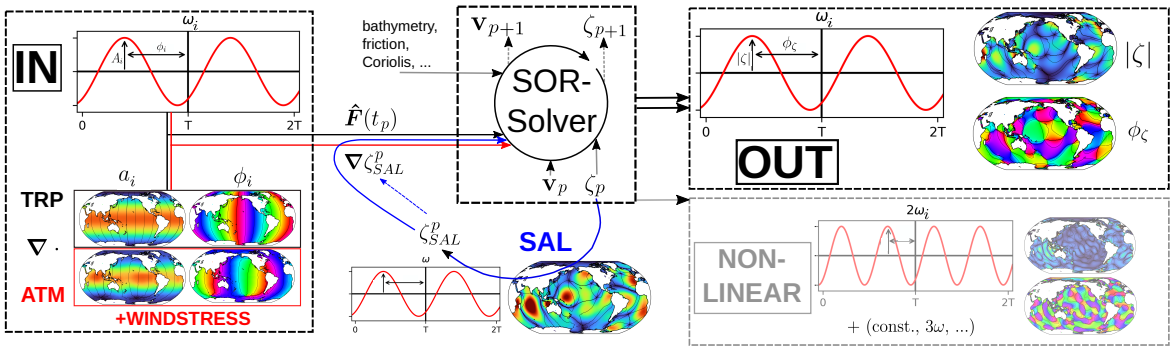

Figure 3.8: Partial tide forcing mode of TiME, exemplary for S_2. Temporal harmonic (frequency ω), and external accelerations (IN) are fed into the SOR-solver of TiME22, which iterates the ocean state variables $(\zeta, \mathbf{v})$, for consecutive time steps $t_p, t_{p+1}, \ldots$. The instantaneous sea surface height anomaly ζ_p is used to predict acceleration by SAL which is fed back into the solver. After an initialization period, OTD converges to temporal harmonic oscillations. The last complete tidal period is used to harmonically analyze for partial tides of frequency $0, \omega, 2\omega$ (OUT). Temporal harmonic input forcing and model output are represented in the amplitude/phase notation, *i.e.*, $|\zeta|_i$ and ϕ_ζ.

discussion focuses on the first (SSH) component of $\boldsymbol{\zeta}^{n\omega}$. Thus, we recall the equivalent description by amplitude $|\zeta|$ and phase ϕ_ζ. The vast majority of tidal variability arises from the linear field component oscillating at frequency ω. The residual tidal circulation $\boldsymbol{\zeta}^{\omega}_{\mathrm{const}}$, a consequence of tidal rectification (*e.g.*, Pérenne and Pichon, 1999), as well as the overtides with $n \geq 2$, are a result of nonlinear interaction, and represent minor contributions to the tidal flow field.

The time step of the model is chosen to be close to 180 seconds. More precisely, TiME selects the time step as an integer fraction of the tidal period $T_i = 2\pi\omega_i^{-1}$. Thus, Δt is set to $\frac{T_{\mathrm{diu}}}{480}$ for diurnal, $\frac{T_{\mathrm{semi}}}{240}$, and for semidiurnal $\frac{T_{\mathrm{ter}}}{160}$ for terdiurnal partial tide forcing. The model spins up for at least 30 days, which is (30, 60, 90) tidal cycles for diurnal to terdiurnal species. The next full oscillation cycle forms the basis to extract the primary tidal constituent, $\boldsymbol{\zeta}^{\omega}_{\cos}$ and $\boldsymbol{\zeta}^{\omega}_{\sin}$, as well as the temporally constant and the double frequency component. The choice of a 30-day spin-up can be motivated by the much shorter half-life of dominant diurnal to terdiurnal eigenmodes in the order of approximately three days and shorter (*e.g.*, Müller, 2007), and similar choices by comparable ocean tide models (*e.g.*, Schindelegger et al., 2018).

Further, the maximum global differences between the complex sea surface elevation vector ζ^{ω} for M_2, extracted after longer spin-up periods of up to 60 days, are estimated. The maximum deviation reaches values of 0.003 cm only in several marginal seas. This uncertainty is far below the average accuracy of the model with respect to geodetic data sets, which is on the order of $3-5$ cm for M_2, and also far below the precision of satellite altimetry constrained ocean tide models and satellite gravimetry. Thus the operation mode does not pose constraints on the avised model applications.

Numerical tests in the new model configuration show that the performance improves slightly by setting the relaxation parameter to $\omega_{\mathrm{r}} = 1.7$. The finally obtained computational speed was 20 node hours to simulate 30 model days with the computer HLRE-3

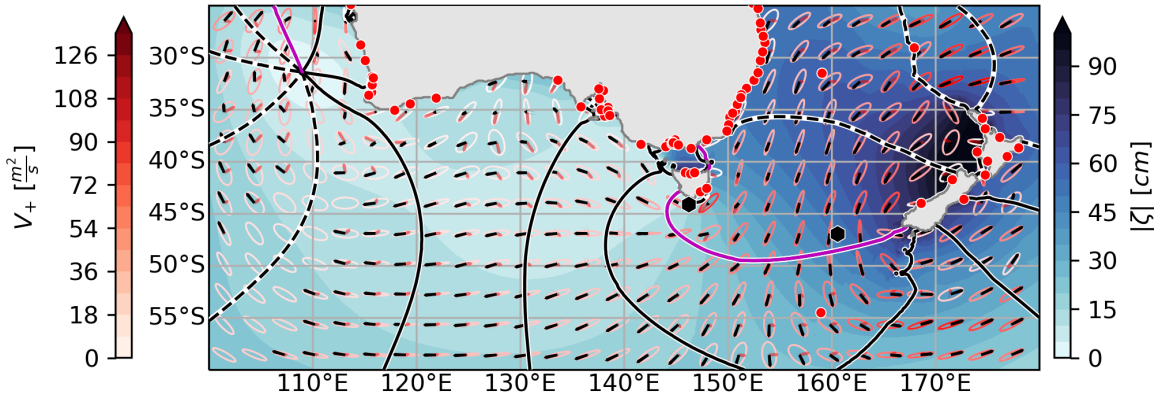

Figure 3.9: Ocean tidal dynamics evoked by the M_2 partial tide around New Zealand and South Australia modeled with TiME. The tidal sea surface anomaly ζ is depicted in the amplitude-phase notation, where tidal phase lags ϕ_ζ (*i.e.*, cotidal lines) appear in increments of 60° (magenta: $\phi_\zeta = 0°$; dashed: $\phi_\zeta < 0°$). Tidal transports $\mathbf{V}$ are integrated as ellipses, where the color coding refers to the maximum tidal transport (*i.e.*, the semi-major axis V_+). Transport phase lags are plotted relative to ϕ_ζ, where black arrows symbolize the transport in phase with the local sea surface anomaly, and red arrows refer to the out-of-phase component (for $\zeta[\mathbf{x}, t] = 0$). The plot is augmented by TICON-3 tide gauge stations (red, ∘) and OBP recorders (black, ⬢) as in Figure 1.2.

'Mistral' at Deutsches Klimarechenzentrum (DKRZ), comparable to the results of Weis (2006) with the predecessor computer. Within, the algorithm spends roughly 10% of the time on SAL calculations in the newly implemented scheme, rendering it relatively light-weight. A significant speedup can is achievable by reducing the model resolution. For example, halving the resolution to $\delta\phi = \frac{1}{6}^\circ$ can reduce the runtime by a factor of up to $2^3 = 8$, as it additionally allows doubling the minimum time step size (CFL-criterion).
The main disadvantage of the partial tide forcing mode is the neglect of nonlinear interactions between different tidal species, which is most notable in shallow water. This interaction gives rise to higher harmonics (compound- and overtides) and acts back on the generating main tides, inducing deviations in shallow waters. The induced deviations between partial tides extracted from partial vs. full-ephemeris forcing (all partial tide-generating forces at once) are discussed by Weis (2006). It is found that the observed small deviations are concentrated in shallow shelf areas and are even smaller in the deep ocean. Moreover, allowing for nonlinear interactions did not significantly affect the validation with geodetic measurements (at that time, the pelagic ST103 data set of Le Provost, 1995). Hence, the interaction effect induced by the nonlinear operators in TiME is comparably small.
Further, the results show that the agreement of the principal lunar, nonlinear tide M_4 with geodetic data sets is much worse than linear tides simulated with TiME. This observation is with a high probability related to the representation of nonlinear effects in TiME, which should be optimized. Another objection to utilizing the full-ephemeris simulation mode resides in the effect of topographic wave drag, which is frequency dependent and thus differs for diurnal and semidiurnal tides. It can not correctly be depicted for partial

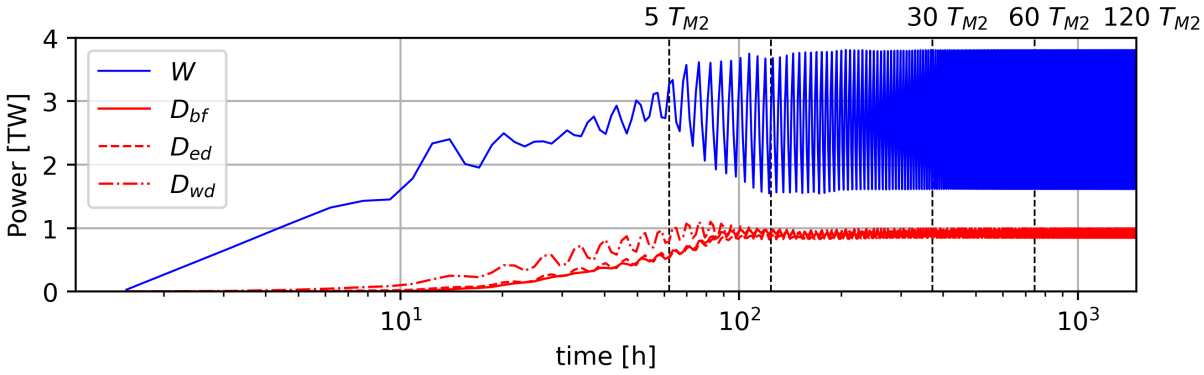

Figure 3.10: Globally integrated dissipation D_i and power consumption W, when forcing TiME with the M_2 partial TRP. The simulation is run for 120 tidal periods (approximately 60 days) and discriminates between dissipation by wave drag (wd), bottom friction (bf), and parameterized eddy viscosity (ed). Dissipation rates are sampled eight times per tidal period. Parameters are chosen for experiments RE as in Figure 3.9. The mean lunar dissipation rate can be observed by Lunar Laser Ranging (cf. Figure 1.1).

tides of both species and thus their compound tides at the same time with the current approach.
The partial tide mode has further advantages. It allows directly targeting an arbitrary partial tide and thus explicitly predicting geophysical signals with a specific frequency. This feature suits the aims of this thesis, which are the simulation of minor tides and the prediction of hard-to-observe tidal signals. Currently, TiME is employed as an operator of the form

$$\underline{\text{TiME}}(\text{IN}^\omega) = \text{OUT}^\omega \ , \tag{3.15}$$

as displayed in Figure 3.8, where IN^ω and OUT^ω refer to partial tide forcing of a certain frequency and the ocean response at the same frequency. The output can be identified with the complex sea surface elevation ζ^ω and the input with the respective TRP of degree l, order m of frequency ω_i. In this case, $\underline{\text{TiME}}(\text{IN}^\omega)$ divided by the equilibrium tidal height is equal to the admittance function Z_{lm} (cf. Equation 2.24). Hence, TiME simulations are numerical approximations of the admittance function.

3.3.4 Important Model Diagnostics

TiME predicts the barotropic ocean state variables ζ and $\mathbf{v}$ (also the depth-integrated transport, $\mathbf{V}$), which are the primary model observables. Harmonic constituents are extracted after the spin-up in the employed partial tide forcing mode and provided as a single NetCDF file. Exemplary, a local simulation result from TiME is displayed in Figure 3.9 (cf. Figure 2.9). Comparing both figures reveals only small differences that are more pronounced for tidal transports than for sea surface elevations. It can be concluded that deviations between TiME and FES14 are much smaller than the mean tidal signal amplitude. Thus, quantifying the model's accuracy requires a precise investigation with

respect to independent geodetic data which will be the subject of the next chapter.
Additionally, TiME can predict dissipation and power consumption densities (unit: $\mathrm{W/m^2}$), which is the energy intake of the model through astronomical and atmospheric accelerations versus energy dissipation differentiated by the individual processes. Densities are obtained by evaluation $d_i = \rho_{\mathrm{sw}} \boldsymbol{a}_i \cdot \mathbf{V}$ ($\overline{d}_i = \rho_{\mathrm{sw}} \overline{\boldsymbol{a}_i \cdot \mathbf{V}}$) and yield global rates D_i after integration over the whole ocean domain. Here, $\boldsymbol{a}_i$ are the individual accelerations acting on the ocean. While the model's energy balance is the topic of the next section, Figure 3.10 displays integrated $\mathrm{M_2}$ dissipation rates for a simulation of 120 tidal periods.
The secondary observables, ζ_{b} (Equation 2.28), $\boldsymbol{\zeta}_{\mathrm{h}}$ (Equation 2.29), $\zeta_{\perp}$ (Equation 2.30), and $V(\zeta^i)$ (Equation 2.31), are derived by evaluating the respective equation separately for in-phase and quadrature components, with the help of the SHTns package. Here, ζ is interpolated in an intermediate step to a $\frac{1}{30}^{\circ}$ regular grid, with land-sea masks constructed from RTopo-2. The maximum spherical harmonic degree is $l_{\max} = 2599$, with other parameters identical to the evaluation of the SAL potential in Equation (3.10).
The calculation of ocean tide levels will be presented separately in Chapter 6.

4

High-Resolution Numerical Modelling of Barotropic Global Ocean Tides for Satellite Gravimetry

This chapter is based on the publication by Sulzbach et al. (2021a), which has a twofold structure. The first part addresses the model development of TiME, which we discussed more elaborately in the previous Chapter 3. Thus, the first part of the article, *i.e.*, its Sections 2-5, is omitted in the chapter at hand.
Benefiting from the model development, the second part of the article discusses improvements in TiME ocean tide solutions quantified by geodetic data sets. The discussion focuses on two key points. First, the sensitivity of the ocean tide solutions on the individual model upgrades, using the example of the main lunar M_2 tide. Then, we extend the analysis to other semidiurnal tides of smaller amplitude and diurnal partial tides. The chapter is concluded with a discussion of the relevance of the presented ocean tide solutions for the dealiasing process of satellite gravimetry. The article's abstract and Sections 1 and 6-9 follow in their original form.

Chapter abstract[1]

The recently upgraded barotropic tidal model TiME is employed to study the influence of fundamental tidal processes, the chosen model resolution, and the bathymetric map on the achievable model accuracy, exemplary for the M_2 tide. Additionally, the newly introduced pole-rotation scheme allows to estimate the model's inherent precision (open ocean $\overline{\text{rms}}$: 0.90 cm) and enables studies of the Arctic domain without numerical deviations originating from pole cap handling. We find that the smallest open ocean rms with respect to the FES14-atlas (3.39 cm) is obtained when tidal dissipation is carried out to similar parts by quadratic bottom friction, wave drag, and parametrized eddy-viscosity. This setting proves versatile to obtaining high accuracy values for a diverse ensemble of

[1]Some symbols and references in this chapter were harmonized with previous chapters.

additional partial tides. Using the preferred model settings, we show that for certain minor tides it is possible to produce solutions that are more accurate than results derived with admittance assumptions from data-constrained tidal atlases. As linear admittance-derived minor tides are routinely used for dealiasing of satellite gravimetric data, this opens the potential for improving gravity field products by employing the solutions from TiME.

Published Manuscript (Reproduced with permission from Wiley)
Sulzbach, R., Dobslaw, H., & Thomas, M. (2021). High-resolution numerical modelling of barotropic global ocean tides for satellite gravimetry. Journal of Geophysical Research: Oceans, 126, e2020JC017097. https://doi.org/10.1029/2020JC017097

Data Availability Statement
The tidal data presented in this study can be obtained from https://doi.org/10.5880/GFZ.1.3.2021.001 in the form of Stokes coefficients including load-tide mass variations (Sulzbach et al., 2021a).

Author Contributions
The results presented in this manuscript represent original work of the author of this thesis, with contributions by the coauthors in conceptualization, planning, drafting and revising the initial article draft.

Acknowledgments
The authors sincerely thank the editor Don Chambers and the anonymous reviewers for their very constructive comments and suggestions regarding our manuscript. The authors acknowledge funding by the NEROGRAV-project (DFG Research Unit 2736, Grant: TH864/15-1). This work used resources of the Deutsches Klimarechenzentrum (DKRZ) granted by its Scientific Steering Committee (WLA) under project ID 499.

4.1 Introduction

Signatures of ocean tidal dynamics are omnipresent in oceanographic and geodetic observations taken either on the ground or from space. This includes periodic variations in ocean currents registered by moored instruments or acoustic tomography (Luyten and Stommel, 1991; Dushaw et al., 1997; Ray, 2001) as well as by induced secondary magnetic fields (Maus and Kuvshinov, 2004; Saynisch et al., 2018), sea surface height changes measured from tide gauges and satellite altimetry, (Doodson, 1928; Schrama and Ray, 1994) and global bottom pressure variations from pelagic pressure recorders and gravimetric satellite missions (Wiese et al., 2016). More recently, even tiny variations in sea surface temperature (Hsu et al., 2020) and tropical precipitation observations (Kohyama and Wallace, 2016) were related to ocean tidal dynamics.

Separating tidal and transient signals in satellite records is not trivial due to the complicated spatiotemporal sampling of observations taken from satellites in non-geostationary orbits. The repeat orbit of the Topex/Poseidon (T/P) satellite altimetry mission (Fu and Cazenave, 2000) has been carefully selected in a way that aliases the major ocean tidal constituents into periods that are well distinct from naturally occurring periodicities, thereby providing tidal charts based on observations that cover the open ocean in a regular spatial pattern (Shum et al., 1997). After assimilating tidal elevations from T/P and other altimetry missions into hydrodynamic models (Carrere et al., 2015; Egbert and Erofeeva, 2002; Taguchi et al., 2014) or using these data to construct empirical corrections to an adopted model (Savcenko et al., 2012; Cheng and Andersen, 2011; Fok, 2012; Ray, 1999), those models are extensively used for the processing of un-related observations, as *e.g.*, satellite gravimetry missions. Presently, all 34 tidal constituents given by the FES14 tidal atlas (Carrere et al., 2015; Lyard et al., 2006) are directly removed from Gravity Recovery And Climate Experiment (GRACE) and GRACE Follow-on (GRACE-FO) data, and more than 300 additional minor constituents inferred by admittance methods are also subtracted (Kvas et al., 2019). The existing weaknesses in present-day admittance methods, however, have been discussed extensively in the past (Ray, 2017), so that explicit tidal simulations with unconstrained numerical ocean tide models provide potentially valuable information on tidal lines less well constrained by satellite altimetry.

The sensitivity of satellite gravimetry to periodic mass re-distributions in the Earth system is expected to increase even further when the full potential of the satellite-to-satellite tracking by means of laser ranging interferometry (Ghobadi-Far et al., 2020) is also used for gravity field processing. Employing end-to-end satellite simulations, Flechtner et al. (2016) found that ocean tide errors are among the top three factors that limit the accuracy of global mass distribution estimates from GRACE-FO. Various concepts of multi-satellite constellations are currently being evaluated by space agencies in Europe, the U.S., and China for possible implementation as a next-generation gravity mission (*e.g.*, Hauk and Wiese, 2020). Scientific requirements and user demands for such new missions almost always request higher spatial resolution and greater accuracy (cf. Pail et al., 2015). Equivalently, in order to re-process the already existing data record from GRACE and GRACE-FO into more precise time series of terrestrial water storage and ocean bottom pressure suited for climate monitoring (Tapley et al., 2019), better ocean tide models are critically important.

While data-constrained tidal models provide highly accurate estimates of tidal constitu-

ents in regions where altimetry data is dense (open ocean residuals below 1cm), model accuracy decreases as the data quality decreases (minor tides, polar, and shelf areas). In effect, the ratio of model uncertainty to signal typically increases considerably for tidal excitations with smaller amplitudes (Stammer et al., 2014). Even more, additional errors can be introduced when estimating minor tidal excitations with admittance methods. These deviations might be reduced by the explicit numerical modelling of minor tides.
In this contribution, we present efforts towards extending a hydrodynamic model of ocean tidal dynamics particularly suited to study minor and compound tides. Our work is based on the Tidal Model forced by Ephemerides (TiME; Weis et al., 2008) introduced in the previous chapter[2]. We describe various improvements to the numerics of the model, including the rotation of the poles (Section 3.2.1), an extension of the physical model by implementing the effects of Self-Attraction and Loading (Section 3.2.6) and the incorporation of topographic wave drag as a new dissipation mechanism (Section 3.2.5). Exemplary for the principal semidiurnal lunar tide M_2, we will report about the accuracy of the simulated tidal heights both with respect to OBP data and the state-of-the-art global tide solution FES14 that is constrained by observations. Various sensitivity experiments are presented, documenting the individual contributions of the various changes made to TiME in terms of achieved accuracy (Section 4.2).
The chapter is augmented with an assessment of energy dissipation patterns of the model and additional simulations of partial tides in the diurnal and semidiurnal tidal bands (Section 4.3). Building on the results of previous sections, we focus in Section 4.4 on selected minor tides that can be simulated with higher accuracy than solutions constructed from linear admittance estimates on data-constrained models. Finally, the chapter is closed with a summary (Section 4.5).

4.2 Tidal Elevations for M_2 from TiME

In order to highlight the importance of individual model changes to TiME as given in the previous chapter, we now report results from a number of sensitivity experiments for the principal lunar tide M_2 as outlined in Table 4.1. The model performance will be benchmarked against a data set comprised of 151 OBP stations compiled by Ray (2013) as well as the global state-of-the-art tidal atlas FES2014 (Carrere et al., 2015; Lyard et al., 2006), that was produced by Noveltis, Legos, and CLS and distributed by Aviso+, with support from CNES. Misfits will be reported in terms of time-averaged rms

$$\mathrm{rms}_{\zeta_1^\omega,\zeta_2^\omega}(\mathbf{x}) = \sqrt{\frac{1}{T}\int_0^T dt\ \left(\mathrm{Re}\left(\zeta_1^\omega(\mathbf{x},t) - \zeta_2^\omega[\mathbf{x},t]\right)\right)^2} = \sqrt{\frac{1}{2}|\zeta_1^\omega(\mathbf{x}) - \zeta_2^\omega(\mathbf{x})|^2}\ , \qquad (4.1)$$

that can be further averaged over a certain ocean domain D_o with area A_o yielding the space-averaged $\overline{\mathrm{rms}}_{\zeta_1^\omega,\zeta_2^\omega} = \sqrt{A_o^{-1}\sum_{\mathbf{x}_{ij}\in D_o} A_{ij}\ \left(\mathrm{rms}_{\zeta_1^\omega,\zeta_2^\omega}[\mathbf{x}_{ij}]\right)^2}$. We calculate averages for shallow water if the ocean depth is smaller than $H = 1000$ m (10.4 % ocean surface) or open ocean if the depth exceeds this limit (83.0 % ocean surface). Both areas are restricted to latitudes with $|\phi| < 66°$ as altimetry data in these regions is dense and guarantees a

[2]The references to the original sections, Figures, and equations of Sulzbach et al. (2021a) were changed to the respective objects of Chapter 3 and the remaining sections of this article.

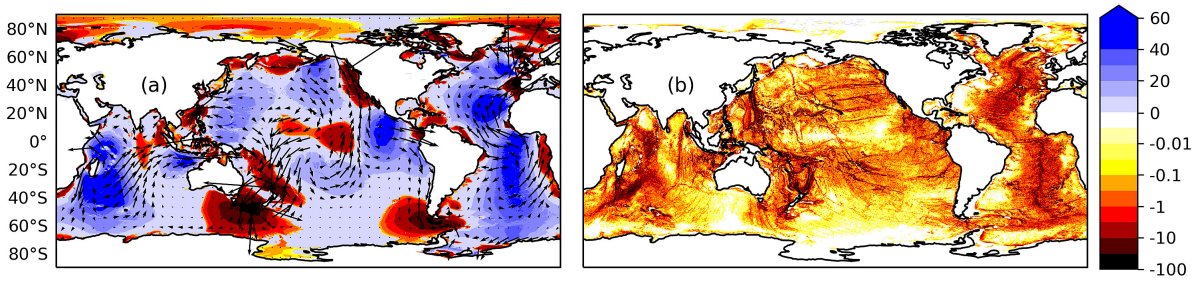

Figure 4.1: Mean tidal power consumption field $\overline{w}$ overlayed with the tidal energy flux vector field $\overline{\mathbf{p}}$ (a) and corresponding wave drag dissipation field $\overline{d}_{\mathrm{wd}}$ in $\frac{\mathrm{mW}}{\mathrm{m}^2}$ (b). Red areas in subfigure (a) indicate regions where water masses experience a net slowdown by tidal forces. While energy fluxes are similar to those obtained by assimilating models (cf. *e.g.*, Egbert and Ray, 2001), deep ocean dissipation is concentrated at strong bathymetric slopes. Note that the scale was truncated at $+60\frac{\mathrm{mW}}{\mathrm{m}^2}$ and extended pseudo-logarithmically for values smaller than $-0.001\frac{\mathrm{mW}}{\mathrm{m}^2}$ to emphasize the underlying fine structured dissipation patterns.

high quality of derived tidal atlases. When mentioned in the following sections, the results for $\overline{\mathrm{rms}} = (a, b)$ are related to validations with FES2014 (a) and pelagic OBP stations (b), where TG-results for Equation (4.1) are quadratically averaged over all stations.
As an additional benchmark for our model, we monitor planetary dissipation conducted by the M_2 tide. Being laid out by Platzman (1984a), the theory of planetary dissipation was employed by Egbert and Ray (2000, 2001) to derive estimates of M_2-tidal dissipation utilizing altimetry data-constrained tidal models. Herein, the planetary dissipation field d was derived by evaluating the relation

$$\overline{d} = \overline{w} - \nabla\overline{\mathbf{p}}, \tag{4.2}$$

that uses the mean tidal energy consumption field $\overline{w} = \rho_{\mathrm{sw}}\overline{\boldsymbol{a}_{\mathrm{c}} \cdot \mathbf{V}}$ (work done by tidal forces) and the energy flux field $\nabla\overline{\mathbf{p}} = \rho_{\mathrm{sw}} g_0 \nabla\overline{(\zeta\mathbf{V})}$. These studies revealed that $25 - 30$ % of global M_2 dissipation $\overline{D}_{M_2} = \int_O dA\, \overline{d} \approx 2.45$ TW is located in the deep ocean[3]. Monitoring these properties can give further insight into the quality of a numerical model.
Within this study, individual contributions to the planetary dissipation field $d = \sum_i d_i$ can be directly computed from the model, with $d_i = \rho_{\mathrm{sw}} \boldsymbol{a}_i \cdot \mathbf{V}$ ($[d_i]$=W/m^2), where $\boldsymbol{a}_i$ are individual dissipation accelerations mentioned in Equation (2.26). Globally integrating the individual fields d_i yields the corresponding planetary dissipation rates D_i ($[D_i]$=W). Since temporal averages of dissipation terms originating from linear forces can be calculated easily ($\overline{\sin \omega t^2} = 0.5$) we calculate the nonlinear dissipation by bottom friction as the residual dissipation evaluating $\overline{D}_{\mathrm{bf}} = (\overline{W} - \overline{D}_{\mathrm{wd}} - \overline{D}_{\mathrm{ed}})$, where $\overline{W}$ is the tidal power consumption $\int_O dA\; w$ caused by $a_c = -g\vec{\nabla}(\zeta_{SAL} + \zeta_{eq})$. This does not introduce a bias into the estimates as the imbalance between tidal energy consumption, and dissipation is

[3]The notation was harmonized with Chapter 3 by adding temporal averages (cf. Figure 3.10).

Table 4.1: Open ocean $\overline{\text{rms}}$ and tidal dissipation for an ensemble of M_2 tidal simulations. The individual experiments highlight the impact of several updated tidal processes and parameters on the achieved accuracy (P: pole position, B: bathymetric map, S: SAL scheme, W: topographic wave drag, R: resolution). Balances sometimes do not check out due to individual rounding.

ID	Grid	Pole	Bath.	SAL	κ_w[%]	A_h [$\frac{m^2}{s}$]	$\overline{\text{rms}}$[2] [cm]	Dissipation[3] [TW]
RE	1/12°	*chi*	RTopo-2	l_{max}=1024	125	$2 \cdot 10^4$	**3.39/4.83**	**2.70** (0.90/0.91/0.88)
P1	1/12°	*arc*	RTopo-2	l_{max}=1024	125	$2 \cdot 10^4$	4.08/5.19	2.61 (0.88/0.82/0.91)
P2	1/12°	*gre*	RTopo-2	l_{max}=1024	125	$2 \cdot 10^4$	3.6/5.21	2.76 (0.95/0.87/0.94)
P2b	1/12°	*gre*	RTopo-2	l_{max}=1024	160	$1.6 \cdot 10^4$	**3.63/5.00**	2.69 (0.88/1.00/0.78)
P3	1/12°	*aus*	RTopo-2	l_{max}=1024	125	$2 \cdot 10^4$	4.75/5.57	2.59 (0.70/1.01/0.82)[4]
B1	1/12°	*chi*	GEBCO[1]	l_{max}=1024	125	$2 \cdot 10^4$	6.49/7.35	2.84 (0.95/0.94/0.95)
B2	1/12°	*chi*	ETOPO1[1]	l_{max}=1024	125	$2 \cdot 10^4$	7.86/9.75	3.06 (1.07/1.03/0.97)
S1	1/12°	*chi*	RTopo-2	l_{max}=100	125	$2 \cdot 10^4$	**3.38/4.82**	**2.69** (0.90/0.91/0.89)
S2	1/12°	*chi*	RTopo-2	l_{max}=10	125	$2 \cdot 10^4$	3.99/5.63	2.69 (0.90/0.90/0.89)
S3	1/12°	*chi*	RTopo-2	$\epsilon = 0.1$	125	$2 \cdot 10^4$	5.41/6.69	2.94 (0.96/1.03/0.95)
S4	1/12°	*chi*	RTopo-2	none	125	$2 \cdot 10^4$	22.91/27.02	3.30 (1.22/1.09/0.99)
W0	1/12°	*chi*	RTopo-2	l_{max}=1024	150	$5 \cdot 10^2$	4.03/6.54	2.57 (1.57/0.94/0.06)
W1	1/12°	*chi*	RTopo-2	l_{max}=1024	100	$2.5 \cdot 10^4$	3.75/5.03	2.75 (0.91/0.79/1.04)
W2	1/12°	*chi*	RTopo-2	l_{max}=1024	175	$1 \cdot 10^4$	4.18/5.39	2.58 (0.92/1.09/0.56)
W3	1/12°	*chi*	RTopo-2	l_{max}=1024	none	$4.5 \cdot 10^4$	8.03/9.74	2.96 (1.14/0/1.82)
R1	1/3°	*chi*	RTopo-2	l_{max}=256	100	$5.5 \cdot 10^4$	7.95/8.07	2.52 (0.80/0.95/0.77)
R2	1/6°	*chi*	RTopo-2	l_{max}=512	100	$3 \cdot 10^4$	5.21/5.95	2.58 (1.00/0.85/0.72)
WE	1/12°	*arc*	GEBCO	$\epsilon = 0.1$	none	$4.5 \cdot 10^4$	15.39/17.85	3.50 (1.26/0/2.24)

[1]: First order conservative remapping (*con*), [2]: open ocean/OBP rms
[3]: Mean Tidal power consumption $\overline{W}$ and dissipation by sinks ($\overline{D}_{bf}/\overline{D}_{wd}/\overline{D}_{ed}$, after Section 4.2)
[4]: Dissipation might be diminished as dissipative processes in the pole cap remain unresolved

far below 1 $\%\overline{D}_{M_2}$ after initializing the simulation[4]. The following subsections present the results obtained from tuning and sensitivity experiments and relate to the experiments summarized in Table 4.1.

4.2.1 Model Tuning

The original experiments conducted by Weis et al. (2008) (experiment WE in Table 4.1) led to an open ocean rms of 15.39 cm. The dissipation rate was overestimated by 43% (1050 GW), and a strong concentration of dissipation in shallow waters indicated missing or not optimally-represented dissipation mechanisms.
Primarily the introduction of topographic wave drag and an improved bathymetric map allowed to reduce of the global M_2 amplitudes and dissipation rates. Tuning experiments concentrated on finding an optimal ratio between damping by eddy viscosity and topographic wave drag, while the bottom friction was left constant at $r = 0.003$. Even though the original Nycander scheme does not contain a free, tunable parameter, experiments with $\kappa_w = 100\%$ showed that additional dissipation is necessary to obtain optimum results, as was also found by Buijsman et al. (2015). This can either be provided by increasing A_h or κ_w (altering r worsened the accuracy). Several tuning experiments with $\kappa_w = 100...225$ % and $A_h = 5...350 \cdot 10^2 \frac{m^2}{s}$ led to a minimum open ocean rms of 3.39 cm

[4]Compare also Figure 3.10.

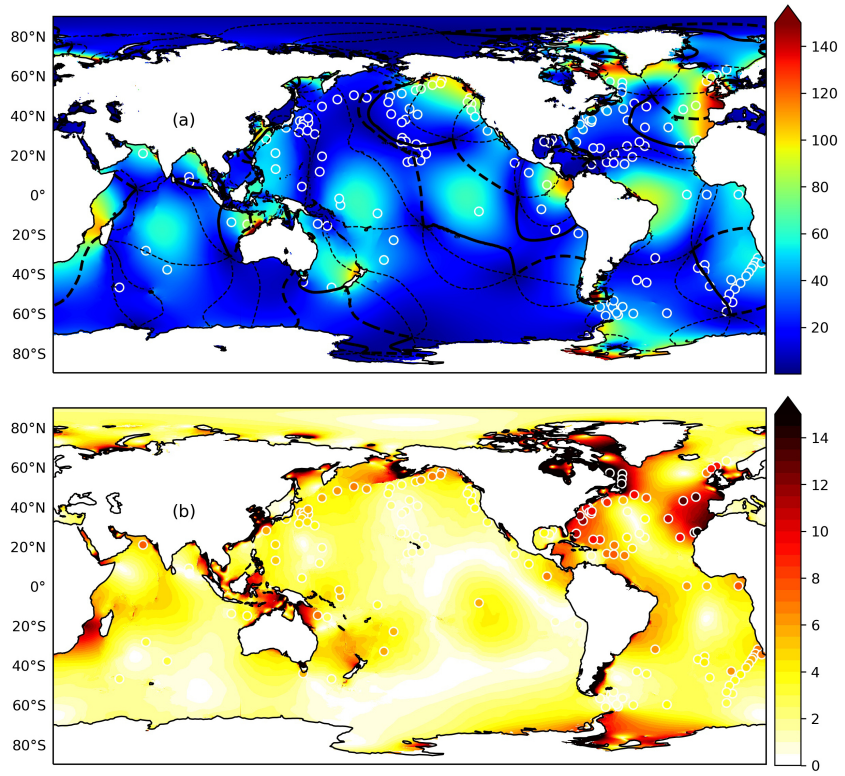

Figure 4.2: (a): TiME M_2 cotidal chart in cm (experiment RE) augmented with tidal amplitudes at OBP stations (151 stations, small circles), where lines indicate the tidal phases in increments of 60° (Thick : 0°, Thick, Dashed : 60°). Further, validation results, expressed as rms (cm) between TiME and tidal constituents at OBP stations and FES2014 data are shown (b).

(experiment RE, OBP rms: 4.83 cm, shallow-water rms: 17.95 cm) with similar combinations of κ_w and A_h leading only to slightly higher rms values (experiments W1,W2). While wave drag dissipation amounts to 34 % (910 GW) of the overall dissipation, the planetary dissipation rate decreased to 2.70 TW, which is still 10 % (250 GW) too large compared to the expected result of 2.45 TW. The resulting mean tidal power consumption field $\overline{w}$ as well as the energy dissipation field by wave drag-acceleration $\overline{d}_{wd}$ (cf. Figure 4.1) match the results derived with altimetric data (cf. Egbert and Ray, 2001).
While the achieved accuracy of experiment RE was the highest in our ensemble, this model setup lacks a solid physical foundation due to the excessive dissipation mediated by parameterized eddy viscosity. A physically more reasonable setting can be obtained when minimizing the dissipation by eddy-viscosity as pursued by most modern barotropic models (*e.g.*, Schindelegger et al., 2018; Egbert et al., 2004). The obtained open ocean rms values of 4.03/6.54 cm for W0 increase with respect to setting RE, while the dissipation-overshoot is reduced to 120 GW (5 %). On the other hand, the shallow-water accuracy is not altered considerably to 17.86 cm. This can be seen as a trade-off between maximized model accuracy and well-founded model physics that will be beneficial with respect to sensitivity studies (*e.g.*, paleo simulations, climatic impacts). On the other hand, this

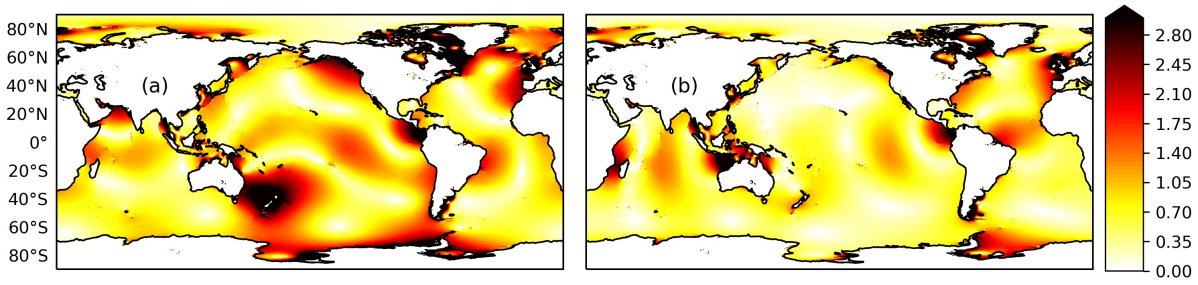

Figure 4.3: rms values obtained by intercomparing experiment RE to P2 (a), an experiment run with identical parameters on a different grid, versus a comparison between RE and P2b (b), where parameters have been readjusted. The open ocean $\overline{\text{rms}}$ amounts to 1.18/0.9 cm (a/b), while the shallow-water rms is 5.46/5.35 cm. Note the different structures of shallow-water residuals in comparison to Figure 4.2b, and the reduced scale.

trade-off is undesirable for high-precision applications such as satellite gravimetry. As the accuracy that has to be sacrificed with setting W0 increases for minor tides (cf. Section 4.3), we decide to favor setting RE for the present study.
The amphidromic system and global rms data for experiment RE is shown in Figure 4.2. In comparison to FES2014 data, M_2 oscillation systems are predicted precisely with the exception of some features around Antarctica (cf. Figure 4.4, top). It is worth noting that the reproduction of large-scale features (*e.g.*, tidal phases defining amphidromic systems) was also possible on a similar level of detail by experiment WE. Exceptions were mainly constituted of bathymetry-induced aberrations around Antarctica (cf. Section 4.2.3). The principal accuracy gain is attributed to a more realistic representation of dissipation, bathymetry, and SAL effects. The remaining critical regions are shelf and coastal areas and are especially concentrated around Antarctica and in the North Atlantic shelf areas. This suggests possible origins for these discrepancies in tide-ice interaction as well as in possible bathymetric inaccuracies or insufficient representation of (nonlinear) shallow-water effects. With respect to similar modern barotropic tidal models, TiME produces solutions on the same level of accuracy, while the shallow-water accuracy is moderately decreased (*e.g.*, +4.4 cm to Schindelegger et al., 2018).

4.2.2 Impact of Pole Location

As a first finding, we note similarly accurate results when performing experiments on alternative grids with land-covered poles (cf. experiment P2 in Table 4.1). The accuracy obtained on the *gre* grid could be increased further to 3.63/5.00 cm open ocean rms, when additional tuning was applied (experiment P2b). Since the zonal model resolution increases towards the numerical poles, the bathymetric information contained in two differently oriented grids differs slightly. This also impacts the wave drag tensor that depends on $H(\phi, \lambda)$. Together, this induces deviations between otherwise identical experiments performed on different grids (P2 vs. RE) that become more prominent when choosing coarser resolutions. Directly comparing the tidal elevations obtained by experi-

ments RE and P2b (land-covered poles), yields an open ocean $\overline{\text{rms}}$ of 0.90 cm, while only 5.35 cm are obtained in shallow waters (entire ocean: 1.97 cm, cf. Figure 4.3). These values estimate the effective precision level that can be obtained when running experiments at the present resolution of $\frac{1}{12}^\circ$. We conclude that optimized parameters vary for experiments on differently oriented grids, but similar accuracy is achievable.
Overall, the rotated-pole scheme did not improve the global accuracy level of present-day tides significantly since tidal elevations in the Arctic (near the former pole cap) are diminutive (experiment P1). Nevertheless, deviations induced by a pole cap situated in an area of presumably high tidal elevation are a source of imprecision (P3) and should be avoided. The non-optimally placed pole cap on the *aus*-grid resulted in altered and diminished dissipation as well as in an increased $\overline{\text{rms}} = 4.75/5.57$ cm.
An additional benefit of the implemented pole-rotation scheme lies in its versatility: The mitigation of the large pole-cap grid cell allows the unbiased study of historical situations in which tidal elevations in the Arctic might have been significant, as proposed by Griffiths and Peltier (2008) and more recently by Velay-Vitow and Peltier (2020) for the Last Glacial Maximum. Additionally, alternative grid orientations can be used to guarantee approximately equal aspect ratios for grid cells in the Arctic (*e.g.*, when using the *chi* grid), further recommending TiME to be used for studies of Arctic tides.

4.2.3 Impact of Bathymetry

Additional experiments were performed with bathymetries constructed from ETOPO1 (Amante and Eakins, 2009) and GEBCO data (GEBCO Compilation Group, 2019), treating sub-ice-shelf cavities as dry grid cells. This configuration resembles the bathymetric maps used in Weis et al. (2008). Interpolation to the model's resolution was done using first-order conservative interpolation.
The results (experiment B1, B2) show that ignoring the effects of Antarctic sub-shelf cavities on ocean tide resonances leads to large-scale deviations of the displayed amphidromic systems, especially in the Southern Ocean (Wilmes and Green, 2014) (cf. Figure 4.4). The most striking deviation hereby occurs in the Weddell Sea. As the RTopo-2 bathymetry is mainly based on GEBCO data, the model setup for experiment B1 can be seen as a blocking experiment for the Antarctic shelf regions. Blocking experiments are useful to investigate the back-action of shelf tides on open ocean tides. Arbic et al. (2009) conducted such simulations for a number of shelf areas (*e.g.*, Patagonian Shelf, Hudson Bay) and also considered analytical solutions. Both approaches predict that blocking a near-resonant shelf region enhances the amplitude of the open ocean tide, as it is shown in Figure 4.4a,c for the Southern Ocean.
As the shelf-blocking increases the open ocean amplitudes, tidal dissipation is also increased and contributes to the overestimated dissipation in experiment WE (B1: + 150 GW, B2: +350 GW). It is possible to reduce this overestimation slightly by enhancing the dampening forces. However, this only leads to minor improvements and cannot rectify the imprecisely represented oscillation systems as depicted in Figure 4.4. It is, therefore, not further investigated.
In summary, the conducted experiments highlight the irreplaceability of constructing a realistic bathymetric map. Further, the results point out that poorly represented areas can have strong near- and far-field effects on tidal dynamics, even if they have only a

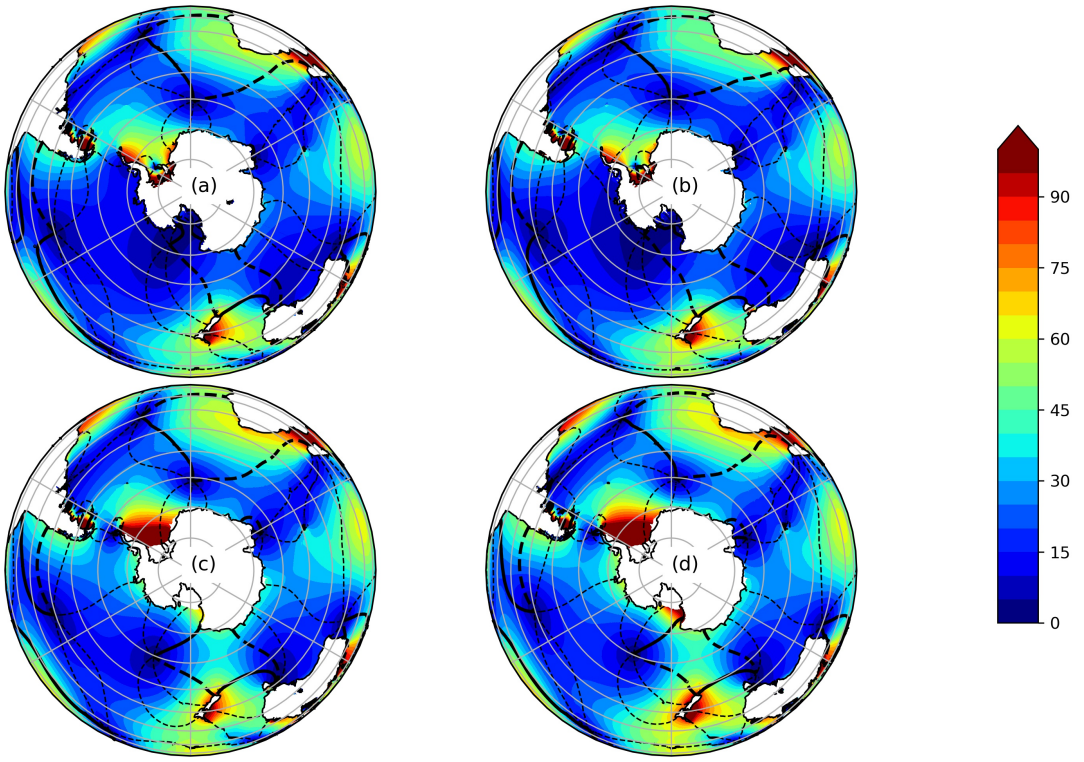

Figure 4.4: M_2-Tidal elevations (cm) around Antarctica obtained from TiME-simulations with different bathymetric charts: (a) RTopo-2 (experiment RE), (c) GEBCO (experiment B1) and (d) (experiment B2). As a reference, (b) shows FES2014 tidal elevations. Note the hydrodynamically blocked sub-shelf cavities for the bottom experiments.

small spatial extent.

4.2.4 Impact of Self-Attraction and Loading

In this section, we discuss the impact of a number of SAL representations on the simulation results. When evaluating Equation (3.10) up to $l_{\max} = 100$ we find that the open ocean rms does not increase, indicating sufficient handling of this effect with regard to open ocean tidal dynamics (experiment S1). The shallow-water rms is also not altered considerably, which might be due to generally less precise model performance in shallow waters. When further decreasing the maximum degree to $l_{\max} = 10$ the open ocean rms increases to 3.99/5.63 cm (S2), which is still a significantly more precise result than S3, which was obtained by the local SAL-parametrization by Accad and Pekeris (1978) (5.41/6.69 cm). However, this result can be seen as a valuable improvement when comparing it to completely neglecting the effect (experiment S4). This leads to a profound misrepresentation of tidal phases and a strongly increased misfit. Overall, the estimated planetary dissipation increases with a less precise SAL representation (S3: +240 GW, S4: +500 GW). Thus, the local SAL-parametrization contributes significantly to the overestimated dissipation in experiment WE.
As discussed by Müller (2007) the inclusion of SAL primarily leads to a phase-shift of os-

cillation systems by altering properties of the underlying normal modes. This phase shift is well approximated in the first order by applying an effectively reduced gravity factor (S3). However, to represent the precise far-field effects of the SAL, a treatment in terms of spherical harmonics with $l_{\max} \geq 100$ is necessary. To precisely represent near-field effects, the maximum degree l has to be extended to higher values (Schindelegger et al., 2018). Since the efficient handling of SAL transformation by the SHTns-package (Schaeffer, 2013) does not considerably increase computation time, we treat the SAL effect up to degree $l_{\max} = 1024$ in our experiments.

4.2.5 Impact of Topographic Wave Drag

The only dissipation agent that leads to considerable deep ocean dissipation included in the model is the excitation of internal tides by topographic effects. Since deep ocean dissipation is an experimental matter of fact, it does not surprise that complete neglection of this effect has severe impacts on the achievable accuracy (experiment W3), causing an rms increase of +4.64/ + 4.91 cm and a surplus dissipation of an additional 260 GW. Finding an optimum interplay between the present dissipation agents, on the other hand, is more complicated. When abstaining from tuning wave drag-strength, *e.g.*, setting $\kappa_{\mathrm{w}} = 100$ %, best results are achieved by allowing significant dissipation by eddy-viscosity (W1). If one instead decides to increase wave drag substantially (W2), as *e.g.*, done by Buijsman et al. (2015), the open ocean results slightly worsened in comparison to experiment RE, without improving shallow-water rms. As discussed in Section 4.2.1 a minimization of the obtained wave drag dissipation leads to the physically well-founded model setting W0 while the open ocean accuracy moderately deteriorates (+0.64/1.71 cm). This setting should always be favorable with respect to sensitivity experiments that benefit from realistically represented tidal physics.
Overall the tuning of the dissipation agents suggested that the best results are obtained when wave drag dissipation contributes about 900 GW to planetary dissipation, which is close to the expected value. The slight tuning of the wave drag tensor (factor 1.25 to the original Nycander-tensor) stresses that it is based on a sound theory and can be expected to provide ad-hoc precise results. This is a valuable result when it comes to adapting the model to other tidal groups or paleo settings.

4.2.6 Impact of Spatial Resolution

Experiments R1 (at $\frac{1}{3}^\circ$) and R2 (at $\frac{1}{6}^\circ$) were designed to represent a similar physical situation as chosen for experiment RE. Therefore, dissipation agents were tuned to achieve comparable dissipation ratios leading to an effective increase in A_{h}. We emphasize that altering the model resolution renders repeated model tuning necessary. Parameters can not be transferred directly without altering tidal dynamics.
We observe that, while overall dissipation decreases, open ocean $\overline{\mathrm{rms}}$-values are considerably increased to 5.21/7.95 cm for R2/R1 (cf. Egbert et al., 2004). The cause for this might originate from the model-inherent resonant behavior of oceanic tides. With reduced spatial resolution, the geometry of the ocean basins determining oceanic normal modes can not be properly represented. The resulting slight shifts in resonance frequencies then strongly impact tidal dynamics, especially in shallow waters, where oscillation systems

reside on smaller spatial scales. Thus, to further increase the precision and accuracy of TiME, an increased resolution beyond $\frac{1}{12}^\circ$ should be considered.

4.3 Additional Tidal Excitations

In this section, we present simulation results for additional partial tides. We selected partial tides that differ in excitation amplitude, and frequency as well as in excitation pattern from M_2 to test the sensitivity of the preferred model settings RE. The overall aim is to demonstrate model setting RE as robust for simulating partial tides of differing characters on a comparable level of accuracy.
As discussed in Section 2.2.2, excitation patterns relate to the spatial dependence of the partial tide forcing that is proportional to the spherical harmonic functions Y_{lm}. Within, l defines the degree, m the order of the spherical harmonic, where $m = 0, 1, 2, 3$ further enumerates the tidal species (0: long period, 1: diurnal, 2: semidiurnal, 3: terdiurnal, cf. Appendix E). Since the tidal forcing strength spans several scales for different partial tides, the level of accuracy obtained for different partial tides cannot be compared directly to each other without considering the overall signal amplitude. To facilitate this comparison we introduce the admittance function[5]

$$Z_{lm}(\mathbf{x}, \omega_i) = g_0 \frac{\zeta^{\omega_i}(\mathbf{x})}{A_i} \ , \tag{4.3}$$

that relates the tidal response, expressed by its elevation ζ^{ω_i}, to its g-normalized forcing amplitude $A_i = \sqrt{(S_i^{lm})^2 + (C_i^{lm})^2}$ (cf. Appendix E). Hereby, Z_{lm} is only evaluated at discrete tidal frequencies for partial tides with forcing pattern Y_{lm}. Since the tidal PDEs are only weakly nonlinear and tidal frequencies within one tidal band only differ slightly, Z_{lm} takes a related shape for each partial tide. Hence, it can be used to compare the response strength and especially the relative level of accuracy compared to the excitation strength for individual excitations by considering $\mathrm{rms}_{Z^\omega_{\mathrm{TiME}}, Z^\omega_{\mathrm{FES}}}(\mathbf{x})$ (cf. Equation 4.1). Please refer to the supporting information where the tidal potential catalog used for this study can be obtained[6].

4.3.1 Semidiurnal Tides

The K_2-excitation is a semidiurnal partial tide of second-degree origin ($l = 2$), thus representing another evaluation point of admittance function Z_{22}. However, its respective forcing strength is only 13 % compared to M_2. Since additionally, its frequency differs from M_2 by $1.10\frac{^\circ}{\mathrm{h}}$, admittance patterns are altered in comparison to M_2. The open ocean validation for K_2 results in an $\overline{\mathrm{rms}}$ of 0.39/0.43 cm. Compared to K_2 signal strength, the obtained accuracy is on the same level of accuracy as the results for M_2. In other words, the uncertainty in Z_{22} is similar for both partial tides.
Further, we considered the tidal response to ν_2 tide (3.7 % M_2-forcing) as a third evaluation

[5] In this formulation, the factor a_l^b is not included as in the original formulation (Equation 2.24), with minor deviations for the K_1 tide and implications for the plotted admittance functions.

[6] The respective catalog can be found in Table E.1 in Appendix E in modified version.

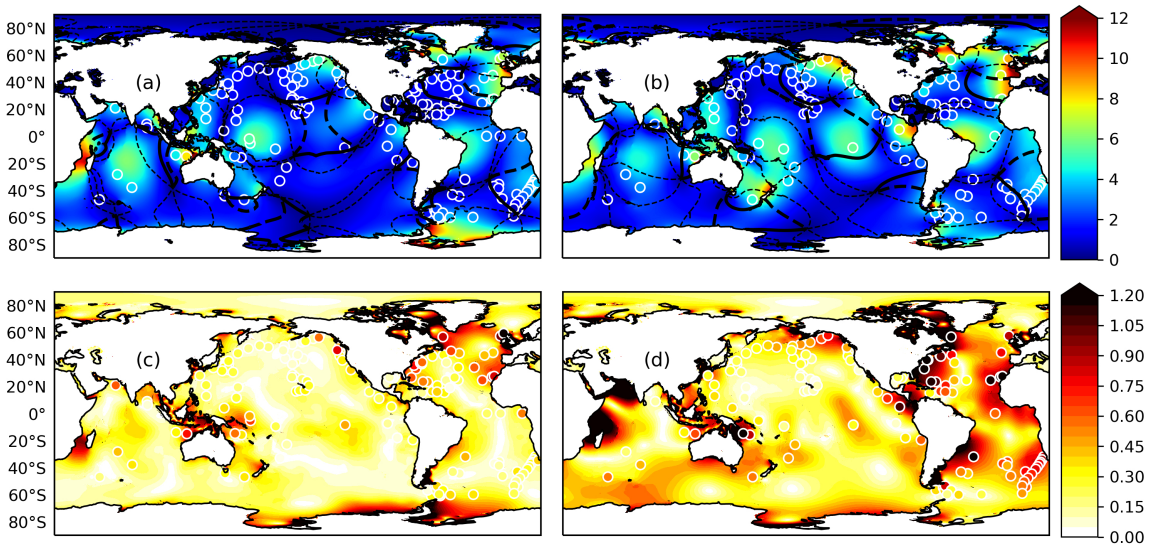

Figure 4.5: Dimensionless admittance-function Z_{22} for K_2 (a) and ν_2 tide (b) and corresponding rms values for Z_{22} (c + d). Note that the scales of the colorbars correspond to Figure 4.2, saying that Figure 4.2 can be read as $Z_{22}(\mathrm{M}_2)$. Rescaling Z_{22}-amplitudes to real ocean elevation amounts to 19.10/5.50 cm for K_2/ν_2.

point of Z_{22}. Here, nonlinear effects will play an even more important role due to the diminished excitation amplitude, while frequency difference to M_2 is reduced ($\delta\omega = 0.47^\circ_{\mathrm{h}}$). The validation of ν_2 resulted in a $\overline{\mathrm{rms}}$ of 0.19/0.18 cm, revealing a moderately enhanced level of inaccuracy compared to K_2-results. The reason for this could be found in an imperfect representation of nonlinearities in tidal dynamics. Nonetheless, the results demonstrate that TiME is able to perform simulations on a similar scale of accuracy within one tidal band (in this case, Z_{22}) without the need to adapt model parameters for each simulation. Results for these partial tides are shown in Figure 4.5.
On the other hand, monitoring tidal dissipation reveals increasingly altered weights for individual dissipation agents. While K_2 dissipates 34.7 GW, partitioning as ($\overline{D}_{\mathrm{bf}}, \overline{D}_{\mathrm{wd}}, \overline{D}_{\mathrm{ed}} =$ 4.9/13.6/16.3 GW) the distribution for ν_2 ($\overline{D}_{\mathrm{bf}}, \overline{D}_{\mathrm{wd}}, \overline{D}_{\mathrm{ed}} = 0.34/1.33/2.21$ GW) is, even more, shifted towards a dominant eddy-dissipation. Not surprisingly, the dissipation by quadratic bottom friction $\sim |\mathrm{v}|^3$ is strongly reduced compared to dissipation by linear forces $\sim |\mathrm{v}|^2$. Remarkably, the overall dissipation lost by reduced bottom friction is transferred to $\overline{D}_{\mathrm{ed}}$, while deep ocean dissipation by $\overline{D}_{\mathrm{wd}}$ amounts to a comparable fraction (33.6/38.4/34.2 % for $\mathrm{M}_2/\mathrm{K}_2/\nu_2$) of dissipation.
On the other hand, simulation results obtained with model setting W0 (cf. Table 4.2) reveal decreasingly accurate results for minor tides. While for M_2 the decrease of open ocean accuracy was at a moderate level of 19% the toll for implementing setting W0 increases by 54 (84) % for the K_2 (ν_2) excitation. The reason for this could reside in a possible overestimation of quadratic (nonlinear) shelf-dissipation mechanisms when adapting the setting W0 for the M_2 tide. The importance of a nonlinear dissipation agent (quadratic bottom friction) reduces strongly for minor tides, which could result in distorted ratios between the deep ocean and shelf-dissipation. As the accentuation of an alternative linear

Table 4.2: Model accuracy as measured by open ocean/OBP $\overline{\text{rms}}$ (cf. Section 4.2) for the discussed ensemble for semidiurnal tides (M_2, K_2, ν_2) as obtained by the default setting RE and setting W0, where eddy-viscosity dissipation has been minimized (cf. Table 4.1).

Partial tide	M_2	K_2	ν_2
$\overline{\text{rms}}$ (cm), RE	3.39/4.83	0.39/0.43	0.19/0.18
$\overline{\text{rms}}$ (cm), W0	4.03/6.54	0.60/0.64	0.35/0.40

dissipation mechanism (eddy-viscosity) in model setting RE improves the results for minor tides drastically, it could be beneficial to consider novel linear shelf-dissipation mechanisms for the precise prediction of minor tides. In spite of the poor physical justification of dominant eddy-dissipation, it might thus be its linear nature that benefits the accuracy of hydrodynamic tidal simulations.

4.3.2 Diurnal Tides

The K_1 tide is the principal excitation in the diurnal band with a magnitude of 58 % M_2-forcing strength. It is important to note that the resulting forcing applied on ocean masses is enhanced by 6.2%, compared to an equivalent forcing at semidiurnal frequencies due to the NDFW-resonance (cf. Table 2.1). In contrast to Z_{22}, the tidal excitation pattern is proportional to Y_{21} and the strongly dispersive wave drag-parametrization is further limited to low latitudes with $|\phi| < 30°$. This causes the admittance function Z_{21} to take a different shape compared to Z_{22}. Tidal elevations are now concentrated in the North Pacific, Indian, and Southern Ocean. Validation performance yields an $\overline{\text{rms}}$ of 0.90/1.32 cm (cf. Figure 4.6). A possible explanation for the overall higher accuracy might be the larger scales of diurnal oscillations systems that are less sensitive to detailed bathymetric information. Moreover, the overall smaller admittance in the diurnal tidal band (Z_{21}) indicates less resonant tidal behavior and thus, less sensitivity to slight changes. We further display a second diurnal oscillation system (Q_1) to demonstrate the achieved accuracy over multiple scales of excitation amplitude. While the forcing strength is reduced by 86.4% compared to K_1, validation accuracy is on a similar level, yielding 0.19/0.25 cm open ocean $\overline{\text{rms}}$. Due to the shift in excitation frequency by 1.70°_{h}, the admittance function Z_{21} changes notably. This also leads to an altered concentration of uncertainty in (shelf)-regions.
Concluding this section, we want to stress that the achieved high accuracy for five partial tides of diverse character proves the model setting RE as suitable and favorable over other settings for high-accuracy applications.

4.4 Tidal Solutions for Satellite Gravimetry

In the previous section, it was shown that with model setting RE, it is possible to simulate minor tides at a similar level of relative accuracy for a wide range of tidal frequencies,

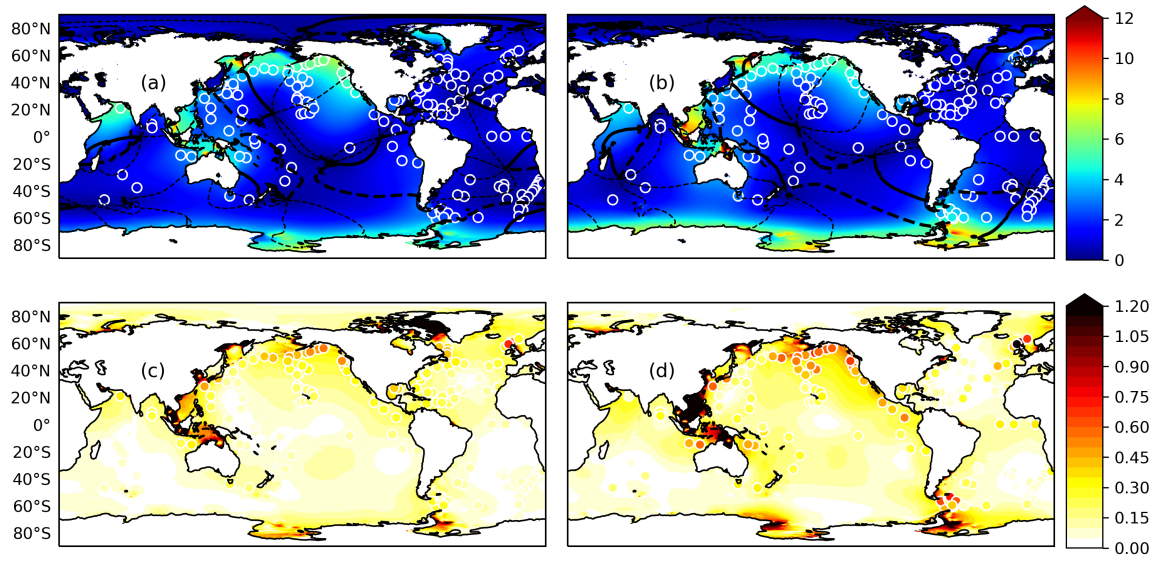

Figure 4.6: Dimensionless admittance-function Z_{21} for K_1 (a) and Q_1 tide (b) and corresponding rms values for Z_{21} (c + d). Rescaling Z_{21} to real ocean elevations amounts to 88.14/12.00 cm for K_1/Q_1. Note the overall lower response level compared to Z_{22} (Figures 4.2 and 4.5).

excitation amplitudes, and excitation patterns. On the other hand, the precision of satellite data-constrained partial tide solutions depends on the available data quality. This quality varies with the respective frequency and domain of tidal observations. Typically, polar tides are less accurately known since many satellite orbits are limited to $|\phi| < 66°$. This leads to prominent GRACE residuals (Ray et al., 2009; Wiese et al., 2016) in polar seas. The same is true for minor tidal constituents that are routinely considered for gravity field de-aliasing (Savcenko et al., 2012) but are often not provided explicitly by data-constrained tidal atlases as the data quality is poor. As this might change at some time with continuously extended altimeter time series (Ray, 2020), minor tides are currently routinely derived by admittance assumptions (Petit and Luzum, 2010), which are prone to reduced accuracy, especially in shallow waters and ice shelf regions (*e.g.*, Pedley et al., 1986) that are governed by nonlinear processes. In this framework, it is natural to ask if purely hydrodynamic solutions can perform more accurately than data-constrained solutions. While this is certainly not true for major constituents (M_2, K_1, ...) we want to take a closer look at minor tidal constituents that are yet relevant for gravity field de-aliasing.

Most promising results can be expected by tides at the edges of tidal bands, as these contain the potentially largest errors when utilizing linear admittance theory (Ray et al., 2009). Thus, we choose the diurnal $2Q_1$ and OO_1 tides (1.0%/1.8% M_2-forcing strength) as first test cases. The validation is performed with a set of tide gauges stations of predominantly coastal character (TICON, Piccioni et al., 2019). Additionally, we probe Q_1-results in the Antarctic region by validation with a data set of Antarctic tide gauges stations (Howard et al., 2020). The respective solutions are either directly included in the

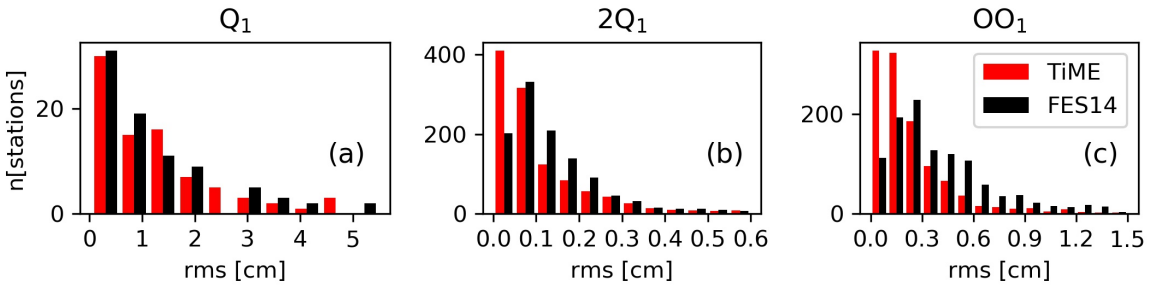

Figure 4.7: Respective rms distributions for the Q_1 tide (Antarctic TGs, a), the $2Q_1$ tide (TICON, b) and the OO_1 tide (TICON, c).

FES2014-atlas (Q_1), or derived via linear admittance supported by Q_1, O_1- and K_1 tide, where we consider perturbations in the tidal potential height by the NDFW-resonance (cf. Table 2.1). Hereby we assume $\partial_\omega Z_{lm} = c_1 + c_2\omega$ (cf. Equation 4.3), evaluate the constants c_1, c_2 by the two closest supporting points and use the result to extrapolate the results linearly to $2Q_1$ (support Q_1, O_1) and OO_1 (support O_1, K_1).
As the distribution of the respective rms values is considerably askew, especially for the TICON data set (cf. Figure 4.7), we decided to utilize the distribution median as an effective validation metric. The median will be listed in the following for the (TiME/FES2014)-distributions. TiME performs on a similar level of accuracy as FES2014 for Q_1 in the Antarctic domain (1.04/0.83 cm). While this is already quite remarkable for an unconstrained model, it proposes that the local, nonlinear particularities of tides below ice shelves must be considered explicitly to obtain more accurate results. On the other hand, the accuracy for $2Q_1$ (0.07/0.11 cm) and even more for OO_1 (0.17/0.34 cm) is clearly increased when TiME solutions are employed. From this improvement of validation accuracy with respect to linear admittance solutions, we draw the conclusion that the utilization of TiME solutions for certain partial tides will result in a reduction of the aliased tidal signal in GRACE data. This de-aliasing potential for GRACE data exhibited by our minor tide solutions emerges from the integrated improvement of the model and its high accuracy over a wide range of partial tides.

4.5 Conclusions

In this chapter, we introduced several modifications to the barotropic tidal model TiME (Weis et al., 2008), which resulted in a considerable increase of the open ocean accuracy.
First, we showed that the introduction of a comprehensive pole rotation scheme allows us for removal of numerical artifacts potentially induced by the former pole cap handling. The realization of two *pari passu* grid orientations with land-covered numerical poles further allowed estimating resolution-connected model uncertainties.
Secondly, the introduction of a non-local online treatment of the effect of SAL (Ray, 1998a) and the implementation of a wave drag-parametrization (Nycander, 2005) allowed for a substantial increase in the model accuracy. We further discussed the relevance of constructing optimized bathymetric maps from different available global data sets. The

Table 4.3: $\overline{\text{rms}}$-increase, *i.e.*, $\Delta\overline{\text{rms}}$, measured by the open ocean and TG metrics, when diverging from the default setting (experiment RE).

Setting	no wave drag	bathymetry[1]	param. SAL	bad pole cap
experiment	W3	B1	S3	P3
$\Delta\overline{\text{rms}}$ [cm]	+4.64/4.91	+3.10/2.52	+2.02/1.86	+1.36/0.74

[1]: Deviations mainly due to blocked ice-shelf cavities.

resulting update on TiME's bathymetry evoked another significant increase in model accuracy, especially due to the inclusion of sub-ice-shelf cavities (Wilmes and Green, 2014). The individual contributions of these updates to model accuracy are summarized in Table 4.3.

Due to the removal of the numerical pole cap, TiME proved to be highly versatile in simulating arbitrary oceanic regions with the same level of accuracy. An open question is the correct representation of (nonlinear) processes in shallow water, beneath ice shelves, and in coastal areas, where the model accuracy considerably drops. Though dissipation by eddy-viscosity (a linear dissipative force) increased the overall model accuracy considerably, the obtained high values for A_h are hard to justify. The question of shallow-water dissipation should be readdressed, also given the persistently overestimated M_2-tidal dissipation.

Tuning experiments of the updated model resulted in a set of model parameters that equally distribute M_2 tidal dissipation to friction by wave drag, bottom-friction, and parametrized eddy-viscosity. The set of model parameters proved robust towards the simulation of diurnal tides and minor tidal excitations, where results with comparable relative accuracy were obtained. On the other hand, parameters had to be adjusted slightly when changing the model's resolution. While the discussed setting is favorable for the gravimetric applications we are envisioning, a second, physically better-founded setting was derived that is favorable for sensitivity studies or paleo experiments.

The achieved model performance qualifies TiME as a purely hydrodynamic tidal model for the simulation of present-day tides. While absolute model deviations from tide gauge data are considerably bigger than results obtained by data-constrained tidal models for major tides, we could show that the accuracy for minor tides can be improved. The same might be possible for polar tides of major origin if crucial polar tidal processes such as sea ice friction are considered. This potential arises from TiME's independence from satellite data and allows for an almost constant relative model accuracy over multiple scales in tidal forcing strength. This fact allows us to aim for explicit studies of small amplitude tidal excitations with TiME, which can result in valuable data constraints. The incorporated nonlinear effects further enable the envisaged small-amplitude studies even for compound and over-tides. To fully benefit from the de-aliasing potential of the obtained solution, a comprehensive study focusing on the accuracy improvement of all relevant minor tides by unconstrained simulations should be conducted and augmented with direct estimates of GRACE-gravity field solutions.

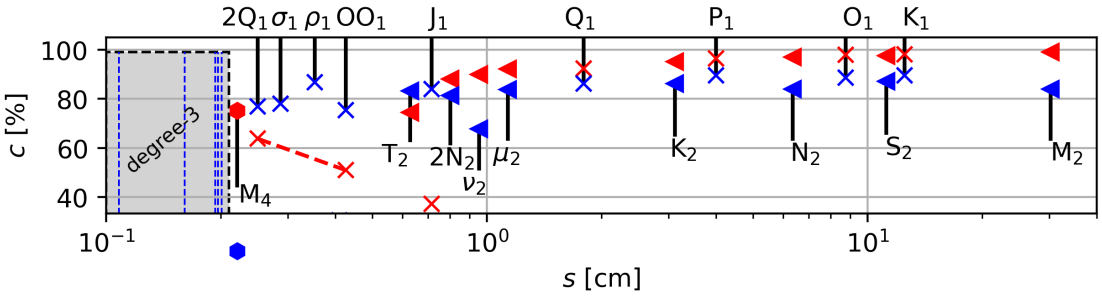

Figure 4.8: Mean captured signal fraction c for TiME (blue) and FES14 (red) with respect to the OBP recorder data set of Ray (2013) for diurnal (x), and semidiurnal tidal species (o) and the 1/4-diurnal M_4 (⬢) partial tide. c is plotted relative to the mean signal s. The red-dashed connected points symbolizes FES14 tides estimated by linear admittance ($2Q_1$ and OO_1, cf. Section 4.4). The gray area shows the mean signal for degree-3 tides predicted by TiME (blue, dashed).

Above all, Chapter 4 is concerned with objective O1, the development of an accurate data-unconstrained ocean tide model. Benefiting from the model upgrades outlined in Section 3.2, it was possible to reduce the model $\overline{\text{rms}}$ for the M_2 tide by 78% (from 15.39 cm) in the non-polar open ocean compared to the altimetry-constrained model FES14, and by 73% (from 17.85 cm) with respect of the OBP recorder data set of Ray (2013). The lowest achieved $\overline{\text{rms}}$ (3.39 cm with respect to FES14 and 4.83 cm with respect to OBP recorders) must be assessed in the context of three other quantities, which are discussed in the following.

First, experiments performed on differently oriented numerical grids with identical physical parameters (cf. Section 4.2.2) deviate from each other on the level of 1 cm (cf. Figure 4.3) in the open ocean. This quantity defines an adequate scale for the model's internal precision, which is primarily related to the model resolution. It is a factor of 4-5 smaller than the open ocean $\overline{\text{rms}}$ with respect to geodetic data. Hence, it is argued that TiME is sufficiently precise to predict OTD.

Second, the $\overline{\text{rms}}$ deviation between the FES14 M_2 tide and the OBP recorders is on the level of 0.3 cm (Stammer et al., 2014), *i.e.*, one order of magnitude smaller than for TiME. This is a typical result for a major partial tide, where satellite altimetry data is of high quality, and thus data assimilation can improve the model accuracy enormously. While this result seems discouraging to pursuing data-unconstrained ocean tide modelling, a third quantity is needed to correctly classify the results.

This third scale is the mean signal of the respective tide s, which results from calculating the mean quadratic amplitude over a certain domain or data set, *i.e.*, by evaluating

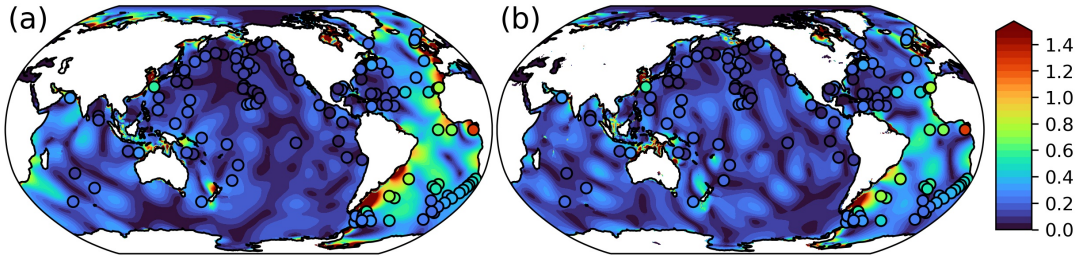

Figure 4.9: Amplitude of the principle 1/4-diurnal overtide M_4 (in cm) from FES14 (a) and TiME (b). The plot is augmented with amplitudes obtained at OBP stations.

Equation (4.1) for $\zeta_1^\omega = 0$. The comparison between s and the $\overline{\text{rms}}$ reveals which fraction of the signal the model can capture correctly. This is done by calculating $c = 1 - \frac{\overline{\text{rms}}}{s}$, which is equal to 87% in the open ocean and 64% in the shallower seas when comparing TiME to FES14 solutions (for M_2). For the following discussion, TiME and FES14 are compared to the OBP data set of Ray (2013), resulting in $c = 84\%$ for TiME and $c = 99\%$ for the FES14 M_2 tide.

It could be shown that c only decreases slightly when constituents of different frequencies and amplitudes are considered. In fact, c does not drop below 68%, even for the minor ν_2-tide, and remains above 80% in most cases (cf. Figure 4.8). While FES14 is still decisively more accurate for ν_2 (*e.g.*, Hart-Davis et al., 2021a), the fraction c drops related to s for data-constrained models. Thus, c depends on the SNR, which decreases with s. The SNR decreases so strongly that data-constrained atlases do not routinely provide tides with tiny signals (cf. Section 4.4) but rely on linear admittance approaches instead (cf. Section 2.2.2). Benefiting from the robust TiME implementation, Chapter 4 shows that several of these tides can be predicted more accurately with a data-unconstrained model (red dashed line in Figure 4.8). Thus, this chapter also contributes towards objective O2 by showing that minor tidal solutions from TiME can improve tidal prediction, as they can be superior to linear admittance estimates in some cases.

On the other hand, linear admittance approaches can't either predict nonlinear shallow-water tides. Thus, the TiME M_4 solution, the principle overtide extracted from experiment RE, is briefly discussed in Figure 4.9. The figure compares both, TiME and FES14 solutions to OBP stations. The mean captured OBP signal fraction equals $c = 73\%$ for FES14, while it is only 18% for TiME. The comparably poor performance of TiME originates from the representation of nonlinearity in PDE (2.26) and its implementation in TiME. As they do not capture a sufficiently large portion of the tidal signal, nonlinear tides are not further discussed in this thesis.

While this statement applies to nonlinear tides, linear admittance is also non-applicable for other groups of minor partial tides comprising degree-3 tides and atmospherically excited tides. They will be the subject of the next chapter[7], which is exclusively dedicated to O2, intensely benefiting from the model developments, *i.e.*, results of O1, outlined in Chapter 3 and validated in this chapter.

[7]Figure 4.8 indicates the signal strength of degree-3 tides and displays the partially atmospherically excited tides S_2 and T_2.

5

Modelling Gravimetric Signatures of Third-Degree Ocean Tides and their Detection in Superconducting Gravimeter Records

Chapter abstract[1]

We employ the barotropic, data-unconstrained ocean tide model TiME to derive an atlas for degree-3 tidal constituents, including monthly to terdiurnal tidal species. The model is optimized with respect to the tide gauge data set TICON-td, that is extended to include the respective tidal constituents of diurnal and higher frequencies. The tide gauge validation shows a root-mean-square (RMS) deviation of $0.9 - 1.3\,\mathrm{mm}$ for the individual species. We further model the load tide-induced gravimetric signals by two means (1) a global load Love number approach and (2) evaluating Greens-integrals at 16 selected locations of superconducting gravimeters. The RMS deviation between the amplitudes derived using both methods is below 0.5 nGal[2] when excluding near-coastal gravimeters. Utilizing ETERNA-x, a recently upgraded and reworked tidal analysis software, we additionally derive degree-3 gravimetric tidal constituents for these stations based on a hypothesis-free wave grouping approach. We demonstrate that this analysis is feasible, yielding amplitude predictions of only a few 10 nGal and that it agrees with the modeled constituents on a level of $63\% - 80\%$ of the mean signal amplitude. Larger deviations are only found for lowest amplitude signals, near-coastal stations, or shorter and noisier data sets.

[1] Some symbols and references in this chapter were harmonized with previous chapters.

[2] 1 nGal $= 0.01 \frac{\mathrm{nm}}{\mathrm{s}^2}$

Published Manuscript (Reproduced with permission from Springer Nature)
Sulzbach, R., Wziontek, H., Hart-Davis, M. *et al.* Modeling gravimetric signatures of third-degree ocean tides and their detection in superconducting gravimeter records. J Geod **96**, 35 (2022). https://doi.org/10.1007/s00190-022-01609-w

Data Availability Statement
The numerical ocean tide simulations presented in this study can be obtained from https://doi.org/10.5880/GFZ.1.3.2021.001 in the form of Stokes coefficients including load-tide induced mass variations (Sulzbach et al., 2021b). The TICON-td data will be available at Pangaea under https://doi.org/10.1594/PANGAEA.943444.

Author Contributions
R.S., H.W., H.D., M.H.-D., D.D. and M.T. conceptualized the idea of the research. R.S. planned and performed the ocean tide simulations and gravimetric modeling and prepared the plots. H.W. performed the tidal analysis of the superconducting gravimeter time series. M.H.-D. performed the tidal analysis of the ocean tide gauge data. H.-G.S., M.V.C., E.D.A., C.V. and O.C.D.O. provided the gravimetric time series and assisted with their interpretation and processing. H.-G.S. and H.W. performed the analysis of the gravity residuals presented in the Appendix. R.S. took the lead in writing the manuscript in collaboration with H.W. and M.H.-D. All authors provided critical feedback and helped shape the research, analysis and manuscript.

Acknowledgements
We thank an anonymous reviewer and the editor Michael Schindelegger for thoroughly reviewing the article and helpful suggestions. Special thanks go to Richard Ray who did not only provide a constructive review of this article but also valuable and comprehensive advice for understanding the phase conventions of the $^3M_1$ tide. We extend our gratitude to the hosts of the data services of IGETS. R.S., M.H.-D., D.D. and M.T. acknowledge funding by TIDUS project within the NEROGRAV research unit (DFG Research Unit 2736, Grants: TH864/15-1, DE2174/12-1). H.D. has been supported by Deutsche Forschungsgemeinschaft within the Collaborative Research Centre TerraQ (Project ID 434617780 - SFB 1464). This work used resources of the Deutsches Klimarechenzentrum (DKRZ) granted by its Scientific Steering Committee (WLA) under project ID 499 for the simulation of ocean tide solutions.

5.1 Introduction

When recapitulating the theory of tides, one finds that the gravitational potential of a celestial body is not symmetric but radially asymmetric at any given distance, d, from its center of mass as it decreases proportionally to $\frac{1}{d}$, thus changing its rate of abatement continuously. However, given the vastness of the distances of these objects relative to the Earth radius, R_e, the lunisolar tide generating potential (TGP) can be approximated to first order by a set of symmetrical degree-2 spherical harmonic functions. The asymmetrical part of the TGP is encoded in harmonic contributions of higher degree ($l \geq 3$), while their magnitudes are reduced by the factor $\left(\frac{R_\mathrm{e}}{d}\right)^{l-2}$ with respect to degree-2 tides. For solar degree-3 tides this factor is as small as $\frac{1}{23000}$, while for the Moon it is close to $\frac{1}{60}$ (*e.g.*, Agnew, 2007). Furthermore, there are planet-moon constellations in the solar system, for which this ratio is even more elevated, *e.g.*, $\frac{3}{10}$ for the Mars–Phobos dyad (Rosenblatt, 2011) augmenting the relative weight of the respective $l > 2$ tides so far that they contribute a significant fraction to tidal dissipation by body tides (Bills et al., 2005).

Although the third-degree TGP can be seen as a small correction to the degree-2 approximation for terrestrial tides, the effect of the respective tide-generating forces on the Earth system is strong enough to be detected with geodetic techniques. This detection is easiest for the terdiurnal $^3\mathrm{M}_3$ wave as it does not neighbor degree-2 excitations, appearing in a practically isolated position of the frequency domain (Melchior and Venedikov, 1968). The detection of degree-3 tides with semidiurnal or even longer periods is more complicated due to significantly stronger degree-2 excitations at nearby frequencies, being only separated by one complete cycle during the precession period of the lunar perigee of 8.85 yr. In addition, some degree-3 partial tides are significantly modulated with the regression period of the lunar nodes of 18.6 yr (Ray, 2020). This dense overlap of closely neighboring partial tides together with their small signal-to-noise ratio implies the need for long-term time series to identify lunar degree-3 tidal constituents (Munk and Hasselmann, 1964). Relying on such long term records, degree-3 signatures were detected in pioneering studies based on tide gauge (Cartwright, 1975; Ray, 2001) and gravimetric records (Dittfeld, 1991; Melchior et al., 1996; Ducarme, 2012) . In particular, records from superconducting gravimeters (Prothero and Goodkind, 1968; Goodkind, 1999; Hinderer et al., 2015) are of very low-noise and high resolution, rendering them well suited for the detection of low amplitude signals (Van Camp et al., 2017).

The derived degree-3 gravimetric factors can be compared to predictions by theoretical Earth models, which were progressively refined (*e.g.*, Wahr, 1981; Dehant et al., 1999; Mathews, 2001). However, body tide gravimetric signatures are superimposed by load tide signals arising from mass redistribution due to ocean tides (*e.g.*, Baker et al., 1996; Jentzsch, 1997; Bos et al., 2000), also for degree-3 tides (Ducarme, 2012; Meurers et al., 2016). The gravitational ocean loading effect comprises both gravity perturbations stemming from the yielding of the solid Earth under the ocean masses and direct Newtonian attraction from the redistributed seawater. This loading effect can be predicted and thus removed by combining ocean tide models with information about the structure of the solid Earth. Possible techniques include global Green's function convolution integrals or spectral approaches constrained by load Love numbers (*e.g.*, Longman, 1963; Farrell, 1972; Boy et al., 2003).

As the induced load tides provoke a significant back-action on ocean tidal dynamics in terms of the induced Self-Attraction and Loading (SAL) potential (*e.g.*, Henderschott, 1972; Ray, 1998a), its precise representation is a vital issue for purely hydrodynamic tidal modeling (*e.g.*, Zahel, 1991; Schindelegger et al., 2018). On the other hand, altimetry-constrained tidal models have reached impressive levels of accuracy (*e.g.*, Egbert and Erofeeva, 2002, updated; Ray, 1999, updated; Lyard et al., 2021; Hart-Davis et al., 2021b) and can provide precise estimates of load tide induced gravimetric fluctuations. As those modern models rely on the quality of available altimetry data, their relative accuracy decreases with the amplitude of the respective tidal constituents and towards the polar regions, where altimetry data coverage is sparse due to the inclination of those satellites and the presence of sea ice. Subsequently, the accuracy of data-constrained ocean tide models is lowest for small amplitude tides (minor tides) and can only increase by prolonging altimetric time series length. As the first tide-dedicated satellite altimetry mission was launched only in 1992, the data basis was not sufficient to extract estimates for degree-3 ocean tides for many years. However, with the continued accumulation of satellite altimetry data, this situation has changed, as the late-breaking study by Ray (2020) shows.
For purely hydrodynamic tide models, the limitations of available empirical data are irrelevant as they are not incorporated into the modeling process. While there were a number of articles that provided data-unconstrained solutions for individual degree-3 tides (Platzman, 1984b; Woodworth, 2019) a full catalog comprising purely hydrodynamic degree-3 tides of all possible orders (0, 1, 2, and 3) has to our knowledge not been published, yet. Clearly, the lack of satisfactory means for identifying tidal loading vectors in degree-3 gravimetric constituents calls for accurate and complete degree-3 ocean tide models (Ducarme, 2012). In turn, such models will enable the correction of gravimetric time series to better assess solid Earth models.
Further, the process of de-aliasing satellite gravimetric data begins to pose the need for degree-3 tidal solutions. In fact, the expected signal strength of minor tides amounts to a relevant fraction of the currently unresolved aliased tidal oscillation. This signal is among the three most prominent sources of uncertainty in Gravity Recovery And Climate Experiment data (GRACE and the successor GRACE-FO) (Tapley et al., 2019; Flechtner et al., 2016).
Here, we complement novel empirical degree-3 solutions (Ray, 2020) by presenting an integrated, data-unconstrained atlas of degree-3 partial tides. These hydrodynamic solutions benefit from several recent advances made with the barotropic model TiME (Sulzbach et al., 2021a). In contrast to the aforementioned empirical solutions, which are confined to latitudes $|\phi| < 66°$, our global results allow for the determination of global load tide solutions. The comparison of those degree-3 solutions to empirical results allows for the validation of the state-of-the-art barotropic modeling approaches. The obtained tidal solutions are subsequently used to derive gravimetric load tide constituents that are compared to the empirically estimated load tide vector at 16 superconducting gravimeter (SG) stations distributed over all continents. The highly sensitive SG instruments offer both an independent way to validate the expected small-amplitude degree-3 tidal solutions and the possibility of verifying the consistency of solid Earth models.
Sections 5.2 and 5.3 describe the employed tidal model and the specification of the tide-raising potential of third degree[3]. Section 5.4 explains the optimization of modeling para-

[3]References were updated to the nomenclature of this thesis.

meters and discusses the performance of the tidal model before we present and discuss the obtained tidal solutions in Section 5.5. The derivation and extraction of gravimetric tidal parameters are outlined in Section 5.6, along with a detailed comparison to the obtained modeling results. We summarize our results and draw conclusions in the final Section 5.7.

5.2 Hydrodynamic Tidal Modeling

To model barotropic tidal dynamics, we employ the purely hydrodynamic (unconstrained by data) computer model TiME that was introduced by Weis et al. (2008) and upgraded by Sulzbach et al. (2021a). TiME integrates the shallow-water equations (*e.g.*, Pekeris, 1974)

$$\begin{aligned} \partial_\mathrm{t}\mathbf{v} + \mathbf{f}\times\mathbf{v} + (\mathbf{v}\cdot\nabla)\,\mathbf{v} &= -g_0\nabla\left(\zeta - \zeta_\mathrm{SAL}(\zeta) - \zeta_\mathrm{eq}\right) - \mathbb{D}\mathbf{v}, \\ \partial_\mathrm{t}\zeta &= -\nabla\left(\left[H+\zeta\right]\,\mathbf{v}\right), \end{aligned} \tag{5.1}$$

in time employing the semi-implicit algorithm developed by Backhaus (1982, 1985). The model is run with partial tide forcing $\zeta_\mathrm{eq} = V_{tid}(\mathbf{x},t)/g_0$, where V_{tid} is proportional to the fully-normalized, real-valued spherical harmonic function of degree l and order m, noted Y_{lm} (cf. Section 5.3). Further, $\mathbf{f} = 2\Omega_\mathrm{e}\sin\phi\ \mathbf{e}_\mathrm{vert}$ is the vertical Coriolis vector at latitude ϕ, $\Omega_\mathrm{e} = \frac{2\pi}{1\mathrm{d}}$ is the Earth rotation angular frequency, and $g_0 = 9.80665\frac{\mathrm{m}}{\mathrm{s}^2}$ (World Meteorological Organisation, 2008) is a conventional, constant value of surface gravity acceleration.
The effect of SAL-potential, $V_\mathrm{SAL} = g_0\ \zeta_\mathrm{SAL}(\zeta)$ (Henderschott, 1972; Ray, 1998a), describes dynamic, gravitational forces induced self-consistently by the redistribution of water mass and the yielding of the Earth. It is calculated by employing a spectral approach, reintroduced by Schindelegger et al. (2018) that is constrained by load Love Numbers (LLNs taken from Wang et al. (2012); PREM), where the spectral decomposition is truncated at maximum degree and order $l_\mathrm{max} = 1024$. Further, a local, scalar approximation of the effect, $\zeta_\mathrm{SAL} = \epsilon\zeta$, can be employed (Accad and Pekeris, 1978).
$H(\mathbf{x})$ is the bathymetric function that is constructed from the RTopo-2 data set (Schaffer et al., 2016) and includes the water column below the lower Antarctic ice shelf boundary.
Dissipative forces are comprised in the expression $\mathbb{D}\mathbf{v}$ that includes dissipation by quadratic bottom friction, parameterized eddy viscosity ($\sim A_\mathrm{h}$: horizontal eddy viscosity coefficient), and topographic wave drag dissipation ($\sim\kappa_\mathrm{w}$: wave drag coefficient) (Nycander, 2005). It is important to note that wave drag is a frequency-dependent effect (Green and Nycander, 2013). While drag is quasi-absent for long-period tides, the individual wave drag tensor differs for diurnal, semidiurnal, and terdiurnal species.
Simulations are performed on a rotated, spherical lat/lon-grid with poles located on dry grid cells at (114.5°E, 28.5°N) in east Asia and the Antipodic point in South America at a resolution of $\frac{1}{12}^\circ$. The zonal resolution is halved at two latitude circles (60° and 75°) towards the poles. This allows for simulations to be performed with time step lengths of $\frac{1}{14400}/\frac{1}{480}/\frac{1}{240}/\frac{1}{160}$ of the respective tidal period for monthly/ diurnal/semidiurnal/ terdiurnal tides yielding numerical values close to 180 seconds.
The initially transient solution is $\boldsymbol{\zeta}(\mathbf{x},t) = (\mathbf{v},\zeta)\,(\mathbf{x},t)$, where $\mathbf{v}$ is the tidal flow velocity

and ζ the sea surface elevation. It converges to the harmonic time series, reading

$$\boldsymbol{\zeta}(\mathbf{x}, \omega t) = \boldsymbol{\zeta}^{\omega}_{\cos} \cos \omega t + \boldsymbol{\zeta}^{\omega}_{\sin} \sin \omega t + (\mathbf{N}) \,, \tag{5.2}$$

for the sea surface elevation. In the following, nonlinear contributions $\mathbf{N}$[4] are neglected as they are generally much smaller than the linear component.
From Equation (5.2) the tidal amplitude $|\zeta^{\omega}| = \sqrt{(\zeta^{\omega}_{\cos})^2 + (\zeta^{\omega}_{\sin})^2}$ and Greenwich-phase-lag ϕ_{ω}[5] can be derived and will be used to present the obtained tidal solutions. We want to stress that $\phi_{\omega} = 0$ usually refers to the TGP having its maximum value at the equator on Greenwich-longitude $\lambda = 0$ (or slightly north of the equator if it is zero at $\phi = 0$). This situation is not reflected at $t = 0$ for all spherical harmonic functions constituting the TGP as later defined in Equation (5.3). For certain combinations of (l, m), including $(2, 0), (3, 0)$ and $(3, 1)$, an additional phase-shift of 180° has to be introduced to obtain the correct phase-convention for $\phi_{\omega} = 0$ at $t = 0$ (cf. Equation 2.7).
We recall that the tidal simulations are run in partial tide forcing mode. This means that only tide-raising forces of a certain frequency are considered, which disables the nonlinear generation of compound tides by the interaction of different partial tides. The nonlinear interactions of certain minor tides can, in principle, generate oscillations at the considered degree-3 frequencies, *e.g.*, $\mathbf{N}(^2\mathrm{M}_2, {}^3\mathrm{M}_1) \rightarrow \mathrm{M}_3$, and would contribute to the modeled tidal solutions. On the other hand, these contributions are expected to be negligible as they can only be produced by the interaction of at least one of the presented minor amplitude, degree-3 tides, with another partial tide. Therefore, these compound tides are smaller by a factor of 60 compared to compound and overtides tides of degree-2 origin. Here, M_4 (cf. *e.g.*, FES14-model: Lyard et al., 2021) is the most prominent example with sub-cm amplitudes in the open ocean. Nonetheless, we acknowledge that those contributions could produce minor modifications of the results.

5.3 Tide-Raising Potential of Second and Third Degree

The TGP allows describing the tidal forces generated by celestial bodies. The astronomical gravity potential exerted by these objects can be decomposed into temporal harmonic functions (Wenzel, 1997b) that excite partial tides in the atmosphere, solid Earth, and ocean. We use the expansion of Hartmann and Wenzel (1994, 1995b) (HW95). The resulting ocean tide-raising potential for a partial tide with frequency ω, degree l and order m can be expressed as[6]

$$V^{\omega lm}_{\mathrm{tid}}(\mathbf{x}, \omega t) = a^{\mathrm{b}}_l A_{\omega} \left(Y_{lm}(\phi, \lambda) \cos \omega t - Y_{l-m}(\phi, \lambda) \sin \omega t \right) , \tag{5.3}$$

where $\mathrm{A}_{\omega} = |\mathrm{A}_{\omega}|$[7] is the excitation amplitude for a partial tide of frequency ω, $a^b_l = 1 + k^b_l - h^b_l$ is a combination of body tide Love numbers that evaluates to $a^b_3 = 0.801$ (Spiridonov

[4] Compare Section 3.3.3.
[5] The notation for the phase lag has been harmonized with Chapter 2.
[6] The notation was harmonized with the TRP as introduced in Chapter 2, cf. Equation (2.8).
[7] In this chapter, partial tide related quantities are labeled by the frequency ω of a given partial tide i, which is equivalent to the definition in Equation (2.8).

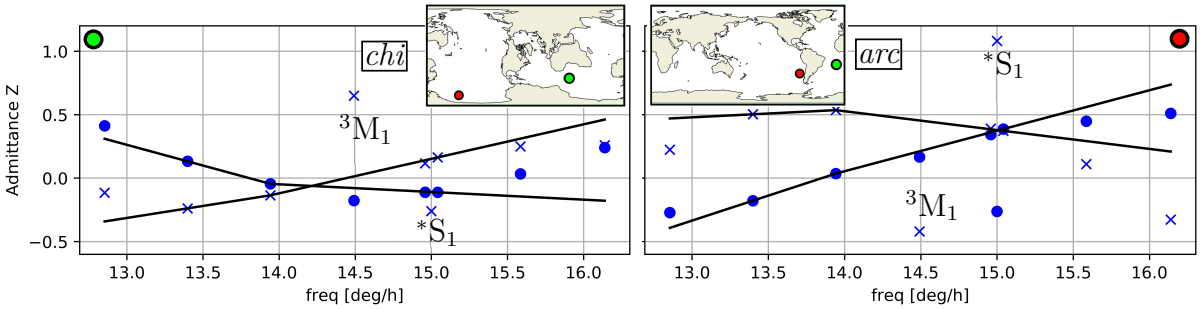

Figure 5.1: Diurnal tide gauge data (TICON-td, cf. Section 5.4.1) for 2 example stations in the Atlantic (left, green •) and southern Pacific Ocean (right, red •). The real (in-phase) part of the admittance function Re(Z) (blue, dot) and the imaginary (quadrature) counterpart Im(Z) (blue, x) are approximated by a linear admittance approach sustained by ^{2}Q$_1$, ^{2}O$_1$, ^{2}K$_1$ (black line). Overlaid the TiME-native *chi*- and the *arc*-grid are shown with the respective TG-positions.

(2018): model 9) and $Y_{l,m\geq 0} \equiv \overline{P}_{lm}(\sin\phi)\cos(m\lambda)$, $Y_{l,m<0} \equiv \overline{P}_{lm}(\sin\phi)\sin(m\lambda)$ are real-valued spherical harmonic functions, where the normalized associated, Legendre functions $\overline{P}_{lm}$ are defined as in Heiskanen and Moritz (1967) or the Appendix of Hartmann and Wenzel (1995a).

Within this thesis, we use the term 'Tide-Raising Potential' (TRP), which is the generator of ocean tides and includes the back-action of solid Earth body tides upon water masses included in a_3^b to demarcate its difference to the concept of the TGP solely including gravitational forces originating from celestial bodies. Our definition of the TRP does not comprise the SAL forces that are induced by the ocean tides themselves but only the forcing potentials that are not influenced by ocean tidal dynamics.

Forces exerted by $V_{\text{tid}}^{\omega lm}(\mathbf{x}, \omega t)$ induce tidal surface oscillations that can be described by the complex-valued solution vector $\zeta^\omega = \zeta^\omega_{\cos} + \mathrm{i}\zeta^\omega_{\sin}$. This quantity will be employed for model validation (cf. Equation 5.2). Normalization by the equilibrium tide length scale, $\frac{A_\omega a_l^{\mathrm{b}}}{g_0}$, yields the admittance function that we define as[8]

$$Z_{lm}(\boldsymbol{x}, \omega) = \frac{\zeta^{\omega,lm}}{A_\omega a_l^{\mathrm{b}}} g_0. \tag{5.4}$$

Here we restored l, m to the superscript of $\zeta^{\omega,lm}$ to recall the degree and order of the respective partial TRP, the generator of $\zeta^{\omega,lm}$. As $\partial_\omega Z_{lm}$ varies only weakly with ω for modern-day tides, the admittance function $Z_{lm}(\omega)$ is often interpolated (and extrapolated) by assuming linear admittance (Munk and Cartwright, 1966; Petit and Luzum, 2010; Rieser et al., 2012) (cf. Figure 5.1 and D.1). As those assumptions are feasible for most tides, this approach is employed to improve tidal predictions substantially, as direct estimation of tides by satellite-data-constrained tidal models shows reduced precision for small tidal amplitudes (Hart-Davis et al., 2021a).

[8]This definition is equivalent to the definition in Chapter 2.

Table 5.1: Third-degree tides and neighboring second-degree tides in the same tidal group as appearing in HW95-TGP of Hartmann and Wenzel (1995b) after the nomenclature of Ray (2020). The Table shows the Doodson-Coefficients, the tidal frequency f, excitation amplitude, as well as degree l and order m of the generating spherical harmonic functions Y_{lm}. Additionally, naming conventions employed in recent publications are listed.

Doodson	f $[\frac{^\circ}{h}]$	l	m	A_ω $[\frac{\mathrm{mm}^2}{\mathrm{s}^2}]$	Ray (2020)[1]	Ducarme (2012)[2]	Woodworth (2019)
065.555	0.54902	3	0	1.0424e+04	$^3\mathbf{Mm}^*$	$3MO_0$	
155.455	14.48741	2	1	1.449e+04	$^2M_1$	LK_1	$M_1'(2)$
155.555	14.49205	3	1	7.833e+03	$^3\mathbf{M}_1$	M_1	M_1
155.655	14.49669	2	1	4.029e+04	$^2M_1$	NO_1	$M_1'(7)$
245.555	28.43509	3	2	7.604e+03	$^3\mathbf{N}_2$	$3MK_2$	
245.655	28.43973	2	2	2.366e+05	$^2N_2$	N_2	
265.455	29.52848	2	2	3.493e+04	$^2L_2$	L_2	
265.555	29.53312	3	2	7.014e+03	$^3\mathbf{L}_2$	$3MO_2$	
355.555	43.47616	3	3	1.497e+04	$^3\mathbf{M}_3$	M_3	

[1]: Notation employed in this chapter.
[2]: also used in the HW95 catalog supplemented to ETERNA-x.
*: Not mentioned by Ray (2020) but proposed in personal communication.

On the other hand, this technique can only be employed for tides with identical degrees and orders. For degree-3 tides, the admittance assumptions sustained by degree-2 tides are generally invalid, as is easily verified with tide gauge data-derived admittance functions. From Figure 5.1 it becomes clear that the degree-3 tide $^3M_1$ as well as the primarily radiational tide $^*S_1$ cannot be estimated by linear admittance assumptions and must be estimated, or simulated, explicitly. Here, * signifies the atmospherically influenced excitation pattern that differs from pure degree-2 excitation.
As degree-3 partial tides are reduced by the factor of approximately $\frac{1}{60}$, they are difficult to detect in observational records. Thus, we only consider the most prominent excitations for the possible tidal bands ($m = 0, 1, 2, 3$) of third-degree origin even though additional excitations can be detected in gravimetric meassurements (Ducarme, 2012) and in several tide gauge records (Ray, 2001). Since the nomenclature for those tides has never been unified (Ray, 2020) and differs in geodetic (Ducarme, 2012) and oceanographic literature (Woodworth, 2019), they are listed in Table 5.1 with respect to their mentioning in recent publications along with neighboring tides of second-degree origin.
Within this chapter, we will utilize the naming convention introduced by Ray (2020), presented in bold font, as it considers historical developments in the oceanographic nomenclature, incorporates a direct reference to the degree of the exciting potential, and excludes confusion with oceanographic compound and overtides. Further, the utilized leading superscript has been extended to all second-degree partial tides (*e.g.*, $^2M_2$, $^2O_1$) mentioned in this chapter for means of continuity.

5.4 Model Setup and Validation

Since TiME is data-unconstrained, simulation errors cannot be rectified by assimilating satellite altimetry data. Therefore, the influence of the model parameters on the simulation results is critical. To optimize the accuracy of the obtained tidal solutions, an ensemble of simulations is prepared where the relative weights of the implemented dissipation mechanisms are tuned. The results are then validated with a reference tide gauge data set.

5.4.1 Tide Gauge Data Set

TICON is a global tide gauge (TG) data set that provides tidal constants of 40 tidal constituents (Piccioni et al., 2019). These constants are estimated by least-squares harmonic analysis on individual tide gauge time series obtained from the Global Extreme Sea Level Analysis (GESLA: Woodworth et al., 2017) project. In this study, the number of tidal constituents is increased to include the $^3M_1$, $^3M_3$, $^3N_2$ and $^3L_2$ tides, and the data set is henceforth called TICON-td. As stated by Ray (2020), these degree-3 tides have frequencies similar to those of larger degree-2 tides and are significantly modulated during the 18.61 yr cycle of the lunar node regression and, therefore, require a long time series of observations to properly separate these tides. The required time series length is hereby related to the noise apparent in the tidal record (Munk and Hasselmann, 1964). The extension of TICON-td was designed to only include tide gauges that exceed 10 years of continuous sampling and include the nodal corrections as presented by Ray (2020). Furthermore, we only include stations that are placed in an open ocean environment (mean surrounding depth > 500 m in a 2° radius), ending up with an ensemble of $N_\mathrm{T} = 134$ stations. We further remove closely neighboring stations by only allowing one station in a 0.2° radius. Formal uncertainties of these tidal estimations are also provided in order to evaluate the comparisons between the model and these data. For these four tidal constituents, the average standard deviation of the individual tide gauge estimations was < 0.01 mm and, therefore, should not influence the comparisons with the model estimations.

Further, we employ $N_R = 130$ selected OBP stations that were analyzed by (Ray, 2013). This data set provides constituents for a large number of partial tides, including $^3M_3$, which allows the comparison to TICON-td for this specific partial tide. The spatial distribution of the data sets is non-uniform, where a concentration of stations around Japan for TICON-td is the most striking feature.
The employed metric is the root-mean-square (RMS) deviation with respect to the data

$$RMS(\zeta^\omega) = \sqrt{\frac{1}{2N}\sum_{i=1}^{N} |\zeta^\omega(\mathbf{x}_i) - \zeta^\omega_\mathrm{TG}(\mathbf{x}_i)|^2}\ , \tag{5.5}$$

where the summation is performed for all $N = N_\mathrm{R}, N_\mathrm{T}$ stations. This deviation can be compared to the respective mean signal $s \equiv RMS(\zeta^\omega = 0)$, depicting the captured signal fraction

$$c = 1 - \frac{RMS}{s}\ , \tag{5.6}$$

that we will employ as an effective score metric.

Table 5.2: Tuning experiments for dynamical degree-3 tides. RMS($^3M_3$) comprises the evaluation for both data sets (TICON-td/ Ray, 2013). All RMS values are given in mm.

ID	SAL	κ_w [%]	A_h [$\frac{m^2}{s}$]	RMS($^3M_1$)	RMS($^3L_2$)	RMS($^3N_2$)	RMS($^3M_3$)
Mean Signal at TG-stations s [mm]:				1.5	2.5	2.0	2.9/2.3
S1	$\epsilon = 0.1$	125	$2 \cdot 10^4$	1.4	1.2	1.2	2.0/1.6
W0	d/o=1024	125	$5 \cdot 10^2$	1.2	1.2	1.4	2.2/1.9
W1	d/o=1024	0	$4 \cdot 10^4$	1.0	1.3	1.2	1.6/1.1
RE	d/o=1024	125	$2 \cdot 10^4$	1.0	0.9	0.9	1.3/0.9
RE-Dissipation by wave drag [%]:				14	39	34	29
$c = 1 - \frac{RMS}{s}$ (experiment RE) [%]:				33	64	55	61/55

5.4.2 Model Tuning

Employing the previously introduced tide gauge metric, an ensemble of tidal simulations was prepared to find an optimum interplay between the implemented dissipation mechanisms (wave drag, bottom friction, eddy viscosity). The results are displayed in Table 5.2. For all partial tides, we obtain the highest accuracy with setting RE, which was initially derived as an optimized setting for the main lunar tide $^2M_2$ (Sulzbach et al., 2021a).
The parameterized eddy viscosity of $A_h = 2 \cdot 10^4 \frac{m^2}{s}$ implies a large lateral momentum transfer which we find hard to justify hydrodynamically (Egbert et al., 2004). Therefore, we further conducted experiments with A_h minimized (W0), which confirmed the results of Sulzbach et al. (2021a), where RE is favorable for enhanced accuracy. Similar to this finding, reduced accuracy is observed when employing setting W1, where wave drag dissipation is completely suppressed. This confirms that terdiurnal and semidiurnal tides are strongly controlled by wave drag dissipation and thus require a precise representation of this effect for accurate modelling results.
The influence on $^3M_1$ on the other hand, is smaller, while ^{3}Mm is simulated with setting W1 as is not expected to dissipate energy by wave drag mechanisms (cf. Table 5.2). In comparison to neighboring degree-2 tides tabulated in Table 5.1, the wave drag dissipation fraction is almost identical ($^2N_2$: 34 %; $^2L_2$: 38 %; $^2M_1$: 16 %) in spite of gravely altered admittance patterns. The overall dissipation is well below 1 GW, with the most prominent contribution of 240 MW coming from the $^3M_3$ tide.
In agreement with results obtained for major tides (Sulzbach et al., 2021a), we find that the full consideration of the effect of SAL is crucial to obtain high-precision results. The locally approximated SAL-effect utilized for experiment S1 showed a substantial RMS increase, especially for the small-scale oscillation systems of $^3M_3$, where the increase was close to 1 mm. A possible explanation is the smoothing effect of the SAL-convolution integral, which is highly important for short-scale oscillation systems such as those of $^3M_3$. The captured signal fraction c (cf. Equation 5.6) exhibits values between 55% and 65%, where the agreement for $^3M_1$ is particularly low (33%). We find that the amount of captured signal for $^3M_3$ by both data sets is similar.

5.5 Global Solutions for Ocean Tides and Loading-Induced Gravity Signals

Ocean tidal loading induces terrestrial gravity variations that can be measured with gravimeters on solid ground, even far away from the coast. In analogy to Equation (5.2), the induced ocean loading induced gravity signal can be described by

$$g(\mathbf{x}, \omega t) = g^{\omega}_{\cos} \cos \omega t + g^{\omega}_{\sin} \sin \omega t + (\mathbf{N}) \,. \tag{5.7}$$

Global solutions $g^{\omega} = g^{\omega}_{\cos} + i g^{\omega}_{\sin}$ for the induced gravity at sea level height can be derived by a spectral approach, constrained by load Love numbers that translate $\zeta^{\omega}_{\cos} \rightarrow g^{\omega}_{\cos}$ and analogously for the sine-coefficients (Agnew, 1997; Merriam, 1980).
Therefore we evaluate

$$g^{\omega}_{\cos}(\mathbf{x}) = -g_0 \frac{3\rho_{\mathrm{sw}}}{2R_e\rho_{\mathrm{se}}} \sum_{l,|m|\leq l}^{l_{\max}} \frac{4h_l - 2k_l(l+1) - 1}{2l+1} \zeta^{\omega}_{lm,cos} Y_{lm}(\phi, \lambda) \ . \tag{5.8}$$

Here $\zeta^{\omega}_{\cos} = \sum_{l,m} \zeta^{\omega}_{lm,cos} Y_{lm}(\phi, \lambda)$, k_l and h_l are LLNs describe the effect of the yielding of the solid Earth on gravity, $\rho_{\mathrm{sw}} = 1024 \frac{kg}{m^3}$ and $\rho_{\mathrm{se}} = 5510 \frac{kg}{m^3}$ are the mean density of seawater and the solid Earth, respectively. This sum converges uniformly as $k_l l \rightarrow (k_l \cdot l)_{\infty}$ and $h_l \rightarrow h_{\infty}$. We take $l_{\max} = 2599$, where the ocean load input is interpolated conservatively to a resolution of $\frac{1}{30}^{\circ}$, with coastlines derived from the RTopo-2 bathymetry (Schaffer et al., 2016). In line with the definition of the tide-raising forces in Equation (5.1), the gravity acceleration in Equation (5.8) acts towards potential maxima: Positive vectors point to the Earth's core. This evaluation is strictly valid only at sea level height ($H = 0$) because otherwise, the spectral decomposition does not converge sufficiently fast with increasing $l_{\max}$ (Merriam, 1980).
This formula solely encompasses the far-field or large-scale effect of the induced gravity variations. In this approximation, mass variations are treated as a layer of depth zero on the ocean surface. The Newtonian attraction of close-by wet grid cells is thus ignored, as they are assumed to be at the same height as the evaluation point (at sea level)[9].
Therefore, this approximation is only valid at locations with a distance from the ocean r_0 and height H forming a ratio $\tan(\beta) = \frac{H}{r_0} \rightarrow 0$. While this is true for most SG stations treated in this chapter, deviations are to be expected for near-coastal stations, which we will define within this chapter as stations with $\beta^{\max} > 1^{\circ}$ comprising the OS ($r_0^{\min} \approx 250\,\mathrm{m} \rightarrow \beta^{\max} \approx 1.6^{\circ}$) and NY station (SG Kongepunktet: $r_0^{\min} \approx 120\,\mathrm{m} \rightarrow \beta^{\max} \approx 20.0^{\circ}$, Breili et al., 2017). Other gravimeters in coastal regions (*e.g.*, TC, LP) are situated at distances $r_0 > 10\,\mathrm{km}$ from the ocean and violate the defined criterion for near coastal stations. However, the restriction to sea level height is only relevant for the introduced spectral approach. The here neglected local attraction effect can be easily incorporated with a Greens-function approach (*e.g.*, Olsson et al., 2009).
In the following subsections, the modeled results for ocean and induced gravity signatures appearing in Table 5.1 are discussed and refer to Figures 5.2 to 5.5.

[9] The identification of the effect of local Newtonian attraction is debated by Voigt et al. (2023).

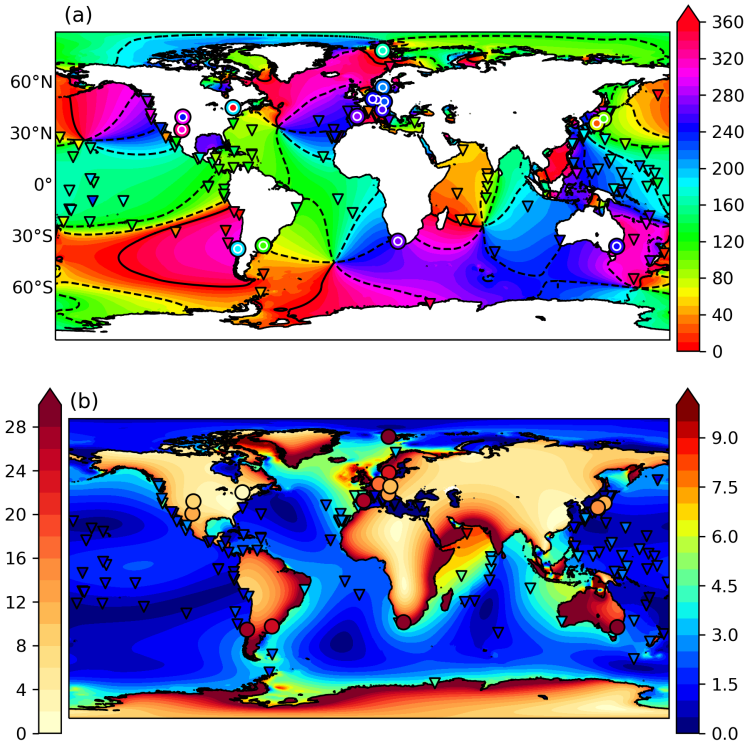

Figure 5.2: $^3M_1$-tide; (a) Greenwich-phase lag ϕ_ω of the modeled ocean tide (degree) with cotidal lines in increments of 60° (Thick: 0°) ; (b) ocean tide amplitude $|\zeta^\omega|$ (right, mm) and ocean loading induced gravity amplitude $|g^\omega|$ (left, nGal). The plots are overlayed with Greenwich phases and amplitudes measured at TICON-td tide gauge stations (triangles) and phases modeled with SPOTL (inner circle) and analyzed (outer circle) for the SG stations. The displayed gravity signal partially exceeds the presented scale by far in near-coastal regions but is cropped at 28 nGal for a better depiction of smaller signals.

5.5.1 Diurnal Species

In close agreement with the results of (Ray, 2020) and (Woodworth, 2019), the displayed $^3M_1$-oscillation patterns have a typically diurnal character with tidal amplitudes that are elevated at coastlines (cf. Figure 5.2). Yet the observed cotidal chart completely contradicts the well-known degree-2 patterns (cf. also Appendix D and Figure D.1 therein). Tidal amplitudes are enhanced in the North Atlantic (in accordance with Cartwright, 1975) and even more pronounced in the Indian Ocean. On the other hand, $^3M_1$-oscillation in the Pacific is strongly suppressed. As TiME is data-unconstrained and includes polar latitudes, we further report large-scale elevations of up to 5 mm in the Southern Ocean around Antarctica as well as high amplitudes in Baffin Bay (max: 14 mm) and the Barents Sea (max: 19 mm east of the Kanin Peninsula), while Arctic $^3M_1$-amplitudes are small but reach up to 3 mm in some places. We further report a number of local maxima, including the Sea of Okhotsk (max: 33 mm), the Patagonian Shelf (max: 12 mm), and south of New Guinea (max: 42 mm).

While the comparison to TICON-td shows a convincing agreement in tidal phases, the amplitudes are depicted less precisely, resulting in an RMS of 10 mm while capturing

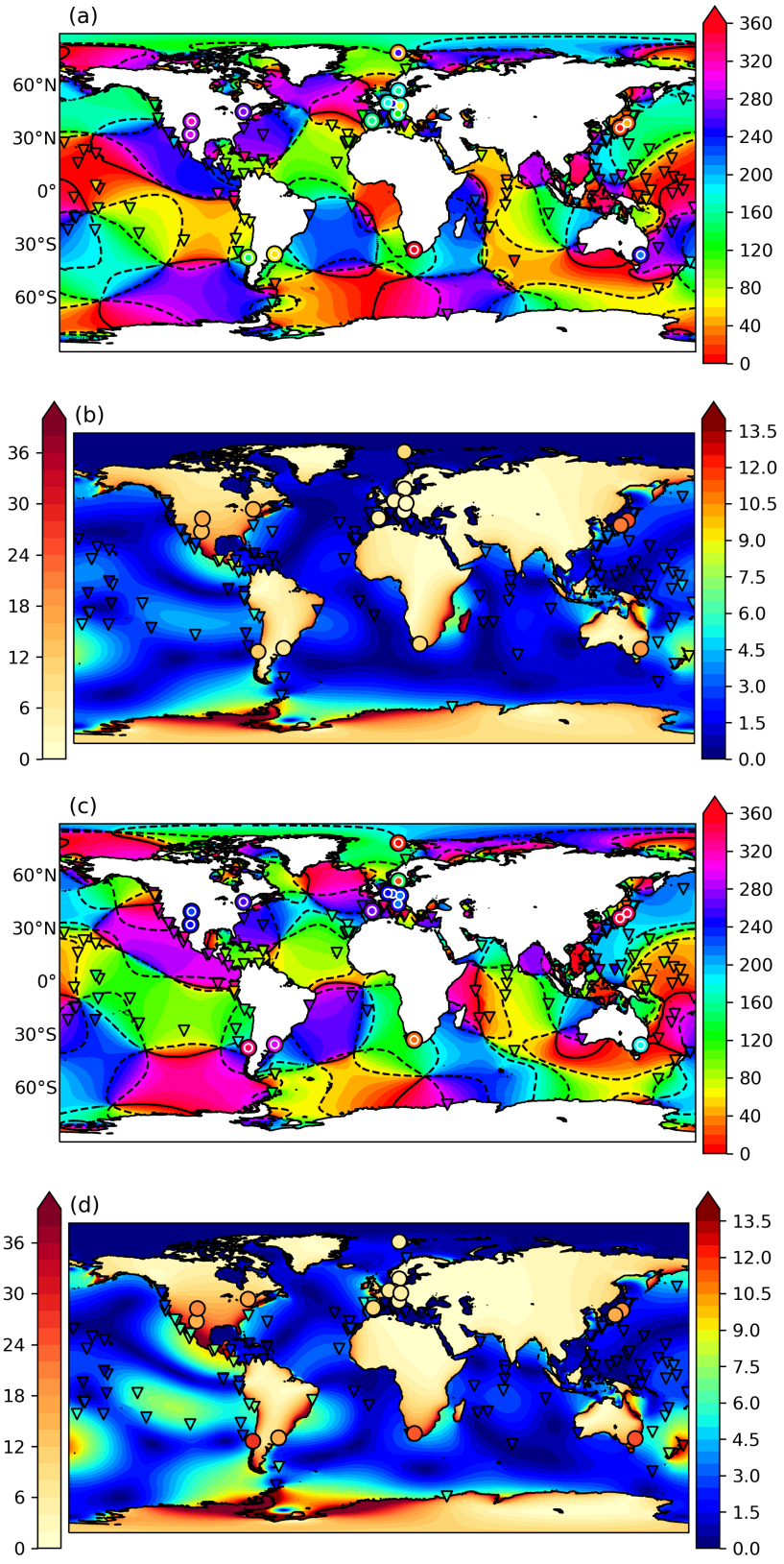

Figure 5.3: ${}^3N_2/{}^3L_2$-tide; (a, c) Greenwich-phase lag ϕ_ω of the modeled ocean tide (degree) with cotidal lines in increments of 60° (Thick: 0°) ; (b, d) ocean tide amplitude $|\zeta^\omega|$ (right, mm) and ocean loading induced gravity amplitude $|g^\omega|$ (left, nGal). The plots are overlayed with Greenwich-phases and amplitudes measured at TICON-td tide gauge stations (triangles) and phases modeled with SPOTL (inner circle) and analyzed (outer circle) for the SGs.

$c = 33\%$ of the signal (Table 5.2). Besides possible shortcomings of the tidal model for the $^3M_1$ (*e.g.*, underestimated bottom friction, shallow-water processes), a possible reason for this low agreement might be the generally small $^3M_1$-signal with especially high concentrations of TG-stations in low amplitude regions (*e.g.*, The Pacific Ocean). In spite of the small $^3M_1$ ocean tide signal, the modeled ocean loading induced gravity signal features high amplitudes in coastal proximity, partially exceeding 100 nGal (*e.g.*, The Horn of Africa) that only slowly decay towards the continental interior. Reasonably high signals are to be expected for gravimeters situated in Europe, South America, and Australia.

5.5.2 Semidiurnal Species

Being members of the same admittance band described by Z_{32}, the $^3N_2$ and $^3L_2$ tides exhibit quite similar oscillation patterns. In agreement with the findings of Ray (2020), TiME predicts the semidiurnal degree-3 response to be strongest in the Pacific Ocean with smaller amplitudes in the southern Atlantic Ocean (cf. Figure 5.3). In contrast to the diurnal results, amplitude maxima of up to 10 mm height appear in the open ocean. The strong semidiurnal response in the Southern Ocean, especially the Weddell Sea, is fully depicted on TiME's global domain with large-scale amplitudes reaching over 10 mm. On the other hand, semidiurnal responses in the Arctic region are found to be negligible. As discussed by Ray (2020), the $^3L_2$-response is observed to be considerably stronger, despite its smaller equilibrium tidal height (-8% to $^3N_2$), which can be related to a more resonant coupling to oceanic normal modes (cf. Müller, 2007).
We report a number of local maxima that reach the highest values north-east of Australia (94 mm), Bristol Bay (Alaska, 77 mm), Western Australia (41 mm), and the Weddell Sea (38 mm) for $^3L_2$.
The validation with TICON-td shows a good agreement in tidal phases and amplitudes that is substantially higher than the results obtained for $^3M_1$ (55%/64%) and comparable to the results obtained by Ray (2020). Relevant gravimetric amplitudes are predicted close to large-scale oceanic signals, with dominant amplitudes in North/South America, South Africa, and Australia. Due to their shorter tidal period, the semidiurnal amphidromic systems have a shorter spatial length scale compared to $^3M_1$. Their respective gravimetric amplitudes decay faster towards the continental centers. For a comparison with degree-2 tidal solutions please consider Appendix D and Figure D.2 therein.

5.5.3 Terdiurnal Species

$^3M_3$ displays the most fine-structured response patterns due to its higher terdiurnal frequency. More than for the semidiurnal species, open ocean amplitude maxima appear in each major basin with amplitudes reaching > 5 mm and even higher in the north-east of Brazil (cf. Figure 5.4). The most prominent large-scale amplitudes are yet again confined to shelf areas and marginal seas (Ray, 2020).
The largest signals are obtained in the Mozambique Channel and Western Europe. Amplitudes up to 5 mm are predicted at Antarctic coasts, while Panarctic $^3M_3$ amplitudes are close to zero. In contrast, small-scale $^3M_3$ shelf resonances can reach considerable heights. Here we only mention the largest predicted amplitudes near Beira (Mozambique Channel: 151 mm), the Suriname river mouth (131 mm), Southern Australia (88 mm), and Bristol

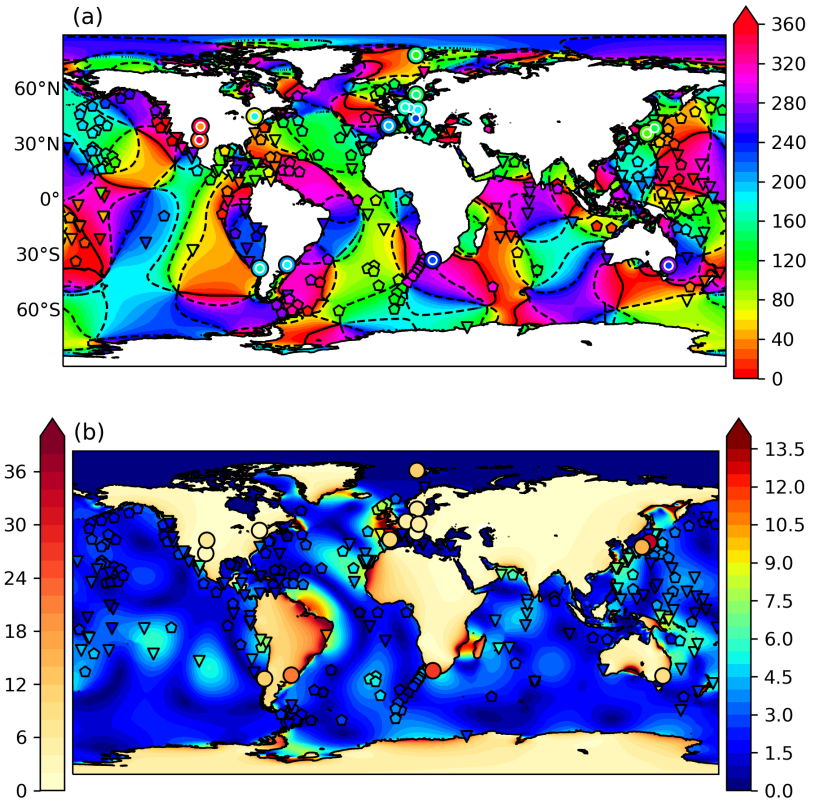

Figure 5.4: $^3M_3$-tide; (a) Greenwich-phase lag ϕ_ω of the modeled ocean tide (degree) with cotidal lines in increments of 60° (Thick: 0°) ; (b) ocean tide amplitude $|\zeta^\omega|$ (right, mm) and ocean loading induced gravity amplitude $|g^\omega|$ (left, nGal). The plots are overlayed with Greenwich-phases and amplitudes measured at TICON-td tide gauge stations (triangles) OBP stations of Ray (2013) (hexagons) and phases modeled with SPOTL (inner circle) and analyzed (outer circle) for the SG stations.

Channel (UK: 69 mm).
As for the semidiurnal tidal species, the comparison to TG data shows a good agreement with both data sets at levels of around $c = 60\%$. Combining both data sets, dense coverage of TG data is achieved. Providing an interesting result for satellite gravimetry, the predicted open ocean amplitude maxima are recorded and confirmed by the TG stations for both terdiurnal and semidiurnal tidal species. As $^3M_3$ oscillation systems are of small scale and often confined to coasts, the resulting ocean loading induced gravity signal reaches high amplitudes in coastal environments while quickly decaying with increasing distance from the coast. The loading-induced gravity signature on the South American continent represents an interesting case: As the coastal terdiurnal ocean tides mainly exhibit phase lags between 240° and 360°, the continent is pushed down in a synchronized way yielding high gravimetric amplitudes that depict relevant magnitudes over the larger part of the continent. As the gravimetric amplitude rapidly changes in coastal margins, the detectability of $^3M_3$ in *e.g.*, European and Japanese stations primarily depends on the exact position of the gravimeter station.

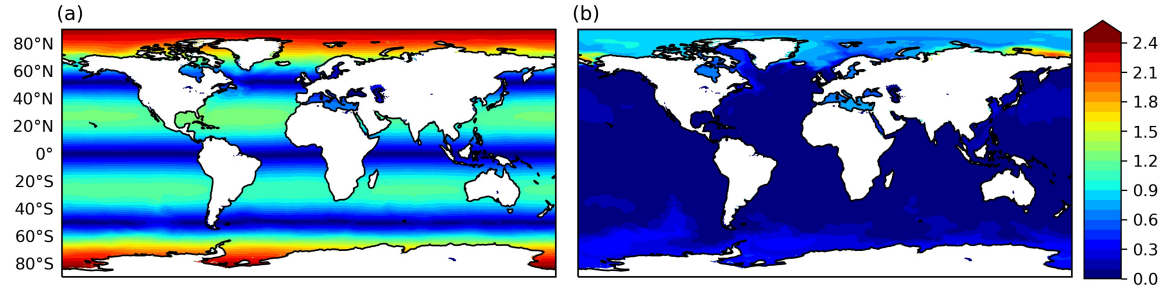

Figure 5.5: Long-period ^{3}Mm-tide (a) and complex deviation $|\zeta_\omega - \zeta_{\mathrm{seqt}}(^3\mathrm{Mm})|$ to self-consistent equilibrium tide (b). Elevations are given in mm.

5.5.4 Long-Period Species

As the ^{3}Mm oscillation period is close to 1 month, dynamic forces are strongly suppressed, resulting in an ocean tide amplitude generally below 3 mm. The results can directly be compared to the self-consistent equilibrium tide ζ_{seqt} resulting from Equation (5.1) with dynamic forces eliminated,

$$\zeta_{\mathrm{seqt}} - \zeta_{\mathrm{eq}} - \zeta_{\mathrm{SAL}}(\zeta_{\mathrm{seqt}}) = \text{const.} \ , \tag{5.9}$$

that depends on the degree and order of the selected partial tide forcing expressed by ζ_{eq}. The constant value has to be chosen to ensure mass conservation[10]. The deviation between ^{3}Mm and $\zeta_{\mathrm{seqt}}(^3\mathrm{Mm})$ that is displayed in Figure 5.5 (b) confirms the non-dynamic character of ^{3}Mm. Aberrations from the equilibrium solution only reach relevant magnitudes in the Panarctic region, especially on the Siberian Shelf, where deviation amplitudes over 2 mm are obtained. Some marginal seas (Baltic Sea, Mediterranean Sea) also exhibit small deviations from equilibrium.
As the ^{3}Mm-constituent is not contained in TICON-td, the results displayed in Figure 5.5 (a) cannot be validated directly in this study. Further, The ^{3}Mm-amplitudes are small compared to the effects of local water storage changes, which appear in the same temporal range (weeks to months). Therefore, it turned out to be difficult to find evidence in the gravimetric time series, but the results may contribute to isolating those hydrological signals.

5.6 Gravimetric Data and Modelling

Long records from superconducting gravimeters (SG) (Goodkind, 1999; Hinderer et al., 2015) provide temporal gravity variations with the highest sensitivity and long-term stability. The excellent signal-to-noise ratio of these instruments, together with recent advances in tidal analysis, enables a separate parameter estimation of degree-3 tidal constituents.

[10] Compare Section 2.1.4, where the constant value is introduced as $c_{\mathrm{m}}(t)$.

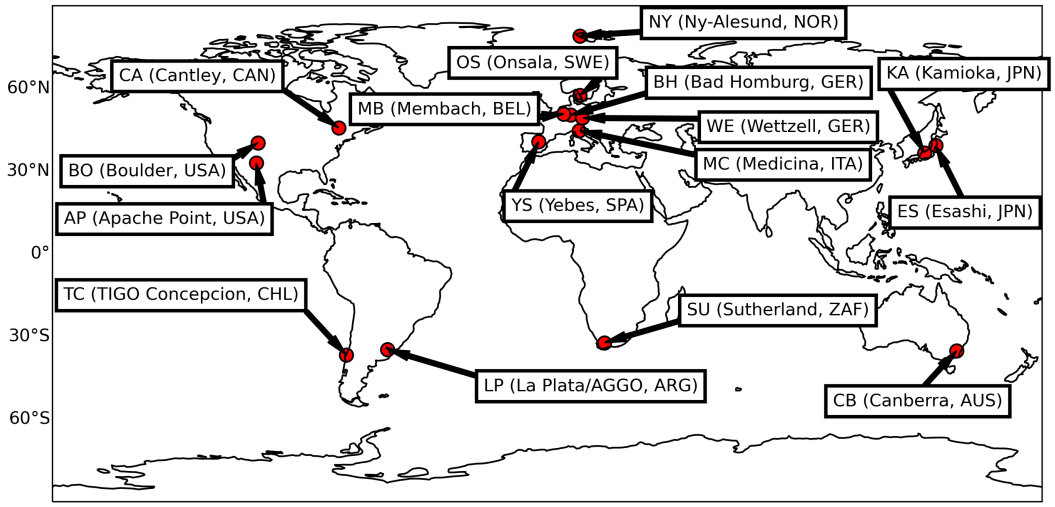

Figure 5.6: Locations of the discussed SG stations over the globe with Station-ID, Site, and Country-ID.

5.6.1 Gravity Time Series

Records from 16 SG stations worldwide (Figure 5.6) contributing to the International Geodynamics and Earth Tide Service (IGETS, Boy et al., 2020) were analyzed. The time series covering periods from 5 to 23 years were selected based on a global simulation of the tidal constituents (Table 5.2, Figures 5.2 to 5.5). Stations having a signal of at least 10 nGal for one component were included. This covers, in particular, the Atlantic coast of Europe, the west coast of North America, southern Australia, and Japan, and includes stations in South Africa and South America.

The data were provided either by the station operators or obtained from the IGETS data base (Voigt et al., 2016). Raw data sets (IGETS Level-1) were pre-processed in a remove-restore procedure by applying preliminary tidal models and atmospheric corrections only to remove spikes and disturbances and correct instrumental steps. Also, IGETS Level-2 data sets were partially post-processed in this way. In data sets provided by the operators and IGETS Level-3, the instrumental drift was already reduced. In some cases, a second-degree polynomial function was applied, while for station OS, a more complex nonlinear drift function was necessary (Scherneck and Rajner, 2019). Only minor revisions of specific Sectionswere found to be necessary. All applied gravity reductions were restored before analysis.

5.6.2 Tidal Analysis

Within the tidal analysis, the complex transfer function of the measured Earth's response to tidal forcing (Wang, 1997) relative to an Earth model is determined from observations. Because it is impossible to resolve a large number of individual frequencies of the TGP (Wenzel (1997b), Section 5.3) even with the longest records, wave groups are introduced. Besides a Bayesian approach (Tamura et al., 1991), parameters for each wave group are usually determined by a least square adjustment (Wenzel, 1997a), including a

trend and regression channels, mostly used to determine an air pressure admittance to correct for atmospheric pressure effects. Following (Schüller, 2015), the basic observation equations (without regression channels) are for a number of wave groups q

$$y_{ET}(t) = \sum_{i=1}^{q} \delta_i^{\star} \sum_{j=a_i}^{b_i} A_{ij}^{EM} \cos(\omega_{ij} t + \varphi_{ij} + \kappa_i) \ , \tag{5.10}$$

where $A_{ij}^{EM} = \delta_{ij}^{EM} \times A_{ij}$ are the amplitudes, scaled by the admittance factor δ^{EM} of the Earth model EM, while φ_{ij} are phases, both for the respective frequency ω_{ij} and harmonic degree and order within the index range $[a_i, b_i]$ of the tidal potential catalogue. This model fits the observations by the relative amplitude factor $\delta^{\star}$ and the phase shift κ. Equation(5.10) is transformed into the linear problem

$$y_{ET}(t) = \sum_{i=1}^{q} x_{c_i} e_i(t) - x_{s_i} f_i(t) \ , \tag{5.11}$$

with the unknown parameters $x_{c_i} = \delta_i^{\star} \cos(\kappa_i)$, $x_{s_i} = \delta_i^{\star} \sin(\kappa_i)$ for each tidal wave group i, relative to the contribution of the partial waves

$$e_i(t) = \sum_{j=a_i}^{b_i} A_{ij}^{EM} \cos(\omega_{ij} t + \varphi_{ij}), \quad f_i(t) = \sum_{j=a_i}^{b_i} A_{ij}^{EM} \sin(\omega_{ij} t + \varphi_{ij}) \ .$$

In order to separate the contributions of different degrees of the harmonic potential development within each wave group, Equation(5.10) can be reordered depending on degree l and order m of the harmonic potential Y_{lm} (Schueller, 2020), reading

$$y_{ET}(t) = \sum_{l=1}^{l_{\max}} \sum_{m=0}^{l} \sum_{i=1}^{q_{lm}} \delta_{lmi}^{\star} \sum_{j=a_i}^{b_i} A_{lmij}^{EM} \cos(\omega_{lmij} + \varphi_{lmij} + \kappa_{lmi}) \ . \tag{5.12}$$

This allows a hypothesis-free wave grouping because a pre-scaling of the response of the Earth to tidal forcing of different harmonic degrees is not required anymore. However, the resolution of this approach is limited by the length and signal-to-noise ratio of the observed time series. Actually, ETERNA-x allows for three different grouping schemes: a) separate groups for selected reference wave groups and a specific degree, b) grouping of selected constituents of a specific degree and order into one group, and c) collecting all selected waves of a specific degree into one group. Here, we include the degree-3 waves under test as separate groups by scheme a), the so-called satellite wave groups. The schemes R04 and R18 from Ducarme and Schüller (2019) were modified, resulting in 76 to 125 wave groups. High correlations between tidal parameters of different degrees need to be avoided. We followed the correlation analysis as proposed by Ducarme and Schüller (2019) and used the ratio between error estimates propagated from the full covariances matrix and the uncorrelated case (Correlation RMSE Amplifier, CRA). A ratio of 1 stands for no correlation, while large values indicate a high dependency between parameters. In this way, it was decided if the more detailed scheme R18 or, the more robust scheme R04 is applied. The majority of parameters showed a CRA close to 1, only for stations BO, AP, LP and TC this indicator was around 2 for $^3M_1$ and $^3L_2$, most likely related to a higher noise level in these registrations.

Table 5.3: Statistical properties of the SG times series used in this study. The instrument names include an abbreviation indicating the generation: T - tidal, C - compact, O - observatory, R - first remote controlled and sensor coils in series, DS - dual sphere. The last column indicates whether the times series was high-pass filtered to suppress signals with periods longer than diurnal tides.

Station	Meter	Source	Period From	To	No. of days	No. of Blocks	No. of Obs.	Scheme	No. of Waves	Filter
NY (EU)	C-039	Kartverket	Sep-1999	Jun-2012	4.667	1	112.014	R18	123	no
OS (EU)	O-054	OSO	Jun-2009	Jan-2021	4.242	1	101.816	R04	76	yes
MB (EU)	C-021	ROB	Jun-1998	Aug-2020	8.088	25	192.811	R18	125	no
BH (EU)	O-044	BKG	Feb-2007	Mar-2017	3.679	9	87.993	R18	125	no
WE (EU)	DS030-1	BKG	Jun-2010	Mar-2020	3.567	7	85.552	R04	88	no
MC (EU)	C-023	BKG	Aug-1997	Dec-2020	8.552	2	205.208	R18	125	no
YS (EU)	O-064	IGETS-L3	Jan-2012	Apr-2020	3.042	1	73.028	R04	103	yes
SU (AF)	DS037-1	GFZ	Jan-2011	Dec-2020	3.652	1	87.665	R04	76	yes
CA (NA)	T-012	IGETS-L3	Jul-1997	Mar-2019	7.942	3	176.070	R18	125	no
BO (NA)	C-024	IGETS-L1	Jun-1996	Oct-2003	2.708	8	63.745	R18	103	yes
AP (NA)	O-046	IGETS-L3	Sep-2013	Sep-2018	1.822	1	43.744	R04	91	no
LP (SA)	R-038	UNLP	Jan-2016	Feb-2021	1.883	1	45.209	R04	76	yes
TC (SA)	R-038	BKG	Mar-2010	Feb-2015	1.802	6	42.214	R04	76	yes
ES (AS)	T-007	IGETS-L2	Jul-1997	Oct-2002	1.932	14	54.579	R04	91	yes
KA (AS)	T-016	IGETS-L3	Oct-2004	Jul-2013	3.204	1	76.899	R04	76	no
CB (OC)	C-031	IGETS-L3	Jul-1997	Dec-2018	7.853	1	188.487	R18	123	no

The parameters relative to those of an ellipsoidal Earth model with an inelastic mantle and a non-hydrostatic initial state (DDW-NHi, Dehant et al., 1999) and the TGP from Hartmann and Wenzel (1995b) were estimated with software ETERNA-x[11] . Shorter time series or records with strong non-tidal effects in the long-period tidal range were high-pass filtered. Whether a filter was applied is documented in the last column of Table 5.3. Otherwise, only an overall linear trend was reduced. Table 5.3 provides an overview of the time span, number of continuous blocks, the applied wave grouping scheme, and filtering, while further properties of the gravity residuals are discussed in Appendix C.

The effects of Earth rotation (polar motion, length-of-day variations) were reduced by a predefined amplitude factor of 1.16 (Wahr, 1985). Atmospheric effects were corrected by a simple regression factor for local air pressure variations. More advanced atmospheric corrections based on numerical weather models from the service Atmacs (Klügel and Wziontek, 2009) or applied in IGETS Level-3 were tested but gave not the same level of agreement - a surprising result that needs further investigation.

5.6.3 Comparison with Simulated Loading Signals

The tidal loading signal from TiME was predicted for the 16 SG stations by two approaches: (1) employing the program NLOADF (Agnew, 1997) from the package SPOTL (Agnew, 2012) that was run with the respective partial tide solutions, and (2) the global solution as described in Section 5.5 based on LLNs. To discuss the agreement between the simulated and analyzed data set, we employ the metrics introduced in Equations 5.5 and 5.6, where we replace $\zeta^\omega \rightarrow g^\omega$ and evaluate at the 16 SG stations. We addi-

[11] version v81 available at (Schüller, 2015) `http://ggp.bkg.bund.de/eterna`

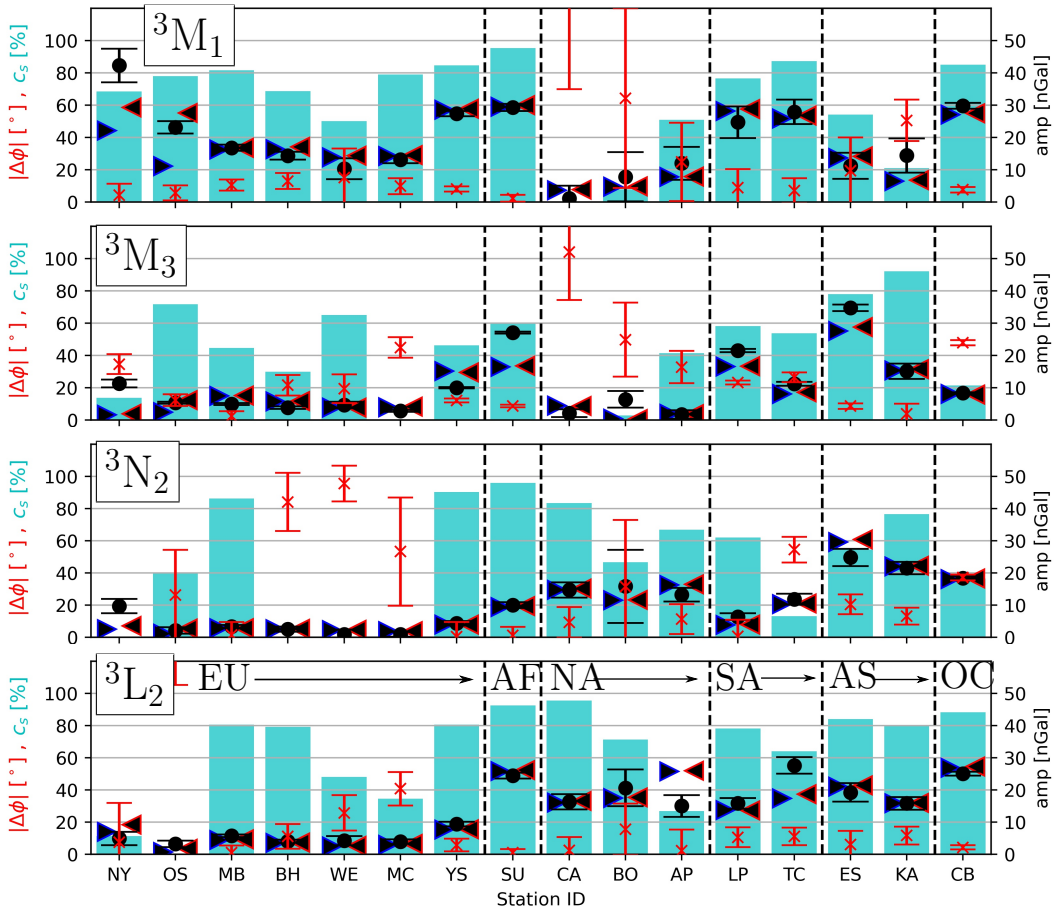

Figure 5.7: Measured amplitudes (black •), modeled amplitudes (SPOTL: red ◀; LLN-approach; blue ▶), phase-difference between SGs and model $|\Delta\Phi| = |\Phi_{\mathrm{SG}} - \Phi_m|$ (red x), and captured signal fraction c_s (cyan columns) evaluated at the considered ensemble of 16 SG stations for $^3M_1$, $^3M_3$, $^3N_2$ and $^3L_2$ (top to bottom). The error bars represent the formal uncertainties Δamp and $\Delta\Phi_{\mathrm{SG}}$ stemming from the tidal analysis. The vertical dashed lines divide the SG stations into global domains (Europe, Africa, North America, South America, Asia, and Oceania).

tionally calculate the captured signal fraction for individual stations, defined as $c_s = 1 - \sqrt{|g^\omega(\mathbf{x}_{\mathrm{SG}}) - g^\omega_{\mathrm{SG}}|^2/|g^\omega_{\mathrm{SG}}|^2)}$, with $g^\omega(\mathbf{x}_{\mathrm{SG}})$ and g^ω_{SG} being the result obtained with SPOTL and ETERNA-x at the SG-location $\mathbf{x}_{\mathrm{SG}}$, respectively.

Amplitudes and phases of the obtained loading vectors are displayed together with the results of the tidal analysis in Figure 5.7. Both simulations, SPOTL and LLN, agree remarkably well, except for stations OS and NY, which are located close to the coast at a finite height above sea level. As described in Section 5.5, these stations exhibit a nonzero angle β, and Newtonian attraction of local ocean mass will affect the gravimeter. This effect is not included in the LLN approach and only to a certain resolution in SPOTL. When excluding the near coastal stations NY and OS, the RMS of the modeled gravity amplitudes between both approaches amounts to 0.28/0.4/0.41/0.45 nGal for $^3N_2/^3M_3/^3L_2/^3M_1$. In the case of $^3M_1$ at OS, the agreement of SPOTL with the observed parameters is much

better, as the distance between SG and coast is larger (approx. 350 m) which means that a coarser representation of the coastline for OS will be sufficient. On the other hand, the effect at NY will require a much finer resolved coastline (distance to coast approx. 150 m; Breili et al., 2017).

For most of the stations and waves, the agreement between simulated and analyzed loading effects is high, where the mean captured signal, Equation (5.6), for all stations ranges between 65% und 79% (Table 5.4). For $^{3}M_{1}$, an excellent agreement is found for stations MB, MC, YS, SU, and CB, as indicated by cyan bars, while for stations CA and BO, the modeled signal is close to zero, confirming the result of the analysis. In these cases, large phase deviations may appear because the phase is not well resolved for non-significant amplitudes. Nonetheless, a correctly predicted zero signal is a confirmation of a high agreement between the model and tidal analysis. Therefore, in cases of non-significant amplitudes, the formally low agreement c_s should not be regarded as poorly modeled stations.

The agreement for station TC and LP in South America is good as well, although with higher uncertainties. The latter is close to the Río de La Plata estuary and is affected by shallow-water tides and storm surge effects (Oreiro et al., 2018). A correction for storm surge effects has not yet been applied because they included small tidal constituents (mainly related to $^{2}M_{2}$) and were not available for the whole analysis period. However, the impact of the estuary should be studied in more detail at a later stage.

In the case of $^{3}N_{2}$, large signals are confirmed for the Japanese SG stations ES and KA, CB in Australia, and for AP, CA, and BO in North America. The results for BO agree well but exhibit large uncertainties, eventually related to the quality of the data set. A zero signal was confirmed by all European stations; the small amplitudes in the range of a few nGal are even significant with 95% confidence but show large phase deviations for the same reasons as explained above.

The results for $^{3}L_{2}$ show the best agreement for almost all stations. The zero signal is confirmed for NY and OS, documenting the high quality of both records and that deviations for the other waves are most certainly not observational artifacts but should be subject to further interpretation. Even the small signal at several European stations is well confirmed and in phase. The only larger deviation is found at AP and TC, located close to the Pacific coast in South America, where the amplitude is significantly underestimated by TiME compared to the tidal analysis result.

The $^{3}M_{3}$ wave's large amplitudes in Japan are well matched by TiME. Also, for YS and SU, larger signals close to 20 nGal are predicted, showing more than 50 % agreement with the TiME solutions. Also, here, the zero signal was well-confirmed by most European and North American stations.

Altogether, there is an agreement of more than 50 % for all the stations having an amplitude of at least 20 nGal, cf. Figure 5.8. This shows not only that TiME is able to predict degree-3 gravimetric signals at a mean level of 63 % to 80 % depending on the respective tidal constituent but also the high resolution of SG records from IGETS in the range of a few nGal and the capabilities of ETERNA-x to resolve independent estimates for constituents of higher degree.

Table 5.4: Degree-3 ocean tide induced gravity validation metrics at 16 SG stations

tide	$^3M_1$	$^3L_2$	$^3N_2$	$^3M_3$
s^ω [nGal]	21.7	15.8	12.4	14.1
RMS$^\omega$ [nGal]	4.4	3.3	4.6	4.1
c [%]	80	79	63	71

5.7 Conclusions

In this study, we presented the first data-unconstrained global atlas for degree-3 ocean tides encompassing at least one partial tide of each tidal band. The validation with a set of tide gauge stations gave an RMS deviation of 1 mm for each partial tide solution and confirmed a good agreement with our solutions. We also made a first assessment of the respective degree-3 signal in a globally distributed set of superconducting gravimeters. The extraction of the respective tidal constituents with nGal-amplitudes proved to be feasible and yielded a tight agreement with the modeled gravimetric signals. The modeled signal was obtained with two different approaches that showed to be equally reliable at altitudes close to mean sea level and far away from coasts. For near-coastal gravimeters at finite height, we found a significantly reduced agreement, presumably due to rather strong gravitational attraction effects by local mass variations.
The presented comparison of ocean tide solution with its associated gravimetric signals bears mutual benefits for geodesy and oceanography. On the one hand, the comparison of modeled vs. observed loading vectors represents an independent approach to validate ocean tides models as *e.g.*, persued by Llubes and Mazzega (1996, 1997); Boy et al. (2003). The potential is also seen in inverting observed loading vectors to obtain information about ocean tidal dynamics (Jourdin et al., 1991). This consideration could be valuable for tidal constituents that cannot yet be resolved by satellite altimetry (*e.g.*, due to small ocean tide amplitudes), as for additional diurnal degree-3 constituents like $^3J_1$, $^3O_1$, $^3O_1$ and $^32Q_1$ that were detected in a number of tide gauge records which were longer than 35 years (Ray, 2001). Complementary to the routinely applied validation with tide gauge data that represents a discrete set of local measurements of tidal heights, each SG constituent contains information about the global ocean mass distribution (via the integrative characteristics of gravity measurements) and is thus sensitive to changes in the tidal solution at much larger spatial scales. In particular, this could be handy for assessing the expected de-aliasing performance for satellite gravimetric solutions as those are sensitive to long-wavelength characteristics of the terrestrial mass distribution. The complementary characteristics of using TG and SG data sets for validating ocean tide models also reflect on their mean signals: While for $^3M_1$ the TG signal was the smallest in the ensemble (1.5 mm vs. 2.9 mm for $^3M_3$), the induced mean SG signal was the most prominent (21.7 nGal vs. 14.1 nGal for $^3M_3$). While this partially reflects on the dense SG concentration in Europe, a second reason is the long spatial wavelength of diurnal tides that leads to higher gravimetric amplitudes in the interior of the continents. As this is also the case for ^{3}Mm, SG data could be a valuable metric for validating small amplitude tides with long periods. Therefore, SG results, as presented here, should serve as additional benchmarks for ocean tide model development that will (in the case of TiME) focus in the near future on the representation of nonlinear effects that are particularly important

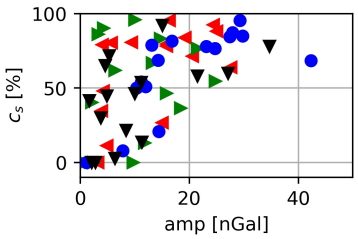

Figure 5.8: Relationship between signal amplitude and captured signal fraction for $^3M_1$ (blue circles), $^3N_2$ (green triangle), $^3L_2$ (red triangle) and $^3M_3$ (black triangle). Negative agreement $c < 0$ is displayed as 0%.

in shallow marginal seas.

Moreover, the high level of agreement between the predictions from the numerical ocean model and the tidal analysis results confirms the advanced methods introduced in ETERNA-x. Potentially, such comparisons may contribute to identifying deficiencies in reductions of non-tidal loading or local mass attraction effects. In principle, the separation of body and load tide component in the gravimetric degree-3 signals is now possible by employing the modeled SG signals enabling further tests of the routinely applied solid Earth models. As discussed by Ray (2020) $^3M_3$, ocean tide signatures correlate with GRACE/GRACE-FO acceleration residuals. Therefore, GRACE-reprocessing is likely to benefit from the inclusion of degree-3 tides, as imperfect tidal background modelling represents a prominent de-aliasing error (Flechtner et al., 2016). Motivated by this finding, unconstrained TiME solutions might be of interest to satellite gravimetry and other geodetic techniques such as GNSS surface loading (Penna et al., 2015), particularly for partial tides that are not readily available from data-constrained atlases.

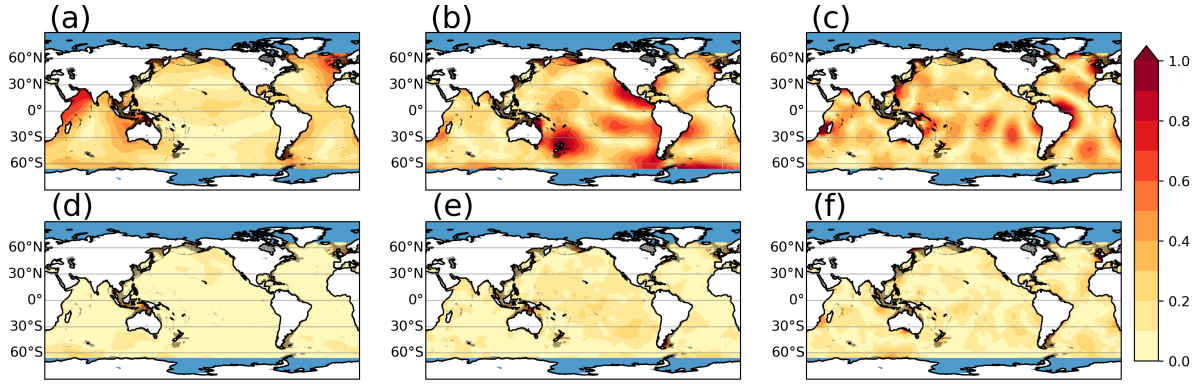

Figure 5.9: Partial tide amplitude (top) of the empirical degree-3 ocean tide solutions of Ray (2020) and RMS with respect to hydrodynamic TiME22 solutions (bottom) from left to right for $^3M_1$, $^3L_2$, and $^3M_3$. Areas shallower than $H = 1000$ m are gray, and areas polewards of $|\phi| = 66°$ are plotted in light blue. All units are in cm.

This chapter represents the principal contribution towards objective O2. While Chapter 4 concentrated on degree-2 minor tides, usually derived with linear admittance estimation, here, the subgroup of degree-3 tides is the focus.
On the one hand, the mean signals of degree-3 tides are comparably small (in the OBP-metric of Figure 4.8 below 0.2 cm). On the other hand, they are inaccessible by degree-2 admittance estimates (cf. Figure 5.1). TiME could capture signal fractions of up to $c = 80\%$, depending on the reference data set. In addition to TG and SG data validation in Chapter 5, it was possible to compare the described TiME solutions to the partial tides of Ray (2020), derived from satellite altimetry. These empirical solutions represent the current maximum precision achievable with satellite altimetry. Comparison to TiME solutions in the deep ($H > 1000$ m), non-polar ocean results in c-values between 60% (for $^3M_3$) and 72% (for $^3M_1$, cf. Figure 5.9).
Thus, three independent data sets originating from tide gauge, terrestrial gravimetry, and satellite altimetry successfully validate the data-unconstrained TiME simulations, which predict signals on the nGal/mm-level. All simulations were conducted with identical model parameters initially optimized for the M_2 tide (cf. Section 4.2). In particular, adapting them to the specific partial tide simulations was not necessary to achieve optimized accuracy (cf. Table 5.2).
Further investigating the lower signal boundary of detectable tidal signatures, the en-

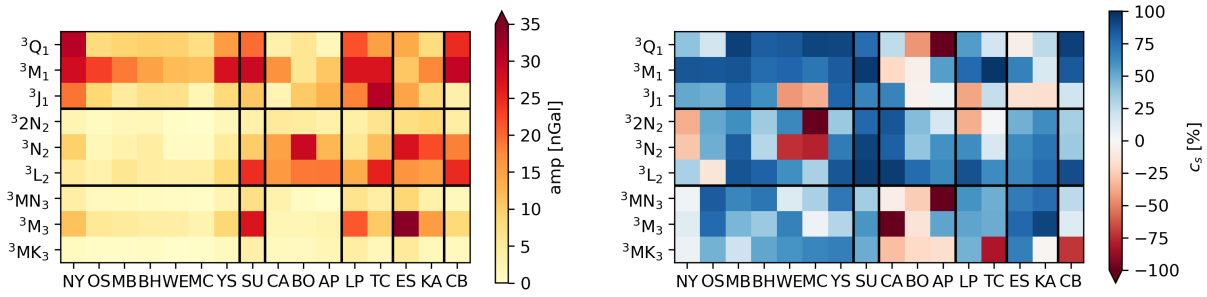

Figure 5.10: Gravimetric amplitude (left) obtained from the tidal analysis of gravity time series registered by 16 superconducting gravimeters (cf. Figure 5.6 and Table 5.3) for nine individual degree-3 tides and respective captured signal fraction c_s (cf. Equation 5.6), when compared to simulated constituents obtained from TiME ocean tide simulation (right). The Figure is modified after Wziontek et al. (2022).

semble of considered degree-3 partial tides was expanded to nine constituents (Wziontek et al., 2022). Their respective equilibrium tidal heights are a factor of $3-8$ smaller than for the tides discussed in Chapter 5 (cf. Table E.1). Despite the smaller signal, the mean captured signal fraction c does not drop below 36% (for $^3J_1$) but decreases with the mean signal amplitude as indicated in Figure 5.8, which drops to 4 nGal[12] for $^32N_2$ (cf. Figure 5.10). The results do not indicate a sudden breakdown of TiME's accuracy, even for the constituents with the smallest amplitudes. Differently phrased, TiME maintains a high accuracy, even for signals on the edge of and below the detectability level.
While the data-constrained solutions of Ray (2020) represent an impressive demonstration of the modern capability of satellite altimetry, Figure 5.9 reinforces their limitations, as they can only be constructed for non-polar latitudes (cf. Figure 1.2). Polewards of $|\phi| = 66°$, TiME is, for now, the only ocean tide model that provides a consistent continuation in polar regions for every degree-3 species (long-period to terdiurnal). Providing solutions with a closed mass budget is especially important for GRACE(-FO) dealiasing, as gravitational attraction is non-local, *i.e.*, satellite orbits are impacted by the global mass distribution and not only by the local mass anomaly directly below. Degree-3 tides were previously not considered for GRACE(-FO) processing. To enable their consideration for gravity field processing, an increased number of degree-3 solutions[13] was included TiME22 tidal atlas (cf. Appendix E), which is intended for gravimetric applications.
While the impact of degree-3 tides on gravity field processing could not yet be extensively investigated, it is likely to be very small due to the minute amplitude of the tides. To provide an example with a proven impact on the gravity field solutions, it is referred to the previously mentioned group of atmospherically excited tides (radiational tides). The respective TiME simulations are comprehensively discussed by Balidakis et al. (2022, 2023). Here, the principal diurnal radiational tide, S_1, was found to exhibit a somewhat increased agreement with the OBP data of Ray (2013), compared to the FES14 solu-

[12]The low-noise character of SGs allows the detection of such small signals. They are much harder to detect in TG records (Ray, 2001).
[13]The final degree-3 ensemble comprises 12 constituents.

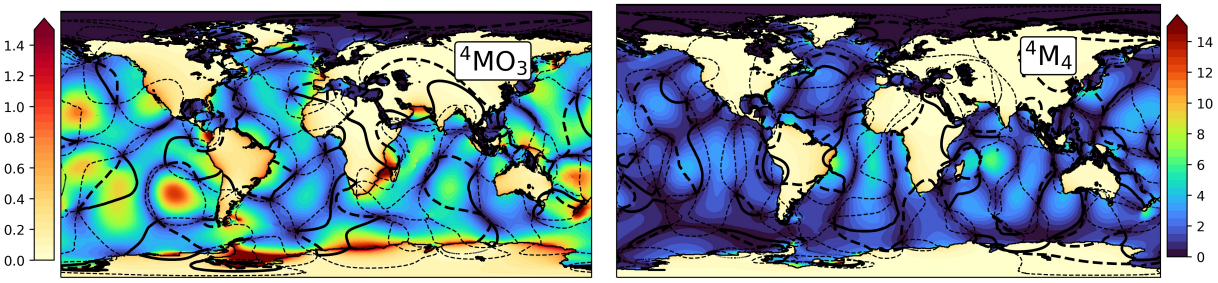

Figure 5.11: Degree-4 admittance functions Z_{43} and Z_{44} for sea surface height elevation (right scale) and for vertical surface gravity (cf. Equation D.2, left scale). The scale factor is 10μm (left) and 17μm (right) for the sea surface elevation and 0.43 nGal (left) and 0.73 nGal (right).

tion. The first simulations found a reduction GRACE gravity residuals when considering TiME's S_1 tide (Balidakis et al., 2022). Also, the annual modulation lines of S_2 ($\pm$1 cpy), *i.e.*, R_2 and T_2, exhibited slightly increased accuracy when compared to FES14. Further, investigating the minor, terdiurnal radiational tides, R_3-S_3-T_3 (*e.g.*, Ray et al., 2023), resulted in convincing results (cf. Figure 2.4). Hence, it is argued that TiME can also predict minor radiational tides with good accuracy. Thus, the 16 tides of Balidakis et al. (2022) are included in the TiME22 atlas, which should be seen as the principal result of O2 (cf. Appendix E).

While this thesis' primary goal is improving ocean partial tide solutions for tidal prediction and dealiasing, the results of Chapter 5 open a second interesting path of investigation. Because it was possible to predict exiguously small secondary tidal observables (nGal-level) with convincing accuracy (cf. Chapter 1 and Section 2.3), SG observations can, in principle, be inverted to recuperate measurements of the solid Earth properties. The data-unconstrained operation mode of TiME allows doing so for frequency bands (*e.g.*, terdiurnal) and harmonic forcing patterns (degree-3), where global data-constrained solutions are unavailable. Ultimately, the high agreement levels indicate that employed solid Earth models (here, DDW-NHi) work reliably for degree-3 tides. Consequently, the straightforward question is if, given the high accuracy of SG measurements, even the detection of degree-4 ocean tides is possible[14], which would allow investigating solid Earth models up to 1/4-diurnal tidal frequencies.

The degree-4 TRP is diminished by another factor of $\frac{R_e}{d} = 60^{-1}$ with regard to degree-3, while $a_4^b = 0.87$ is slightly larger compared to $a_3^b = 0.80$. The most prominent partial components of the orders $m = 1$ and $m = 2$ happen to have identical frequencies to $(d/R_e)^2 = 3600$-times stronger tides of degree-2 (*e.g.*, $^4M_2$ and $^2M_2$). Thus, the focus is on the terdiurnal and 1/4-diurnal band of degree-4, with the most prominent constituents $^4M_4$ (455.555) and $^4MO_3$ (345.555). For these partial tides, TiME simulations with

[14]The most significant degree-4 component of the TRP ($^4M_4$) is still approximately 40 times stronger than the most pronounced partial tide induced by a non-lunisolar body - a Venusian partial tide. This tide has the Doodson code 277.055 and the multiplier '3' as the ninth argument of the HW95 TGP (mean longitude of Venus). Even for the closest approach of Venus and Earth (approximately $38 \cdot 10^6$ km), Venusian degree-2 tides are still a factor of 5 less significant than lunar degree-4 tides.

barotropic forcing of degree-4 (cf. Appendix A) are performed. The model parameters are chosen according to the formerly introduced policy, with the 1/4-diurnal time step set to $\Delta t = \frac{T_{1/4}}{120} \approx 180$ s.
The ${}^4\mathrm{M}_4$ tide is much smaller in amplitude compared to the M_4 shallow-water tide (cf. Figure 4.9) and has a very weakly pronounced resonance strength, which is revealed by the small values of Z_{44} compared to other Z_{lm} up to $l = 4$ (cf. Figures 5.11, and D.2 and D.1). A possible detection of ${}^4\mathrm{M}_4$ would require both the SG instrument precision and the M_4 model accuracy to be better than 0.1 nGal, which is not possible with the currently achieved accuracy. On the other hand, detection of ${}^4\mathrm{MO}_3$ would require the precision of approximately $0.5 - 1.0$ nGal for the gravimetric measurement and the modeled nonlinear MO_3-tide ($\mathrm{M}_2 + \mathrm{O}_1 \rightarrow \mathrm{MO}_3$) if the SG position is carefully selected (*e.g.*, on the Japanese archipelago). Given the agreement of TiME and the SG constituents on the few-nGal-level (Figure 5.10), this seems to be a promising exercise in the future. However, improvements in TiME's shallow-water tides are required to provide compound tides on the necessary accuracy level (cf. Context Section of Chapter 4).
Chapter 5 thus fully supports the hypothesis that the TiME implementation and setup of Chapter 4, even though optimized for the present-day M_2 tide, realistically depicts OTD for a large variety of partial tides (minor amplitude, degree-3, radiational forcing). Hence, the implementation has proven a certain versatility proposing a realistic representation of ocean tide physics. This characteristic lays the groundwork for investigating O3 in the next chapter, where no geodetic data sets are available to validate the modelling results precisely.

6

Evolution of Global Ocean Tide Levels Since the Last Glacial Maximum

Chapter Abstract

This chapter addresses the evolution of global tidal dynamics since the Last Glacial Maximum focusing on the extraction of tidal levels that are vital for the interpretation of sea level index points. For this purpose, we employ a truly-global barotropic ocean tide mode which considers the non-local (non-sparse) effect of Self-Attraction and Loading. A comparison to a global tide gauge data set for modern conditions yields agreement levels of $65 - 70\%$. As the chosen model is data-unconstrained, and the considered dissipation mechanisms are well understood, it does not have to be re-tuned for altered paleoceanographic conditions. In agreement with prior studies, we find that changes in bathymetry during glaciation and deglaciation do exert critical control over the modelling results with minor impacts by ocean stratification and sea ice friction. Simulations of 4 major partial tides are repeated in time steps of 0.5 to 1 ka and augmented by 4 additional partial tides estimated by linear admittance. These are then used to derive time series from which the tidal levels are determined and provided as a global data set confirming the HOLSEA format. The modelling results indicate a strengthened tidal resonance by M_2, but also by O_1, under glacial conditions. Especially a number of local resonances are identified that impact the tidal levels up to several meters difference. Among other regions, resonant features are predicted for the North Atlantic, the South China Sea, and the Arctic Ocean[1].

[1]The article follows in a modified form (submitted version), where parts of the content are transferred to the Context section. However, the content of the original published article is not modified. Additionally, the nomenclature has been harmonized with the previous chapters.

Published Manuscript (Reproduced with permission from Wiley)
Sulzbach, R., Klemann, V., Knorr, G., *et al.* (2023). Evolution of global ocean tide levels since the Last Glacial Maximum. Paleoceanography and Paleoclimatology, 38, e2022PA004556. https://doi.org/10.1029/2022PA004556

Open research
The modelling data discussed in this paper are published separately (Sulzbach et al., 2022b). We provide tidal levels and the temporal evolution of tidal dissipation as NetCDF files. Further, the individual partial tide solutions for all directly simulated tides are included. They can provide open boundary conditions for regional paleotidal simulations or can be employed to derive other statistical observables of tidal dynamics. The data are provided on the employed rotated-pole grid and supplemented by a routine to project the data to standard longitude-latitude coordinates. Graphics were created with Inkscape (Inkscape Project, 2020). Plots were generated with matplotlib (Hunter, 2007), cartopy (Met Office, 2010 - 2015) and gmt6 (Wessel et al., 2019), while data processing was done applying the software package numpy (Harris et al., 2020). This study used the FES2014 tidal atlas, which was produced by Noveltis, Legos and CLS and distributed by Aviso+ with support from CNES (Lyard et al., 2021).

Author Contributions
R. S., V. K., and H. Do. conceptualized the idea of the research. G. K. and G. L. provided paleotidal stratification data and helped with their implementation into the wave drag scheme. H. Dü. helped analyze and evaluate the paleotidal data set. R.S. carried out the paleotidal simulations and construction of tidal levels and performed the model development, model validation, and data analysis. The first author prepared the plots and figures and drafted the article in collaboration with V. K. and H. Do. All authors provided critical feedback on the manuscript and the creation of this article.

Acknowledgements
The authors acknowledge funding by the German climate modelling project PalMod (FKZ: 01LP1918A) supported by the German Federal Ministry of Education and Research (BMBF) as a Research for Sustainability initiative (FONA) and by the DFG Research Unit 2736 (Grant: TH864/15-1). This work used resources of the Deutsches Klimarechenzentrum (DKRZ) granted by its Scientific Steering Committee (WLA) under project ID 499. We are very thankful for the constructive recommendations by two anonymous reviewers and the editor Matthew Huber that have improved this study.

6.1 Introduction

Global mean sea level (GMSL) has been rising at a speed of 3.25 mm yr^{-1} during the last three decades due to the increased rate of ice loss of the Greenland and Antarctic ice sheets, as well as thermal expansion of the ocean water and glacial mass loss (IPCC, 2022). This observation is fundamentally important for protecting low-elevation coastal areas, which are often densely populated, as the risk of flooding increases with GMSL rise.
The relative sea level (RSL), which measures the observed sea level with respect to the coast, is more complex and depends on many factors, including changes in the GMSL, the Geoid or vertical motion of the Earth's surface, for instance, caused by tectonics, local subsidence or glacial isostatic adjustment (GIA). Changes in the RSL generate the main threat to coastal communities and ecosystems. In addition to RSL variations which typically act over centuries, or even millennia, changes in frequency and probability of extreme sea level events can have profound consequences for human or marine coastal life. Thus, the local sea level variability on short time scales is the second important factor in understanding the development of coastal regions besides the RSL, as well as quantifying its impact. For example, storm surges have a much more significant impact during high astronomical tides (storm tides). As they represent a huge part of the sea-surface variability at diurnal and semidiurnal time-scales, the tidal levels are of high importance to understand the frequency of said extreme events. Similarly, tide levels can change with the rising sea level (*e.g.*, Idier et al., 2017; Schindelegger et al., 2018) or be subjected to long-period cycles of the lunar tides (Ray and Merrifield, 2019; Peng et al., 2019).

6.1.1 Tidal Levels and Sea Level Reconstruction

A further aspect of tidal levels is their relevance for the interpretation of sea-level data like sea-level index points (SLIPs) or terrestrial as marine limiting points. Such geological or archeological samples do not represent the actual sea level height at the time of their deposition but the environmental conditions at which the specific specimen lived or was deposited, or a specific structure was built up. For instance, typical shore facies can be separated into a sequence of different marsh environments like high tidal marsh (MHW [Mean High Water] to HAT [Highest Astronomical Tide]) or low tidal marsh (MLW [Mean Low Water] to MHW). Also, specific coastal sediments like coquina are found only below HAT (Garrett et al., 2020), or beach rock is usually formed between MLW and HAT (Stattegger et al., 2013; Mauz et al., 2015 in Khan et al., 2017). Considering such a catalog of sea-level data types, tidal levels have to be considered to define a mean deviation of an indicator's height with respect to MSL and a corresponding uncertainty due to its specific indicative range (IR) (Hijma et al., 2015). Accordingly, the authors suggested providing estimates of relevant tidal levels together with further information when publishing sea level data in a unified way, and international initiatives usually follow these suggestions. In the so-called HOLSEA format for providing sea level data (Khan et al., 2019), a list of tidal levels is required for correcting the indicative meaning of respective data types: MLWS, MLWN, MLLW, MLW, MTL, MHHW, MHWN, MHWS, HAT[2].

[2]For details see the Workbook instructions at `https://www.holsea.org/archive-your-data`.

Because it is a well-established fact that ocean tidal dynamics have significantly changed with time, the precise knowledge of the present-day tidal regime which relies on empirical observations (*e.g.*, Schrama and Ray, 1994; Cartwright, 1999; Stammer et al., 2014) only brings a limited return when trying to interpret paleo-sea level markers. Data-unconstrained ocean tide models can provide the required data (*e.g.*, Wang et al., 2021), which depend directly on (paleo)oceanographic conditions, changes of GMSL and RSL, tide generating forces, and the configuration of the continental plates.
The latter effects are most important on geological times of 10^6 to 10^8 a and must be considered for deep-time simulations (*e.g.*, Green et al., 2017; Haigh et al., 2020; Davies et al., 2020), where the primary interest usually focuses on tidal dissipation and the evolution of the Earth-Moon-Sun system (*e.g.*, Kagan and Sündermann, 1996; Daher et al., 2021).
On shorter time-scales, the continental configuration can be considered static, particularly on the temporal scale of the repeated glacial cycles during the Pleistocene. During this epoch, tidal dynamics are most considerably influenced by GMSL and RSL, which varied during the last million years globally by more than 100 m (Berends et al., 2021). SLIPs are abundant only after the Last Glacial Maximum (LGM), granting the sea level reconstruction an increased amount of accuracy and allowing comparisons to modelling results. Accordingly, many paleotidal studies target this epoch.

6.1.2 Paleotidal Studies Since the Last Glacial Maximum

With the compilation of global paleo topographies (*e.g.*, Peltier, 1994), *i.e.*, reconstructions of the RSL history since the LGM (*e.g.*, Tushingham and Peltier, 1992), global studies of the respective tidal regime could be conducted (*e.g.*, Thomas and Sündermann, 1999). A common feature of most studies is the strengthening of the North Atlantic M_2 oscillation and, related to this, the semidiurnal tidal dissipation (*e.g.*, Egbert et al., 2004). This can be explained by the reduced sea level, that drastically reduces the extent of shelf areas, which serve as an energy sink by turbulent bottom friction dissipation (*e.g.*, Wilmes and Green, 2014) and enhances tidal resonance (*e.g.*, Green, 2010). The energy dissipation diverts to the deep ocean, where barotropic tidal energy transitions into the internal tide, which ultimately induces diapycnal tidal mixing (*e.g.*, Wunsch, 2003; Green et al., 2009), a process that is important for the general circulation and climate. When considering the increased tidal dissipation under glacial conditions in a climate model, a significant impact, *i.e.*, strengthing, on the Atlantic Meridional Overturning Circulation (AMOC) is proposed by Schmittner et al. (2015) and Wilmes et al. (2019), who report special sensitivity to the poorly constrained position of the Antarctic ice sheet grounding line (*e.g.*, Hillenbrand et al., 2014) in line with Wilmes and Green (2014). Another repeatedly observed feature is the transition of the Arctic M_2 to a megatidal regime (Griffiths and Peltier, 2008, 2009), a possible trigger of Heinrich events (Arbic et al., 2004b; Velay-Vitow et al., 2020).
While the mentioned global studies did not focus on extracting tidal levels, it is, in principle, possible to derive charts of tidal levels from paleotidal simulations, which can be applied to interpret SLIPs. However, reversely, the reconstruction of the sea level history is typically constrained by SLIPs (and present-day geodetic data for GIA rates). GMSL changes during a glacial cycle are on a scale of tens to hundreds of meters (Clark et al.,

2016), while changes in tidal levels are expected only on a few-meter scale. Therefore, the feedback-loop tidal level → sea level reconstruction → tidal level is feeble, and global tidal reconstructions are reckoned as robust (Neill et al., 2010).
While the sea level interpretation bias which arises from ignoring changes of the paleotidal regime is usually the order of a few percent of the sea level change, it is of more relevance in the region surrounding formerly glaciated areas, where land surface uplift and sea level rise can partially compensate each other (Hijma et al., 2015).
Despite the outlined relevance, paleotidal changes are only discussed in a limited number of paleo sea level studies on SLIP-driven sea level reconstructions since the LGM. Horton et al. (2013) recommended combining a regional with a global tidal model when reconstructing paleo-tides and interpolating in time from sufficiently high resolved time-slices, *e.g.*, all 1-ka intervals, as was done in Ward et al. (2016). Such a model combination was motivated by Uehara et al. (2006), who had found a significant increase of MHWS before 10 ka BP (before present) by 25 – 50%, whereas the modification after 8 ka BP was reduced. Nevertheless, the modelling effort is great, and the numerical expense of regional densification likely exceeds that of the considered global model (Griffiths and Hill, 2015). Such a model setup was applied mainly for the North Atlantic: Northwest European shelf seas (Uehara et al., 2006; Ward et al., 2016) and the North Atlantic west coast from the Artic to the Caribbean (Hill et al., 2011). The model of Hill et al. (2011) was applied by Horton et al. (2013) to the US Atlantic Coast, by Khan et al. (2017) to the Caribbean, and by Vacchi et al. (2018) to those sites of the Canadian Atlantic. The model of Ward et al. (2016) was applied, for instance, by Barnett et al. (2020) for the evolution of Scilly Island and by Vasskog et al. (2019) for the Norwegian coast.
Different approximations are considered to estimate regional paleotidal changes to overcome numerical modelling of regional tides. For instance, Cooper et al. (2018) suggested using modern tidal levels in South Africa, where he applied tides of nearby lagoons of similar shape to those reconstructed from paleo shorelines. Hijma and Cohen (2019) considered the evolution of the flood basin in the Rhine-Meuse delta during the Holocene sea level rise by increasing the tidal amplitude as a function of the estimated evolution of the flooded basin. A similar approach was discussed by Uehara and Saito (2019) for Tokyo Bay, where in addition, a numerical tidal model was applied. Another solution is to increase the uncertainties of the considered tidal levels and, accordingly, the indicative range (*e.g.*, Briggs and Tarasov, 2013; Hijma et al., 2015).

6.1.3 Objective and Outline of this Study

In this study, we present a global reconstruction of tidal levels since the LGM (21 ka BP) with a temporal resolution of 0.5 to 1 ka, that allows for tracking the temporal evolution of IRs for each arbitrary coastal location on the globe. To achieve this, we employ a modern, data-unconstrained ocean tide model, which is validated for present-day conditions by geodetic data sets (Sulzbach et al., 2021a). The employed model combines several key characteristics, which have to our knowledge, not yet been considered in combination for paleo studies, (C1) a 'full' (non-local) implementation of the Self-Attraction and Loading effect (SAL), (C2) a 'truly-global' domain (*i.e.*, no open boundaries), (C3) the simulation of 4 major partial tides for each epoch, and (C4) a paleo bathymetry derived from the RTopo-2 bathymetry (Schaffer et al., 2016) and the ICE-7G reconstruction. In addition,

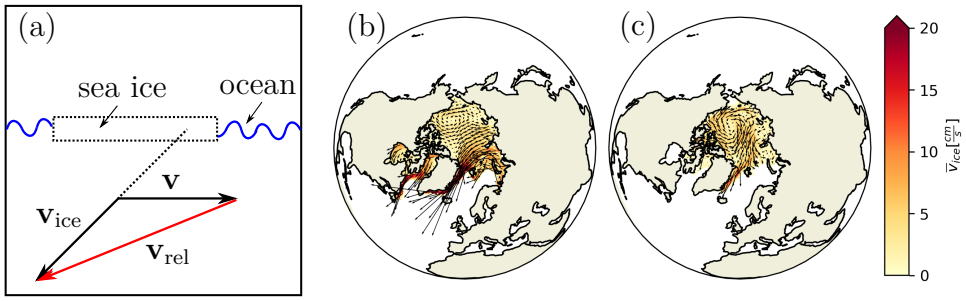

Figure 6.1: Climatological sea ice coverage and ice drift velocity $\mathbf{v}_{\text{ice}}$ (1995-2019) for winter (FMA, b) and summer (ASO, c) conditions, where arrows indicate drift directions. Ice friction is proportional to the relative velocity $\mathbf{v}_{\text{rel}}$ as indicated by (a), containing a purely dissipative part proportional to $-\mathbf{v}$ and a second part proportional to $\mathbf{v}_{\text{ice}}$ that excites a barotropic background circulation.

we found the extraction of tidal levels on a preferably broad data basis by augmenting the tidal ensemble to eight major tides by linear admittance theory (C5). The so-created paleotidal data is used to create time series and rigorously extract a set of 9 tidal levels conforming to the HOLSEA format to interpret SLIPs. As a result, an easy-to-use, global data set of dense temporal resolution is provided. The spatial resolution of $\frac{1}{6}^\circ$ is fit to precisely capture the evolution of large-scale tidal resonances that govern the apparent tidal regime while increased uncertainties remain in extended shelf seas. To further facilitate the derivation of regional paleotidal models, we also provide tidal transports and elevations for selected partial tides, which are necessary to derive realistic boundary conditions for those models. This comprehensive analysis of paleotidal levels is complemented by assessing the global tidal dissipation. This can provide valuable constraints for paleoclimate modelling and corroborates our findings by allowing comparisons to other formerly conducted paleotidal studies.
After this introduction, the chapter is structured as follows: In Section 6.2, we introduce the numerical model, discuss the methods employed to extract the selected observables (tidal levels and dissipation), and validate the model. Afterward, we recapitulate the construction of paleo-oceanographic conditions in Section 6.3, which is the basis for the simulations presented thereupon in Section 6.4. Here, observed tidal resonances are discussed, which are characteristic of individual partial tides and often affect global dissipation. Separately, results for global tidal levels are presented at the center of this study. We close this study with Section 6.5, presenting a summary, conclusions, and an outlook toward possible future research directions.

6.2 Barotropic Ocean Tide Modelling

To obtain estimates of tidal dynamics and tidal levels during the last 21 ka BP, we employ an observational data-unconstrained ocean tidal model that we optimize for the accurate prediction of present-day tides on a global scale. In the following subsections, this model is introduced and discussed with respect to its performance at present-day conditions, the extraction of tidal levels, and tidal dissipation.

6.2.1 Numerical Model

We employ the barotropic ocean tidal model TiME, described by Sulzbach et al. (2021a), which is unconstrained by empirical data (*e.g.*, tide gauge, satellite altimetry, satellite gravimetry). The model is run in a global $\frac{1}{6}^\circ$-grid with numerical poles located in East Asia and South America (*chi*-configuration). The simulation is set up to dissipate energy dominantly by quadratic bottom friction and topographic wave drag (setting W0 of Sulzbach et al. (2021a) with eddy viscosity coefficient $A_h = 2 \times 10^3$ m^2 s^{-1}) dissipation mechanisms, which are theoretically well understood. Thus, this setup also possesses a high degree of reliability in altered (paleo-)oceanographic conditions (Arbic et al., 2008; Egbert et al., 2004).
Within, the model includes wave drag dissipation by a parameterization introduced by Nycander (2005) that is directly inferred from information about ocean stratification and bathymetry. The employed bathymetry H is derived from the RTopo-2 data set (Schaffer et al., 2016). The effect of Self-Attraction and Loading (SAL) that exerts a strong influence on tidal dynamics (Ray, 1998a) is included by spherical harmonic decomposition and load Love numbers (*e.g.*, Schindelegger et al., 2018). In contrast to the local estimation of SAL, $\zeta_{SAL} = \epsilon\zeta$ (Accad and Pekeris, 1978) that relates SAL to local sea surface elevation ζ by a constant ϵ, here the non-local (*i.e.*, global) gravitational interaction of water masses mediated by SAL is considered. The non-approximated, in-line inclusion of SAL in TiME is in contrast to most formerly employed paleotidal models (cf. Section 6.1.2), that with the exception of Hill et al. (2011), employ local approximations, iterative approaches, or completely neglect the effect.
Changes in sea ice and shelf ice cover are prominent features of glacial-interglacial climate variations (*e.g.*, CLIMAP-Project-Members, 1981; Jakobsson et al., 2014; Sejrup et al., 2000; Stein et al., 2017; Tarasov et al., 2012). Therefore, in addition to the TiME model characteristics documented in Sulzbach et al. (2021a), we consider the long-range interaction of the barotropic ocean flow with floating ice, possibly exhibiting a drift velocity $\mathbf{v}_{\text{ice}}$, by introducing the barotropic acceleration (cf. Figure 6.1a)

$$\mathbf{a}_{\text{ice}} = \frac{r_{\text{ice}}\, f_{\text{ice}}}{H} \left|\mathbf{v}_{\text{rel}}\right| \left(\mathbf{v}_{\text{ice}} - \mathbf{v}\right) \tag{6.1}$$

into the numerical model (*e.g.*, Kagan and Sofina, 2009; Müller et al., 2014; Cancet et al., 2016; Bij de Vaate et al., 2021). This acceleration is structurally identical to quadratic bottom friction, where the bottom friction coefficient $r = r_{\text{ice}}$ is retained (doubled bottom friction). However, the relative velocity between ice and ocean flow, $\mathbf{v}_{\text{rel}} = \mathbf{v}_{\text{ice}} - \mathbf{v}$, controls the dynamics and is constrained by the fractional ice cover $0 < f_{\text{ice}}(\mathrm{x}) < 1$, where $\mathrm{x} = (\lambda, \theta)$ denotes the longitude-latitude pair. It is important to note that this parameterization induces two distinct effects. First, a dissipative, dampening effect proportional to $-\mathbf{v}$, similar to bottom friction, and second an acceleration proportional to $\mathbf{v}_{\text{ice}}$, denoted $\boldsymbol{a}_{\text{ice}}$, that will induce a residual, non-periodic circulation. The later considered realizations of $\mathbf{v}_{\text{ice}}$ and f_{ice} are shown in Figure 6.1b and c.
Altogether, TiME integrates the nonlinear shallow-water equations to simulate barotropic ocean dynamics, which are forced with the tide-raising potential (TRP, cf. Sulzbach et al., 2021a, 2022c). Within this study, we only consider the individual excitation of partial tides (frequency ω) as listed in the tide-generating potential (TGP) HW95 (Hartmann and Wenzel, 1994, 1995b), *i.e.*, setting the potential proportional to $\overline{P}_{lm}(\sin\theta)\, \cos(\omega t + m\,\lambda)$, where

$\overline{P}_{lm}$ are the normalized associated Legendre polynomials (partial tide forcing mode). Disregarding minor, nonlinear tides, we extract the harmonic constituents for a partial tide, with label i, the amplitude $|\zeta^i|(\mathbf{x})$ and Greenwich-phase lag $\phi_i(\mathbf{x})$, for the sea surface elevation after an initialization time of at least 1 month, denoted

$$\zeta^i_{\mathrm{mod}}(t) \;=\; |\zeta^i|(\mathbf{x})\,\cos\left(\omega_i t \;-\; \phi_i[\mathbf{x}]\right)\;. \tag{6.2}$$

Comprising the results of this Section, TiME is employed as a transformation operator that translates a certain partial tTRP V^{ilm}_{tid} into the respective ocean tidal response described by $|\zeta^i|(\mathbf{x})$ and $\phi_i(\mathbf{x})$, considering the relevant oceanographic conditions.
With respect to other ocean tide models adapted to paleo conditions, the presented TiME configuration primarily distinguishes itself by the combination of two properties that were not considered together by other studies, which are the implementation of the non-local effect of SAL (C1), and a truly-global grid (C2), that allows the unbiased investigation of Arctic tides (cf. Section 6.1.3). Additional novel features are the implementation of the Nycander wave drag scheme with estimated paleo stratification data and the ice friction effect, which did not considerably impact the study, as we will show. While the model resolution of $\frac{1}{6}^\circ$ is among the higher-resolving models. Several studies employ finer resolutions of $\frac{1}{8}^\circ$ (*e.g.*, Wilmes et al., 2019) and even higher (*e.g.*, Velay-Vitow et al., 2020).

6.2.2 Model Setup and Validation

To validate the model results for present-day tidal conditions, empirical data is employed. In order to further quantify the impact of the newly introduced ice friction parameterization, we consider a set of 3 simulation experiments: no sea ice (*mod*), non-drifting sea ice (*mod-ice*), and drifting sea ice (*mod-ice-v*). Validation of tidal solutions is pursued by employing bottom pressure records (OBP) compiled by Ray (2013) and the data-constrained tidal model FES14 (Lyard et al., 2021) for the main lunar M_2 tide.
We calculate the root-mean-square error (RMS) between TiME and the data sets, where the comparison to FES14 is restricted to a non-polar ($|\mathrm{lat}|< 66^\circ$) open ocean (H>1000 m) domain. For experiment *mod*, an RMS of 6.78 cm (FES14) and 6.05 cm (OBP) is obtained. Compared to the results obtained on a $\frac{1}{12}^\circ$-grid by Sulzbach et al. (2021a), the employment of experiment *mod* leads to an RMS-increase of 2.66 and 1.95 cm, respectively. Similar results are obtained with experiments in *mod-ice* and *mod-ice-v*, hinting at a minor improvement by an RMS reduction on the mm-level. An inter-comparison of the three experiments reveals that the most significant deviations due to sea ice friction arise in the direct vicinity of shallow, ice-covered regions and a smaller impact in the northern mid-latitudes. For a more detailed discussion of the ice effect, we refer to Appendix F.
Evaluating the global dissipation of the M_2 partial tide, we find 2.49 TW[1] for *mod* with only minor changes for the other experiments. Here, the dissipation by ice friction is found to be considerably affected by winter (134 GW) and summer (46 GW) conditions in the Northern Hemisphere (cf. Müller et al., 2014). Figure 6.1 (b, c) show the most prominent differences in seasonal ice coverage, which are found in the Hudson Bay and Hudson Straight, *i.e.*, shallow marginal seas that are known to possess relatively large M_2

[1] 1 TW = 1000 GW = 10^{12} J/s

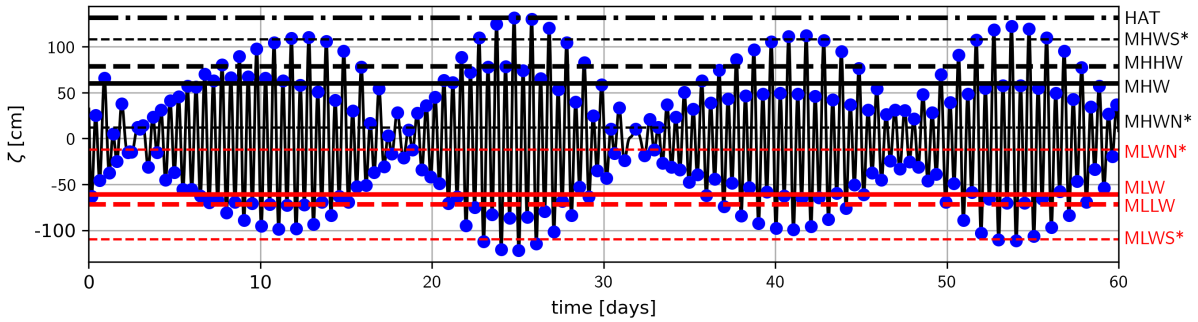

Figure 6.2: Example time series (60 days) and derived tidal levels synthesized of eight major partial tides (black curve) at Gulf Saint Vincent, Australia (35°S, 138.3°E) for present-day conditions. High and low tides (blue points) are used to derive the tidal levels (horizontal lines). As the tidal constituents for S_2 and M_2 have nearly equivalent amplitude, the time series shows a pronounced spring/neap-asymmetry. Spring/neap tide-related parameters derived with the help of $p_{\pm}$ (cf. Equation G.1) appear with an asterisk.

flow amplitudes.
As the sea ice friction, Equation (6.1), is proportional to H^{-1} and $|\mathbf{v}_{\text{rel}}|$, this points to an essential prerequisite for ice friction to impact tidal dynamics: The ice coverage must occur in shallow seas with large tidal flow velocities. On the one hand, the impact of sea ice was relatively small compared to the mean tidal signal for the modern M_2 tide. On the other hand, the extent of shallow shelf seas is known to reduce during the LGM (Wilmes and Green, 2014). Hence, we ignore the effect of sea ice in the presented simulations. However, we will present additional simulations considering exaggeratedly expanded sea ice (polewards of $|45°|$) to estimate the maximum effect of sea ice.
As TiME is barotropic and has been optimized for open ocean dynamics, the validation in this section primarily targeted those areas with a less precise representation of shelf and coastal regions. However, because SLIPs are inherently located in coastal vicinity, we discuss the accuracy of TiME concerning reconstructed coastal tide levels based on tide gauge data in the next section.

6.2.3 Reference Levels for Tidal Heights

Tidal levels like MLLW to HAT introduced in Section 6.1 describe the periodic sea surface variability at a specific location. They are composed of several harmonic constituents with frequencies related to astronomical processes (*e.g.*, Doodson, 1921; Bretagnon, 1982). This temporal harmonic behavior can be described by

$$\zeta_{\text{mod}}(\mathbf{x}, t) \;=\; \sum_{i}^{N} |\zeta^{i}|(\mathbf{x}) \, \cos\left(\chi_i(t) \;-\; \phi_i[\mathbf{x}]\right) \;, \tag{6.3}$$

where $\chi_i(t) = \sum_{j=1}^{6} q_j^i \, D_j^{\text{astro}}(t) + q_7^i \, \frac{\pi}{2}$, is a combination of astronomical arguments $D_j^{\text{astro}}(t)$ multiplied with integers[3] (*i.e.*, related to Doodson numbers) and $q_7^i \, \frac{\pi}{2}$ is the Doodson-Warburg phase shift related to the definition of the TGP (Petit and Luzum, 2010). While an elaborate tidal analysis of the TGP (here HW95, Hartmann and Wenzel, 1994, 1995b) and sea surface dynamics (*e.g.*, Lyard et al., 2021; Piccioni et al., 2019) are typically composed of a large number of constituents, the most significant part of the variability can be captured by considering eight major tidal constituents.

These partial tides, comprising four diurnal (K_1, O_1, P_1, and Q_1) and four semidiurnal (M_2, S_2, N_2, and K_2) constituents, are employed to predict global ocean tidal dynamics for a given epoch. To reduce the computational effort, only two partial tides per tidal band (M_2, K_2, K_1, and O_1) are simulated. The residual four tidal solutions are estimated by assuming the ocean admittance function Z_{lm} to be a linear function of the excitation frequency ω.

This linear admittance approach builds upon the assumption that barotropic ocean tidal dynamics are only weakly nonlinear in ζ and ω (for small $\delta\omega$), a fact that is well-confirmed by observational data for present-day tides (*e.g.*, Munk and Cartwright, 1966; Hart-Davis et al., 2021a; Rieser et al., 2012).

To discuss tidal amplitudes, we follow three approaches. The considered major partial tides are predominantly varied only by integral multiples of the mean lunar time τ (diurnal), the mean lunar longitude s (monthly), and the mean solar longitude h (annually). Solely Q_1 and N_2 are impacted by variations of longer periods (mean longitude of the lunar perigee, 8.85 yr). As they are below the smaller amplitude components of the considered tides, we decided to neglect this long-period variation of Q_1 and N_2 and consider Equation (6.3) for 1000 lunar days (approx. 3 yr), evaluating 65 time steps per lunar day. The astronomical arguments within $\chi_i(t)$ are evaluated employing the development of Simon et al. (1994). The resulting time series (cf. Figure 6.2) is then further processed to derive tidal levels in agreement with the HOLSEA format for MLLW, MLW, MHW, MHHW, and HAT (approach A). Therein, the tidal levels or datums are defined as statistical measures of the high-tide or low-tide variability. MTL was found to be on the order of only a few cm and thus can be assumed to be zero within this approach.

SLIPs are typically found in coastal proximity. Therefore, we validate the accuracy of the derived tidal levels with respect to a set of coastal tide gauges as a proxy for the accuracy of paleotidal levels. For this purpose, we utilize the tide gauge data set TICON (Piccioni et al., 2019) consisting of 1145 tide gauge stations with 40 tidal constituents (amplitude: $|\zeta^i|_{\text{tg}}$; phase: ϕ_i^{tg}) each and derive tidal levels by two means: First, by employing the identical procedure as for TiME (eight major tides, 1000 lunar days: approach B) and second, by considering 29 partial tides of TICON for 7000 lunar days covering multiple cycles of the lunar perigee (29 partial tides, approach C). Only nonlinear and seasonally-modulated tides that are not included in HW95 (M_8, S_4, S_3, MKS, MS_4, R_2, MA_2, and MB_2) and minor, long-period tides (M_{sf}, M_{sq}, M_{tm}) are ignored.

To quantify the mean agreement between two approaches, x and y, we calculate the RMS and normalize it to the mean quadratic amplitude obtained from the second data set, y, thus expressing the mean captured signal fraction $c(x, y) = 1 - \text{RMS}(x, y)/\text{RMS}(0, y)$, which takes values between 100% (perfect agreement) and $-\infty$. We find a high mean agreement for approaches B and C between 92.3% (HAT) and 97.2% (MLLW), indicating

[3] The notation was harmonized with Chapter 2.

that 8 major tides and simulation for 1000 lunar days will be sufficient to predict tidal levels to a high level of accuracy. In the next step, tidal levels are calculated on the rotated TiME grid (*chi*) and are interpolated (nearest-neighbor interpolation) to standard coordinates. Here the coordinate transformation as depicted in Chapter 3 is employed.
Interpolation on the rotated grid is preferred because iit is the most distinct possibility for predicting near-coastal tidal levels. We find a mean captured signal fraction of 70.6% (HAT) and 71.7% (MLLW) between approaches A and B. Recalling the high agreement between approaches B and C, we conclude that the mean agreement between predicted and measured tidal levels is 65–70%, when employing approach A.
The results for approaches A and C are presented in Figure 6.3. The plots generally indicate a close match between TiME and TICON, with larger relative deviations in microtidal marginal seas (*e.g.*, Baltic Sea, Mediterranean Sea, ...) and moderately reduced agreement in extended shelf seas (*e.g.*, European Shelf) in comparison to the deep ocean where the agreement is best. While it was to be expected that a global tidal model with comparably low resolution in coastal areas would exhibit increased deviations with coastal tide gauges, the apparent level of 70% is still relatively high. In addition, we will focus on the evolution of temporal model differences, *e.g.*, differences of tidal levels between two epochs, that are likely to partially absorb systematic model deviations.
To enlarge the procured set of tidal levels, we further estimate the parameters MLWN, MLWS, MHWN, and MHWS. To achieve this, MLW and MHW are multiplied with a factor $p_{\pm}$ based on the tidal amplitudes of the two largest tides per tidal band (M_2 and S_2 vs. K_1 and O_1) that are the main drivers for spring/neap-cycles (cf. Appendix G). Please note that those parameters exhibit an increased uncertainty due to the qualitative nature of this approach but integrate reasonably into the set of directly derived parameters. For example, Figure 6.2 shows a synthetic 60-day time series from Gulf Saint Vincent. Due to comparably strong S_2 and M_2 constituents, this location is known to exhibit a pronounced spring/neap tide cycle, locally known as *dodge tide*, which is reasonably well predicted by employing $p_{\pm}$.
The employed extraction scheme for tidal levels features two key elements which were not considered in prior paleotidal studies (cf. Section 6.1.3). First, the continuous simulation of four partial tides per epoch (C3) and the linear admittance constrained augmentation to eight partial tides with the proper extraction of tidal levels conforming to the HOLSEA format (C5).

6.2.4 Ocean Tide Dissipation

Tides mediate energy transfer in the Earth–Moon–Sun system by frictional processes controlling, *e.g.*, the evolution of the lunar orbit (Mignard, 1979; Kagan and Sündermann, 1996; Ray et al., 2001; Green et al., 2017; Daher et al., 2021). Within, the predominant part of ocean tidal dissipation is carried out through turbulent bottom friction on the continental shelves and the excitation of internal waves in the deep ocean (Egbert and Ray, 2000; Nycander, 2005). For example, the main lunar ocean tide M_2 dissipates 2.45 TW, of which about 1 TW can be attributed to the generation of internal waves in the deep ocean (Egbert and Ray, 2001). As internal waves ultimately dissipate their energy by breaking into turbulent mixing (St. Laurent et al., 2002), they can influence baroclinic processes as the MOC, thus ultimately linking the tidal regime of a particular epoch to

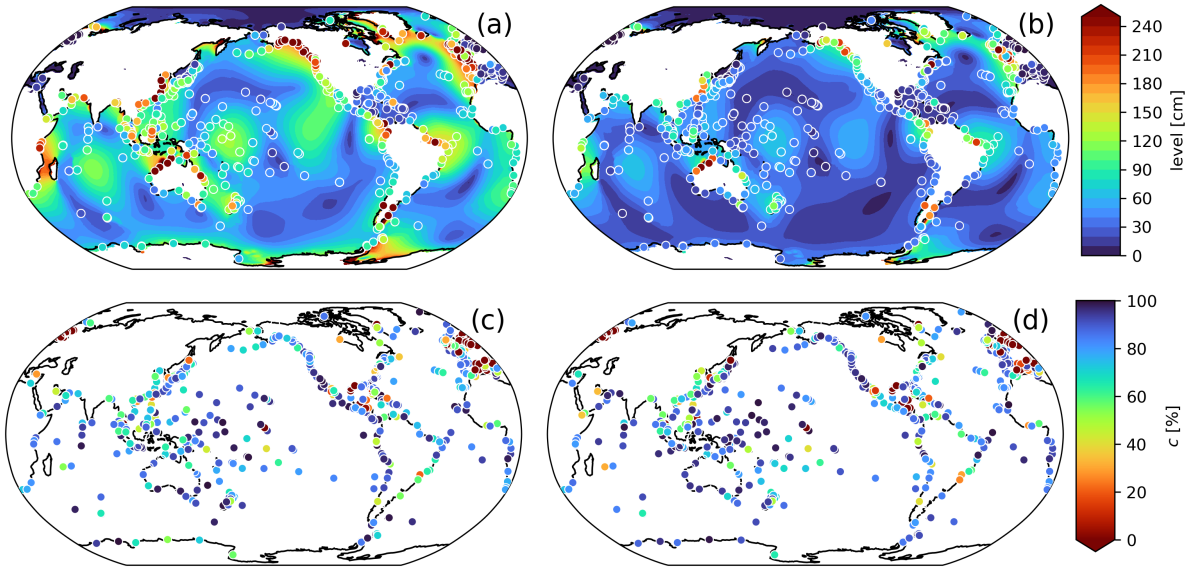

Figure 6.3: Tidal levels as derived from TiME (approach A, global field) and TICON (approach C, circles) in cm, exemplary for HAT (a) and MHW (b), and respective agreement c in % at tide gauge stations (c, d).

its climate (Müller et al., 2010; Schmittner et al., 2015; Wilmes et al., 2019).
Therefore, predicting and monitoring tidal dissipation can provide boundary conditions for paleo-climate reconstructions and the evolution of the lunar orbit. Furthermore, it can serve as an additional benchmark for validating present-day tidal models with observations of tidal dissipation. Thus, tidal dissipation was selected as an additional model output in addition to the tidal levels discussed in the previous section.
Assuming linear admittance, the global dissipation of tides of identical degree (here $l = 2$) and order (here $m = 1, 2$) follows the equation

$$\overline{D}_i \;=\; (\alpha_2^{\mathrm{b}}(\omega_i)\, A_i)^2\, (c_{2m}^0 \;+\; c_{2m}^1\, \omega_i)\;, \tag{6.4}$$

where A_i is the amplitude of the TGP, α_2^{b} is a combination of body tide Love numbers and c_{2m}^i are constants stemming from global integrals of $\mathbf{v}_i$ and $\boldsymbol{\nabla} Y_{2m}$ (cf. Appendix H). As two partial tides per tidal band m are simulated, the c_{2m}^i can be extracted, thus allowing the exploitation of Equation (6.4) to estimate dissipation by additional partial tides.
Tidal sea surface height variations estimated by linear admittance are proportional to A_i. In contrast, Equation (6.4) is proportional to A_i^2. Thus tidal dissipation concentrates on the highest amplitude tides diminishing quickly for minor tides. Attention has to be paid when employing this approach, as dissipation estimates can change the sign for far-extrapolated tides. This nonphysical behavior should be discarded as an artifact of the linear admittance approach, but it did not occur in our simulations.
Applying this approach to modern-day tidal dynamics, we obtain a total dissipation by the considered major tides of 3682 GW (partitioning as M_2: 2494 GW, S_2: 481 GW, K_1: 334 GW, O_1: 199 GW, N_2: 97 GW, K_2: 35 GW, P_1: 34 GW and Q_1: 8 GW). These results match the reference values for Earth–Moon–Sun dissipation (3.7 TW) and pure

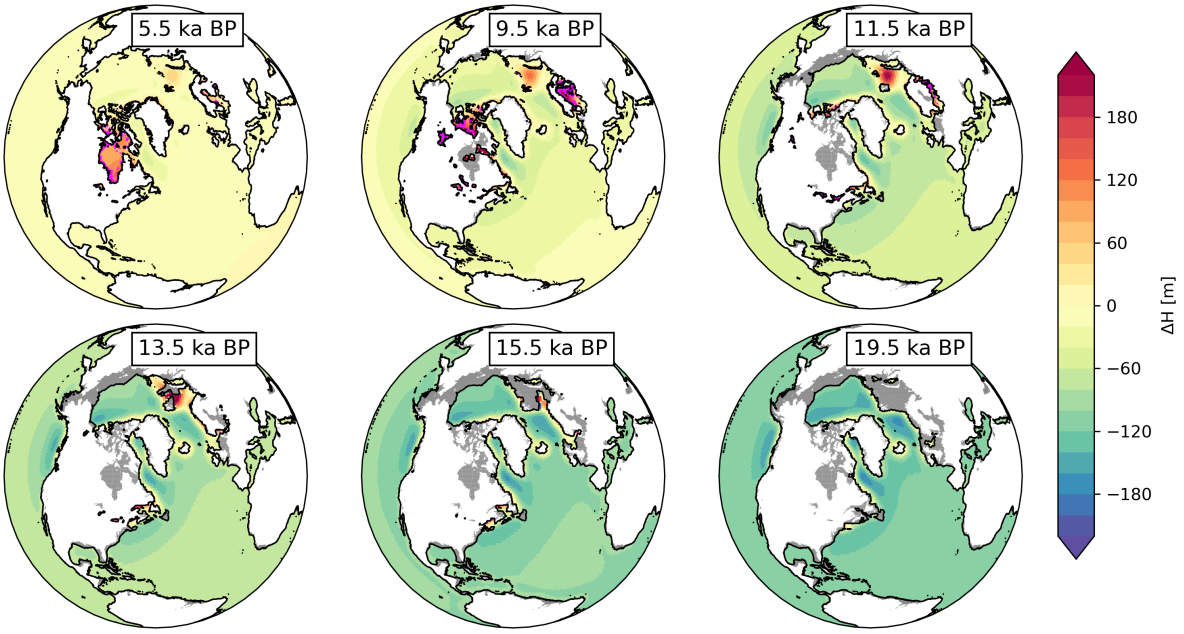

Figure 6.4: Relative depth change with respect to the present-day bathymetric map (0 ka BP) in meter. Coastlines are drawn as for the respective epoch, with increased land area in gray and flooded grid cells in magenta (Hudson Bay, Baltic Sea). As the topography considers ice sheets, areas of Northern Canada, Barents Sea and Baltic Sea appear gray due to ice cover.

M_2 dissipation of 2.45 TW (Egbert and Ray, 2001). The dissipation is dominated by M_2 to O_1, with only minor contributions by N_2 to Q_1.
Employing the presented linear admittance approach, it is possible to estimate the temporal evolution of the global tidal dissipation by all eight major tides, not only K_1 and M_2, that dominate the dissipation spectrum.

6.3 Paleotidal Conditions

In this section, we discuss changes of the paleoceanographic conditions which impact the tidal regime mapped by the ocean tide model introduced in the last section. While changes in the Coriolis parameter, the TRP, and the surface gravity are negligibly small in the time span of interest, we focus on changes in non-astronomical factors that are known to be relevant on the discussed time scale from prior studies (*e.g.*, Wilmes and Green, 2014; Haigh et al., 2020; Daher et al., 2021).
Changes of the paleoclimate are expected to impact the quantity and distribution of sea and shelf ice. As floating ice masses interact with the mean tidal flow via frictional forces, these changes can, in principle, affect the paleotidal dynamics. Due to the reasons discussed in Section 6.2.2 we ignore the effect of sea ice friction and restrain ourselves to evaluating a number of estimates by considering extreme ice coverage for certain time slices (7.5, 10, 12.5, 15, 17.5 ka BP).
Secondly, the changed climatic conditions impact the stratification of the ocean and,

therefore, the coupling between the here studied barotropic ocean tides and their baroclinic counterparts (internal tides) that can be parameterized as topographic wave drag (*e.g.*, Bell, 1975; Llewellyn Smith and Young, 2003; Nycander, 2005).
Estimates of the ocean stratification were obtained from three different climate simulations using the fully coupled Earth system model (COSMOS) (Jungclaus et al., 2010) for pre-industrial, LGM, and deglacial conditions. The corresponding climate states for pre-industrial and the LGM (21 ka BP) are experiments PI and LGMW from (Zhang et al., 2013). The deglacial state is representative of conditions at 16 ka BP at a time of substantial ice sheet disintegration and associated meltwater flux to the North Atlantic, which has been simulated as experiment 16_0.21 (Sun et al., 2022). For technical details of the model components, model configuration, and experimental setup, we would like to refer to these base studies (Zhang et al., 2013; Sun et al., 2022) and references therein.
Employing these data sets, we constructed topographic wave drag tensors (Nycander, 2005) for diurnal and semidiurnal tidal species for four different epochs: First, we assume modern conditions as described in Sulzbach et al. (2021a) utilized for times slices 0 to 0.5 ka BP (regime *I*). Further, preindustrial conditions for time slices 0.5 to 7.5 ka BP (regime *II*), Heinrich-stadial conditions before the Bølling/Allarød (B/A) for time slices 7.5 ka BP to 18.5 ka BP (regime *III*), and LGM conditions from 18.5 to 21 ka BP (regime *IV*) were employed. Already anticipating the results of the following section, we found the impact of the changed wave drag dissipation to be of minor importance. Admittedly, the impact of the altered ocean stratification on the vertical current profile and, connected to this, the tidal ocean bottom friction was not considered in this study, while this effect is known to impact the seasonal variations of M_2 (Müller et al., 2014; Howarth, 1998). The quantification of this effect would be an intriguing application of a global, baroclinic paleo-ocean tidal model and is thus out of the scope of this study.
The most considerable influence on ocean tides is known to originate from changes in the bathymetric conditions triggered by glaciation and deglaciation processes (*e.g.*, Thomas and Sündermann, 1999; Griffiths and Peltier, 2008; Velay-Vitow et al., 2020). These bathymetric changes, implicitly including progressing and receding shorelines, directly impact the barotropic resonance conditions that can be elegantly described by a set of ocean normal modes (*e.g.*, Müller, 2007). Reconstructing the sea level history is complicated, as it is not sufficient to know the amount of water bound in ice sheets, *i.e.*, the GMSL. Additionally, the local sea level is impacted by changes in the Earth's shape, the geoid, which is again controlled by mass redistribution in the ocean, glaciers, and the solid Earth. These changes depend on quantities like the mantle viscosity, the insolation, and the resulting global ice history that exhibit large uncertainties but control the effect of GIA (*e.g.*, Abe-Ouchi et al., 2013).
Modern geodetic techniques such as GNSS or satellite gravimetry set precise, large-scale constraints for uplift rates due to GIA and, therefore, effectively reduce the uncertainty of the respective reconstruction. In this study, we rely on the reconstruction ICE-7G_NA that considers a comprehensive amount of said constraining data on the North American continent (Roy and Peltier, 2015, and references therein). Even though no constraining data was used in this area, Roy and Peltier (2018) showed that the obtained sea level reconstruction agrees well with SLIPs in the Mediterranean and also certain far-field areas.
To obtain high-resolution bathymetric maps, we employ the data set RTopo-2 (Schaffer et al., 2016) to derive a bathymetric map for modern conditions as described in Sulzbach

et al. (2021a), *i.e.*, containing sub-ice shelf cavities as free water column. Paleo bathymetries are obtained by modifying these high-resolution data sets by the topographic and bathymetric differences from ICE-7G_NA. As a result, a set of high-resolution bathymetries is obtained for individual time slices (cf. Figure 6.4). Due to changes in the Geoid, the sea level might rise locally. Therefore, it is important to also allow apparent sea level rise when calculating paleobathymetries, which is considered here. This phenomenon is most notable in the Baltic Sea and Hudson Bay. While this study is not focused on estimating the impact of different paleo reconstructions as, *e.g.*, Wilmes and Green (2014) and Wilmes et al. (2019), the combination of ICE-7G and RTopo-2 has to our knowledge not been considered, yet. We will focus on comparing the obtained dissipation rates to results obtained by others.
To conclude this discussion, it is important to mention that uncertainties in the Antarctic grounding line are not considered within this study. Nonetheless, we acknowledge that this effect could considerably impact the obtained tidal levels, also on the Northern Hemisphere, and therefore represents a source of uncertainty within this study (Wilmes and Green, 2014; Wilmes et al., 2019).

6.4 Paleo Ocean Tidal Dynamics

In this section, we discuss the results of the paleo tide simulations. First, we focus on changes in the partial tide oscillation systems and the accompanying shifts in tidal dissipation. Afterward, consequences for tidal levels are discussed, focusing on a number of exemplary regions that exhibit the most notable changes in tidal levels. Basin masks are obtained from the World Ocean Atlas 2009[3] (Levitus, 2009), with the mask for Hudson Bay adjusted for the increased sea level.

6.4.1 Tidal Resonances and Dissipation

The following discussion relates to the tidal dissipation displayed in Figure 6.5. Please also consider changes in tidal amplitudes in Figures I.1 to I.8 in the Appendix. Going backward in time, we first note that changes in tidal dissipation are relatively small until approximately 9 ka BP, where the shelf area fraction begins to decrease, which is in line with the findings of Wilmes and Green (2014). A notable variation in this period is the slightly augmented M_2 resonance in the Hudson Straight and Hudson Bay that peaks at 4.5 ka BP and later at 8 ka BP. The reason for this is the locally-increased sea level with respect to the present-day sea level (*e.g.*, Simon et al., 2014), which improves the coupling between shelf sea and open ocean. Thereby it induces a slight decrease in dissipation and a drop on the North Atlantic M_2 amplitude (Uehara et al., 2006), and can be understood in terms of a coupled oscillator model (Arbic et al., 2009). The feedback of the improved shelf resonance on the open ocean is significant as the dominant semidiurnal eigenmode of this region is known to be near resonant to the M_2 frequency (Arbic et al., 2007).
The most pronounced change in the global M_2 resonance is also related to this region. Mainly due to the blocking of the Hudson Straight and the global sea level drop, the North Atlantic M_2 amplitude is strongly amplified at 10 ka BP and earlier (Wilmes and Green,

[3] `ftp://ftp-oceans.ncei.noaa.gov/www/sites/woa.data.nodc/WOA09/MASKS/basin.msk`

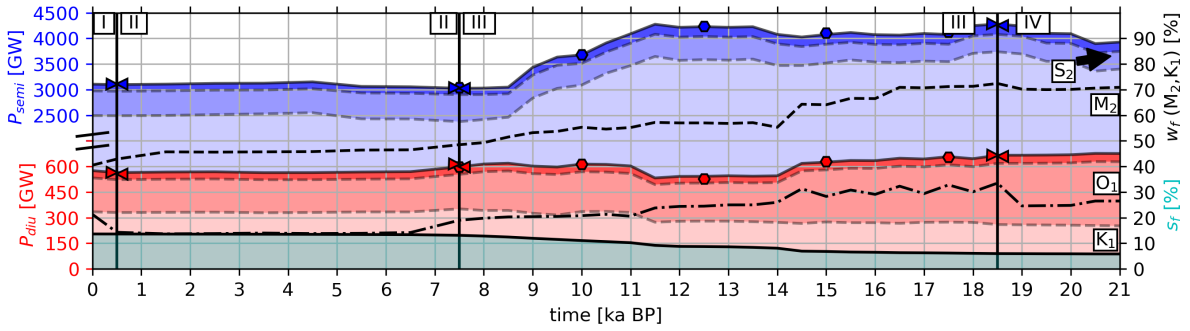

Figure 6.5: Cumulative tidal dissipation during the last 21 ka for semidiurnal tides (blue) and diurnal tides (red), where the individual shadings represent the dissipation by M_2, S_2, $N_2 + K_2$ and K_1, O_2, $P_1 + Q_1$, respectively. Dissipation for diurnal and semidiurnal tidal species is presented on different scales. Further, the dissipation fraction by wave drag, w_f, for M_2 and K_1 (black, dashed/dashed-dotted), and the shelf-area fraction, s_f (cyan-shaded) are superimposed. Additionally, the regimes *I* to *IV* that mark the change in stratification parameters employed for performing tidal simulations are overlaid (▷/◁: solutions in two neighboring regimes). The ⬣-markers present solutions obtained by employing an extreme ice cover polewards of $|45|°$.

2014; Haigh et al., 2020). The M_2 dissipation reaches a level of around 3.4–3.6 TW persisting approximately from 10.5 ka BP to the LGM. While the large-scale North Atlantic amphidromic system is responsible for the prominent increase in M_2 dissipation by 1 TW, several more localized resonances are observed, of which the transition of the Arctic tidal regime from microtidal to megatidal between 11.5 and 15.5 ka BP is the most prominent. The described changes also map to increased tidal levels, *e.g.*, HAT, which are displayed in Figs. 6.6, 6.7, and 6.8.

We further compare the predicted deep ocean dissipation under glacial conditions of this study (Ti23) to the findings of several recent studies, namely Wilmes and Green (2014); Wilmes et al. (2019), denoted W14 and W19, Velay-Vitow et al. (2020), denoted VV20, and Griffiths and Peltier (2008, 2009), denoted GP09. All studies predict a general increase in tidal dissipation, which is most prominent for M_2, and shifted towards dissipation by internal tide generation, *i.e.*, wave drag, which carries out approximately $60 - 70\%$ of the dissipation. Ti23 predicts enhancement of wave drag dissipation by a factor of 2.4 (W19: $1.8 - 3$; W14: $3 - 3.5$; VV20: 1.4; GP09: 2.4). W19 computes the indicated range from variations of the Antarctic grounding line position, where paleo bathymetries derived from ICE5G and ICE6G result in a dissipation difference of 0.9 TW. The predictions of Ti23 appear amid this estimate (similar to GP09). However, Ti23 and GP09 consider the Arctic resonance ('Arctic Megatide', cf. the following section), which was computationally hampered in W19 and W14. It is reasonable to assume that the Arctic resonance enhances Atlantic deep ocean dissipation and would presumably increase the dissipation estimates of W19. Thus, the dissipation estimates in this study would be closer to the lower boundary predicted by W19, obtained with ICE-6G.

The dissipation by diurnal tides changes only slightly but continuously with time. Even more, a weakly negative trend in the K_1 dissipation, also predicted by W14, VV20, and

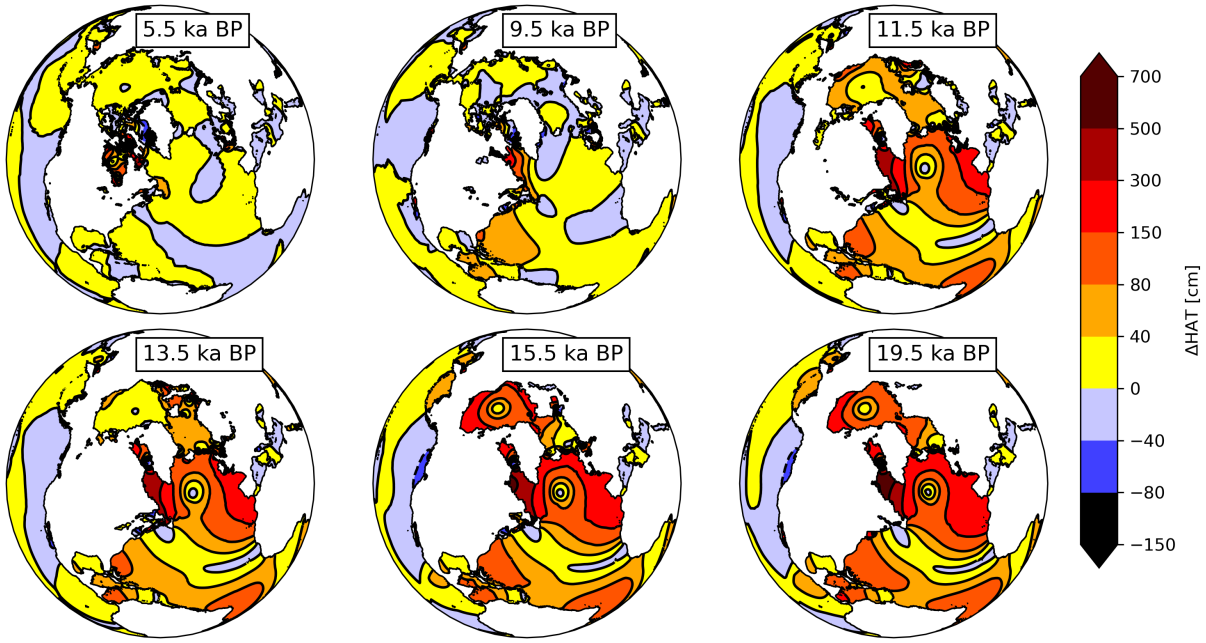

Figure 6.6: Relative change of the HAT with respect to the present-day tidal range (0 ka BP) for selected time slices in cm. Regions of interest include the Atlantic Ocean, the Arctic Ocean, and the Caribbean Sea.

GP09, is overcompensated by a positive trend in the O_1 dissipation rate towards the LGM even though the tide-generating forces for O_1 are approximately 30 % weaker than for K_1. Similar to this, VV20 finds an overall increase in the global and deep ocean dissipation of O_1 (+25%), but to a smaller extent than Ti23 (+250%). In contrast to W14 and VV20, which estimate the glacial deep ocean dissipation fraction by diurnal tides to approximately $40 - 60\%$, Ti23 only predicts approximately 30% related to different parameterizations of topographic wave drag. O_1 becomes the most effective contributor to diurnal dissipation during the LGM, increasing the overall diurnal dissipation from 575 GW at present-day to 675 GW under LGM conditions. This large-scale O_1 resonance in the Pacific Ocean is accompanied by several shelf resonances, most notably in the South China Sea (cf. Figa 6.9).

The generally increased deep ocean dissipation is ultimately a consequence of the decreasing shelf sea fraction s_f to values around 8%, resulting in the blocking of the Hudson Straight and drying-out of the Siberian shelf and large parts of the European shelf. This development removes these areas as energy sinks by turbulent bottom friction. Additionally, the emergence of the described shelf resonances, *e.g.*, in Hudson Bay, can have implications for global ocean dissipation. As shelf resonances tend to decrease the ocean tide amplitude in the coupled deep ocean, especially if they exhibit only weak frictive forces (Arbic et al., 2008; Arbic and Garrett, 2010). Thus, they can decrease the amount of energy dissipated by internal waves in the nearby deep ocean. This might be different for the Arctic resonance, which takes place in the deep ocean, altering the Atlantic Ocean's resonance conditions as a whole.

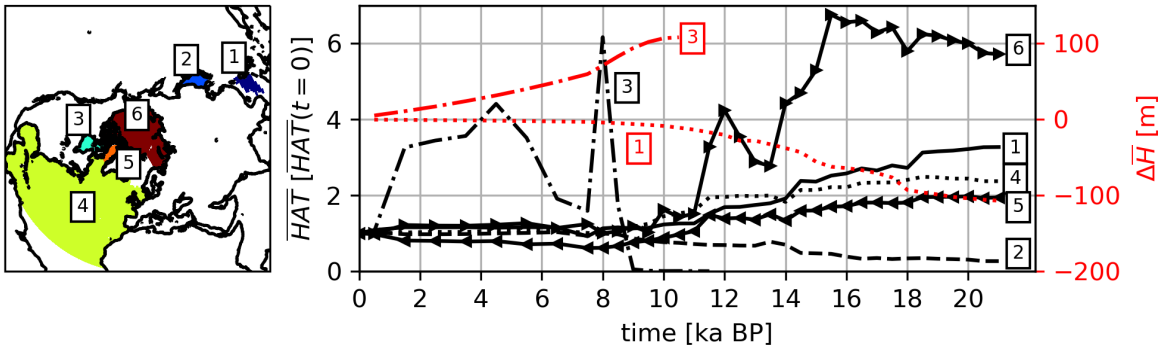

Figure 6.7: Development of the spatially averaged Highest Astronomical Tide, $\overline{\text{HAT}}$, with respect to the present-day value, $\overline{\text{HAT}}$(t=0 ka BP) for several regions: South China Sea (1), Sea of Japan (2), Hudson Bay (3), North Atlantic (4), Baffin Bay (5) and the Arctic Ocean (6). The development of the mean depth $\overline{H}$ with respect to its modern value for 1 + 3 is shown, denoted $\Delta\overline{H}$. Please note that this value is not identical to $\overline{\Delta H}$, which is larger in Hudson Bay due to the variable shoreline.

We performed additional simulations to quantify the impact of an exuberant sea ice cover (polewards of $|45|^\circ$) and report a minor impact on the observed dissipation pattern. We follow the reasoning that a decreased shelf area fraction s_f minimizes the dissipation by turbulent bottom friction, which also applies to turbulent ice friction (*i.e.*, doubled bottom friction). Both effects can only represent an efficient energy sink in shallow shelf areas with large barotropic current velocities, which are very sparse under glacial conditions (cf. Figure 6.8).
As the ocean stratification was changed between regimes *I* to *IV*, simulations at regime boundaries (0.5, 7.5, 18.5 ka BP) are repeated with wave drag tensors based on both regimes to quantify the impact of the ocean stratification on the simulation outcome. Figure 6.5 shows that, while w_f can be affected by this parameter, the overall dissipation remains almost constant. In line with the results of Griffiths and Peltier (2009), this finding suggests that stratification changes are significant for baroclinic processes while the here discussed global barotropic tidal dynamics are pretty robust to changes in this parameter: Critical transitions of the tidal regime are triggered by bathymetric changes and the resulting resonance conditions and to a far smaller extent by wave drag or sea ice friction.

6.4.2 Tidal Levels

The following discussion relates to Figs. 6.6, 6.7, 6.8, and 6.9 and exemplary focuses on the temporal evolution of the Highest Astronomical Tide, HAT. Changes in other tidal levels are found to be similar in character and are therefore not presented in detail. Please also consider Figures I.1 to I.8 in the Appendix.
In line with the results of prior paleotidal studies (*e.g.*, Thomas and Sündermann, 1999; Egbert et al., 2004; Wilmes and Green, 2014), we find that the most significant global-scale change of the tidal levels is driven by the North Atlantic M_2 resonance discussed

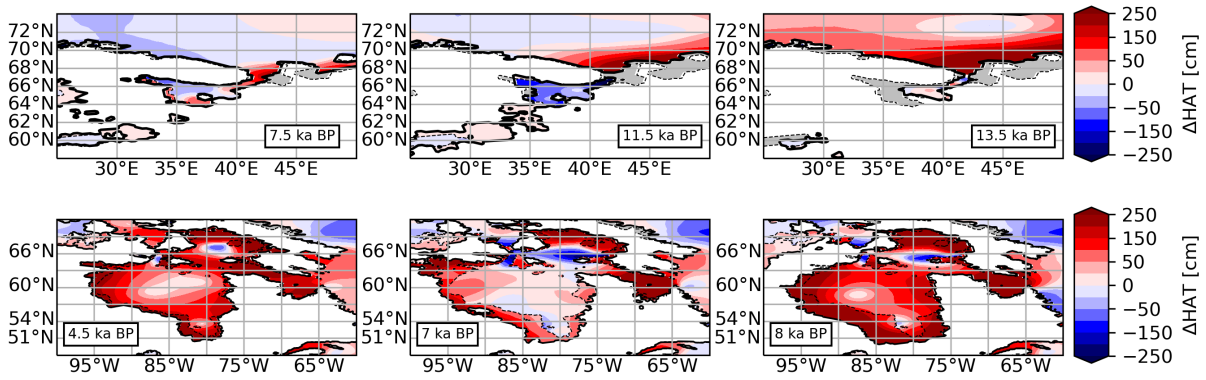

Figure 6.8: Changes in HAT for selected time slices for the White Sea (top) and Hudson Bay (bottom) with respect to present-day conditions. Changes in the coastline are indicated by the dashed (present-day) and solid (past) lines, with differences of the land mask in gray shading.

in the previous section, which is related to blocking of Hudson Straight (Arbic et al., 2004a; Uehara et al., 2006). Setting in around 10 ka BP and before, the absolute value of the tidal levels strongly increases in most coastal regions of the North Atlantic. The increase is non-uniform, with hot spots reaching over +700 cm (*e.g.*, Baffin Bay) and regions where even a slight decrease can be reported (*e.g.*, the zone from Newfoundland to the Cap Verde). Marginal seas are affected in different ways. While tidal amplitudes in the Mediterranean and the Baltic Sea remain small, prominent increases are observed for the Caribbean Sea up to +200 cm under LGM conditions (cf. Figure 6.9, bottom) and Hudson Bay (cf. Figure 6.8, bottom), where tidal levels peak at 4.5 and 8 ka BP due to an increased sea level before falling dry at $9 - 10$ ka BP. On the other hand, K_1 exhibits similar global resonance characteristics under present-day and glacial conditions, except for an increased amplitude around Antarctica that is counterbalanced by a slight decrease of tidal amplitudes in other oceans (cf. Figure I.4), as reported by other studies (*e.g.*, Griffiths and Peltier, 2009; Wilmes and Green, 2014). Accompanying the increase of global O_1 dissipation (cf. Figure 6.5) we report increases in global O_1 amplitudes, especially in the Pacific Ocean, with even larger impacts on tidal levels in Pacific marginal seas (cf. Figure I.2). While the S_2 amplitudes increase in the North Atlantic, similar to M_2, a reduction in the Pacific Ocean is predicted, which is the main driver of the HAT reduction on the North American West Coast under glacial conditions.

Another intriguing development is proposed for the White Sea (cf. Figure 6.8, top). The reduced sea level promotes the isolation of the respective basin between 9 and 13 ka BP, which causes HAT to drop close to zero. At the same time, the level at the nearby Barents Sea is elevated by over +350 cm. Interestingly this isolation only appears for the most recent bathymetry RTopo-2, whereas ETOPO5 or ETOPO2 (*e.g.*, Amante and Eakins, 2009) show a deep channel on the western flank of the outlet, excluding isolation.

The most remarkable change is predicted for the Arctic Ocean. While the present-day tidal regime can be described as microtidal, several studies predict the transition to a megatidal regime under glacial conditions (Griffiths and Peltier, 2008, 2009; Velay-Vitow

et al., 2020; Velay-Vitow and Peltier, 2020). While some tidal models employed for studying paleo-tides exclude a fully-unconstrained development of Arctic tides (*e.g.*, Egbert et al., 2004), the rotated-pole numerical grid of TiME is suited for studies of this region. In agreement with the findings of Velay-Vitow and Peltier (2020), a strong increase in tidal levels, mainly driven by the M_2 and N_2 tide (cf. Figure I.5 to I.8), is predicted between the B/A and LGM. On the other hand, the predicted Arctic M_2 amplitude increase within this study is approximately 30% smaller than reported by VV20. This difference originates from the representation of SAL, which was parameterized as $\zeta_{SAL} = 0.085\zeta$ by VV20, as we report an equivalent increase in the Arctic M_2 amplitude when considering the same ϵ-implementation. This finding suggests a high sensitivity of the Arctic tide to the implementation of SAL and recommends this area for further study.
Further, changes in tidal levels in other world regions are predicted. The most substantial increases in HAT are found in several semi-enclosed basins developing around the Indonesian Archipelago with falling sea levels (cf. Figure 6.9, top). The simulations predict a HAT increase in the South China Sea by up to +250 cm, which is caused by K_1 and even more by O_1, in line with the findings of Griffiths and Peltier (2009) and Uehara et al. (2006). On the other hand, the resonances in the Banda and the Coral Sea are caused and dominated by the semidiurnal M_2 tide. Other basins experiencing changes to a smaller extent are, *e.g.*, the Patagonian shelf and the seas around New Zealand (not shown), as well as the Caribbean Sea (cf. Figure 6.9, bottom). The latter was investigated by Hill et al. (2011), who found tidal levels to rise from 7 ka BP up to a factor of approximately 2 at 10 ka BP, with respect to present-day conditions which agrees with this study. Further, they describe a local maximum at 9 ka BP (up to a factor of 3), which was not reproduced by TiME. The presented results can also be compared to the study by Ward et al. (2016), who investigated the European Shelf region, showing a good qualitative agreement. *E.g.*, both studies predict an increased M_2 amplitude up to 400 cm at the coast of Brittany under glacial conditions, with a reduced amplitude of only 100 cm maximum South of Ireland and in the Irish Sea (cf. Figure 6.9).
A notable special case is the Sea of Japan (cf. Figure 6.7). While this sea is microtidal under present-day conditions, the glacially-induced GMSL drop isolates it even stronger from the deep ocean, leading to a considerable drop in the tidal levels. As previously mentioned, a larger source of uncertainty remains the position of the Antarctic grounding line. Therefore, the predicted increases in HAT in the Weddell Sea of up to +200 cm should be considered cautiously.

6.5 Conclusions

In this study, we have applied the barotropic ocean model TiME (Sulzbach et al., 2021a) to paleo-topographic conditions from the Last Glacial Maximum to the present time. To investigate the impact of temporal changes in the ocean state on tidal dynamics, we discussed deviations in ocean stratification, sea-ice dynamics, and the geometry of ocean basins, *i.e.*, changes in bathymetry and shoreline position. We identified paleo bathymetry being the dominant factor, whereas ocean stratification and sea ice only marginally impact tidal amplitudes (*e.g.*, Griffiths and Peltier, 2009).
We also show that at a moderately high global resolution of $\frac{1}{6}^\circ$ (about 18.5 km), the tidal model agrees on a high level with present-day tide gauge data. As TiME is a

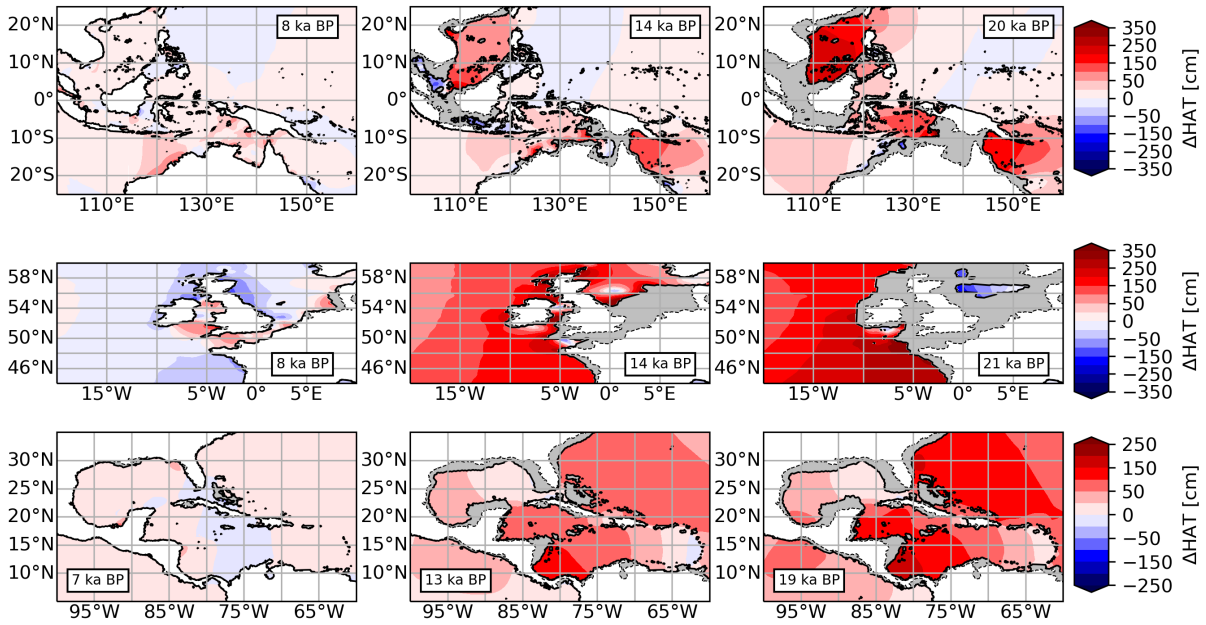

Figure 6.9: Changes in HAT for selected time slices for the Indonesian Archipelago (top) and Caribbean Sea (bottom). Changes in the coastline are indicated by the dashed (present-day) and solid (past) lines, with differences of the land mask in gray shading.

data-unconstrained model, it can be applied directly to paleo topographies and allows the reconstruction of paleotidal dynamics consistently. Furthermore, in TiME the spatial coordinate system can be rotated, allowing adjustment of the setup to a specific region of interest. In this study, the configuration was chosen so that the North Atlantic and the Arctic Ocean were located in the center of the numerical domain. Here, the aspect ratio of the grid cells only varies slightly[4]. Similar setups are possible for other regions of interest, *e.g.*, East Asia. In addition to this truly-global domain, comparable to Griffiths and Peltier (2008) and Velay-Vitow et al. (2020), TiME considers the non-local effect of SAL. This effect was formerly solitarily implemented in the global paleo model of Hill et al. (2011), with a much coarser resolution of approximately $\frac{1}{2}^\circ$. Additional technical novelties in paleo-ocean tide modelling are the wave drag scheme of Nycander (2005) and ice friction, with a minor impact on the simulation results.

Applying it to paleo topographies derived from ICE7G and the present-day RTopo-2 bathymetry, a combination that has not been investigated before, we model tidal amplitude changes of the main partial tides and also derive tidal levels which are of importance for the interpretation of sea level data like SLIPs. Here, we employ a novel approach that is based on simulating four partial tides and augmenting the results with 4 additional tides utilizing linear admittance theory and the extraction of tidal levels in the HOLSEA format from constructed time series. The constructed data set is thus explicitly designed to be a handy tool for paleo-sea level science.

The sea level was much lower during the Pleistocene. Accordingly, the tidal levels are

[4]cf. Figure 3.3 in Chapter 3.

expected to be larger due to less flooded continental shelves where the shallow waters serve as an efficient damping mechanism for ocean tide amplitudes, which prior paleotidal studies have repeatedly reported. Hence, in agreement to the findings of Egbert et al. (2004); Griffiths and Peltier (2009); Wilmes et al. (2019); Velay-Vitow et al. (2020), the simulations predict a strong increase in semidiurnal deep ocean dissipation by internal tide generation. The here-reported dissipation rates are within the span of former predictions. As especially M_2 is very sensitive to minor changes in the Antarctic paleo bathymetry (Wilmes and Green, 2014; Wilmes et al., 2019), the provided dissipation rates are afflicted with considerable uncertainty, which also maps to the tidal levels to a restricted degree, *i.e.*, tidal levels on the Northern Hemisphere are more robust than close to Antarctica. Nonetheless, the provided data set allows us to reconstruct the temporal development of the deep ocean dissipation, which can be used to constrain paleo climate simulations (*e.g.*, Green et al., 2009; Schmittner et al., 2015; Wilmes et al., 2019). A formerly not-discussed change is related to the O_1 tide, which is shifted towards a resonant state and becomes the main diurnal dissipator under glacial conditions.

Comparison to prior studies shows convincing qualitative agreement in most cases (Section 6.4.2). Yet, deviations from prior studies are found in some cases (*e.g.*, North American East Coast, Arctic tides). An interesting open question remains about the back action of the Arctic M_2 resonance on the abyssal dissipation in the North Atlantic with impacts on ocean mixing and general circulation. While this study proposes a minor magnitude of this effect compared to changes in global M_2 resonance conditions, the local effect could be more pronounced. This secondary effect could be quantified within a future study where only the Arctic bathymetry is modified while keeping global conditions constant and observing changes in the basin-wise deep ocean dissipation for individual time slices.

In addition to glacial resonances discussed in prior studies (*e.g.*, North Atlantic, Arctic, South China Sea, Antarctic Kelvin wave), several new features are predicted by the global model. *e.g.*, for the Atlantic region (cf. Figure 6.8), we found a Holocene high-tide episode around 5 ka BP for the Hudson Bay preceded by a further episode after deglaciation of this region around 8 ka BP. The White Sea shows diminishing tidal amplitudes around 11.5 ka BP due to isolation from the Barents Sea. This result is based on the recent RTopo-2 bathymetry data set. In contrast, previous bathymetries showing deeper waters east of the Kola Peninsula do not support the isolation of the White Sea. In the tropical regions (cf. Figure 6.9), the separation of the Pacific from the Indian Ocean around 11 ka BP resulted in the emergence of resonant conditions with a tidal level increase of 2 to 3 m in the South China Sea (*e.g.*, Griffiths and Peltier, 2008), as well as in the Banda Sea and Coral Sea southwest and southeast of Java, respectively. These appear despite the fact that the semidiurnal tides of the open Pacific are only weakly affected by the paleo conditions (strongest reduction for S_2), but instead are related to the near-resonant conditions of the Pacific O_1 tide. Another curious example is the Sea of Japan, where tidal levels further decrease under glacial conditions.

Detailed examination of all regional patterns of tidal changes is beyond the scope of this study, and – as shown for the White Sea – also depends critically on the applied bathymetry. Moreover, a higher spatial resolution is likely necessary to represent specific basin geometries more realistically. Nevertheless, the data underlying this chapter allows the closer inspection of arbitrary regions of interest to investigate their paleotidal

dynamics and resulting tidal levels. We hypothesize that temporal differences in tidal levels, as presented in the figures, are likely to partially absorb residual modelling errors and should thus be considered in combination with a modern data-constrained tidal model (*e.g.*, Hart-Davis et al., 2021b; Lyard et al., 2021; Egbert and Erofeeva, 2002) for maximum accuracy when interpreting SLIPs.
Accordingly, we provide the governing partial tides and the derived tidal levels for different time slices during the last deglaciation. These can be applied easily for further investigations. The tidal levels can directly be used to provide consistent paleotidal levels for Pleistocene and Holocene sea level data which are necessary to derive the indicative meaning and ranges of respective sample types.
As partial tide solutions are provided comprising tidal transports, they can be used to force regional paleotidal models (*e.g.*, Hill et al., 2011). They can also be included in baroclinic oceab models that are, for example, used to study climate or sedimentation (Drinkorn et al., 2021).
As a final note, the flexibility of the tidal model TiME allows for further increasing the tidal solution's spatial resolution. This can be met by using a well-tested configuration with $\frac{1}{12}^\circ$ horizontal grid sampling (Sulzbach et al., 2021a) or experimental setups with even higher resolution. Reaching the 10 km resolution level reduces the need to employ regional numerical models, which are both computationally expensive and challenging to implement due to the need for consistent open boundary conditions.

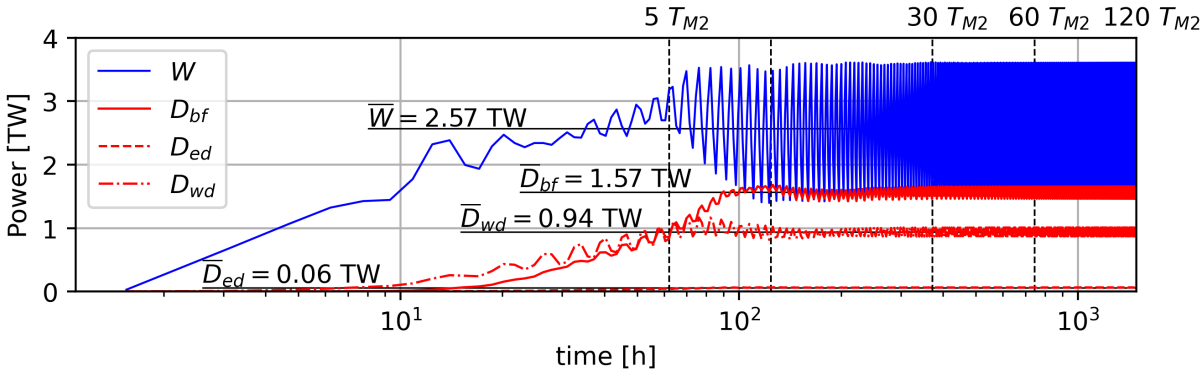

Figure 6.10: Globally integrated dissipation D_i and power consumption W when forcing TiME with the M_2 partial TRP. The simulation is run for 120 tidal periods (approximately 60 days) and discriminates between dissipation by wave drag (wd), bottom friction (bf), and parameterized eddy viscosity (ed). Dissipation rates are sampled eight times per tidal period. Parameters are chosen for experiment W0 of Table 4.1, which was the default setting for Chapter 6. Horizontal black lines indicate mean equilibrium dissipation rates.

Building on the insights accumulated in the previous chapters, which mostly concerned objectives O1 and O2, Chapter 6 is dedicated to predicting paleo-ocean tide levels and paleotidal dissipation, *i.e.*, O3. A major modification concerning the default simulation setting RE, which was preferred in Chapters 4 and 5, is the rebalancing of the tidal dissipation mechanisms. Figure 6.10 shows the ocean tide dissipation predicted by TiME for setting W0, which, in contrast to setting RE (cf. Figure 3.10), predicts more realistic, *i.e.*, reduced with respect to RE, dissipation rates for present-day conditions. Optimizing the model setup to a resolution of $\frac{1}{6}^\circ$ resulted in a further improved global M_2 dissipation estimate of 2.49 TW for the present-day (reference value: 2.45 TW). Comparing the two figures, the different weighting of dissipation mechanisms (red curves) is prominently visible in the equilibrium state.
Setting W0 minimizes dissipation by parameterized horizontal eddy viscosity and is employed by many modern data-unconstrained ocean tide models (*e.g.*, Schindelegger et al., 2018; Egbert et al., 2004). Consequently, all active dissipation mechanisms of TiME depend on distinct oceanographic and geophysical quantities (*i.e.*, stratification, bathymetry, ...) and are virtually free of undefined tuning parameters. Therefore, ocean tide simulations could be performed for past epochs since the LGM. Based on the simulated

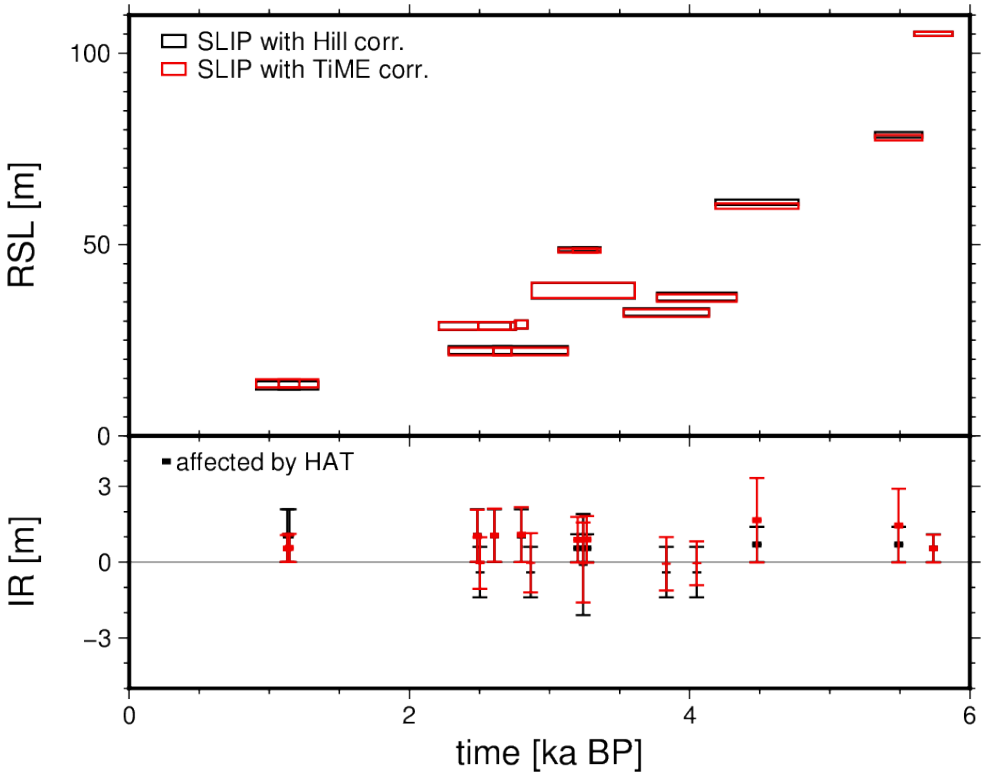

Figure 6.11: Relative sea level (RSL) and indicative range (IR) of SLIPs from Hudson Bay. Top: RSL inferred from specific SLIPs; bottom: corresponding IR. Values published in Vacchi et al. (2018) (black), values determined with TiME (red). Error boxes at the top are specified only by IR and the dating of the SLIP. Provided by V. Klemann and H. Dümpelmann (personal communication, March 7, 2023).

data, it was possible to provide the first global data set of tidal levels designed to interpret sea level markers (Sulzbach et al., 2022b). Tidal levels and sea-level reconstruction are central to the discussion in this thesis chapter, but tidal dissipation is also briefly touched on.

To illustrate the application and capability of the created data set, the tidal levels simulated with TiME were applied to the samples published by Vacchi et al. (2018) in the following, which are found in the Hudson Bay region (cf. Figure 6.11). The figure shows both the derived RSL and the IR, which is spanned by the underlying tidal levels. For the presented figure, samples specified by MTL only and those from gravel beaches, where a constant storm-beach correction of 3 m was added, were excluded (for details, cf. Vacchi et al., 2018, Table 1). For the remaining samples, derived IRs and the RSL were compared between the results of this thesis and Vacchi et al. (2018).

The Hudson Bay is located in a region of post-glacial uplift. Accordingly, during the last 6 ka, a significant RSL fall of more than 100 m was observed, and the differences in RSL due to deviations in the considered tidal levels appear to be small. In the compilation of Vacchi et al. (2018), the paleotidal model of Hill et al. (2011) was applied, which covers the western North Atlantic, but not the Arctic. Accordingly, the authors did not consider deviations from present-day tidal levels for SLIPs of Hudson Bay. For all samples, the

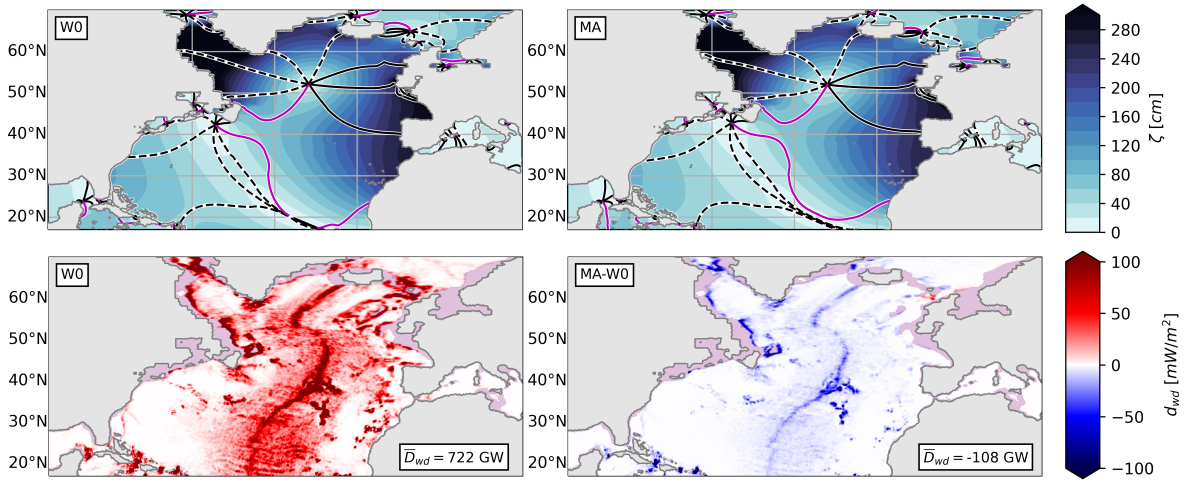

Figure 6.12: M_2 cotidal chart in the North Atlantic for experiment W0 and MA (top) and respective wave drag dissipation density (bottom) under glacial conditions (17 ka BP) for W0 and the difference MA-W0. The dissipation density is integrated over the depicted domain, yielding the dissipation rate $\overline{D}_{\mathrm{wd}}$. Ocean regions with depths smaller than 500 m appear in purple.

IR is specified by two tidal levels. For instance, the tidal range between MTL and HAT defines the IR of macrofossils representing intertidal facies, marked as box symbols in the lower plot of Figure 6.11. The IR generally shows a good agreement between the two tidal correction models. It is evident that the IR predicted by TiME increases with time due to larger tidal levels (cf. Figure 6.8) and so is significantly larger than the values of Vacchi et al. (2018). As the IR is usually considered as an uncertainty (e.g., Khan et al., 2017), these changes influence the statistical analysis of paleo-sea level change in this region.

Another curious paleotidal feature peripherally discussed in Chapter 6 was the drastic increase of the Arctic tidal levels under glacial conditions (cf. Figures 6.6 and 6.7). This phenomenon is also known as 'Arctic Megatide' and was previously predicted by numerical experiments of multiple studies (Egbert et al., 2004; Griffiths and Peltier, 2008, 2009; Velay-Vitow et al., 2020; Velay-Vitow and Peltier, 2020), which were conducted on truly-global domains. However, the emergence of this phenomenon is suppressed if the considered models employ open boundary conditions in the Arctic Ocean (*e.g.*, Wilmes and Green, 2014; Wilmes et al., 2019). As the emergence and suppression of Arctic megatidal conditions were not yet reported within the same modelling framework, its influence on lower latitude regions could not yet be quantified.

The additional experiment MA was designed for the M_2 partial tide, as it dominates the Arctic tidal regime. The setup is identical to W0 introduced in Section 6.2.2 but retains the Arctic bathymetry at a non-resonant state. To this means, the glacial bathymetry (here, at 17 ka BP) transitions to present-day conditions at the north of the $\phi_{\mathrm{cut}} = 75°\mathrm{N}$ latitude circle under consideration of a $\phi_{\mathrm{w}} = 5°$ Gaussian overlap zone. This means that south of ϕ_{cut}, the present-day bathymetry tapers off with $f_{\mathrm{g}}(\phi) = \exp\left(\frac{(\phi-\phi_{\mathrm{cut}})^2}{\phi_{\mathrm{w}}^2}\right)$. In contrast, the paleo bathymetry is superseded with $(1 - f_g)$. The experiment is then performed following the procedure outlined in Chapter 6 and evaluated for the North At-

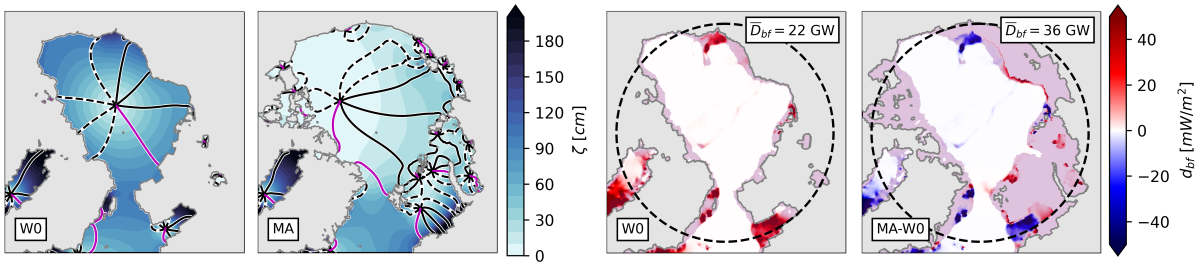

Figure 6.13: M_2 cotidal chart in the Arctic Ocean for experiment W0 and MA (left) and bottom friction dissipation density (right) under glacial conditions (17 ka BP) for W0 and the difference MA-W0. The dissipation density is integrated north of 72° N (dashed circle), yielding the dissipation rate $\overline{D}_{\mathrm{bf}}$. Ocean regions with depths smaller than 500 m appear in purple.

lantic (cf. Figure 6.12) and the Arctic Ocean (cf. Figure 6.13), where the mean dissipation density by bottom friction d_{bf} and wave drag d_{wd} is resolved and integrated to regional values.

The experiments show that the Arctic bathymetry modification of experiment MA can effectively suppress the formation of the Arctic Megatide, which leads to increased dissipation by turbulent bottom friction in the Arctic of $\overline{D}_{\mathrm{bf}} = +36$ GW. At the same time, the large tidal amplitude all over the Arctic basin is prohibited (cf. Figure 6.13). The predicted dissipation by wave drag in the Arctic Ocean is negligible, *i.e.*, smaller than 5 GW. On the other hand, the signs of the changes in the North Atlantic basin are inverted. For experiment MA, the M_2 tidal amplitude in the North Atlantic decreases, which can be attributed to the suppressed feedback from the Arctic Kelvin wave. The effect also impacts the wave drag dissipation in the North Atlantic, which decreases by 108 GW (approximately 15%).

While experiment MA proposed that the Arctic tidal regime represents only a second-order impact on the North Atlantic, the results allows comparing the findings of studies with a truly-global domain (*e.g.*, Velay-Vitow and Peltier, 2020) and with restricted Arctic coverage (*e.g.*, Wilmes et al., 2019). Further, conclusions can be drawn on how Arctic tidal feedback might affect diapycnal mixing and general circulation in the North Atlantic.

In summary, Chapter 6 demonstrates that the continuous simulation of paleotidal dynamics and the detailed assessment of derived quantities like dissipation and tidal levels is feasible with the updated TiME version. The comparison to geologic sea-level proxies and previously published studies on the subject has been started and will be continued in the future.

7 Résumé

This thesis' primary goal was to develop an ocean tide model that significantly improves the quality of ocean tidal corrections. Emphasis was given to cases where the quality of available geodetic data is comparably low, so empirical estimates are of limited precision. These situations comprise geographical regions, tidal frequencies, and past epochs, *i.e.*, the polar oceans, minor tides, and tides since the LGM. To achieve this goal, three main objectives, O1-O3, were formulated in Chapter 1. They are revisited in the following.

7.1 Summary

The core element of O1 was the development of a truly-global and versatile data-unconstrained ocean tide model with high accuracy based on the model TiME (Weis et al., 2008). While the model coverage was already global before the conducted upgrades, the near-Arctic domain was affected by numerical artifacts originating from the utilized 'pole cap' formulation.
This limitation was overcome in this thesis by introducing rotated-pole grids, which allowed relocating the problematic areas around the numerical North and South Poles to land-covered geographical regions. The numerically-lightweight formulation proved robust and versatile and allowed the implementation of two *pari passu* formulations. The selected formulation brought a multitude of benefits. First, it facilitated running twin experiments on grids with different locations of the poles. The results indicated that the derived internal model precision is a factor of $4-5$ better than the model accuracy with respect to empirical data. Second, it provides tidal predictions for the polar regions with undiminished accuracy, which is in contrast to satellite altimetry data-constrained ocean tide models and ocean tide models with open boundary conditions in the Arctic (cf. Figures 4.7a and 5.9). Third, it is an indispensable prerequisite for conducting unbiased paleotidal simulations to address O3 (cf. Figure 6.13).
Major improvements in TiME's accuracy, as quantified by the root-mean-square deviation to geodetic data sets (OBP recorders, TG stations, altimetry data), could be achieved by implementing an updated formulation of the ocean tide PDEs. Including the modern high-resolution bathymetry RTopo-2, the consideration of the non-local effect of SAL,

and particularly the consideration of energy dissipation by topographic wave drag allowed to reduce the modelling misfit for the M_2-tide by $73 - 78\%$ depending on the reference data set. With these improvements, the model accuracy for M_2 is on a similar level as data-unconstrained ocean tide models implementing comparable concepts of ocean tide physics (*e.g.*, Schindelegger et al., 2018; Blakely et al., 2022; Barton et al., 2022; Pal et al., 2023), which is a mean deviation of 3.39 cm for the non-polar deep ocean. A benefit of the selected formulations, especially concerning the wave drag effect in the formalism of Nycander (2005), is that all implemented effects can be employed virtually free of weakly-constrained tuning parameters. In contrast, they depend directly on well-known geophysical quantities, like stratification, bathymetry, and the solid Earth's elasticity. Based on the efficient implementation of tidal hydrodynamics in TiME, the simulation of geophysical signals on the edge of detectability was tackled (O2 and O3).
During the model development, two complementary model setups were fostered. The first setup, labeled RE, relies on substantial energy dissipation by parameterized horizontal eddy viscosity in the tradition of former TiME developments (*e.g.*, Weis et al., 2008). This setting improves the agreement to empirical data in the open ocean, especially for minor tides. Hence, setting RE was preferred for present-day applications, where maximum accuracy is required. On the other hand, this setup lacks a solid foundation in tidal hydrodynamics and overestimates M_2 tidal dissipation by +250 GW.
This is different for the second setup W0, where dissipation by parameterized horizontal eddy viscosity is minimized. The result is a slightly increased root-mean-square deviation in the open ocean while the overestimation of M_2 tidal dissipation decreases to +120 GW. The probable reason for the worse performance of W0 compared to RE is the imperfect representation of shallow-water processes in TiME. Future developments should consider revisiting this topic with the ultimate goal of making W0 the standard setting for all conducted experiments. For this thesis, W0 was only used for experiments toward achieving O3, which calls for an accurate representation of physical processes under variable oceanographic conditions and a realistic tidal dissipation prediction.
Drawing on the successful realization of O1, our results corroborate that TiME can predict partial ocean tides on a reliably high accuracy level of $70 - 85\%$ with respect to the mean tidal signal, regardless of the partial tide amplitude (cf. Figure 4.8).
Objective O2 was the accurate prediction of formerly non-explicitly modeled minor partial tides. Here, degree-2 tides in the edges of the tidal bands were the first example of multiple subgroups of partial tides introduced in Section 2.2.3. The second group was degree-3 ocean tides at the center of Chapter 5. Within this thesis, comprehensive simulations of third-degree tides were performed. The produced solutions comprise at least one tidal constituent from all possible degree-3 species (monthly to terdiurnal) and offer global coverage. In terms of SG, TG, and altimetric validation, it could be shown that the high relative accuracy of TiME extends to this tidal subgroup. Within the study presented in Chapter 5, it was possible to successfully model and validate terrestrial gravimetric signals on the few nGal (*i.e.*, $100\frac{\mathrm{pm}}{\mathrm{s}^2} = 10^{-11} g_0$) level, scratching the theoretically achievable limit of precision of superconducting gravimetry (*e.g.*, Hinderer et al., 2015).
The third group, explicitly addressed with TiME simulations, is radiational (or atmospherically excited) tides. The simulation results were validated on a high accuracy level with the help of OBP and TG data (Balidakis et al., 2022). Hence, the model's radiative partial tides and the tidal subgroups mentioned before were included in the TiME22 tidal

atlas. This compilation emerged from objective O2 (Sulzbach et al., 2022a) and comprises 57 ocean tides, transformed to Stokes coefficients. It includes many minor tides (degree-2, degree-3, radiational), which are not routinely included in state-of-the-art ocean tide atlases. The produced atlas is designed to function as a tidal prediction and correction model for satellite gravimetry. While extended tests of the TiME22 atlas are still to be performed, first results indicate that for several partial tides, *e.g.*, the radiational S_1 tide, tidal aliasing can be reduced (cf. Figure 8 of Balidakis et al., 2022), when considering the provided solutions. Currently, the compilation of a gridded tidal atlas comprising primary (*e.g.*, tidal height) and secondary (*e.g.*, vertical displacement) tidal observables is in progress. It will allow considering TiME22 tides in processing various geodetic techniques, as compiled in Figure 1.2.

The research premise that motivated O1 and O2 can be verified, as it could be proven that data-unconstrained ocean tide modelling can improve the accuracy of existing tidal atlases in several aspects (*e.g.*, spatial coverage and minor tides). Nonetheless, the modelling results showed that altimetry-constrained ocean tide models are superior in accuracy for major tidal excitations that comprise the largest tidal variability. Our results (cf. Figure 4.8) suggest that the most accurate predictions of tidal dynamics would be achieved when combining data-constrained ocean tide solutions for large- and medium-signal ocean tides and data-unconstrained solutions for the smallest signals, *i.e.*, by this creating a *hybrid ocean tide atlas*. The threshold between these two regimes is located on the few-mm signal level. Whether it is beneficial to derive minor constituents with linear admittance remains to be tested. However, this approach will likely benefit several partial tides (*e.g.*, Hart-Davis et al., 2021a).

At present, including few-mm and sub-mm tides into the GRACE(-FO) dealiasing process will likely have a minor impact on the gravimetric fields or could even remain hidden below the current noise level. However, extensive validation should be performed. Additionally, such small tidal signatures will become more important when other sources of error, *e.g.*, satellite accelerometer noise or non-tidal high-frequency oceanic mass transport, are minimized or better constrained (Flechtner et al., 2016). The impact of hybrid models on terrestrial measurements is possibly more pronounced than for GRACE, especially for terrestrial SG measurements (cf. Chapter 5).

Objective O3 was the continuous simulation of primary and secondary tidal observables since the last glacial maximum. Without a dense network of paleotidal observations, internal model plausibility was central for supporting the credibility of the results. To achieve maximum plausibility, the simulations relied on the model setting W0. Extended present-day model validation was pursued with TG, OBP, and altimetric reference data sets, which returned agreement values between 65% (HAT by TG stations) and 80% (M_2, non-polar, deep ocean by FES14). The model run, which was performed on a $\frac{1}{6}^\circ$ grid, also proved very accurate for the present-day M_2 tidal dissipation, which was only overestimated by approximately 2% (50 GW).

The modelling results for dissipation and tidal levels since the LGM appear within the range of formerly conducted studies. However, the combination of TiME's model features, especially the truly-global grid, the inclusion of SAL, the bathymetry, and the simulation of 4 partial tides per epoch, allows for revisiting several aspects of paleotidal dynamics with unprecedented precision.

These aspects include creating a global data set of paleotidal levels with a dense temporal

coverage, which can be applied to interpret SLIPs at arbitrary locations (cf. Figure 6.11). The TiME simulations show that the derived IR for SLIPs vary in space and time, with deviations up to 10 m in extreme cases. The largest deviations are often related to local resonances, for example, the Arctic megatidal regime that emerges under glacial conditions. This repeatedly debated phenomenon formed in TiME's default run. It could be shown that the implications of suppressing this phenomenon in the simulations for the North Atlantic are non-negligible and could affect tidal mixing on a 15%-level.
In summary, the implementation of O1-O3 was successful. However, it was accompanied by newly-emerging research questions and possibilities for improving the obtained results, which is discussed in the next section.

7.2 Outlook

While the implemented model upgrades successfully enabled TiME to specifically simulate the largest part of the tidal spectrum (cf. Figure 2.8), several subgroups cannot yet be predicted with sufficiently high accuracy. First, this comprises shallow-water tides (*e.g.*, M_4, cf. Figure 4.9) and is related to the representation of hydrodynamic nonlinearity in TiME. As the most significant nonlinear effect is turbulent bottom friction, which accounts for the largest part of present-day tidal dissipation (cf. Figure 6.10), improvement of this effect will impact the accuracy of major tides, *e.g.*, M_2. The achieved accuracy for M_2 is relatively high. Yet, it is still approximately a factor of 10 worse than for data-constrained models, especially in shallow water, where bottom friction predominantly occurs. Here, the regional optimization of bottom friction and topographic wave drag led to significant improvements in other data-unconstrained ocean tide models (*e.g.*, Blakely et al., 2022) and is also considered for data-assimilating ocean tide models (*e.g.*, Lyard et al., 2021). Thus, an equivalent approach should be considered for TiME.
Based on this avised improvement, the full-ephemeris operation mode of TiME could be employed to augment the TiME22 ocean tide atlas by terdiurnal and higher frequency compound- and overtides and improve the quality of existing major partial tide solutions. Recomissioning the full-ephemeris mode conjures the challenge of correctly representing the effect of topographic wave drag, which is frequency-dependent (cf. Equation 3.7), *e.g.*, it strongly differs for diurnal and semidiurnal tides (Egbert and Ray, 2003). However, the precise representation of this effect caused the most noticeable improvement in the model accuracy (cf. Table 4.3). Thus, the accurate simulation of terdiurnal compound tides originating from diurnal-semidiurnal nonlinear tidal interaction will likely depend on a proper broadband wave drag implementation.
Further, seasonal satellite tides like M_2^α and M_2^β are not yet covered by TiME22. While the sea ice module introduced in Chapter 6 allows for studying the effects of seasonal ice coverage on major ocean tides (cf. Figure F.1), additional effects such as temporally varying stratification (*e.g.*, Schindelegger et al., 2022) should be considered.
The above-outlined upgrades are focused on expanding the TiME22 atlas. Additionally, general model developments that improve the overall accuracy of all included partial tides should be taken into account. For this, one possibility is increasing the model's resolution in the global mean or by regional nesting approaches. In the present configuration, a global minimum meridional resolution of $\delta\phi = \frac{1}{20}^\circ$ and maximum nested regions of up to $\frac{1}{40}^\circ$ are feasible, which would allow targeting specific regions with complex shallow-water

dynamics, *e.g.*, the North Sea or the Irish Sea.
Another promising step would be to consider the assimilation of empirical tidal constituents derived from satellite altimetry (*e.g.*, EOT20) or tide gauge data (*e.g.*, TICON-3) into TiME to create a data-constrained derivative of TiME22. The upgraded tidal atlas would then benefit from the upgraded model physics of TiME and the full potential of existing empirical data sets.
On the other hand, the already addressable ensemble of applications includes multiple aspects. Within Chapter 6, the emergence of the Arctic Megatide was discussed. The question of how this apparent tidal regime acts back on the North Atlantic should be addressed in more detail, also investigating possible impacts on general circulation, which would require using a general circulation model. Overall, the conducted paleo study would benefit from further increased model resolution.
Further, it was remarked in the last section that extensive tests of tidal corrections by TiME22 in a pure or a hybrid configuration are still to be conducted. It should be considered to expand the ensemble of secondary tidal observables in TiME22 to Earth Rotation Parameters (ERP, cf. Weis et al., 2008) and mean tidal dissipation estimates. By extending the base of observational data sets that could be contrasted against TiME, additional information for validation (or calibration) of model experiments might be explored.
Another intriguing possibility would be to force TiME with atmospheric reanalysis data to predict high-frequency non-tidal mass variability. The current community standard for removing suchlike signals from GRACE data is AOD1B (Shihora et al., 2022; Dobslaw et al., 2017), which relies on the baroclinic model MPIOM (Jungclaus et al., 2013). It is critical to stress that a barotropic (single-layer) model like TiME cannot depict baroclinic processes essential for the general circulation. On the other hand, the effect of barotropic pressure excitation and the mean impact (*i.e.*, the barotropic component) of wind stress forcing can be successfully captured, which has been shown for radiational tides (*e.g.*, Carrère and Lyard, 2003; Arbic, 2005; Balidakis et al., 2022, 2023) and non-tidal dynamics for altimetric (*e.g.*, Carrere et al., 2016) and gravimetric (*e.g.*, Schindelegger et al., 2021) signals. Further, barotropic models are typically numerically less expensive than baroclinic models, allowing the advantage of increased horizontal resolution, which is particularly beneficial for depicting semi-enclosed marginal seas and narrow straights. On the one side, the spatially non-local implementation of SAL in TiME, known to impact the atmosphere-driven high-frequency ocean dynamics (*e.g.*, Shihora et al., 2021), will benefit the representation of non-tidal ocean dynamics. Additionally, provided the successful update of barotropic-baroclinic conversion to account for temporal non-locality, this endeavor seems promising. Therefore, it should be investigated if the advantages of a modern barotropic ocean model with parameterized baroclinic processes can provide improved mass distribution estimates for the limited case of predicting high-frequency mass variability.
Chapter 5 motivates that data-unconstrained numerical models can be powerful tools to model and identify minuscule geoscientific signals on the edge of detectability, such as third-degree ocean tides. This allowed us to study load tide and body tide signals in the terdiurnal frequency band. Given the successful upgrade of TiME, especially in the field of tidal nonlinearity, it would be a good plan to revisit this topic, *e.g.*, by trying to discriminate lunar degree-4 tides (cf. Figure 5.11) from shallow-water tides, terdiurnal

and 1/4-diurnal radiational tides from their shallow-water counterparts (*e.g.*, Ray et al., 2023), or even approach the ψ_1 tide. This tide is generally considered problematic and is additionally affected by the insufficiently-constrained FCN-resonance (cf. Table 2.1) and seasonal variations (Ray, 2017; Ray et al., 2021).
In conclusion, the work conducted within this thesis advanced the numerical modelling of ocean tidal dynamics in several aspects and provided novel ocean tide solutions for processing geodetic data. Regardless of the long history of ocean tide science, there remain numerous intriguing research questions to answer, which the continuous efforts in tidal modelling have brought within reach. Accordingly, it is expected that the research of tidal phenomena will maintain its significance within planetary sciences in the future.

Appendices

A Spherical Harmonic Functions

The fully-normalized spherical harmonic base functions employed within this thesis are real-valued (in contrast to their generally complex definition in quantum mechanics). This difference implies a modification with respect to the usually employed normalization factor in complex notation, which can ultimately induce misinterpretation of base functions. The normalization factor N_{lm} was implicitly introduced in Equation (2.3) as the scale factor of the associated Legendre Polynomials $\overline{P}_{lm} = N_{lm} P_{lm}$, and is given by (*e.g.*, Heiskanen and Moritz, 1967, p. 24, 31)

$$N_{lm} = \sqrt{(2l+1)(2-\delta_{m0})\frac{(l-m)!}{(l+m)!}} \ , \tag{A.1}$$

where the Kronecker-δ modifies the normalization factor for $m = 0$ harmonics and '!' signifies the factorial. It is stressed that Heiskanen and Moritz (1967) and Hartmann and Wenzel (1994, 1995b) refer to these functions as 'fully-normalized', as they fulfill the relation

$$\frac{1}{4\pi} \int d\Omega \ (Y_{lm})^2 = 1 \ , \tag{A.2}$$

where integration is performed over the entire solid angle domain. It could also be argued that Y_{lm} should include the factor $\frac{1}{\sqrt{4\pi}}$ for full normalization. One would then speak of the notation mentioned above as 4π-normalized. However, this thesis follows the introduced nomenclature that builds the basis for the employed TRP.
The associated Legendre Polynomials up to degree-4 are listed in the following Table.

l	0	1	2	3	4
P_{l0}	1	$\sin\phi$	$\frac{1}{2}(3\sin^2\phi - 1)$	$\frac{1}{2}(5\sin^3\phi - 3\sin\phi)$	$\frac{1}{8}(35\sin^4\phi - 30\sin^2\phi + 3)$
P_{l1}		$\cos\phi$	$3\sin\phi\ \cos\phi$	$\frac{3}{2}\cos\phi\,(5\sin^2\phi - 1)$	$\frac{5}{2}(7\sin^3\phi - 3\sin\phi)\cos\phi$
P_{l2}			$3\cos^2\phi$	$15\cos^2\phi\ \sin\phi$	$\frac{15}{2}(7\sin^2\phi - 1)\cos^2\phi$
P_{l3}				$15\cos^3\phi$	$105\sin\phi\cos^3\phi$
P_{l4}					$105\cos^4\phi$

Here, the functions are defined in terms of the latitude ϕ to be compatible with the geographical coordinates to which the ocean model refers. In general, it is standard to define P_{lm} in terms of the colatitude $\theta = \frac{\pi}{2} - \phi$. This implies the identities $\cos\phi = \sin\theta$ and $\sin\phi = \cos\theta$, which can be used to transform the P_{lm}. Please also consider the spatial representation of the introduced Y_{lm} in Figure A.1.

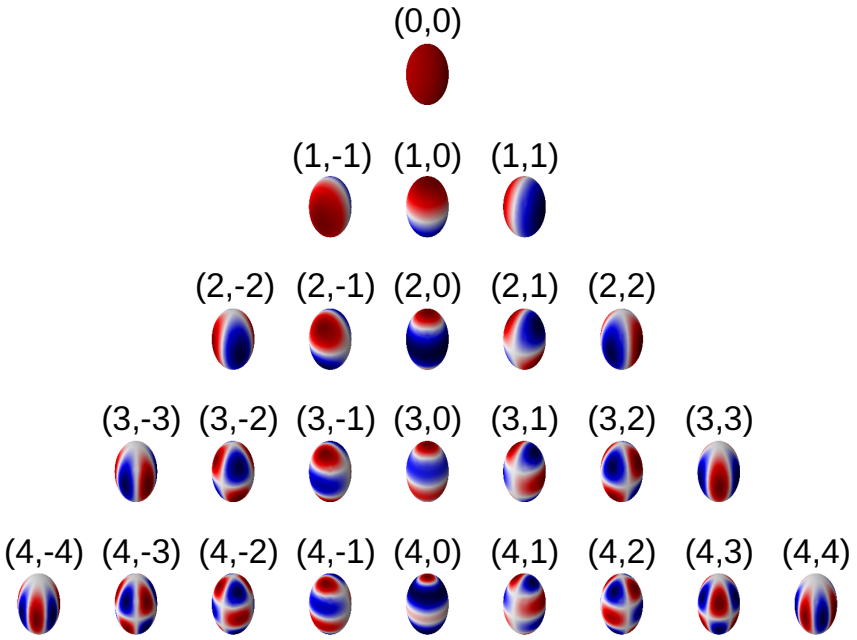

Figure A.1: Global representation of the real-valued spherical harmonic functions Y_{lm} for degree/order (l, m) up to $l_{\max} = 4$, where red (blue) colors represent positive (negative) extreme values for each function.

B Bathymetric Interpolation Algorithm

The spatially high-resolution bathymetric data set[1] RTopo-2 (Schaffer et al., 2016) is regridded to the tidal model's lower resolution ($\frac{1}{12}^\circ$...1°). Seeking an algorithm that optimally conserves the bathymetric information obtained from high resolution, we consider the shallow-water equations in the abbreviated form

$$\left([\hat{\mathcal{O}}_1 + \hat{\mathcal{O}}_2(H)]\ \boldsymbol{\zeta}^\omega - \mathbf{F}_0 \right) e^{i\omega t} = 0 \tag{B.1}$$

where three groups of operators are defined: Group $\hat{\mathcal{O}}_2(H)$, which explicitly depends on the bathymetric function H , group $\hat{\mathcal{O}}_1$ independent of H, and the external forcing $\mathbf{F}_0 = -g\nabla\zeta_{eq}$, additionally independent of $\boldsymbol{\zeta}$. We further assume $H = H_0 + \delta B$ and $\boldsymbol{\zeta}^\omega = \boldsymbol{\zeta}_0 + \delta\boldsymbol{\zeta}$, thus introducing a tiny bathymetric disturbance δB to a known bathymetric function H_0, that causes an exiguous disturbance $\delta\boldsymbol{\zeta}$ in the corresponding solution vector $\boldsymbol{\zeta}_0$. Since this disturbance is small, $\delta\boldsymbol{\zeta}$ is determined by

$$(\mathcal{O}_1 + \mathcal{O}_2[H_0 + \delta B])\,\delta\boldsymbol{\zeta} = \begin{pmatrix} r|\mathbf{v}_0|\frac{1}{H_0^2}\mathbf{v}_0 \\ \mathbf{v}_0 \cdot \boldsymbol{\nabla} + \frac{(\boldsymbol{\nabla}H_0)\mathbf{v}_0 - \partial_t\zeta_0}{H_0} \end{pmatrix} \delta B \equiv \mathbf{F}_\epsilon(\delta B, H_0, \boldsymbol{\zeta}_0)\ . \tag{B.2}$$

This equation describes shallow water dynamics for $\delta\boldsymbol{\zeta}$ driven by the external force $\mathbf{F}_\epsilon$. We define the bathymetric disturbance introduced by a drastic reduction of the initial

[1] This Appendix is transcribed from the Supporting Information of Sulzbach et al. (2021a).

resolution as

$$\delta B_{ij} = H_{ij}^{(h)} - H_{kl}^{(l)} \ . \tag{B.3}$$

Here, we added the indices h/l to indicate whether the bathymetries are defined at high or low resolution. We allow both fields to be evaluated at high resolution suggested by the index (i,j). Here, the coarsely resolved fields are assigned values in terms of nearest-neighbor interpolation $H_{ij}^{(l)} = H_{kl}^{(l)}$ in the vicinity of $H_{kl}^{(l)}$, denoted roi(k,l)[2]. Due to the huge resolution difference, the disturbance δB_{ij} will have a 'bumpy structure' with minor differences between grid cells in one roi(k,l) and bigger jumps, where the next-neighbor interpolation value of $H_{ij}^{(l)}$ changes.

The overall goal is to choose $H_{kl}^{(l)}$ in such a way that it minimizes the quantum of tidal dynamics evoked by $\mathbf{F}_\epsilon$. Since the forcing is proportional to δB_{ij}, it has a noisy structure and will thus not show pronounced resonance with the oceanic eigenmodes (cf. Section 2.2.2). Its impact on OTD is best reduced by minimizing $||\mathbf{F}_\epsilon||$ under variation of $H_{kl}^{(l)}$. The forcing operator can thus be rewritten as

$$\mathbf{F}_\epsilon^{ij} = \mathbf{F}_{res}^{ij} + \begin{pmatrix} c_1^{(kl)} \left(H_{ij}^{(h)}\right)^{-2} \\ c_2^{(kl)} \left(H_{ij}^{(h)}\right)^{-1} \end{pmatrix} \delta B_{ij} \ , \text{with } (i,j) \in \text{roi}(k,l) \tag{B.4}$$

where the complex $c_1^{(kl)}, c_2^{(kl)}$ are constants depending on the local value of $\boldsymbol{\zeta_0}$ and $\boldsymbol{\nabla} H_0$. In the following, we assume that tidal solutions are well resolved within one roi, thus allowing us to treat $c_{1,2}^{(kl)}$ as constants within one roi. $\mathbf{F}_{res}^{ij}$ contains all forces that do not depend on the absolute depth value $H_{ij}^{(h)}$.

Equation (B.4) states that the individual contributions to the noisy forcing will be proportional to δB_{ij} but weighted with individual weights proportional to H_0^{-1} and H_0^{-2} multiplied with coefficients $c_{1,2}$, respectively. We concentrate on the contribution proportional to H_0^{-1} as it originates from the conservation of mass as a fundamental principle of hydrodynamics. We only have to evaluate the third vector component in terms of the $||\ ||^2$-norm, yielding

$$\partial_{H_{kl}^{(l)}} || \left(\mathbf{F}_\epsilon - \mathbf{F}_{res}\right) \cdot \mathbf{e}_3 ||^2 = \partial_{H_{kl}^{(l)}} \sum_{ij} |c_2^{(kl)}|^2 \left(1 - \frac{H_{kl}^{(l)}}{H_{ij}^{(h)}}\right)^2 = 0 \ , \tag{B.5}$$

resulting in the minimization condition

$$H_{kl}^{(l)} = \sum_{ij} \left(H_{ij}^{(h)}\right)^{-1} / \sum_{ij} \left(H_{ij}^{(h)}\right)^{-2} \ . \tag{B.6}$$

Equation (B.6) states that individual weights inversely-proportional to the bathymetric depths are the right choice to minimize resolution-dependent disturbances. Please note that consideration of terms proportional to c_1 instead of c_2 would lead to a similar result with powers of H_0 changed by -1, further increasing the weight of shallow water grid

[2] roi = region of interest

cells[3]. In light of this finding, we want to stress that Equation (B.4) proposes to perform a resolution reduction operation with weights that grow for shallow depths.
The prerequisite $c_{1,2}$ = const. within one roi, is only broken in coastal regions (rois containing ocean and land), where the tidal elevation can change drastically. As a byproduct of the depth-inverse regridding, these rois are evaluated as dry (shrinking ocean area), leading to the problem of closing narrow passages as, *e.g.*, the Straight of Gibraltar.
We overcome this problem by using weights proportional to depth in coastal areas (first-order conservative interpolation). This scheme evaluates rois containing at least one wet grid cell as wet (growing ocean area) and conserves the cross-section of straights. We finally emphasize that the differences between the discussed scheme and first-order conservative remapping are small at a resolution of $\frac{1}{12}^\circ$ but much more significant at a lower resolution.
Despite the partially rough approximations and assumptions, these considerations resulted in a physically meaningful and versatile interpolation technique that allows the construction of bathymetric maps for any given spatial grid with rotated poles automatically.

C Properties of the Gravity Residuals

The interpretation of the standard deviation derived by error propagation as the confidence interval depends on the spectral characteristics of the gravity residuals[4], which are required to be normally distributed. With the quantities given in Table C.1, the properties are summarized for each station: the RMS, a power spectrum, and the power vs. frequency ratio providing the noise color. The effect of high-pass filtering in ETERNA-x in the underlying data series has been restored when applied (last column of Table C.1).

Together with the RMS value of each site's residual, the spectra indicate the presence of a signal, be it from instrumental or environmental sources, that has escaped reduction in the tidal analysis because it was neither included in the functional model nor as prior data correction. The noise color, as given by the ratio $\log(P)/\log(f)$ in Table C.1, is mostly close to red (*i.e.*, Brownian), with larger deviations for some sites, as indicated by the chi-squared test for the linear fit of this parameter from the power spectrum.
The average power within spectral bands defined equally wide in $\log(f)$ is shown in blue in the small figures of Table C.1. Diurnal and semidiurnal tidal frequencies are covered in the 5th bar from the left in those small figures of Table C.1, while the other bars are assumed to be dominated by non-tidal sources, *i.e.*, periods longer than one day, and are typically dominated by the effects of water storage changes. Strong but narrow spectral lines occur at specific periods and are represented by an amber surplus above the average. Such deviations indicate that attention is required, specifically if appearing in band 5. For most conspicuous stations such as BO, SU, or YS, the non-stationary behavior of solar tides ${}^*S_n$ is the most likely cause, suggesting an advanced atmospheric correction.

[3]This change is due to the origin of the c_1-term from bottom friction, which is strongest in shallow waters.

[4]This Appendix originates from the Supporting Information of Sulzbach et al. (2022c).

Table C.1: Properties of gravity residuals after tidal analysis. In the cases of filtered data, the unfiltered residual has been restored. cf. Figure C.1 for a detailed explanation of the equally scaled tiny power spectra in column PSP. The ratio $\log(P)/\log(f)$ was obtained from the average amplitude in dB per octave. The goodness of this fit is provided by the chi-squared test. Values $\chi^2/n >> 1$ indicate larger fluctuations in the spectrum, also visible in the deviations of the mean (blue) and maximum (amber) magnitude of the PSP. The RMS is given in nm/s^2, and the last column flags whether the time series were filtered before tidal analysis.

Site	RMS	PSP	$\log(P)/\log(f)^*$	χ^2/n	Filter
AP	24.0	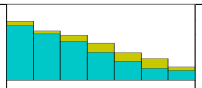	-2.05	0.8	no
BH	7.4	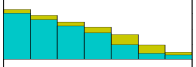	-1.75	2.6	no
BO	28.6	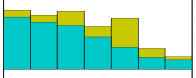	-1.75	7.2	yes
CA	67.7	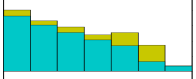	-1.69	0.3	no
CB	34.1	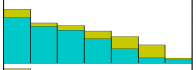	-1.69	2.3	no
ES	161.3	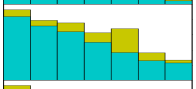	-2.01	1.8	yes
KA	131.0	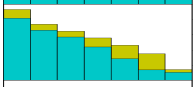	-2.25	2.3	no
LP	42.8	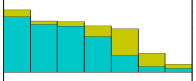	-2.09	17.6	yes
MB	23.7	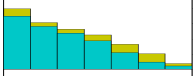	-2.00	1.3	no
MC	11.9	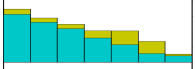	-1.73	0.3	no
NY	35.1	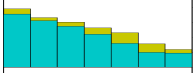	-1.69	1.4	no
OS	9.9	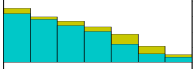	-1.67	4.4	yes
SU	17.1	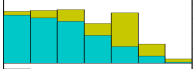	-1.84	12.3	yes
TC	87.1	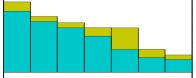	-2.07	2.9	yes
WE	45.1	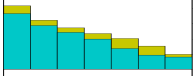	-1.90	2.2	no
YS	32.1	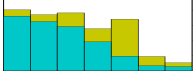	-2.30	13.7	yes

*: Assuming an uncertainty for $\log(P)$ of 0.16, the uncertainty of $\log(P)/\log(f)$ is 0.07 throughout.

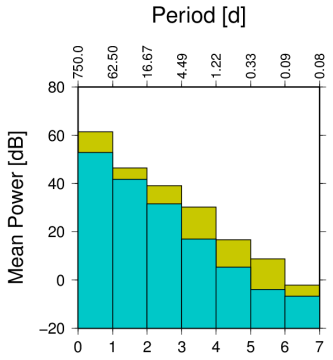

Figure C.1: Average power spectrum of gravity residuals explaining the tiny images in column PSP of Table C.1. The abscissa is logarithmic in frequency, and the corresponding periods are given at the top. The resolution has been devised such that bar number 5 contains the diurnal, semidiurnal, and terdiurnal periods. All bars are equally wide in $\log(f)$. The amber-colored part shows the maximum power in each band, and the blue part is the arithmetic average of the dB values of power within the bin.

D Global Admittance Functions

Here, we present the global admittance functions of selected tides appearing in Table 5.1 to highlight differences in the underlying response patterns[5]. The depiction of Z_{lm} that was introduced in Equation (5.4) facilitates a direct comparison between partial tides that possess excitation amplitudes encroaching several scales as ocean responses are normalized by their excitation amplitudes. We extend this concept to the gravimetric response g^ω induced by ocean tide ζ^ω (cf. Equation 5.7). For this purpose, $g^\omega = g^\omega_{\cos} + \mathrm{i} g^\omega_{\sin}$ is normalized with the Newtonian gravitational shift induced by a localized, uniform layer of seawater of height $\frac{A_\omega a_l^b}{g_0}$, which is the measure we employed for the equilibrium tidal height. This corresponds to the limit of a locally flat Earth, covered with said layer and amounts to half the gravity of a uniformly water-covered sphere

$$g_{\mathrm{eq}} = 2\pi G \rho_{\mathrm{sw}} \frac{A_\omega a_l^b}{g_0} = \frac{3\rho_{\mathrm{sw}}}{2\rho_{\mathrm{se}}} \frac{A_\omega a_l^b}{R_e} \ . \tag{D.1}$$

The resulting ocean loading-induced gravity admittance function is then obtained by

$$Z^*_{lm}(\phi, \lambda, \omega) = \frac{g^\omega}{A_\omega a_l^b} \frac{2\rho_{\mathrm{se}}}{3\rho_{\mathrm{sw}}} R_{\mathrm{e}} = g_0 \frac{\sum_{l'm'} \beta_{l'} \zeta^{\omega,lm}_{l'm'} Y_{l'm'}}{A_\omega a_l^b} \ , \tag{D.2}$$

where β_l is the LLN-composed prefactor in Equation (5.7). Results for Z_{lm} and Z^*_{lm} are presented in a combined plot in Figures D.1 and D.2. ${}^3\mathrm{M}_3$ results are not presented as they cannot be compared to a neighboring degree-2 tide. The following features can be identified

- Degree-2 and degree-3 admittance functions take unrelated, independent shapes both in terms of amplitude and phase.

[5]This Appendix originates from the Supporting Information of Sulzbach et al. (2022c).

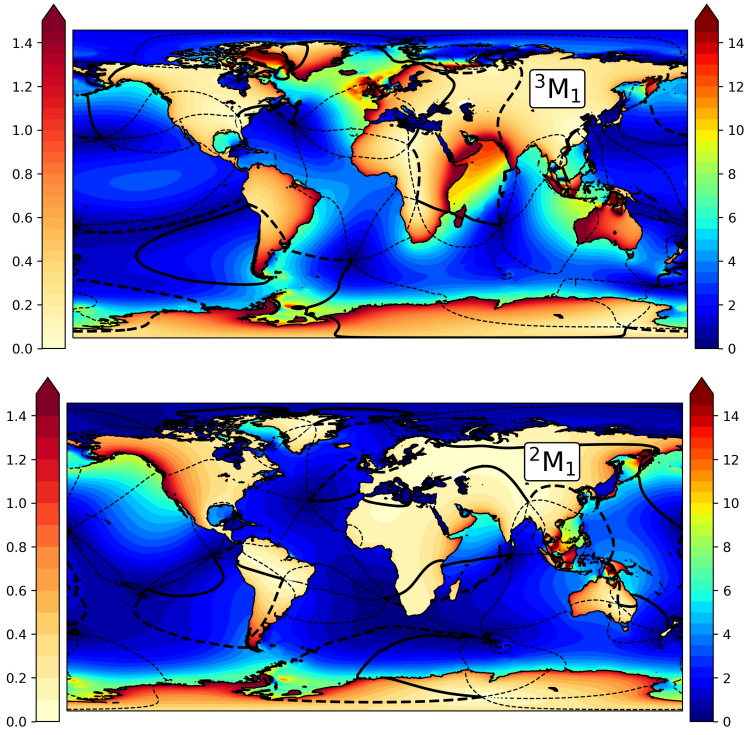

Figure D.1: Dimensionless, diurnal admittance functions Z_{l1} (right color bar) and Z^*_{l1} (left color bar) evaluated for diurnal excitations (top: $l = 3$ for $^3M_1$; bottom: $l = 2$ for $^2M_1$). Lines indicate the tidal phase ϕ_i in increments of 60°, where the continuous fat line marks 0° and the dashed fat line represents 60° phase lag.

- At coastal margins, the phase lag of ocean tide and is the respective induced gravity signal is not a steady function but can exhibit visible phase shifts due to the non-local character of ocean tidal loading (*e.g.*, $^3M_1$ tide at the West African coast).
- The strongly enhanced $^3L_2$-admittance can be easily identified and clearly exceeds $^3N_2$ (Ray, 2020).
- Inverted behavior can be asserted in the case of semidiurnal degree-2 tides where $^2N_2$ admittance exceeds the $^2L_2$ response in the Atlantic and Pacific oceans. This result seems to be counter-intuitive. On the other hand, this behavior is not unexpected as the different excitation patterns of degree-3 and degree-2 tides will profoundly change the underlying normal mode decomposition of the respective partial tide, hence changing the relative importance of modes with specific resonance frequencies (Müller, 2007).

E TiME22 Tidal Atlas

Based on the simulations performed by Sulzbach et al. (2021a, 2022c) and Balidakis et al. (2022), the TiME22 tidal atlas was created (Sulzbach et al., 2022a) and comprises

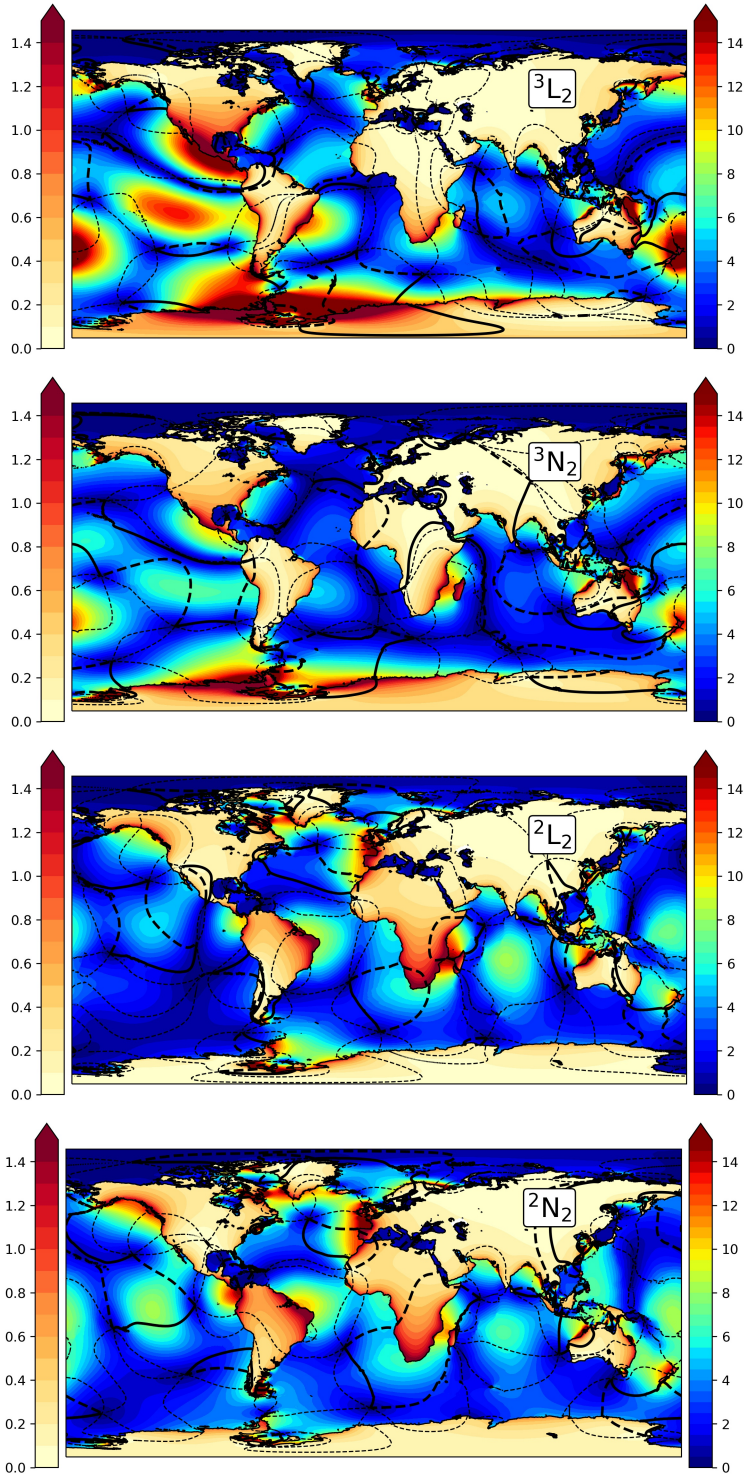

Figure D.2: Dimensionless, semidiurnal admittance functions Z_{l2} (right color bar) and Z^*_{l2} (left color bar) evaluated for semidiurnal excitations (top to bottom: $l = 3$ for $^3L_2$ and $^3N_2$; $l = 2$ for $^2L_2$ and $^2N_2$). Lines indicate the tidal phase ϕ_i in increments of 60°, where the continuous fat line marks 0° and the dashed fat line represents 60° phase lag.

mass variations from atmospheric and oceanic tides in the form of Stokes Coefficients. The data set is designed for dealiasing of satellite gravimetric data. Therefore, this data publication not only provides mass anomaly coefficients but also includes an introduction to the theory of linear admittance and computational building blocks to compute linear admittance estimates from the TiME22 atlas.

The ocean component (OCN) comprises 57 partial tides, including many minor tides discussed in Section 2.2.3 (*i.e.*, degree-2 tides in the edges of tidal bands, degree-3 tides, and atmospherically-excited or *radiational* tides). In the current form, nonlinear and climatologically-induced tides are not included for the reasons discussed in Chapter 7.

In Figures E.1 to E.3, the TiME22 atlas is presented, with the classification of each partial tide following in Table E.1. The transition from SEQT to the dynamical tidal regime can be studied by comparing Figures 2.2 to the figures of this Appendix, *i.e.*, the patterns of TGPs for long-period tides can be easily identified in Figure E.1, which is impossible for diurnal and higher frequency tides. The figures indicate which tides are excluded from linear admittance estimation and where degree-3 admittance must be considered.

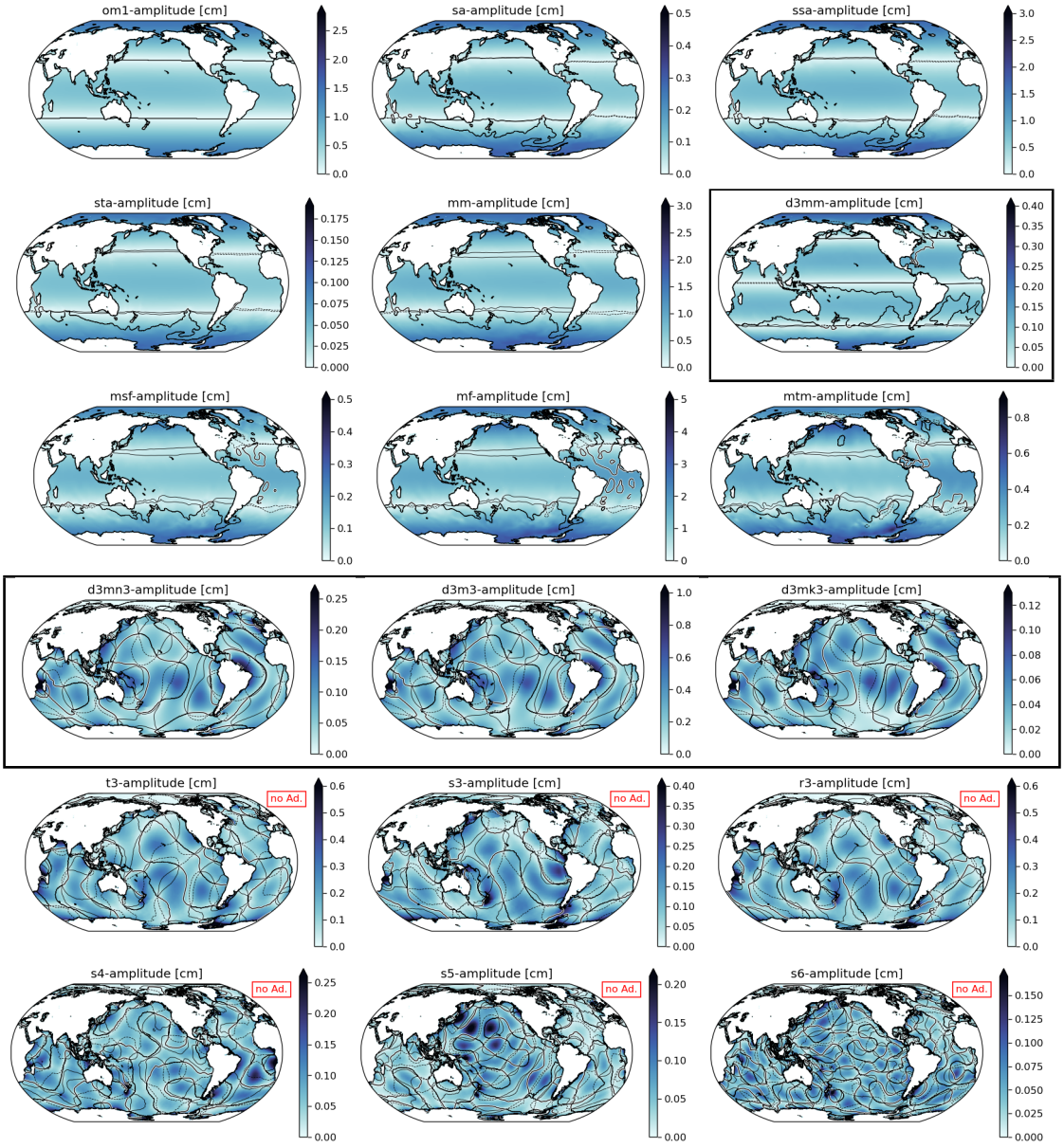

Figure E.1: Long-period, terdiurnal and high-frequency tides of the TiME22 OCN catalog. Degree-3 tides are framed in black and radiationally-excited tides that are not approved for admittance estimation are marked in red. Here, and in the following plots the Greenwich-phase lags $-180° < \phi_i < 180°$ are represented as black lines in increments of 60°, where dashed lines represent negative values and $\phi_i = 0°$ is marked by the white background line. The phase-lag for om1 is zero at each point, as the tide is modeled to be in phase with the TGP (equilibrium tide). Modified from Sulzbach et al. (2022a).

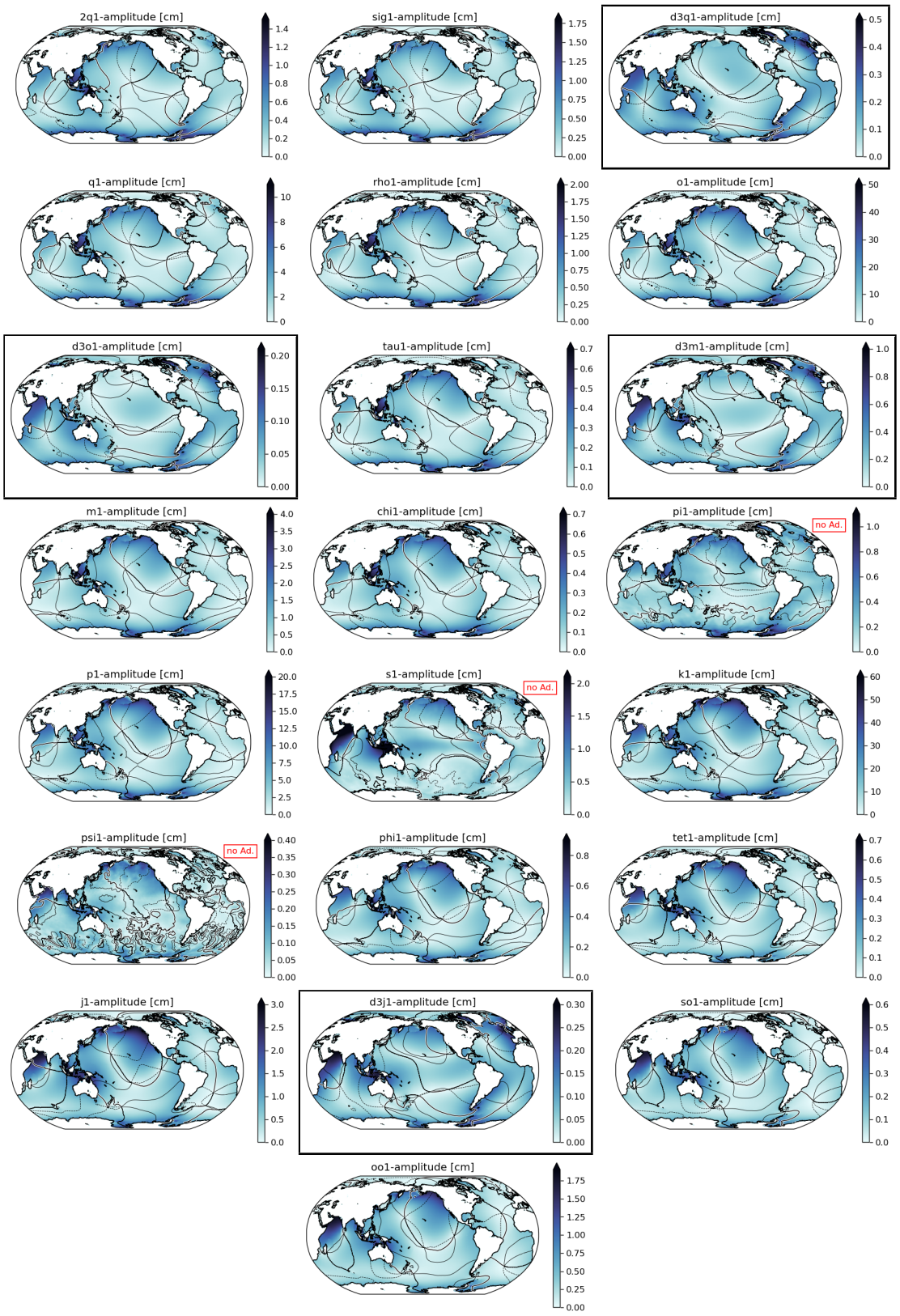

Figure E.2: Diurnal tides of the TiME22 OCN catalog. Degree-3 tides are framed in black and radiationally-excited tides that are not approved for admittance estimation are marked in red. Modified from Sulzbach et al. (2022a).

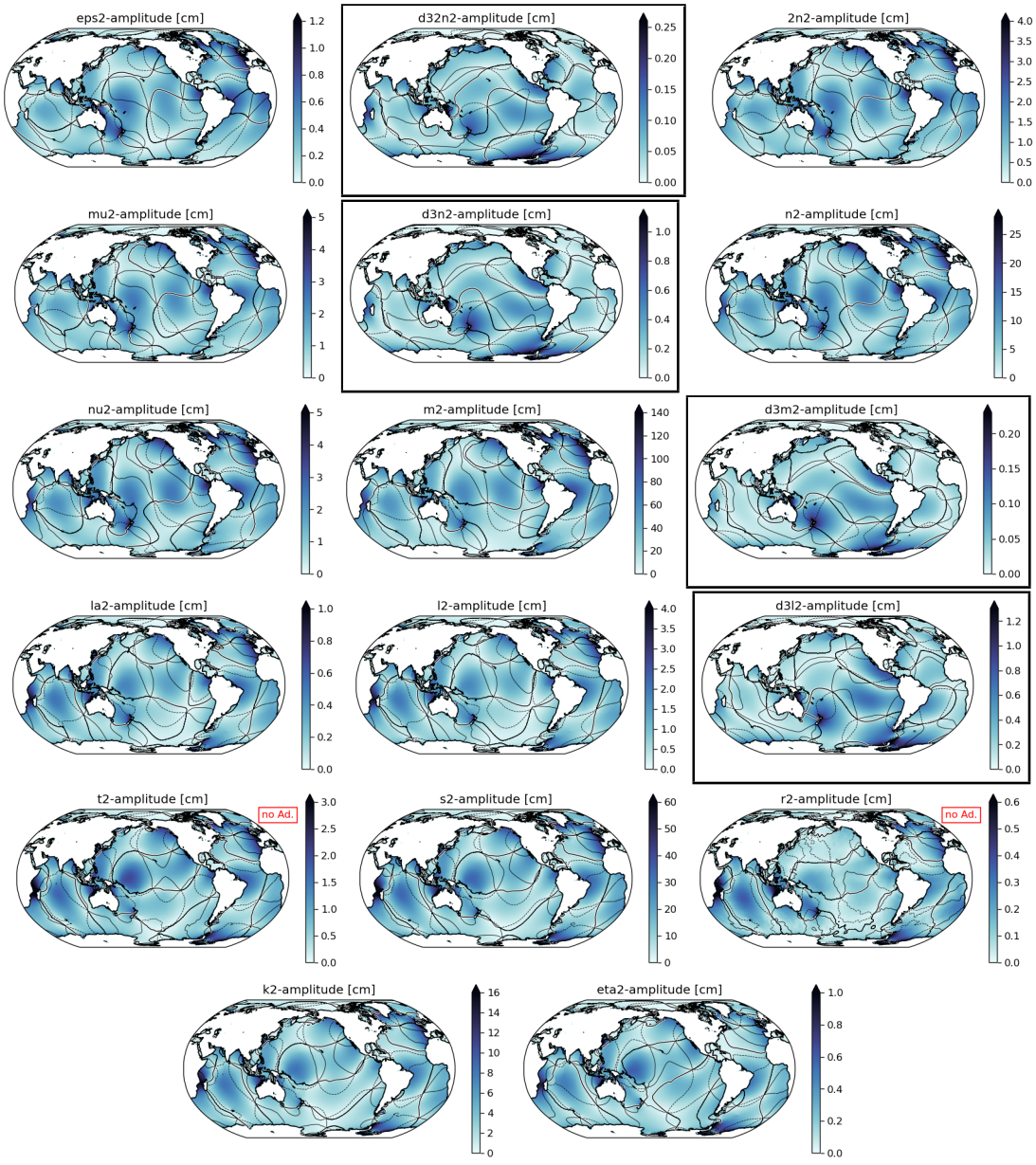

Figure E.3: Semidiurnal tides of the TiME22 OCN catalog. Degree-3 tides are framed in black and radiationally-excited tides that are not approved for admittance estimation are marked in red. Modified from Sulzbach et al. (2022a).

Table E.1: 57 partial tides (label i) as appearing in TiME22. Column idx refers to the numbering in the supporting information of Sulzbach, Dobslaw, & Thomas (2021), ATM states whether atmospheric forcing was considered and LINAD whether the tide is considered for linear admittance. l is the degree of the partial TGP, and A_i the respective amplitude. Further, the trivial name of the partial tide and the tag (ID) that is used in the file naming convention is presented.

idx	Doodson	ATM	LINAD	l	A_i $[\frac{mm^2}{s^2}]$	name	ID	n
1	055.565	n	y	2	7.719645e+04	Ω_1	om1	1[1]
2	056.554	n	y	2	1.360322e+04	S_a	sa	2[2]
3	057.555	n	y	2	8.565377e+04	S_{sa}	ssa	3[2]
4	058.554	n	y	2	5.006949e+03	S_{ta}	sta	4[2]
7	065.455	n	y	2	9.725014e+04	Mm	mm	5
9	065.555	n	y[3]	3	1.042363e+04	^{3}Mm	d3mm	6
11	073.555	n	y	2	1.613284e+04	M_{sf}	msf	7
13	075.555	n	y	2	1.841040e+05	M_f	mf	8
17	085.455	n	y	2	3.525008e+04	M_{tm}	mtm	9
20	125.755	n	y	2	1.298572e+04	$2Q_1$	2q1	10
21	127.555	n	y	2	1.565932e+04	σ_1	sig1	11
	135.555	n	y	3	2.504000e+03	$^3Q_1$	d3q1	12
23	135.655	n	y	2	9.813054e+04	Q_1	q1	13
24	137.455	n	y	2	1.862609e+04	ρ_1	rho1	14
	145.655	n	y	3	1.280000e+03	$^3O_1$	d3o1	15
26	145.555	n	y	2	5.125255e+05	O_1	o1	16
27	147.555	n	y	2	6.680540e+03	τ_1	tau1	17
29	155.555	n	y	3	7.832888e+03	$^3M_1$	d3m1	18
30	155.655	n	y	2	4.028717e+04	M_1	m1	19
32	157.455	n	y	2	7.709119e+03	χ_1	chi1	20
33	162.556	y	n	2	1.393773e+04	π_1	pi1	21
34	163.555	y	y	2	2.384377e+05	P_1	p1	22
35	164.555	y[4]	n	2	5.636309e+03	S_1	s1	23
37	165.555	y	y	2	7.205113e+05	K_1	k1	24
39	166.554	y	n	2	5.638973e+03	ψ_1	psi1	25
40	167.555	n	y	2	1.025988e+04	ϕ_1	phi1	26
41	173.655	n	y	2	7.706830e+03	θ_1	tet1	27
42	175.455	n	y	2	4.030173e+04	J_1	j1	28
	175.555	n	y	3	3.859000e+03	$^3J_1$	d3j1	29
44	183.555	n	y	2	6.683724e+03	SO_1	so1	30
45	185.555	n	y	2	2.204454e+04	OO_1	oo1	31
47	227.655	n	y	2	9.129880e+03	ϵ_2	eps2	32
	235.655	n	y	3	2.086800e+03	$^32N_2$	d32n2	33
48	235.755	n	y	2	3.130700e+04	$2N_2$	2n2	34
49	237.555	n	y	2	3.778507e+04	μ_2	mu2	35
50	245.555	n	y	3	7.604162e+03	$^3N_2$	d3n2	36
52	245.655	n	y	2	2.365822e+05	N_2	n2	37
53	247.455	n	y	2	4.494047e+04	ν_2	nu2	38
55	255.555	y	y	2	1.235635e+06	M_2	m2	39
	255.655	n	y	3	1.1463000+03	$^3M_2$	d3m2	40
56	263.655	n	y	2	9.111517e+03	λ_2	la2	41
57	265.455	n	y	2	3.492889e+04	L_2	l2	42
58	265.555	n	y	3	7.013920e+03	$^3L_2$	d3l2	43
60	272.556	y	n	2	3.360070e+04	T_2	t2	44
61	273.555	y	y	2	5.748299e+05	S_2	s2	45
	274.554	y	n	2	/	R_2	r2	46
62	275.555	y	y	2	1.561924e+05	K_2	k2	47
65	285.455	n	y	2	8.737090e+03	η_2	eta2	48
	345.655	n	y	3	4.102100e+03	$^3MN_3$	d3mn3	49
66	355.555	n	y	3	1.496874e+04	$^3M_3$	d3m3	50
	375.555	n	y	3	1.950000e+03	$^3MK_3$	d3mk3	51
	381.555	y	n	/	/	T_3	t3	52
	382.555	y	n	/	/	S_3	s3	53
	383.555	y	n	/	/	R_3	r3	54
	491.555	y	n	/	/	S_4	s4	55
	5A0.555	y	n	/	/	S_5	s5	56
	6BZ.555	y	n	/	/	S_6	s6	57

[1] : Simulated as selfconsitent equilibrium tide ($\frac{1}{12}^\circ$-grid); [2] : Simulated on $\frac{1}{3}^\circ$-grid
[3] : Long-period degree-3 tides are considered with a constant admittance approach
[4] : The atmospheric S_1 tide possesses the Doodson number 164.556, while the oceanic S_1 tide follows Doodson/Schureman-convention, cf. Appendix of Ray and Egbert (2004).

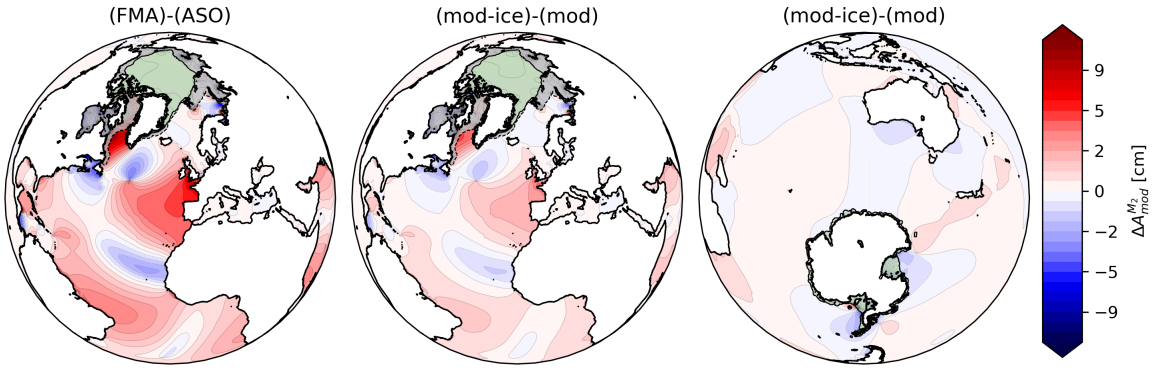

Figure F.1: M_2 amplitude-differences $\Delta A^{M_2}_{mod}$ between the seasonal (FMA) and (ASO) experiments (left) and between the (mod-ice) and (mod) on the Northern and Southern Hemisphere (mid/right). The (ASO) ice-mask is presented as green shading, while the (FMA) ice-mask is presented as gray shading. Both masks are identical in the Southern Hemisphere, as seasonal changes were only considered in the Panarctic region.

F Impact of Sea Ice Friction

The newly implemented sea ice friction parameterization[6] (6.1) depends on the spatial distributions of the parameters r_{ice}, f_{ice}, and $\mathbf{v}_{\text{ice}}$. While $r_{\text{ice}} = r = 0.003$ is set constant, the ice mask f_{ice} and drift velocity $\mathbf{v}_{\text{ice}}$ are constructed from a data set obtained from Copernicus Marine Services (`https://doi.org/10.48670/moi-00007`), where monthly mean values are averaged over the period Jan 1995 – Dec 2019 to obtain climatological mean values for winter (FMA) and summer (ASO). The fractional ice cover is rounded to 1 or 0, not allowing for intermediate values (cf. Figure 6.1a, b). The data set shows clear deviations between winter and summer mean that induce seasonal variations of the tidal solutions (cf. Figure F.1, left). Therefore, the presented solutions, *mod-ice* and *mod-ice-v*, are constructed as annual mean values of winter and summer solutions.

The most notable impact of sea ice friction is observed when it occurs in Hudson Bay and Hudson Straight with large-scale effects on the North Atlantic oscillation systems, both in seasonal fluctuations and the mean M_2 tide (cf. Figure F.1) as discussed, *e.g.*, by Müller et al. (2014). In addition, we consider ice friction of the Antarctic shelf ice constructed from the RTopo-2 data set.

Seasonal sea ice cover in the Southern Hemisphere is not considered but could, in principle, be included in subsequent studies. Validation with OBP and FES14 data only yields improvements on the mm-level when considering ice friction, where allowing for ice drift is even more insignificant (files 2 and 3 of Table F.1). Intercomparisons between experiments *mod* to *mod-ice-v* indicate a mean deviation between 2 mm (deep ocean) and 8 mm (global ocean), which must be seen in relation to the M_2 signal rms, which is on the order of 300 mm.

We conclude that the considered ice friction parameterization induces a seasonal M_2 amplitude variation up to 5 cm, which could be interesting for studying seasonally induced, annual satellite lines. Global mean deviations are yet tiny with respect to the mean

[6]This Appendix originates from the Supporting Information of Sulzbach et al. (2023).

Table F.1: rms-differences of individual simulation experiments and reference data sets for the present-day M_2 partial tide in cm. The labels d/g mark the evaluation over a non-polar, deep ocean domain (d) and the global ocean (g).

	OBP	FES14 (d)	*mod-ice* (d/g)	*mod-ice-v* (d/g)
mod	6.78	6.05	0.24/0.86	0.24/0.87
mod-ice	6.75	5.98	/	0.01/0.03
mod-ice-v	6.74	5.99	/	/

amplitude. Hence, the effect of ice friction is not considered within Chapter 6, which which focuses on the more pronounced large-scale evolution of paleotidal levels.

G Estimating Spring/Neap Tidal Levels

To derive estimates for the spring/neap-cycle[7] related parameters MLWS, MHWS, MLWN, and MHWN from given the given set of 8 partial tides, we employ the auxiliary functions

$$p_{\pm} = \frac{f_{\pm}(A^{\mathrm{O_1}}_{\mathrm{mod}}, A^{\mathrm{K_1}}_{\mathrm{mod}}) \sqrt{(A^{\mathrm{K_1}}_{\mathrm{mod}})^2 + (A^{\mathrm{O_1}}_{\mathrm{mod}})^2} \; + \; f_{\pm}(A^{\mathrm{S_2}}_{\mathrm{mod}}, A^{\mathrm{M_2}}_{\mathrm{mod}}) \sqrt{(A^{\mathrm{S_2}}_{\mathrm{mod}})^2 + (A^{\mathrm{M_2}}_{\mathrm{mod}})^2}}{\sqrt{(A^{\mathrm{K_1}}_{\mathrm{mod}})^2 + (A^{\mathrm{O_1}}_{\mathrm{mod}})^2} \; + \; \sqrt{(A^{\mathrm{S_2}}_{\mathrm{mod}})^2 + (A^{\mathrm{M_2}}_{\mathrm{mod}})^2}} \; , \tag{G.1}$$

with $f_{\pm}(a,b) = |a \pm b|/\max(a,b)$. These dimensionless factors ($\pm$: spring/neap) fulfill the condition $0 \leq p_- \leq 1 \leq p_+ \leq 2$. The idea is to weigh the maximum possible constructive interference, $|a+b|$ of the two dominant partial tides per band (M_2 and S_2 vs. O_1 and K_1) with the respective mean quadratic amplitude per tidal band for an estimate of the spring tide modification. Correspondingly, the respective neap tide values relate to the minimum possible amplitude through destructive interference $|a-b|$.

H Linear Admittance Assumptions for Tidal Dissipation

The mean energy dissipation[7] $\overline{D}_i$ by a certain partial tide i equals the respective mean tidal energy consumption and can be estimated by the global integral

$$\overline{D}_i = \rho_{\mathrm{sw}} \int dA \, \overline{\boldsymbol{\nabla} V^{ilm}_{\mathrm{tid}}(\boldsymbol{x}, \omega_i\, t) \, \cdot \, \mathbf{V}^i(\boldsymbol{x}, \omega_i\, t)} \; , \tag{H.1}$$

where $\mathbf{V}^i = H\,\mathbf{v}^i$ is the tidal transport and V^{ilm}_{tid} the respective partial tide generating potential. We only consider partial tides of second-degree as higher-degree tides (*e.g.*, degree-3) only dissipate energy to a negligible extent (< 1 GW) (Sulzbach et al., 2022c). Thus, we set

$$V^{ilm}_{\mathrm{tid}}(\boldsymbol{x}, \omega_i t) \; = \; \alpha^{\mathrm{b}}_2(\omega_i)\, A_i \, (Y_{2m}(\boldsymbol{x}) \, \cos[\omega_i\, t] \; - \; Y_{2\,-m}(\boldsymbol{x}) \, \sin[\omega_i\, t]) \; , \tag{H.2}$$

[7]This Appendix originates from the Appendix of Sulzbach et al. (2023).

introducing the factor $\alpha_2^{\mathrm{b}}(\omega_i) = 1 + k_2(\omega_i) - h_2(\omega_i)$, a combination of body tide Love numbers, the amplitude factor $A_i(\omega_i)$, and the real-valued, fully-normalized spherical harmonic functions $Y_{lm}(\boldsymbol{x})$ as defined in Heiskanen and Moritz (1967). Please note that $\alpha_2^{\mathrm{b}}(\omega_i)$ is a frequency-dependent factor due to the NDFW-resonance and experiences considerable variations for some diurnal tides (*e.g.*, K_1). Further, we assume linear admittance of the tidal velocities $\mathbf{v}^i$ setting

$$\mathbf{v}^i(\boldsymbol{x}, \omega_i t) \;=\; A_i\, \alpha_2^{\mathrm{b}}(\omega_i) \left[\left(\mathbf{v}_0^{\cos}(\boldsymbol{x}) + \mathbf{v}_1^{\cos}(\boldsymbol{x})\, \omega_i\right) \cos\omega_i t \;+\; \left(\mathbf{v}_0^{\sin}(\boldsymbol{x}) + \mathbf{v}_1^{\sin}(\boldsymbol{x})\, \omega_i\right) \sin\omega_i t \right] . \tag{H.3}$$

Employing the latter equation, the mean values in Equation (H.1) can be calculated, resulting in Equation (6.4), which is then fitted to the data points obtained from M_2, K_2, O_1, and K_1. While this 2-point evaluation per tidal band helps to sharpen the image of global tidal dissipation, it increases the uncertainty of the obtained result, as admittance is only approximately linear. The precision of this result can be improved by simulating more partial tides and considering a piece-wise steady approximation of the admittance function. Within the current approach, Q_1 and N_2 inherit the largest uncertainty, as they possess the most prominent frequency difference from the simulated tides.

I Partial Tide Amplitudes Since the Last Glacial Maximum

In this study, the calculation of tidal levels[8] is based on four partial tides (M_2, K_2, O_1, K_1) that are explicitly simulated and four partial tides (S_2, N_2, P_1, Q_1) that are derived by linear admittance. Changes in their global amplitude patterns are presented in this section to facilitate comparisons to prior studies, which often discuss individual partial tides. The following plots feature changes in tidal amplitudes of 8 partial tides, which comprise the tidal levels discussed in the main article. In addition, the relative deviation of the mean amplitude with respect to present-day conditions, δr, is added.

Different patterns are observed in the following figures. While K_1 and P_1 show a weak strengthening of the Antarctic Kelvin wave under glacial conditions, as reported by, *e.g.*, Uehara et al. (2006) and Griffiths and Peltier (2009), O_1 and Q_1 show a more pronounced global resonance. This resonance is likely to be driven by a single ocean normal mode (cf. Figure 2.7, 26.19h-mode), known to dominate the diurnal tidal dynamics (Müller, 2007).

Similarly, the glacial resonance is most potent for M_2 and N_2 and much weaker pronounced for K_2 and S_2, showing reduced amplitudes in the Pacific Ocean. Overall, the plots suggest that individual constituents of the same tidal band can show quite different changes under glacial conditions in terms of spatial patterns and also the mean amplitude. While, *e.g.*, the mean amplitude M_2 and N_2 increases up to $+44\%$, S_2 and K_2 are reduced by -10%. The same holds for K_1 and O_1, which increase only by 11% and up to $+43\%$, respectively.

[8] This Appendix originates from the Supporting Information of Sulzbach et al. (2023).

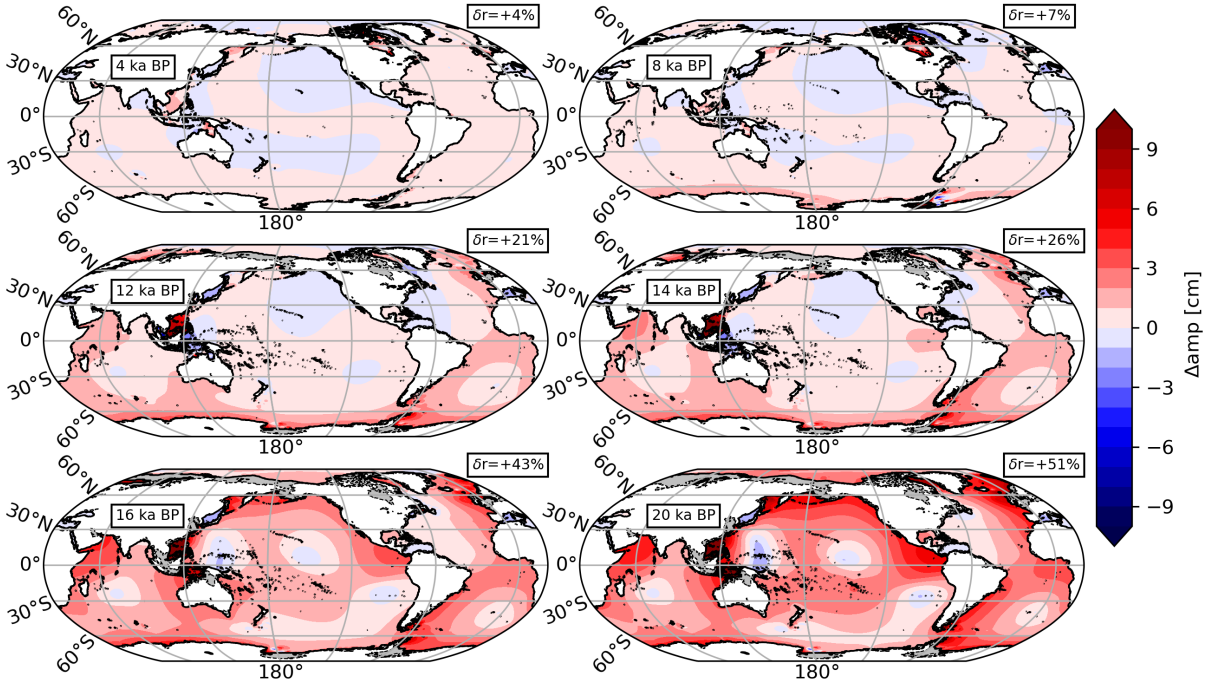

Figure I.1: Amplitude change of the Q_1 tide with respect to present-day conditions

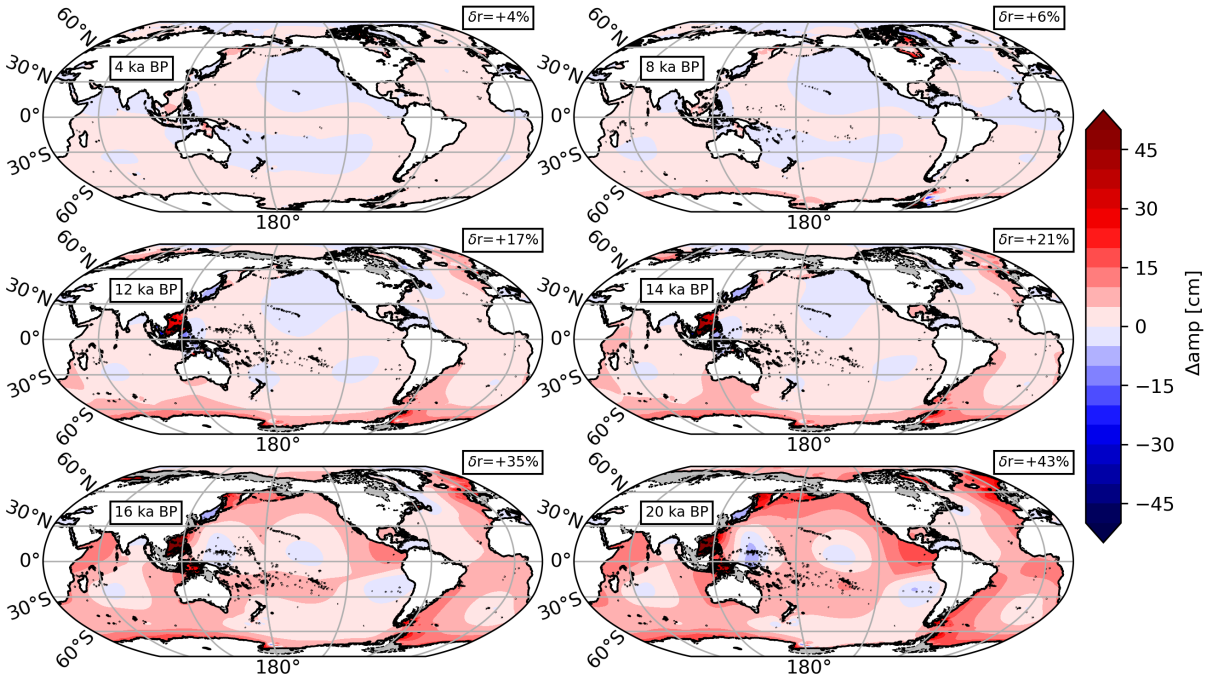

Figure I.2: Amplitude change of the O_1 tide with respect to present-day conditions

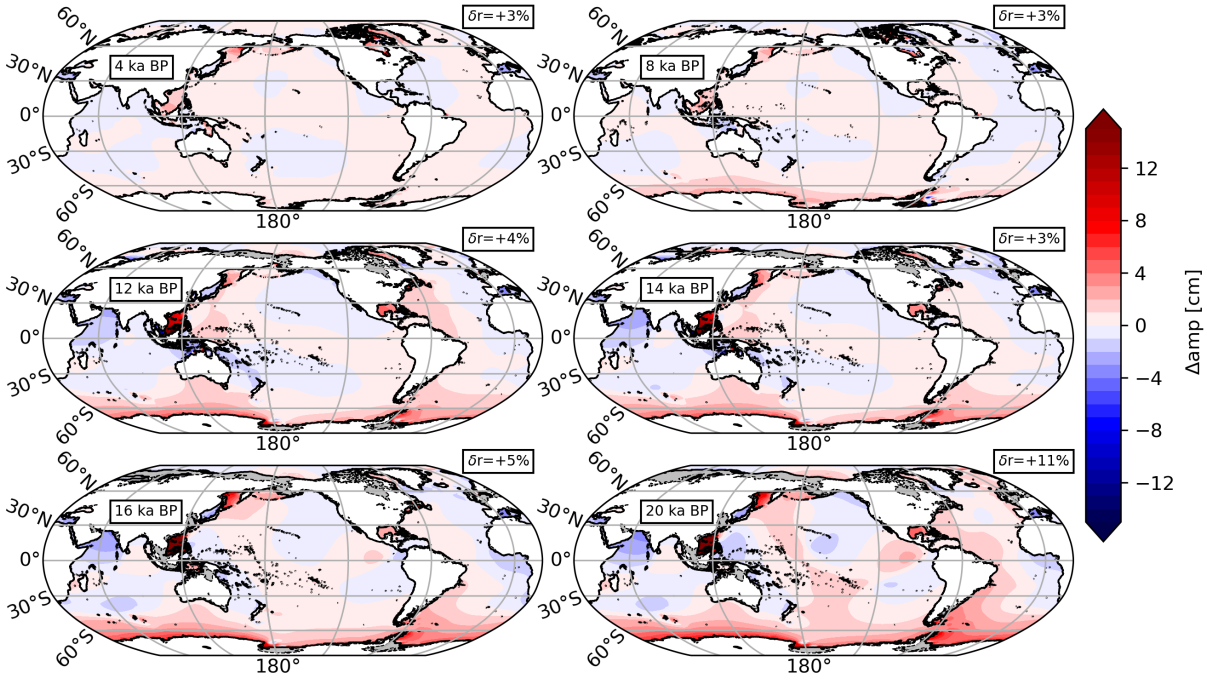

Figure I.3: Amplitude change of the P_1 tide with respect to present-day conditions

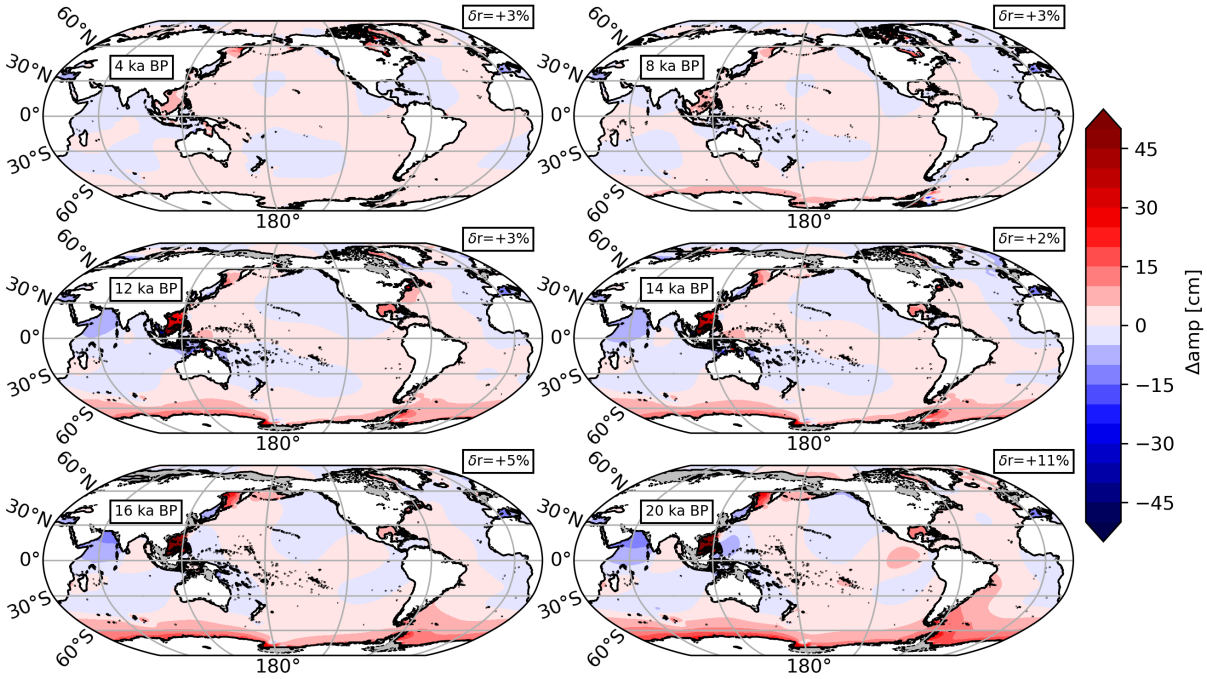

Figure I.4: Amplitude change of the K_1 tide with respect to present-day conditions

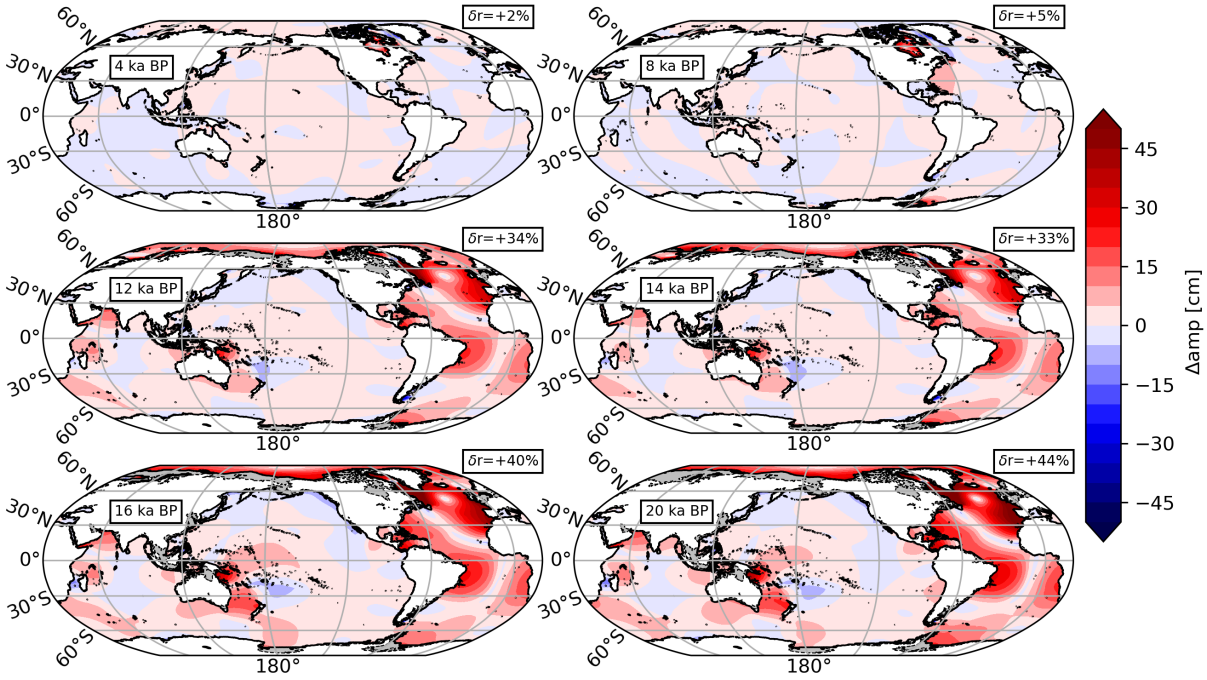

Figure I.5: Amplitude change of the N_2 tide with respect to present-day conditions

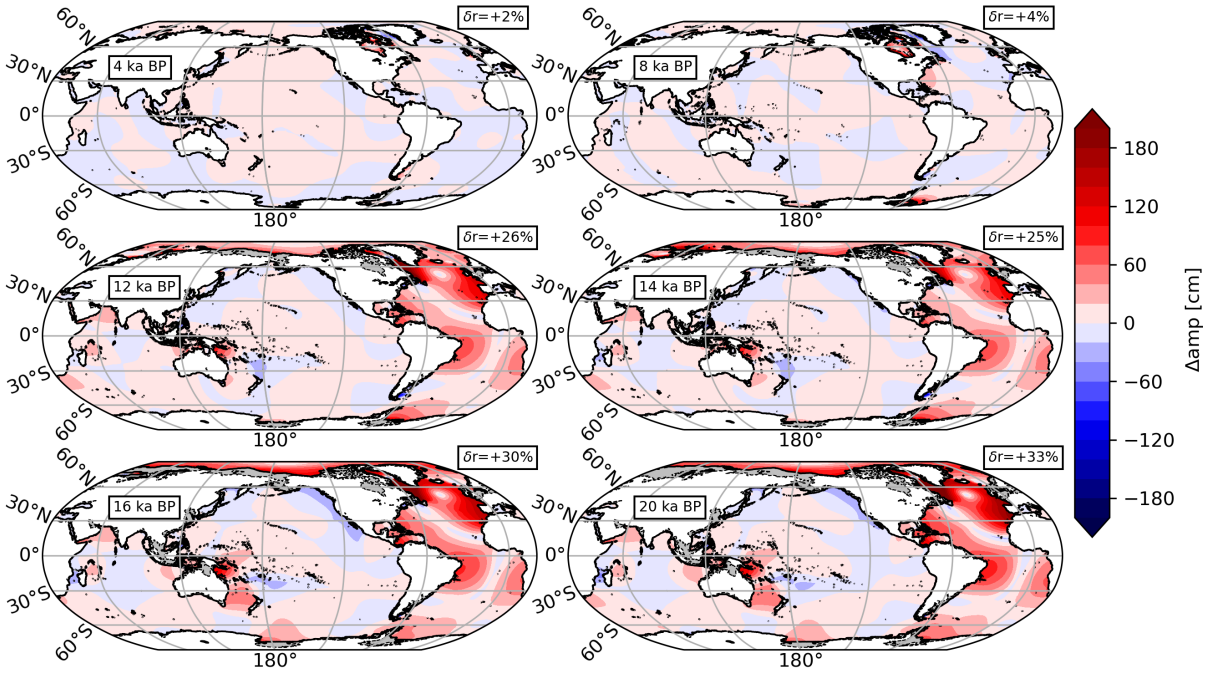

Figure I.6: Amplitude change of the M_2 tide with respect to present-day conditions

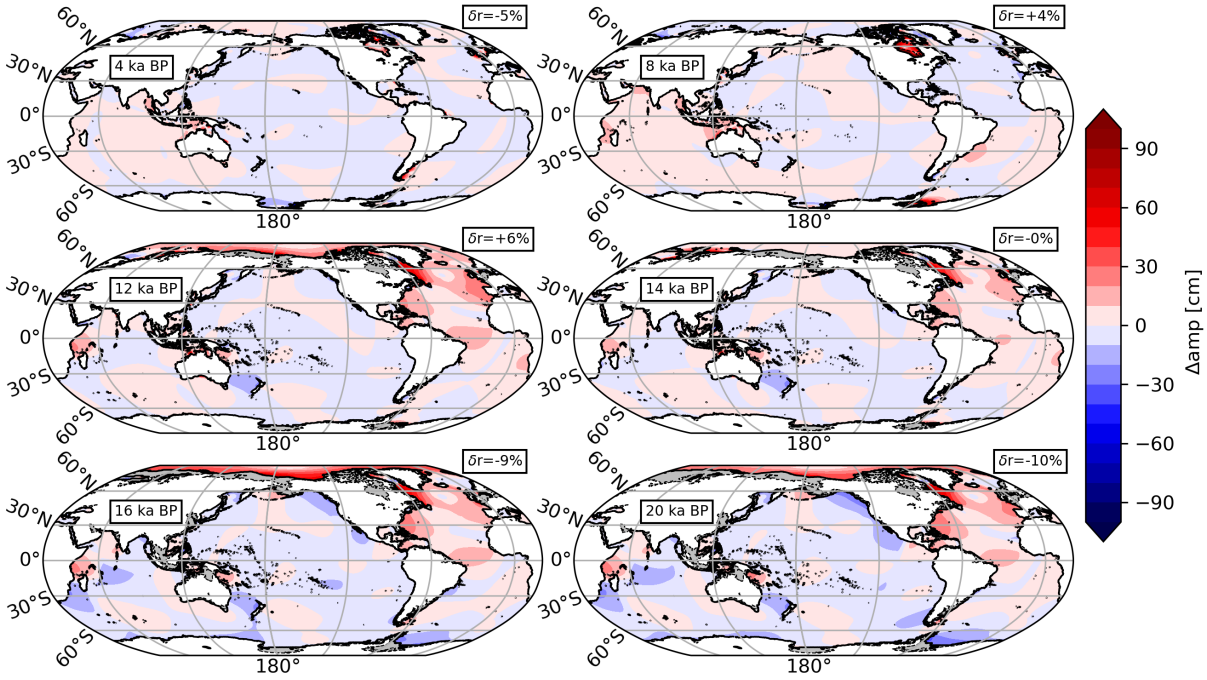

Figure I.7: Amplitude change of the S_2 tide with respect to present-day conditions

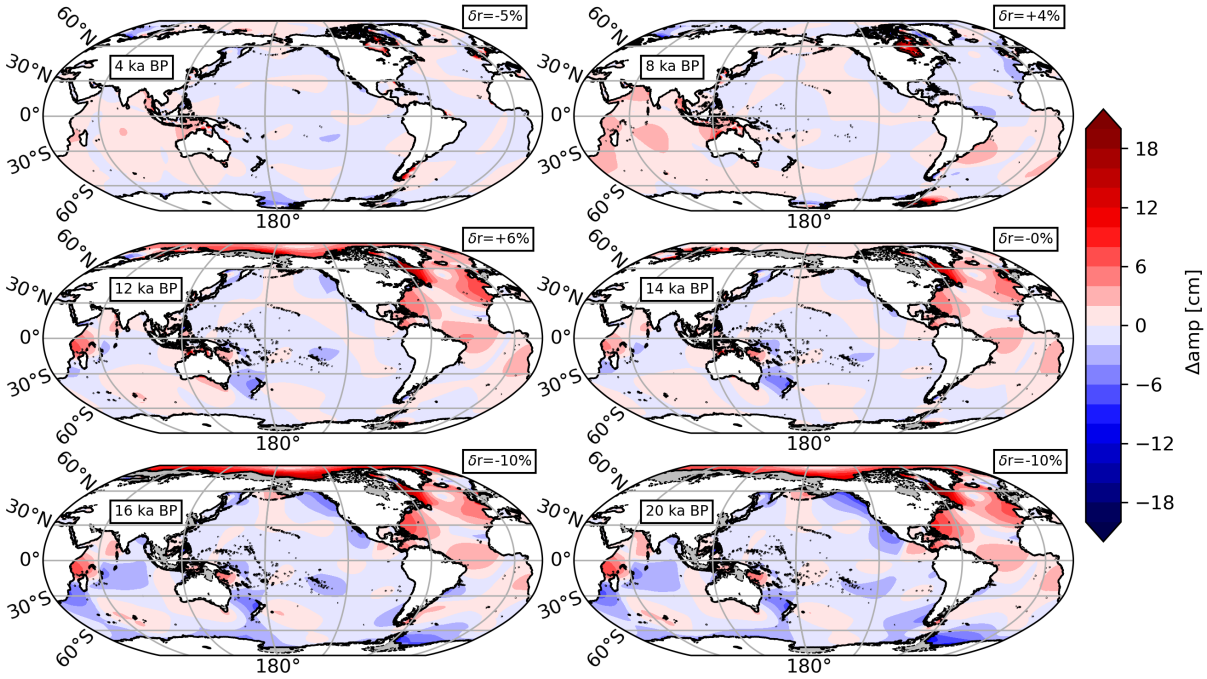

Figure I.8: Amplitude change of the K_2 tide with respect to present-day conditions

List of Figures

Nomenclature

Abbreviations

AMOC	**A**tlantic **M**eridional **O**verturning **C**irculation
arc	Standard grid with North Pole in the **Arc**tic Ocean
aus	Rotated grid with poles in the Atlantic Ocean and **Aus**tralia
B/A	**B**ølling/**A**llarød interstadial
BP	**B**efore **P**resent
CDO	**C**limate **D**ata **O**perators
CFL	**C**ourant–**F**riedrichs–**L**ewy
chi	Rotated grid with poles in **Chi**na and Argentina
cpd	**c**ycles **p**er **d**ay
cpy	**c**ycles **p**er **y**ear
CHAMP	**CHA**llenging **M**inisatellite **P**ayload
con	**con**servative interpolation
CRA	**C**orrelation **R**MSE **A**mplifier
CSL	**C**aspian–**S**ea–**L**evel
DKRZ	**D**eutsches **K**lima **R**echen**Z**entrum
ERP	**E**arth **R**otation **P**arameters
FCN	**F**ree **C**ore **N**utation
GIA	**G**lacial **I**sostatic **A**djustment
GMSL	**G**lobal **M**ean **S**ea **L**evel
GNSS	**G**lobal **N**avigation **S**atellite **S**ystem
GRACE(-FO)	**G**ravity **R**ecovery and **C**limate **E**xperiment (**F**ollow-**O**n)
gre	Rotated grid with poles in **Gre**enland and Antarctica
HAT	**H**ighest **A**stronomical **T**ide
HW95	Harmonic development of the TGP by **H**artmann and **W**enzel (19**95**)
IGETS	**I**nternational **G**eodynamics and **E**arth **T**ide **S**ervice
inv-con	**inv**erse-**con**servative interpolation
IPCC	**I**ntergovernmental **P**anel on **C**limate **C**hange
IR	**I**ndicative **R**ange
LAAL	**L**and-bound **A**tmospheric **A**ttraction and **L**oading
LGM	**L**ast **G**lacial **M**aximum
LLN	**L**oad **L**ove **N**umber
LLR	**L**unar **L**aser **R**anging
LOD	**L**ength **O**f **D**ay

LTE	**L**aplace **T**idal **E**quations
MHW	**M**ean **H**igh **W**ater
MHHW	**M**ean **H**igher **H**igh **W**ater
MHWN	**M**ean **H**igh **W**ater **N**eaps
MHWS	**M**ean **H**igh **W**ater **S**prings
MLW	**M**ean **L**ow **W**ater
MLLW	**M**ean **L**ower **L**ow **W**ater
MLWN	**M**ean **L**ow **W**ater **N**eaps
MLWS	**M**ean **L**ow **W**ater **S**prings
NDFW	**N**ear-**D**iurnal **F**ree **W**obble
NSE	**N**avier-**S**tokes **E**quations
OAAL	**O**cean-bound **A**tmospheric **A**ttraction and **L**oading
OBP	**O**cean **B**ottom **P**ressure
OGCM	**O**cean **G**eneral **C**irculation **M**odel
OTD	**O**cean **T**idal **D**ynamics
PDE	**P**artial **D**ifferential **E**quation
PREM	**P**reliminary **R**eference **E**arth **M**odel
roi	**r**egion **o**f **i**nterest
RSL	**R**elative **S**ea **L**evel
SAL	**S**elf-**A**ttraction and **L**oading
SEQT	**S**elf-consistent **EQ**uilibrium **T**ide
SG	**S**uperconducting **G**ravimeter
SHTns	High performance **S**pherical **H**armonic **T**ransform for **n**umerical **s**imulations
SLIP	**S**ea-**L**evel **I**ndex **P**oint
SLR	**S**atellite **L**aser **R**anging
SNR	**S**ignal-to-**N**oise **R**atio
SNREI	**S**pherical, **N**on-**R**otating, **E**lastic, **I**sotropic
SOR	**S**ucessive **O**ver-**R**elaxation
SPOTL	**S**ome **P**rograms for **O**cean-**T**ide **L**oading
SSH	**S**ea **S**urface **H**eight
SWE	**S**hallow-**W**ater **E**quations
TG	**T**ide **G**auge
TGP	**T**ide-**G**enerating **P**otential
TiME	**Ti**dal **M**odel forced by **E**phemerides
T/P	**T**opex/**P**oseidon
TRP	**T**ide-**R**aising **P**otential
TT	**T**errestrial **T**ime
UV	**U**ltra**V**iolet
VLBI	**V**ery-**L**ong-**B**aseline **I**nterferometry
WOA	**W**orld **O**cean **A**tlas

List of Symbols

Symbol	Definition
$\partial_\mathrm{x} = \frac{\partial}{\partial_\mathrm{x}}$	Partial derivative after x
$\vec{\nabla}\vec{f}, \vec{\nabla}\cdot\vec{f}, \vec{\nabla}\times\vec{f}$	Nabla: Gradient of $\vec{f}$, Divergence of $\vec{f}$, Rotation of $\vec{f}$
$\overline{\mathrm{x}(t)} = \overline{\mathrm{x}}$	Average of $\mathrm{x}(t)$
α	Rotation angle from rotated to unrotated grid
α_l	Combination of load Love numbers for SAL
$\mathbf{a}_\mathrm{atm}$	Tide-generating acceleration exerted by the atmopshere
$\mathbf{a}_\mathrm{bf}$, $\mathbf{a}_\mathrm{wd}$, $\mathbf{a}_\mathrm{ed}$, $\mathbf{a}_\mathrm{ice}$	Frictional tidal accelerations
a_i^{lm}	Amplitude of the partial TRP of degree l and order m
a_l^b	Combination of body tide Love numbers for the TRP
A_i	Amplitude of the partial TGP component i
A_h	Horizontal eddy viscosity coefficient
$c(, c_\mathrm{s})$	Mean captured signal fraction (per individual station)
c_m	Darwin's correction
c_sw	Shallow-water wave speed
$\boldsymbol{\mathcal{C}}$	Wave drag tensor
$\mathbb{C}$	Complex numbers
$\delta\lambda$	Zonal resolution
$\delta\phi$	Meridional resolution
δ_{ij}	Kronecker-δ
$\delta(\mathrm{x})$	Dirac-δ function
Δt	Temporal resolution of the SOR solver
$\Delta\mathrm{x}(, \Delta\mathrm{x}^\mathrm{min})$	(Mininum) spatial resolution of the numerical grid
$\Delta\phi_{NP}, \Delta\phi_{SP}$	Radius of the North Pole/South Pole region of the grid
d	Mean Earth-Moon distance
$\mathrm{d} = 86164$ s	Sidereal day
$d\Omega$	Solid angle element
d_i	Spatial tidal dissipation density by mechanism i
$D_i = \int_O dA\, d_i$	Global tidal dissipation rate by mechanism i
$\mathbb{D}(, \mathbb{D}_\mathrm{lin})$	(Linearized) tidal dissipation operator
$\mathbf{e}_\mathrm{N}$, $\mathbf{e}_\mathrm{N}$'	Unit vector in North direction
$\mathbf{e}_\mathrm{vert}$	Vertical unit vector
$\boldsymbol{f}$	Vertical Coriolis vector
f_ice	Fractional sea ice cover
f_NDFW	Frequency of the near-diurnal free wobble
$g_0 = 9.80665\ \frac{\mathrm{m}}{\mathrm{s}^2}$	Mean vertical surface gravity
$g_\perp$	Vertical gravity field component on the Earth surface
$\boldsymbol{g}$	Gravity field
g^i_cos, g^i_sin	In-phase/quadrature component of the vertical surface gravity for partial tide i
H	Bathymetric depth
im	imaginary unit $\mathrm{i} = \sqrt{-1}$
$\mathrm{Im}(\mathrm{x})$	Imaginary part of $\mathrm{x} \in \mathbb{C}$

κ_{w}	Weighting coefficient of the wave drag tensor
λ	Geographical longitude
λ_{p}	Longitude of the rotated pole
l	Degree of the spherical harmonic function Y_{lm}
$l_{\max}$	Maximum degree of the harmonic development
m	Order of the spherical harmonic functions Y_{lm}
M_{ext}^{j}	Mass of celestial body j
$M_{\mathrm{l}}, M_{\mathrm{o}}$	Land mask/ocean mask
$\mathbf{N}$	Nonlinear ocean tide contributions
N	Ocean buoyancy frequency
N_{b}	Ocean bottom buoyancy frequency
ω_i	Tidal angular velocity of tide i
ω_k^{eig}	Eigenfrequency of ocean normal mode k
$\Omega_{\mathrm{e}} = 2\pi \mathrm{d}^{-1}$	Mean angular velocity of the Earth's rotation
O	Domain including the entire ocean
ϕ	Geographical latitude
ϕ_{p}	Latitude of the rotated pole
ϕ_i^m	Phase of the partial TRP of order m
$\mathbf{p}$	Tidal energy flux vector
p_{atm}	Atmopsheric surface pressure
$\overline{P}_{lm}$	Fully-normalized Legendre Polynomials
q_j^i	j-th Doodson multiplier of partial tide i
$\rho_{\mathrm{se}} = 5510\ \frac{\mathrm{kg}}{\mathrm{m}^3}$	Mean density of the solid Earth
$\rho_{\mathrm{sw}} = 1024\ \frac{\mathrm{kg}}{\mathrm{m}^3}$	Mean density of sea water
$r = 0.003$	Turbulent bottom friction coefficient
$r_{\mathrm{ice}} = 0.003$	Turbulent ice friction coefficient
$\boldsymbol{r}_{lm\mu}$	Rotation tensor for spherical harmonic function Y_{lm}
$\mathbb{R}$	Real numbers
Re(x)	Real part of x $\in \mathbb{C}$
$R_{\mathrm{e}} = 6371$ km	Earth radius
rms, RMS	Root-mean-square (error)
$\hat{\mathbf{R}}\mathbf{v}$	Horizontal eddy viscosity acceleration
$s(, s_s)$	Mean tidal signal (per individual station)
$\Theta_H(\mathrm{x})$	Heaviside-Function
t	General time variable
$T = 2\pi\omega^{-1}$	Tidal period
$\boldsymbol{T}_\alpha$	Rotation matrix for vectorial quantities on rotated grids
$\mathbf{v}$	Ocean tidal flow velocity vector
u	Ocean tidal flow velocity: East component
v	Ocean tidal flow velocity: North component
$\mathbf{v}_{\mathrm{ice}}$	Ice drift velocity
$\mathbf{v}_{\mathrm{rel}}$	Relative velocity of sea ice and the ocean
$\mathbf{V} = H\mathbf{v}$	Ocean tidal transport
V_+	Semi-major axis of the tidal transport ellipse
V_{atm}	Combination of the entity of primary and secondary atmospheric potentials

V_{grav}	Astronomical Tide-Generating Potential
$V_{\text{l}}, V_{\text{o}}$	Land-bound/ocean-bound atmospheric potential
V_{p}	Atmospheric surface pressure potential
V_{SAL}	Self-Attraction and Loading potential
V_{tid}	Tide-Raising Potential
V_{tid}^{ilm}	Partial TRP of degree l and order m
$\boldsymbol{W}$	Wind-stress acceleration
W	Global tidal energy consumption
w_{f}	Energy dissipation fraction by wave drag
χ_i	Astronomical phase argument of partial tide i
$\mathbf{x}$	General position vector
Y_{lm}	Spherical harmonic function
yr	Julian year
ζ	Sea surface anomaly with respect to the undisturbed geoid height
$\boldsymbol{\zeta} = (\zeta, \mathbf{v})$	Barotropic ocean state vector
ζ_{cos}^{i}, ζ_{sin}^{i}	In-phase/quadrature component of the SSH-elevation for partial tide i
$\tilde{\boldsymbol{\zeta}}_k(, \tilde{\boldsymbol{\zeta}}_k^{ad})$	k-th (adjoint) ocean normal mode
$\zeta_{\text{b}}, \boldsymbol{\zeta}_{\text{h}}$	Vertical/horizontal displacement of the Earth's crust by ocean tidal loading
ζ_h^+	Semi-major axis of the vertical displacement ellipse
ζ_{eq}	Equlibrium tidal height induced by the TRP
ζ_{seqt}	Tidal height of the self-consistent equilibrium tide
ζ_{SAL}	Equlibrium tidal height induced by SAL
Z_{lm}	Ocean tide admittance function of degree l and order m
Z_{lm}^{*}	Surface gravity admittance function of degree l and order m

Bibliography

Abe-Ouchi, A., Saito, F., Kawamura, K., Raymo, M. E., Okuno, J., Takahashi, K., and Blatter, H.: Insolation-driven 100,000-year glacial cycles and hysteresis of ice-sheet volume, Nature, 500, 190–193, doi:10.1038/nature12374, 2013.

Abrykosov, P., Sulzbach, R., Pail, R., Dobslaw, H., and Thomas, M.: Treatment of ocean tide background model errors in the context of GRACE/GRACE-FO data processing, Geophysical Journal International, 228, 1850–1865, doi:10.1093/gji/ggab421, 2021.

Accad, Y. and Pekeris, C. L.: Solution of the tidal equations for the M2 and S2 tides in the world oceans from a knowledge of the tidal potential alone, Philosophical Transactions of the Royal Society of London Series A, 290, 235–266, doi:10.1098/rsta.1978.0083, 1978.

Agnew, D. C.: NLOADF: A program for computing ocean-tide loading, Journal of Geophysical Research, 102, 5109–5110, 1997.

Agnew, D. C.: Earth tides, in: Treatise on Geophysics - Geodesy, vol. 3, pp. 163–196, doi:10.1029/RG013i003p00260, 2007.

Agnew, D. C.: SPOTL : Some programs for ocean-tide loading, Scripps Institution of Oceanography Technical Report, URL `https://escholarship.org/uc/item/954322pg`, 2012.

Amante, C. and Eakins, B.: ETOPO1 1 arc-minute global relief model: procedures, data sources and analysis., NOAA Technical Memorandum NESDIS NGDC-24. National Geophysical Data Center, NOAA., doi:10.7289/V5C8276M, 2009.

Anaconda: Anaconda software distribution - documentation (2020), URL `https://docs.anaconda.com/`, 2020.

Andersen, O. B.: Global ocean tides from ERS 1 and TOPEX/POSEIDON altimetry, Journal of Geophysical Research, 100, 25 249–25 259, doi:10.1029/95JC01389, 1995.

Arbic, B. K.: Atmospheric forcing of the oceanic semidiurnal tide, Geophysical Research Letters, 32, L02 610, doi:10.1029/2004GL021668, 2005.

Arbic, B. K. and Garrett, C.: A coupled oscillator model of shelf and ocean tides, Continental Shelf Research, 30, 564–574, doi:10.1016/j.csr.2009.07.008, 2010.

Arbic, B. K., Garner, S. T., Hallberg, R. W., and Simmons, H. L.: The accuracy of surface elevations in forward global barotropic and baroclinic tide models, Deep Sea

Research Part II: Topical Studies in Oceanography, 51, 3069–3101, doi:10.1016/j.dsr2.2004.09.014, 2004a.

Arbic, B. K., MacAyeal, D. R., Mitrovica, J. X., and Milne, G. A.: Ocean tides and Heinrich events, Nature, 432, 460–460, doi:10.1038/432460a, 2004b.

Arbic, B. K., St.-Laurent, P., Sutherland, G., and Garrett, C.: On the resonance and influence of the tides in Ungava Bay and Hudson Strait, Geophysical Research Letters, 34, 1–7, doi:10.1029/2007GL030845, 2007.

Arbic, B. K., Mitrovica, J. X., MacAyeal, D. R., and Milne, G. A.: On the factors behind large Labrador Sea tides during the last glacial cycle and the potential implications for Heinrich events, Paleoceanography, 23, 1–14, doi:10.1029/2007PA001573, 2008.

Arbic, B. K., Karsten, R., and Garrett, C.: On tidal resonance in the global ocean and the back-effect of coastal tides upon open-ocean tides, Atmosphere - Ocean, 47, 239–266, doi:10.3137/OC311.2009, 2009.

Arbic, B. K., Richman, J., Shriver, J., Timko, P., Metzger, E., and Wallcraft, A.: Global modeling of internal tides within an eddying ocean general circulation model, Oceanography, 25, 20–29, doi:10.5670/oceanog.2012.38, 2012.

Arnoso, J., Bos, M. S., Benavent, M., Penna, N. T., and Sainz-Maza, S.: Anelastic response of the Earth's crust underneath the Canary Islands revealed from ocean tide loading observations, Geophysical Journal International, doi:10.1093/gji/ggad205, URL https://doi.org/10.1093/gji/ggad205, ggad205, 2023.

Backhaus, J. O.: A semi-implicit scheme for the shallow water equations for application to shelf sea modelling, Continental Shelf Research, 2, 243–254, doi:10.1016/0278-4343(82)90020-6, 1982.

Backhaus, J. O.: A three-dimensional model for the simulation of shelf sea dynamics, Deutsche hydrographische Zeitschrift, 4, 165–186, doi:10.1007/BF02328975, 1985.

Baker, T. F., Curtis, D. J., and Dodson, A. H.: A new test of Earth tide models in central Europe, Geophysical Research Letters, 23, 3559–3562, doi:10.1029/96GL03335, 1996.

Balidakis, K., Sulzbach, R., Shihora, L., Dahle, C., Dill, R., and Dobslaw, H.: Atmospheric contributions to global ocean tides for satellite gravimetry, Journal of Advances in Modeling Earth Systems, 14, doi:10.1029/2022MS003193, 2022.

Balidakis, K., Sulzbach, R., Dobslaw, H., and Dill, R.: How Do Atmospheric Tidal Loading Displacements Vary Temporally as Well as across Different Weather Models?, pp. 1–6, Springer Berlin Heidelberg, Berlin, Heidelberg, doi:10.1007/1345_2023_201, URL https://doi.org/10.1007/1345_2023_201, 2023.

Barnett, R. L., Charman, D. J., Johns, C., Ward, S. L., Bevan, A., Bradley, S. L., Camidge, K., Fyfe, R. M., Gehrels, W. R., Gehrels, M. J., Hatton, J., Khan, N. S., Marshall, P., Maezumi, S. Y., Mills, S., Mulville, J., Perez, M., Roberts, H. M., Scourse, J. D., Shepherd, F., and Stevens, T.: Nonlinear landscape and cultural response to sea-level rise, Science Advances, 6, eabb6376, doi:10.1126/sciadv.abb6376, 2020.

Bartels, J.: Gezeitenkraefte, Handbuch der Physik, Band XLVIII, Geophysik II., p. 525, 1957.

Barton, K. N., Pal, N., Brus, S. R., Petersen, M. R., Arbic, B. K., Engwirda, D., Roberts, A. F., Westerink, J. J., Wirasaet, D., and Schindelegger, M.: Global barotropic tide modeling using inline Self-Attraction and Loading in MPAS-Ocean, Journal of Advances in Modeling Earth Systems, 14, doi:10.1029/2022MS003207, 2022.

Bell, T. H.: Topographically generated internal waves in the open ocean, Journal of Geophysical Research, 80, 320–327, doi:10.1029/jc080i003p00320, 1975.

Beni, A. N., Lahijani, H., Harami, R. M., Arpe, K., Leroy, S. A., Marriner, N., Berberian, M., Andrieu-Ponel, V., Djamali, M., Mahboubi, A., and Reimer, P. J.: Caspian sea-level changes during the last millennium: Historical and geological evidence from the south Caspian Sea, Climate of the Past, 9, 1645–1665, doi:10.5194/cp-9-1645-2013, 2013.

Berends, C. J., de Boer, B., and van de Wal, R. S. W.: Reconstructing the evolution of ice sheets, sea level, and atmospheric CO_2 during the past 3.6 million years, Climate of the Past, 17, 361–377, doi:10.5194/cp-17-361-2021, 2021.

Bij de Vaate, I., Vasulkar, A. N., Slobbe, D. C., and Verlaan, M.: The influence of Arctic landfast ice on seasonal modulation of the M2 tide, Journal of Geophysical Research: Oceans, 126, doi:10.1029/2020JC016630, 2021.

Bills, B. G., Neumann, G. A., Smith, D. E., and Zuber, M. T.: Improved estimate of tidal dissipation within Mars from MOLA observations of the shadow of Phobos, Journal of Geophysical Research E: Planets, doi:10.1029/2004JE002376, 2005.

Blakely, C. P., Ling, G., Pringle, W. J., Contreras, M. T., Wirasaet, D., Westerink, J. J., Moghimi, S., Seroka, G., Shi, L., Myers, E., Owensby, M., and Massey, C.: Dissipation and bathymetric sensitivities in an unstructured mesh global tidal model, Journal of Geophysical Research: Oceans, 127, doi:10.1029/2021JC018178, 2022.

Blewitt, G.: Self-consistency in reference frames, geocenter definition, and surface loading of the solid Earth, Journal of Geophysical Research: Solid Earth, 108, doi:10.1029/2002jb002082, 2003.

Bos, M. S., Baker, T. F., Lyard, F. H., Zürn, W. E., and Rydelek, P. A.: Long-period lunar Earth tides at the geographic South Pole and recent models of ocean tides, Geophysical Journal International, 143, 490–494, doi:10.1046/j.1365-246X.2000.01260.x, 2000.

Bos, M. S., Penna, N. T., Baker, T. F., and Clarke, P. J.: Ocean tide loading displacements in western Europe: 2. GPS-observed anelastic dispersion in the asthenosphere, Journal of Geophysical Research: Solid Earth, 120, 6540–6557, doi:10.1002/2015JB011884, 2015.

Boy, J.-P., Llubes, M., Hinderer, J., and Florsch, N.: A comparison of tidal ocean loading models using superconducting gravimeter data, Journal of Geophysical Research: Solid Earth, 108, 1–17, doi:10.1029/2002jb002050, 2003.

Boy, J.-P., Llubes, M., Ray, R., Hinderer, J., Florsch, N., Rosat, S., Lyard, F., and Letellier, T.: Non-linear oceanic tides observed by superconducting gravimeters in Europe, Journal of Geodynamics, 38, 391–405, doi:10.1016/j.jog.2004.07.017, 2004.

Boy, J.-P., Ray, R., and Hinderer, J.: Diurnal atmospheric tide and induced gravity variations, Journal of Geodynamics, 41, 253–258, doi:10.1016/j.jog.2005.10.010, 2006.

Boy, J.-P., Barriot, J.-P., Förste, C., Voigt, C., and Wziontek, H.: Achievements of the first 4 years of the International Geodynamics and Earth Tide Service (IGETS) 2015–2019, doi:10.1007/1345_2020_94, 2020.

Breili, K., Hougen, R., Lysaker, D. I., Omang, O. C. D., and Tangen, B.: A new gravity laboratory in Ny-Ålesund, Svalbard, Journal of Geodetic Science, 7, 18–30, doi:10.1515/jogs-2017-0003, 2017.

Bretagnon, P.: Théorie du mouvement de l'ensemble des planètes. Solution VSOP82*, Astron. Astrophys., 114, 278–288, 1982.

Briggs, R. D. and Tarasov, L.: How to evaluate model-derived deglaciation chronologies: a case study using Antarctica, Quaternary Science Reviews, 63, 109–127, doi:10.1016/j.quascirev.2012.11.021, 2013.

Brus, S. R., Barton, K. N., Pal, N., Roberts, A. F., Engwirda, D., Petersen, M. R., Arbic, B. K., Wirasaet, D., Westerink, J. J., and Schindelegger, M.: Scalable Self Attraction and Loading calculations for unstructured ocean tide models, Ocean Modelling, 182, 102 160, doi:10.1016/j.ocemod.2023.102160, 2023.

Buijsman, M. C., Arbic, B. K., Green, J. A., Helber, R. W., Richman, J. G., Shriver, J. F., Timko, P. G., and Wallcraft, A.: Optimizing internal wave drag in a forward barotropic model with semidiurnal tides, Ocean Modelling, 85, 42–55, doi:10.1016/j.ocemod.2014.11.003, 2015.

Cancet, M., Andersen, O., Lyard, F., Schulz, A., Cotton, D., and Benveniste, J.: A new high resolution tidal model in the arctic ocean, European Space Agency, (Special Publication) ESA SP, SP-740, 2016.

Carrere, L., Lyard, F., Cancet, M., and Guillot, A.: FES 2014, a new tidal model on the global ocean with enhanced accuracy in shallow seas and in the Arctic region, EGU General Assembly Conference Abstracts, 17, 5481, URL `http://adsabs.harvard.edu/abs/2015EGUGA..17.5481C`, 2015.

Carrere, L., Faugère, Y., and Ablain, M.: Major improvement of altimetry sea level estimations using pressure-derived corrections based on ERA-Interim atmospheric reanalysis, Ocean Science, 12, 825–842, doi:10.5194/os-12-825-2016, 2016.

Carrère, L. and Lyard, F.: Modeling the barotropic response of the global ocean to atmospheric wind and pressure forcing - comparisons with observations, Geophysical Research Letters, 30, doi:10.1029/2002GL016473, 2003.

Cartwright, D. E.: A subharmonic lunar tide in the seas off Western Europe, Nature, 257, 277–280, doi:10.1038/257277a0, 1975.

Cartwright, D. E.: Robert Paul de Lamanon: An unlucky naturalist, Annals of Science, 54, 585–596, doi:10.1080/00033799700200391, 1997.

Cartwright, D. E.: Tides: A Scientific History, Cambridge University Press, 1999.

Cartwright, D. E. and Ray, R. D.: Observations of the Mf ocean tide from Geosat altimetry, Geophysical Research Letters, 17, 619–622, doi:10.1029/GL017i005p00619, 1990.

Chao, B. F.: On inversion for mass distribution from global (time-variable) gravity field, Journal of Geodynamics, 39, 223–230, doi:10.1016/j.jog.2004.11.001, 2004.

Chapman, S. and Lindzen, R. S.: Atmospheric Tides, Springer Netherlands, doi:10.1007/978-94-010-3399-2, 1970.

Chen, J. L., Pekker, T., Wilson, C. R., Tapley, B. D., Kostianoy, A. G., Cretaux, J. F., and Safarov, E. S.: Long-term Caspian Sea level change, Geophysical Research Letters, 44, 6993–7001, doi:10.1002/2017GL073958, 2017.

Cheng, Y. and Andersen, O. B.: Multimission empirical ocean tide modeling for shallow waters and polar seas, Journal of Geophysical Research: Oceans, 116, 1–11, doi:10.1029/2011JC007172, 2011.

Clark, P. U., Shakun, J. D., Marcott, S. A., Mix, A. C., Eby, M., Kulp, S., Levermann, A., Milne, G. A., Pfister, P. L., Santer, B. D., Schrag, D. P., Solomon, S., Stocker, T. F., Strauss, B. H., Weaver, A. J., Winkelmann, R., Archer, D., Bard, E., Goldner, A., Lambeck, K., Pierrehumbert, R. T., and Plattner, G.-K.: Consequences of twenty-first-century policy for multi-millennial climate and sea-level change, Nature Climate Change, 6, 360–369, doi:10.1038/nclimate2923, 2016.

CLIMAP-Project-Members: Map and Chart Ser. MC-36, Chap. Seasonal reconstruction of the Earth surface at the last glacial maximum, URL `https://www.ncei.noaa.gov/access/paleo-search/study/2516`, 1981.

Cooper, J. A. G., Green, A. N., and Compton, J. S.: Sea-level change in Southern Africa since the Last Glacial Maximum, Quaternary Science Reviews, 201, 303–318, doi:10.1016/j.quascirev.2018.10.013, 2018.

Daher, H., Arbic, B. K., Williams, J. G., Ansong, J. K., Boggs, D. H., Müller, M., Schindelegger, M., Austermann, J., Cornuelle, B. D., Crawford, E. B., Fringer, O. B., Lau, H. C., Lock, S. J., Maloof, A. C., Menemenlis, D., Mitrovica, J. X., Green, J. A., and Huber, M.: Long-term Earth-Moon evolution with high-level orbit and ocean tide models, Journal of Geophysical Research: Planets, 126, 1–39, doi:10.1029/2021JE006875, 2021.

Darwin, G.: Attempted evaluation of the rigidity of the Earth from the tides of long period, in: The scientific papers of Sir George Darwin (2009), pp. 340–346, Cambridge University Press, doi:10.1017/CBO9780511703461.011, 1907.

Darwin, G. H.: The Scientific Papers of Sir George Darwin: Tidal Friction and Cosmogony (2009), Cambridge University Press, doi:10.1017/CBO9780511703478, 1908.

Davies, H. S., Green, J. A. M., and Duarte, J. C.: Back to the future II: Tidal evolution of four supercontinent scenarios, Earth System Dynamics, 11, 291–299, doi:10.5194/esd-11-291-2020, 2020.

Dehant, V., Defraigne, P., and Wahr, J. M.: Tides for a convective Earth, Journal of Geophysical Research: Solid Earth, 104, 1035–1058, doi:10.1029/1998JB900051, 1999.

Dickey, J. O., Bender, P. L., Faller, J. E., Newhall, X. X., Ricklefs, R. L., Ries, J. G., Shelus, P. J., Veillet, C., Whipple, A. L., Wiant, J. R., Williams, J. G., and Yoder, C. F.: Lunar laser ranging: A continuing legacy of the Apollo Program, Science, 265, 482–490, doi:10.1126/science.265.5171.482, 1994.

Dieminger, W., Hartmann, G., and Leitinger, R.: Atmospheric tides, in: The Upper Atmosphere., edited by Dieminger, W., Hartmann, G., and Leitinger, R., pp. 97–108, Springer, Berlin, Heidelberg, 1996.

Dittfeld, J.: Analysis of third degree waves with diurnal and semidiurnal frequencies, Bulletin d'Information des Marees Terrestres, 111, 8053–8061, URL `http://www.bim-icet.org/`, 1991.

Dobslaw, H., Bergmann-Wolf, I., Dill, R., Poropat, L., Thomas, M., Dahle, C., Esselborn, S., König, R., and Flechtner, F.: A new high-resolution model of non-tidal atmosphere and ocean mass variability for de-aliasing of satellite gravity observations: AOD1B RL06, Geophysical Journal International, 211, 263–269, doi:10.1093/GJI/GGX302, 2017.

Doodson, A. T.: The harmonic development of the tide-generating potential, Proceedings of the Royal Society of London, 100, 305–329, doi:10.1098/rspa.1921.0088, 1921.

Doodson, A. T.: The analysis of tidal observations, Philosophical Transactions of the Royal Society of London . Series A , Containing Papers of a Mathematical or Physical Character, 227, 223–279, URL `http://www.jstor.org/stable/91217`, 1928.

Drinkorn, C., Saynisch-Wagner, J., Uenzelmann-Neben, G., and Thomas, M.: Decadal climate sensitivity of contouritic sedimentation in a dynamically coupled ice-ocean-sediment model of the North Atlantic, Palaeogeography, Palaeoclimatology, Palaeoecology, 572, 110 391, doi:10.1016/j.palaeo.2021.110391, 2021.

Ducarme, B.: Determination of the main Lunar waves generated by the third degree tidal potential and validity of the corresponding body tides models, Journal of Geodesy, 86, 65–75, doi:10.1007/s00190-011-0492-9, 2012.

Ducarme, B. and Schüller, K.: Canonical wave grouping as the key to optimal tidal analysis, Bulletin d'Information des Marees Terrestres, 150, 12 131–12 244, URL `http://maregraph-renater.upf.pf/bim/BIM/bim150.pdf`, 2019.

Dushaw, B. D., Egbert, G. D., Worcester, P. F., Cornuelle, B. D., Howe, B. M., and Metzger, K.: A TOPEX/POSEIDON global tidal model (TPXO.2) and barotropic tidal currents determined from long-range acoustic transmissions, Progress in Oceanography, 40, 337–367, doi:10.1016/S0079-6611(98)00008-1, 1997.

Egbert, G. D. and Erofeeva, S. Y.: Efficient inverse modeling of barotropic ocean tides, Journal of Atmospheric and Oceanic Technology, 19, 183–204, doi:10.1175/1520-0426(2002)019<0183:EIMOBO>2.0.CO;2, 2002.

Egbert, G. D. and Ray, R. D.: Significant dissipation of tidal energy in the deep ocean inferred from satellite altimeter data, Nature, 405, 775–778, doi:10.1038/35015531, 2000.

Egbert, G. D. and Ray, R. D.: Estimates of M_2 tidal energy dissipation from TOPEX/Poseidon altimeter data, Journal of Geophysical Research: Oceans, 106, 22 475–22 502, doi:10.1029/2000jc000699, 2001.

Egbert, G. D. and Ray, R. D.: Semi-diurnal and diurnal tidal dissipation from TOPEX/Poseidon altimetry, Geophysical Research Letters, 30, doi:10.1029/2003GL017676, 2003.

Egbert, G. D., Ray, R. D., and Bills, B. G.: Numerical modeling of the global semidiurnal tide in the present day and in the Last Glacial Maximum, Journal of Geophysical Research: Oceans, 109, 1–15, doi:10.1029/2003jc001973, 2004.

Farhat, M., Auclair-Desrotour, P., Boué, G., and Laskar, J.: The resonant tidal evolution of the Earth-Moon distance, A&A, 665, L1, doi:10.1051/0004-6361/202243445, 2022.

Farrell, W. E.: Deformation of the Earth by surface loads, Reviews of Geophysics, 10, 761–797, doi:10.1029/RG010i003p00761, 1972.

Filloux, J. H.: Deep sea tide gauge with optical readout of bourdon tube rotations, Nature, 226, 935–937, doi:10.1038/226935a0, 1970.

Flechtner, F., Neumayer, K. H., Dahle, C., Dobslaw, H., Fagiolini, E., Raimondo, J. C., and Güntner, A.: What can be expected from the GRACE-FO laser ranging interferometer for Earth science applications?, Surveys in Geophysics, 37, 453–470, doi:10.1007/s10712-015-9338-y, 2016.

Fok, H. S.: Ocean Tides Modeling using Satellite Altimetry, doi:10.1017/CBO9781107415324.004, 2012.

Friis-Christensen, E., Lühr, H., and Hulot, G.: Swarm: A constellation to study the Earth's magnetic field, Earth, Planets and Space, 58, 351–358, doi:10.1186/BF03351933, 2006.

Fu, L.-L. and Cazenave, A.: Satellite Altimetry and Earth Sciences, vol. 69, Academic Press, 1 edn., 2000.

Fu, L.-L., Christensen, E. J., Yamarone, C. A., Lefebvre, M., Ménard, Y., Dorrer, M., and Escudier, P.: TOPEX/POSEIDON mission overview, Journal of Geophysical Research, 99, 24 369–24 381, doi:10.1029/94JC01761, 1994.

Garrett, E., Melnick, D., Dura, T., Cisternas, M., Ely, L. L., Wesson, R. L., Jara-Muñoz, J., and Whitehouse, P. L.: Holocene relative sea-level change along the tectonically active Chilean coast, Quaternary Science Reviews, 236, 106 281, doi:10.1016/j.quascirev.2020.106281, 2020.

Gauss, C. F.: Intensitas vis magneticae terrestris ad mensuram absolutam revocata, in: Werke, pp. 293–304, Springer Berlin Heidelberg, doi:10.1007/978-3-642-49319-5_10, 1877.

GEBCO Compilation Group: GEBCO 2019 Grid, doi:10.5285/836f016a-33be-6ddc-e053-6c86abc0788e, 2019.

Ghobadi-Far, K., Shin-Chan, H., McCullough, C., Wiese, D., Dah-Ning, Y., Landerer, F., and Sauber, J.: GRACE Follow-On laser ranging interferometer measurements uniquely distinguish short wavelength gravitational perturbations, Geophysical Research Letters, 47, doi:10.1029/2020GL089445, 2020.

Gill, A. E.: Chapter Nine - Forced Motion, in: Atmosphere—Ocean Dynamics, edited by Gill, A. E., vol. 30 of *International Geophysics*, pp. 317–370, Academic Press, doi:https://doi.org/10.1016/S0074-6142(08)60034-0, 1982.

Gooding, R. H. and Wagner, C. A.: On the inclination functions and a rapid stable procedure for their evaluation together with derivatives, Celestial Mechanics and Dynamical Astronomy, 101, 247, doi:10.1007/s10569-008-9145-6, 2008.

Gooding, R. H. and Wagner, C. A.: On a Fortran procedure for rotating spherical-harmonic coefficients, Celestial Mechanics and Dynamical Astronomy, 108, 95–106, doi:10.1007/s10569-010-9293-3, 2010.

Goodkind, J. M.: The superconducting gravimeter, Review of Scientific Instruments, 70, doi:10.1063/1.1150092, 1999.

Gould, W. J. and McKee, W. D.: Vertical structure of semi-diurnal tidal currents in the Bay of Biscay, Nature, 244, 88–91, doi:10.1038/244088a0, 1973.

Green, J. A. M.: Ocean tides and resonance, Ocean Dynamics, 60, 1243–1253, doi:10.1007/s10236-010-0331-1, 2010.

Green, J. A. M. and Nycander, J.: A comparison of tidal conversion parameterizations for tidal models, Journal of Physical Oceanography, 43, 104–119, doi:10.1175/jpo-d-12-023.1, 2013.

Green, J. A. M., Green, C. L., Bigg, G. R., Rippeth, T. P., Scourse, J. D., and Uehara, K.: Tidal mixing and the meridional overturning circulation from the Last Glacial Maximum, Geophysical Research Letters, 36, n/a–n/a, doi:10.1029/2009GL039309, 2009.

Green, J. A. M., Huber, M., Waltham, D., Buzan, J., and Wells, M.: Explicitly modelled deep-time tidal dissipation and its implication for Lunar history, Earth and Planetary Science Letters, 461, doi:10.1016/j.epsl.2016.12.038, 2017.

Griffiths, S. D. and Hill, D. F.: Tidal modeling, chap. 29, pp. 438–451, John Wiley & Sons, Ltd, doi:10.1002/9781118452547.ch29, 2015.

Griffiths, S. D. and Peltier, W. R.: Megatides in the Arctic Ocean under glacial conditions, Geophysical Research Letters, 35, 1–5, doi:10.1029/2008GL033263, 2008.

Griffiths, S. D. and Peltier, W. R.: Modeling of polar ocean tides at the Last Glacial Maximum: Amplification sensitivity, and climatological implications, Journal of Climate, 22, 2905–2924, doi:10.1175/2008JCLI2540.1, 2009.

Hackmann, E. and Lämmerzahl, C.: Generalized gravitomagnetic clock effect, Physical Review D, 90, 044 059, doi:10.1103/PhysRevD.90.044059, 2014.

Haigh, I. D., Pickering, M. D., Green, J. A., Arbic, B. K., Arns, A., Dangendorf, S., Hill, D. F., Horsburgh, K., Howard, T., Idier, D., Jay, D. A., Jänicke, L., Lee, S. B., Müller, M., Schindelegger, M., Talke, S. A., Wilmes, S. B., and Woodworth, P. L.: The tides they are a-changin': A comprehensive review of past and future nonastronomical changes in tides, their driving mechanisms, and future implications, Reviews of Geophysics, 58, 1–39, doi:10.1029/2018RG000636, 2020.

Han, S.-C., Jekeli, C., and Shum, C. K.: Time-variable aliasing effects of ocean tides, atmosphere, and continental water mass on monthly mean GRACE gravity field, Journal of Geophysical Research: Solid Earth, 109, doi:10.1029/2003JB002501, 2004.

Harris, C. R., Millman, K. J., van der Walt, S. J., Gommers, R., Virtanen, P., Cournapeau, D., Wieser, E., Taylor, J., Berg, S., Smith, N. J., Kern, R., Picus, M., Hoyer, S., van Kerkwijk, M. H., Brett, M., Haldane, A., del Río, J. F., Wiebe, M., Peterson, P., Gérard-Marchant, P., Sheppard, K., Reddy, T., Weckesser, W., Abbasi, H., Gohlke, C., and Oliphant, T. E.: Array programming with NumPy, Nature, 585, 357–362, doi:10.1038/s41586-020-2649-2, 2020.

Hart-Davis, M. G., Dettmering, D., Sulzbach, R., Thomas, M., Schwatke, C., and Seitz, F.: Regional evaluation of minor tidal constituents for improved estimation of ocean tides, Remote Sensing, 13, doi:10.3390/rs13163310, 2021a.

Hart-Davis, M. G., Piccioni, G., Dettmering, D., Schwatke, C., Passaro, M., and Seitz, F.: EOT20: A global ocean tide model from multi-mission satellite altimetry, Earth System Science Data Discussions, pp. 1–23, doi:10.5194/essd-2021-97, 2021b.

Hart-Davis, M. G., Dettmering, D., and Seitz, F.: TICON-3: Tidal Constants based on GESLA-3 sea-level records from globally distributed tide gauges including gauge type information (data), doi:10.1594/PANGAEA.951610, 2022.

Hartmann, T. and Wenzel, H.: The harmonic development of the Earth tide generating potential due to the direct effect of the planets, Geophysical Research Letters, 21, 1991–1993, doi:10.1029/94GL01684, 1994.

Hartmann, T. and Wenzel, H.-G.: Catalogue HW95 of the Tide Generating Potential., Marées Terrestres - Bulletin d'Informations, 123, 9278–9301, doi:10.1029/95GL03324, URL `http://www.bim-icet.org`, 1995a.

Hartmann, T. and Wenzel, H.-G.: The HW95 tidal potential catalogue, Geophyical Research Letters, 22, 3553–3556, 1995b.

Hauk, M. and Wiese, D. N.: New methods for linking science objectives to remote sensing observations: a concept study using single- and dual-pair satellite gravimetry architectures, Earth and Space Science, 7, doi:10.1029/2019EA000922, 2020.

Heiskanen, W. A. and Moritz, H.: Physical Geodesy, W. H. Freeman and company, 1967.

Henderschott, M. C.: The effects of solid Earth deformation on global ocean tides, Geophysical Journal of the Royal Astronomical Society, 29, 389–402, doi:10.1111/j.1365-246X.1972.tb06167.x, 1972.

Hersbach, H., Bell, B., Berrisford, P., Hirahara, S., Horányi, A., Muñoz-Sabater, J., Nicolas, J., Peubey, C., Radu, R., Schepers, D., Simmons, A., Soci, C., Abdalla, S., Abellan, X., Balsamo, G., Bechtold, P., Biavati, G., Bidlot, J., Bonavita, M., Chiara, G., Dahlgren, P., Dee, D., Diamantakis, M., Dragani, R., Flemming, J., Forbes, R., Fuentes, M., Geer, A., Haimberger, L., Healy, S., Hogan, R. J., Hólm, E., Janisková, M., Keeley, S., Laloyaux, P., Lopez, P., Lupu, C., Radnoti, G., Rosnay, P., Rozum, I., Vamborg, F., Villaume, S., and Thépaut, J.: The ERA5 global reanalysis, Quarterly Journal of the Royal Meteorological Society, 146, 1999–2049, doi:10.1002/qj.3803, 2020.

Hewitt, E. and Hewitt, R. E.: The Gibbs-Wilbraham phenomenon: An episode in Fourier analysis, Archive for History of Exact Sciences, 21, 129–160, doi:10.1007/BF00330404, 1979.

Hijma, M. P. and Cohen, K. M.: Holocene sea-level database for the Rhine-Meuse Delta, The Netherlands: Implications for the pre-8.2 ka sea-level jump, Quaternary Science Reviews, 214, 68–86, doi:10.1016/j.quascirev.2019.05.001, 2019.

Hijma, M. P., Engelhart, S. E., Törnqvist, T. E., Horton, B. P., Hu, P., and Hill, D. F.: A protocol for a geological sea-level database, in: Handbook of Sea-Level Research, edited by Shennan, I., Long, A. J., and Horton, B. P., pp. 536–553, John Wiley & Sons, Ltd, doi:10.1002/9781118452547.ch34, 2015.

Hill, D. F., Griffiths, S. D., Peltier, W. R., Horton, B. P., and Törnqvist, T. E.: High-resolution numerical modeling of tides in the Western Atlantic, Gulf of Mexico, and Caribbean Sea during the Holocene, Journal of Geophysical Research: Oceans, 116, doi:10.1029/2010JC006896, 2011.

Hillenbrand, C.-D., Bentley, M. J., Stolldorf, T. D., Hein, A. S., Kuhn, G., Graham, A. G., Fogwill, C. J., Kristoffersen, Y., Smith, J. A., Anderson, J. B., Larter, R. D., Melles, M., Hodgson, D. A., Mulvaney, R., and Sugden, D. E.: Reconstruction of changes in the Weddell Sea sector of the Antarctic ice sheet since the Last Glacial Maximum, Quaternary Science Reviews, 100, 111–136, doi:10.1016/j.quascirev.2013.07.020, 2014.

Hinderer, J., Crossley, D., and Warburton, R. J.: 3.04 - Superconducting Gravimetry, in: Treatise on Geophysics (Second Edition), edited by Schubert, G., pp. 59–115, Elsevier, second edi edn., doi:10.1016/B978-0-444-53802-4.00062-2, 2015.

Hollingsworth, A.: The effect of ocean and Earth tides on the semi-diurnal lunar air tide, Journal of the Atmospheric Sciences, 28, 1021–1044, doi:10.1175/1520-0469(1971)028<1021:TEOOAE>2.0.CO;2, 1971.

Horton, B. P., Engelhart, S. E., Hill, D. F., Kemp, A. C., Nikitina, D., Miller, K. G., and Peltier, W. R.: Influence of tidal-range change and sediment compaction on Holocene

relative sea-level change in New Jersey, USA, Journal of Quaternary Science, 28, 403–411, doi:10.1002/jqs.2634, 2013.

Hough, S. S.: On the Application of Harmonic Analysis to the Dynamical Theory of the Tides, I - On Laplace's 'oscillations of the first species', and on the dynamics of the ocean currents, Phil. Trans. R. Soc. London A, 189, 201–257, doi:10.1098/rspl.1897.0028, 1897.

Howard, S., King, M., and Padman, L.: Antarctic Tide Gauge Database, version 1, U.S. Antarctic Program (USAP) Data Center, 2020.

Howarth, M. J.: The effect of stratification on tidal current profiles, Continental Shelf Research, 18, 1235–1254, doi:10.1016/S0278-4343(98)00042-9, 1998.

Hsu, P. C., Lee, H. J., Zheng, Q., Lai, J. W., Su, F. C., and Ho, C. R.: Tide-Induced Periodic Sea Surface Temperature Drops in the Coral Reef Area of Nanwan Bay, Southern Taiwan, Journal of Geophysical Research: Oceans, 125, 1–21, doi:10.1029/2019JC015226, 2020.

Huang, P., Sulzbach, R. L., Tanaka, Y., Klemann, V., Dobslaw, H., Martinec, Z., and Thomas, M.: Anelasticity and lateral heterogeneities in Earth's upper mantle: Impact on surface displacements, Self-Attraction and Loading, and ocean tide dynamics, Journal of Geophysical Research: Solid Earth, 126, 1–18, doi:10.1029/2021JB022332, 2021.

Huang, P., Sulzbach, R. L., Klemann, V., Tanaka, Y., Dobslaw, H., Martinec, Z., and Thomas, M.: The influence of sediments, lithosphere and upper mantle (Anelastic) with lateral heterogeneity on ocean tide loading and ocean tide dynamics, Journal of Geophysical Research: Solid Earth, 127, doi:10.1029/2022JB025200, 2022.

Hunter, J. D.: Matplotlib: A 2D graphics environment, Computing in Science and Engineering, 9, 90–95, doi:10.1109/MCSE.2007.55, 2007.

Idier, D., Paris, F., Cozannet, G. L., Boulahya, F., and Dumas, F.: Sea-level rise impacts on the tides of the European Shelf, Continental Shelf Research, 137, doi:10.1016/j.csr.2017.01.007, 2017.

Inkscape Project: Inkscape [Software], URL `https://inkscape.org`, 2020.

IPCC: Climate Change 2022: Impacts, Adaptation and Vulnerability Working Group II Contribution to the IPCC Sixth Assessment Report Citations to the Sixth Assessment Report of the Intergovernmental Panel on Climate Change, Cambridge University Press. Cambridge University Press, Cambridge, UK and New York, NY, USA, doi:10.1017/9781009325844, 2022.

Jakobsson, M., Andreassen, K., Bjarnadóttir, L. R., Dove, D., Dowdeswell, J. A., England, J. H., Funder, S., Hogan, K., Ingólfsson, Ó., Jennings, A., Larsen, N. K., Kirchner, N., Landvik, J. Y., Mayer, L., Mikkelsen, N., Möller, P., Niessen, F., Nilsson, J., O'Regan, M., Polyak, L., Nørgaard-Pedersen, N., and Stein, R.: Arctic Ocean glacial history, Quaternary Science Reviews, 92, 40–67, doi:10.1016/j.quascirev.2013.07.033, 2014.

Jeffreys, H.: Tidal Friction in Shallow Seas, Philosophical Transactions of the Royal Society of London, 220, 1–33, URL https://www.jstor.org/stable/91194, 1920.

Jentzsch, G.: Earth tides and ocean tidal loading, in: Tidal Phenomena, edited by Wilhelm, H., Zürn, W., and Wenzel, H.-G., pp. 145–171, Springer Berlin Heidelberg, doi: 10.1007/BFb0011461, URL 10.1007/BFb0011461, 1997.

Jones, P. W.: First- and second-order conservative remapping schemes for grids in spherical coordinates, Monthly Weather Review, 127, 2204–2210, doi:10.1175/1520-0493(1999)127<2204:FASOCR>2.0.CO;2, 1999.

Jourdin, F., Francis, O., Vincent, P., and Mazzega, P.: Some results of heterogeneous data inversion for oceanic tides, Journal of Geophysical Research, 96, 20,267–20, doi: 10.1029/91JB00426, 1991.

Jungclaus, J. H., Lorenz, S. J., Timmreck, C., Reick, C. H., Brovkin, V., Six, K., Segschneider, J., Giorgetta, M. A., Crowley, T. J., Pongratz, J., Krivova, N. A., Vieira, L. E., Solanki, S. K., Klocke, D., Botzet, M., Esch, M., Gayler, V., Haak, H., Raddatz, T. J., Roeckner, E., Schnur, R., Widmann, H., Claussen, M., Stevens, B., and Marotzke, J.: Climate and carbon-cycle variability over the last millennium, Climate of the Past, 6, 723–737, doi:10.5194/cp-6-723-2010, 2010.

Jungclaus, J. H., Fischer, N., Haak, H., Lohmann, K., Marotzke, J., Matei, D., Mikolajewicz, U., Notz, D., and von Storch, J. S.: Characteristics of the ocean simulations in the Max Planck Institute Ocean Model (MPIOM) the ocean component of the MPI-Earth system model, Journal of Advances in Modeling Earth Systems, 5, 422–446, doi:10.1002/jame.20023, 2013.

Kagan, B. A. and Sofina, E.: Ice-induced seasonal variability of tidal constants in the Arctic Ocean, Continental Shelf Research, 30, 643–647, doi:10.1016/j.csr.2009.05.010, 2009.

Kagan, B. A. and Sündermann, J.: Dissipation of tidal energy, paleotides, and the evolution of the Earth-Moon system, Adv. Geophys., 38, 179–266, doi:10.1016/S0065-2687(08)60021-7, 1996.

Khan, N. S., Ashe, E., Horton, B. P., Dutton, A., Kopp, R. E., Brocard, G., Engelhart, S. E., Hill, D. F., Peltier, W. R., Vane, C. H., and Scatena, F. N.: Drivers of Holocene sea-level change in the Caribbean, Quaternary Science Reviews, 155, 13–36, doi:j.quascirev.2016.08.032, 2017.

Khan, N. S., Horton, B. P., Engelhart, S., Rovere, A., Vacchi, M., Ashe, E. L., Törnqvist, T. E., Dutton, A., Hijma, M. P., Shennan, I., and HOLSEA working group: Inception of a global atlas of sea levels since the Last Glacial Maximum, Quaternary Science Reviews, 220, 359–371, doi:10.1016/j.quascirev.2019.07.016, 2019.

Klügel, T. and Wziontek, H.: Correcting gravimeters and tiltmeters for atmospheric mass attraction using operational weather models, Journal of Geodynamics, 48, 204–210, doi:10.1016/j.jog.2009.09.010, 2009.

Kohyama, T. and Wallace, J. M.: Rainfall variations induced by the lunar gravitational atmospheric tide and their implications for the relationship between tropical rainfall and humidity, Geophysical Research Letters, 43, 918–923, doi:10.1002/2015GL067342, 2016.

Korn, P.: Formulation of an unstructured grid model for global ocean dynamics, Journal of Computational Physics, 339, 525–552, doi:10.1016/j.jcp.2017.03.009, 2017.

Kuhlmann, J., Dobslaw, H., and Thomas, M.: Improved modeling of sea level patterns by incorporating Self-Attraction and Loading, Journal of Geophysical Research: Oceans, 116, 1–8, doi:10.1029/2011JC007399, 2011.

Kushner, D.: The controversy surrounding the secular acceleration of the Moon's mean motion, Archive for History of Exact Sciences, 39, 291–316, doi:10.1007/BF00348444, 1989.

Kvas, A., Behzadpour, S., Ellmer, M., Klinger, B., Strasser, S., Zehentner, N., and Mayer-Gürr, T.: ITSG-Grace2018: Overview and evaluation of a new GRACE-only gravity field time series, Journal of Geophysical Research: Solid Earth, 124, 9332–9344, doi:10.1029/2019JB017415, 2019.

Laplace, P.-S.: Sur l'équation séculaire de la lune, Mém. Acad. Roy. Sci., pp. 235–246, 1788.

Laplace, P. S., Gordon, H., and Gordon, J.: Traité de mécanique céleste, De L'Imprimerie de Crapelet : Chez J.B.M. Duprat, doi:10.5479/sil.338664.39088005644752, 1798.

Lau, H. C. and Schindelegger, M.: Solid Earth tides, in: A Journey Through Tides, pp. 365–387, Elsevier, doi:10.1016/B978-0-323-90851-1.00016-9, 2023.

Levitus, S.: NODC Standard Product: World Ocean Atlas 2009 (NCEI Accession 0094866), US DOC/NOAA/NESDIS > National Oceanographic Data Center (2013) NOAA National Centers for Environmental Information. Accessed 01.12.2021, URL `https://accession.nodc.noaa.gov/0094866`, 2009.

Llewellyn Smith, S. G. and Young, W. R.: Tidal conversion at a very steep ridge, Journal of Fluid Mechanics, 495, 175–191, doi:10.1017/S0022112003006098, 2003.

Llubes, M. and Mazzega, P.: The ocean tide gravimetric loading reconsidered, Geophyical Research Letters, 23, 1481–1484, doi:10.1029/96GL01262, 1996.

Llubes, M. and Mazzega, P.: Testing recent global ocean tide models with loading gravimetric data, Progress in Oceanography, 40, 369–383, doi:10.1016/S0079-6611(98)00014-7, 1997.

Locarnini, R. A., Mishonov, A. V., Baranova, O. K., Boyer, T. P., Zweng, M. M., Garcia, H. E., Reagan, J. R., Seidov, D., Weathers, K. W., Paver, C. R., and Smolyar, I. V.: World Ocean Atlas 2018, Volume 1: Temperature, A. Mishonov, Technical Editor. NOAA Atlas NESDIS, 1, 52pp, URL `https://www.ncei.noaa.gov/sites/default/files/2020-04/woa18_vol1.pdf`, 2019.

Longman, M.: A Green's function for determining the deformation of the Earth under surface mass loads, Journal of Geophysical Research, 68, 485–496, doi:10.1029/JZ068i002p00485, 1963.

Longuet-Higgins, M. S.: The electrical and magnetic effects of tidal streams, Geophysical Supplements to the Monthly Notices of the Royal Astronomical Society, 5, 285–307, doi:10.1111/j.1365-246X.1949.tb02945.x, 1949.

Love, A. E. H.: The yielding of the Earth to disturbing forces, Proc. R. Soc. Lond., A82, 73–88, doi:10.1098/rspa.1909.0008, 1909.

Luyten, J. R. and Stommel, H. M.: Comparison of M2 tidal currents observed by some deep moored current meters with those of the Schwiderski and Laplace models, Deep Sea Research Part A. Oceanographic Research Papers, 38, S573–S589, doi:10.1016/s0198-0149(12)80024-0, 1991.

Lyard, F., Lefevre, F., Letellier, T., and Francis, O.: Modelling the global ocean tides: Modern insights from FES2004, Ocean Dynamics, 56, 394–415, doi:10.1007/s10236-006-0086-x, 2006.

Lyard, F. H., Allain, D. J., Cancet, M., Carrère, L., and Picot, N.: FES2014 global ocean tide atlas: Design and performance, Ocean Science, 17, 615–649, doi:10.5194/os-17-615-2021, 2021.

Marchuk, G. I. and Kagan, B. A.: Dynamics of Ocean Tides, Kluwer Academic Publishers, doi:10.1007/978-94-009-2571-7, 1983.

Mathews, P. M.: Love numbers and gravimetric factor for diurnal tides, Journal of the Geodetic Society of Japan, 47, 231–236, doi:10.11366/sokuchi1954.47.231, 2001.

Maus, S. and Kuvshinov, A.: Ocean tidal signals in observatory and satellite magnetic measurements, Geophysical Research Letters, 31, 4–7, doi:10.1029/2004GL020090, 2004.

McDougall, T. J. and Barker, P.: Getting started with TEOS-10 and the Gibbs Seawater (GSW), URL `http://www.teos-10.org/pubs/gsw/v3_04/pdf/Getting_Started.pdf`, 2011.

Medvedev, I. P., Rabinovich, A. B., and Kulikov, E. A.: Tides in three enclosed basins: The Baltic, Black, and Caspian seas, Frontiers in Marine Science, 3, doi:10.3389/fmars.2016.00046, 2016.

Medvedev, I. P., Kulikov, E. A., and Rabinovich, A. B.: Tidal oscillations in the Caspian Sea, Oceanology, 57, 360–375, doi:10.1134/S0001437017020138, 2017.

Melchior, P.: The Tides of the Planet Earth, Pergamon Press, Oxford, 1981.

Melchior, P. and Venedikov, A.: Derivation of the wave M3 (8h.279) from the periodic tidal deformations of the Earth, Physics of the Earth and Planetary Interiors, 1, 363–372, doi:10.1016/0031-9201(68)90032-0, 1968.

Melchior, P., Ducarme, B., and Francis, O.: The response of the Earth to tidal body forces described by second- and third-degree spherical harmonics as derived from a 12 year series of measurements with the superconducting gravimeter GWR/T3 in Brussels, Physics of the Earth and Planetary Interiors, 93, 223–238, doi:10.1016/0031-9201(95)03073-5, 1996.

Melet, A., Nikurashin, M., Muller, C., Falahat, S., Nycander, J., Timko, P. G., Arbic, B. K., and Goff, J. A.: Internal tide generation by abyssal hills using analytical theory, Journal of Geophysical Research: Oceans, 118, 6303 – 6318, doi:10.1002/2013JC009212, 2013.

Merriam, J. B.: The series computation of the gravitational perturbation due to an ocean tide, Physics of the Earth and Planetary Interiors, 23, 81–86, doi:10.1016/0031-9201(80)90003-5, 1980.

Met Office: Cartopy: a cartographic python library with a matplotlib interface [Software], URL `http://scitools.org.uk/cartopy`, 2010 - 2015.

Meurers, B., Van Camp, M., Francis, O., and Pálinkáš, V.: Temporal variation of tidal parameters in superconducting gravimeter time-series, Geophysical Journal International, 205, 284–300, doi:10.1093/gji/ggw017, 2016.

Mignard, F.: The evolution of the lunar orbit revisited, The Moon and the Planets, 20, 301–315, doi:10.1007/BF00907581, 1979.

Munk, W. H.: Once again - Tidal friction, Quarterly Journal of the Royal Astronomical Society, 9, 352, 1968.

Munk, W. H.: Once again: Once again - Tidal friction, Progress in Oceanography, 40, 7–35, doi:10.1016/S0079-6611(97)00021-9, 1997.

Munk, W. H. and Cartwright, D. E.: Tidal spectroscopy and prediction, Philosophical Transactions of the Royal Society A: Mathematical, Physical and Engineering Sciences, 259, 533–581, doi:10.2307/j.ctt211qv60.7, 1966.

Munk, W. H. and Hasselmann, K.: Super-resolution of tides, Studies on Oceanography, pp. 339–344, 1964.

Munk, W. H. and MacDonald, G. J. F.: The Rotation of the Earth, Cambridge University Press, 1960.

Munk, W. H. and Wunsch, C.: Abyssal recipes II: energetics of tidal and wind mixing, Deep Sea Research Part I: Oceanographic Research Papers, 45, 1977–2010, doi:10.1016/S0967-0637(98)00070-3, 1998.

Müller, M.: The free oscillations of the world ocean in the period range 8 to 165 hours including the full loading effect, Geophysical Research Letters, 34, 1–5, doi:10.1029/2006GL028870, 2007.

Müller, M.: A Large Spectrum of Free Oscillations of the World Ocean Including the Full Ocean Loading and Self-attraction Effects, 2008.

Müller, M., Haak, H., Jungclaus, J. H., Sündermann, J., and Thomas, M.: The effect of ocean tides on a climate model simulation, Ocean Modelling, 35, 304–313, doi:10.1016/j.ocemod.2010.09.001, 2010.

Müller, M., Cherniawsky, J. Y., Foreman, M. G., and Storch, J. S. V.: Seasonal variation of the M2 tide, Ocean Dynamics, 64, 159–177, doi:10.1007/s10236-013-0679-0, 2014.

Nansen, F.: Fram over polhavet: den norske polarfærd 1893-1896, vol. 2, 1897.

Neill, S. P., Scourse, J. D., and Uehara, K.: Evolution of bed shear stress distribution over the northwest European shelf seas during the last 12,000 years, Ocean Dynamics, 60, 1139–1156, doi:10.1007/s10236-010-0313-3, 2010.

Nicolaus, M., Perovich, D. K., Spreen, G., Granskog, M. A., von Albedyll, L., Angelopoulos, M., Anhaus, P., Arndt, S., Belter, H. J., Bessonov, V., Birnbaum, G., Brauchle, J., Calmer, R., Cardellach, E., Cheng, B., Clemens-Sewall, D., Dadic, R., Damm, E., de Boer, G., Demir, O., Dethloff, K., Divine, D. V., Fong, A. A., Fons, S., Frey, M. M., Fuchs, N., Gabarró, C., Gerland, S., Goessling, H. F., Gradinger, R., Haapala, J., Haas, C., Hamilton, J., Hannula, H.-R., Hendricks, S., Herber, A., Heuzé, C., Hoppmann, M., Høyland, K. V., Huntemann, M., Hutchings, J. K., Hwang, B., Itkin, P., Jacobi, H.-W., Jaggi, M., Jutila, A., Kaleschke, L., Katlein, C., Kolabutin, N., Krampe, D., Kristensen, S. S., Krumpen, T., Kurtz, N., Lampert, A., Lange, B. A., Lei, R., Light, B., Linhardt, F., Liston, G. E., Loose, B., Macfarlane, A. R., Mahmud, M., Matero, I. O., Maus, S., Morgenstern, A., Naderpour, R., Nandan, V., Niubom, A., Oggier, M., Oppelt, N., Pätzold, F., Perron, C., Petrovsky, T., Pirazzini, R., Polashenski, C., Rabe, B., Raphael, I. A., Regnery, J., Rex, M., Ricker, R., Riemann-Campe, K., Rinke, A., Rohde, J., Salganik, E., Scharien, R. K., Schiller, M., Schneebeli, M., Semmling, M., Shimanchuk, E., Shupe, M. D., Smith, M. M., Smolyanitsky, V., Sokolov, V., Stanton, T., Stroeve, J., Thielke, L., Timofeeva, A., Tonboe, R. T., Tavri, A., Tsamados, M., Wagner, D. N., Watkins, D., Webster, M., and Wendisch, M.: Overview of the MOSAiC expedition: Snow and sea ice, Elementa: Science of the Anthropocene, 10, doi:10.1525/elementa.2021.000046, 2022.

Nikurashin, M. and Ferrari, R.: Global energy conversion rate from geostrophic flows into internal lee waves in the deep ocean, Geophysical Research Letters, 38, doi:10.1029/2011GL046576, 2011.

Nycander, J.: Generation of internal waves in the deep ocean by tides, Journal of Geophysical Research C: Oceans, 110, 1–9, doi:10.1029/2004JC002487, 2005.

Olsson, P. A., Scherneck, H. G., and Ågren, J.: Effects on gravity from non-tidal sea level variations in the Baltic Sea, Journal of Geodynamics, 48, 151–156, doi:10.1016/j.jog.2009.09.002, 2009.

Oreiro, F. A., Wziontek, H., Fiore, M. M. E., D'Onofrio, E. E., and Brunini, C.: Non-tidal ocean loading correction for the Argentinean-German geodetic observatory using an empirical model of storm surge for the Río de la Plata, Pure and Applied Geophysics, 175, 1739–1753, doi:10.1007/s00024-017-1651-6, 2018.

Pail, R., Bingham, R., Braitenberg, C., Dobslaw, H., Eicker, A., Güntner, A., Horwath, M., Ivins, E., Longuevergne, L., Panet, I., and Wouters, B.: Science and user needs for observing global mass transport to understand global change and to benefit society, Surveys in Geophysics, 36, 743–772, doi:10.1007/s10712-015-9348-9, 2015.

Pal, N., Barton, K. N., Petersen, M. R., Brus, S. R., Engwirda, D., Arbic, B. K., Roberts, A. F., Westerink, J. J., and Wirasaet, D.: Barotropic tides in MPAS-Ocean (E3SM V2): impact of ice shelf cavities, Geoscientific Model Development, 16, 1297–1314, doi:10.5194/gmd-16-1297-2023, 2023.

Pedley, M., Paren, J. G., and Potter, J. R.: The tidal spectrum underneath Antarctic ice shelves, Journal of Geophysical Research, 91, 13 001–13 009, doi:10.1029/jc091ic11p13001, 1986.

Pekeris, C. L.: A derivation of Laplace's tidal equation from the theory of inertial oscillations, Proceedings of the Royal Society of London, 374, 81–86, URL `http://www.jstor.org/stable/2990346`, 1974.

Peltier, W. R.: Ice age paleotopography, Science, 265, 195–201, doi:10.1126/science.265.5169.195, 1994.

Peng, D., Hill, E. M., Meltzner, A. J., and Switzer, A. D.: Tide gauge records show that the 18.61-year nodal tidal cycle can change high water levels by up to 30 cm, Journal of Geophysical Research: Oceans, 124, 736–749, doi:10.1029/2018JC014695, 2019.

Penna, N. T., Clarke, P. J., Bos, M. S., and Baker, T.: Ocean tide loading displacements in Western Europe: 1. Validation of kinematic GPS estimates, Journal of Geophysical Research: Solid Earth, 120, 6523–6539, doi:10.1002/2015JB011882, 2015.

Petereit, J., Saynisch-Wagner, J., Irrgang, C., and Thomas, M.: Analysis of ocean tide-induced magnetic fields derived from oceanic in situ observations: climate trends and the remarkable sensitivity of shelf regions, Journal of Geophysical Research: Oceans, 124, 8257–8270, doi:10.1029/2018JC014768, 2019.

Petit, G. and Luzum, B.: IERS Conventions (2010), Bureau International Des Poids Et Mesures Sevres (France), Technical Note No. 36, URL `http://www.iers.org/TN36/`, 2010.

Piccioni, G., Dettmering, D., Bosch, W., and Seitz, F.: TICON: TIdal CONstants based on GESLA sea-level records from globally located tide gauges, Geoscience Data Journal, 6, 97–104, doi:10.1002/gdj3.72, 2019.

Platzman, G. W.: Planetary energy balance for tidal dissipation, Review of Geophysics and Space Physics, 22, 73–84, doi:10.1029/RG022i001p00073, 1984a.

Platzman, G. W.: Normal modes of the world ocean. Part IV: Synthesis of diurnal and semidiurnal tides, Journal of Physical Oceanography, 14, doi:10.1175/1520-0485(1984)014%3C1532:NMOTWO%3E2.0.CO;2, 1984b.

Platzman, G. W.: An observational study of energy balance in the atmospheric lunar tide, Pure and Applied Geophysics PAGEOPH, 137, 1–33, doi:10.1007/BF00876887, 1991.

Platzman, G. W.: Normal Modes of the World Ocean. Part III: A Procedure for Tidal Synthesis, doi:10.1175/1520-0485(1984)014<1521:nmotwo>2.0.co;2, 2002.

Pnueli, A. and Pekeris, C. L.: Free tidal oscillations in rotating flat basins of the form of rectangles and of sectors of circles, Philosophical Transactions of the Royal Society, 263, 149–171, URL https://www.jstor.org/stable/73572, 1968.

Pollmann, F.: Global characterization of the ocean's internal wave spectrum, Journal of Physical Oceanography, 50, 1871 – 1891, doi:10.1175/JPO-D-19-0185.1, 2020.

Press, W. H., Teukolsky, S. A., Vetterling, W. T., and Flannery, B. P.: Numerical Recipes : The Art of Scientific Computing, Cambridge University Press, 3 edn., 2007.

Prothero, W. A. and Goodkind, J. M.: A superconducting gravimeter, Review of Scientific Instruments, 39, 1257–1262, doi:10.1063/1.1683645, 1968.

Puetzfeld, D. and Lämmerzahl, C., eds.: Relativistic Geodesy, vol. 196, Springer International Publishing, 1 edn., doi:10.1007/978-3-030-11500-5, 2019.

Pugh, D. and Woodworth, P.: Sea-Level Science: Understanding Tides, Surges, Tsunamis and Mean Sea-Level Changes, Cambridge University Press, 2014a.

Pugh, D. and Woodworth, P.: Tidal analysis and prediction, in: Sea-Level Science: Understanding Tides, Surges, Tsunamis and Mean Sea-Level Changes, pp. 60–96, doi:10.1017/cbo9781139235778.007, 2014b.

Pérenne, N. and Pichon, A.: Effect of barotropic tidal rectification on low-frequency circulation near the shelf break in the northern Bay of Biscay, Journal of Geophysical Research: Oceans, 104, 13 489–13 506, doi:10.1029/1999jc900050, 1999.

Ray, R. D.: Ocean Self-Attraction and Loading in numerical tidal models, Marine Geodesy, 21, 181–192, doi:10.1080/01490419809388134, 1998a.

Ray, R. D.: Diurnal oscillations in atmospheric pressure at twenty-five small oceanic islands, Geophysical Research Letters, 25, 3851–3854, doi:10.1029/1998GL900039, 1998b.

Ray, R. D.: A global ocean tide model from TOPEX / POSEIDON altimetry: GOT99.2, NASA Tech Memo 1999209478, pp. 1–66, URL https://ntrs.nasa.gov/api/citations/19990089548/downloads/19990089548.pdf, 1999.

Ray, R. D.: Resonant third-degree diurnal tides in the Seas off Western Europe, Journal of Physical Oceanography, 31, 3581–3586, doi:10.1175/1520-0485(2001)031<3581:RTDDTI>2.0.CO;2, 2001.

Ray, R. D.: Precise comparisons of bottom-pressure and altimetric ocean tides, Journal of Geophysical Research: Oceans, 118, 4570–4584, doi:10.1002/jgrc.20336, 2013.

Ray, R. D.: On tidal inference in the diurnal band, Journal of Atmospheric and Oceanic Technology, 34, 437–446, doi:10.1175/jtech-d-16-0142.1, 2017.

Ray, R. D.: First global observations of third-degree ocean tides, Science advances, 6, 1–8, doi:10.1126/sciadv.abd4744, 2020.

Ray, R. D. and Egbert, G. D.: The global S1 tide, Journal of Physical Oceanography, 34, 1922–1935, doi:10.1175/1520-0485(2004)034<1922:TGST>2.0.CO;2, 2004.

Ray, R. D. and Merrifield, M. A.: The semiannual and 4.4-year modulations of extreme high tides, Journal of Geophysical Research: Oceans, 124, 5907–5922, doi:10.1029/2019JC015061, 2019.

Ray, R. D., Eanes, R. J., and Lemoine, F. G.: Constraints on energy dissipation in the Earth's body tide from satellite tracking and altimetry, Geophysical Journal International, 144, 471–480, doi:10.1046/j.1365-246X.2001.00356.x, 2001.

Ray, R. D., Rowlands, D. D., and Egbert, G. D.: Tidal models in a new era of satellite gravimetry, Space Science Reviews, 108, 271–282, doi:10.1023/A:1026223308107, 2003.

Ray, R. D., Luthcke, S. B., and Boy, J. R.: Qualitative comparisons of global ocean tide models by analysis of intersatellite ranging data, Journal of Geophysical Research: Oceans, 114, 1–11, doi:10.1029/2009JC005362, 2009.

Ray, R. D., Boy, J.-P., Arbic, B. K., Egbert, G. D., Erofeeva, S. Y., Petrov, L., and Shriver, J. F.: The problematic Ψ_1 ocean tide, Geophysical Journal International, 227, 1181–1192, doi:10.1093/gji/ggab263, 2021.

Ray, R. D., Boy, J.-P., Erofeeva, S. Y., and Egbert, G. D.: Terdiurnal radiational tides, Journal of Physical Oceanography, doi:10.1175/JPO-D-22-0175.1, 2023.

Renault, L. and Marchesiello, P.: Ocean tides can drag the atmosphere and cause tidal winds over broad continental shelves, Communications Earth & Environment, 3, 70, doi:10.1038/s43247-022-00403-y, 2022.

Rieser, D., Tr, T. M.-G., Savcenko, R., Bosch, W., Wünsch, J., Dahle, C., and Flechtner, F.: The ocean tide model EOT11a in spherical harmonics representation, Technical Note, pp. –, URL `url:http://portal.tugraz.at/portal/page/portal/Files/i5210/files/projekte/COTAGA/TN_EOT11a.pdf`, 2012.

Risbo, T.: Fourier transform summation of Legendre series and D-functions, Journal of Geodesy, 70, 383–396, doi:10.1007/s001900050028, 1996.

Rosat, S. and Lambert, S. B.: Free core nutation resonance parameters from VLBI and superconducting gravimeter data, A&A, 503, 287–291, doi:10.1051/0004-6361/200811489, 2009.

Rosenblatt, P.: The origin of the Martian moons revisited, Astronomy and Astrophysics Review, 19, doi:10.1007/s00159-011-0044-6, 2011.

Roy, K. and Peltier, W.: Glacial Isostatic Adjustment, relative sea level history and mantle viscosity: reconciling relative sea level model predictions for the U.S. East coast with geological constraints, Geophysical Journal International, 201, 1156–1181, doi: 10.1093/gji/ggv066, 2015.

Roy, K. and Peltier, W.: Relative sea level in the Western Mediterranean basin: A regional test of the ICE-7G-NA (VM7) model and a constraint on late Holocene Antarctic deglaciation, Quaternary Science Reviews, 183, 76–87, doi:10.1016/j.quascirev.2017.12.021, 2018.

Savcenko, R., Bosch, W., Dettmering, D., and Seitz, F.: EOT11a - Global Empirical Ocean Tide model from multi-mission satellite altimetry, doi:10.1594/PANGAEA.834232,, 2012.

Saynisch, J., Irrgang, C., and Thomas, M.: Estimating ocean tide model uncertainties for electromagnetic inversion studies, Annales Geophysicae, 36, 1009–1014, doi:10.5194/angeo-36-1009-2018, 2018.

Saynisch-Wagner, J., Petereit, J., Irrgang, C., and Thomas, M.: Phase changes of electromagnetic oceanic tidal signals, Journal of Geophysical Research: Oceans, 125, 1–10, doi:10.1029/2019JC015960, 2020.

Schaeffer, N.: Efficient spherical harmonic transforms aimed at pseudospectral numerical simulations, Geochemistry, Geophysics, Geosystems, 14, 751–758, doi:10.1002/ggge.20071, 2013.

Schaffer, J., Timmermann, R., Arndt, J. E., Kristensen, S. S., Mayer, C., Morlighem, M., and Steinhage, D.: A global, high-resolution data set of ice sheet topography, cavity geometry, and ocean bathymetry, Earth System Science Data, 8, 543–557, doi: 10.5194/essd-8-543-2016, 2016.

Scherneck, H.-G.: A parametrized solid earth tide model and ocean tide loading effects for global geodetic baseline measurements, Geophysical Journal International, 106, 677–694, doi:10.1111/j.1365-246X.1991.tb06339.x, 1991.

Scherneck, H. G. and Rajner, M.: Using a superconducting gravimeter in support of absolute gravity campaigning — A feasibility study, Geophysica, 54, 117–135, doi: 10.31223/OSF.IO/YXVJC, 2019.

Schindelegger, M. and Dobslaw, H.: A global ground truth view of the lunar air pressure tide L2, Journal of Geophysical Research, 121, 95–110, doi:10.1002/2015JD024243, 2016.

Schindelegger, M., Green, J. A., Wilmes, S. B., and Haigh, I. D.: Can we model the effect of observed sea level rise on tides?, Journal of Geophysical Research: Oceans, 112, 95–110, doi:10.1029/2018JC013959, 2018.

Schindelegger, M., Harker, A. A., Ponte, R. M., Dobslaw, H., and Salstein, D. A.: Convergence of daily GRACE solutions and models of submonthly ocean bottom pressure variability, Journal of Geophysical Research: Oceans, 126, doi:10.1029/2020JC017031, 2021.

Schindelegger, M., Kotzian, D. P., Ray, R. D., Green, J. A. M., and Stolzenberger, S.: Interannual changes in tidal conversion modulate M2 amplitudes in the Gulf of Maine, Geophysical Research Letters, 49, doi:10.1029/2022GL101671, 2022.

Schindelegger, M., Sakazaki, T., and Green, M.: Atmospheric tides—An Earth system signal, in: A Journey Through Tides, pp. 389–416, Elsevier, doi:10.1016/B978-0-323-90851-1.00007-8, 2023.

Schlichting, H. and Gersten, K.: Boundary-Layer Theory, Springer Berlin Heidelberg, doi:10.1007/978-3-662-52919-5, 2017.

Schmittner, A., Green, J. A., and Wilmes, S. B.: Glacial ocean overturning intensified by tidal mixing in a global circulation model, Geophysical Research Letters, 42, 4014–4022, doi:10.1002/2015GL063561, 2015.

Schrama, E. J. and Ray, R. D.: A preliminary tidal analysis of TOPEX/POSEIDON altimetry, Journal of Geophysical Research, 99, doi:10.1029/94jc01432, 1994.

Schueller, K.: Program systems for Earth and ocean tide analysis and prediction release notes, pp. 1–10, 2020.

Schuh, H. and Moehlmann, L.: Ocean loading station displacements observed by VLBI, Geophysical Research Letters, 16, 1105–1108, doi:10.1029/GL016i010p01105, 1989.

Schulzweida, U.: CDO User Guide (2.1.0), Zenodo, doi:10.5281/zenodo.7112925, 2022.

Schuster, A.: The diurnal variation of terrestrial magnetism, Philosophical Transactions of the Royal Society of London. Series A, Containing Papers of a Mathematical or Physical Character, 208, 163–204, URL `http://www.jstor.org/stable/90973`, 1908.

Schwiderski, E. W.: Ocean tides, part I: Global ocean tidal equations, Marine Geodesy, 3, 161–217, doi:10.1080/01490418009387997, 1980.

Schüller, K.: Theoretical Basis for Earth Tide Analysis with the New ETERNA34-ANA-V4.0 Program, "Bulletin d'Information des Marées Terrestres", 149, 12 024–12 061, URL `http://maregraph-renater.upf.pf/bim/BIM/bim149.pdf`, 2015.

Scott, R. B., Goff, J. A., Garabato, A. C. N., and Nurser, A. J. G.: Global rate and spectral characteristics of internal gravity wave generation by geostrophic flow over topography, Journal of Geophysical Research, 116, C09 029, doi:10.1029/2011JC007005, 2011.

Seiler, U.: Periodic changes of the angular momentum budget due to the tides of the world ocean, Journal of Geophysical Research, 96, 10 287, doi:10.1029/91jb00219, 1991.

Sejrup, H. P., Larsen, E., Landvik, J., King, E. L., Haflidason, H., and Nesje, A.: Quaternary glaciations in southern Fennoscandia: evidence from southwestern Norway and the northern North Sea region, Quaternary Science Reviews, 19, 667–685, doi:10.1016/S0277-3791(99)00016-5, 2000.

Shihora, L., Sulzbach, R., Dobslaw, H., and Thomas, M.: Self-Attraction and Loading feedback on ocean dynamics in both shallow water equations and primitive equations, Ocean Modelling, 169, 101 914, doi:10.1016/j.ocemod.2021.101914, 2021.

Shihora, L., Balidakis, K., Dill, R., Dahle, C., Ghobadi-Far, K., Bonin, J., and Dobslaw, H.: Non-Tidal Background Modeling for Satellite Gravimetry Based on Operational ECWMF and ERA5 Reanalysis Data: AOD1B RL07, Journal of Geophysical Research: Solid Earth, 127, 1–15, doi:10.1029/2022jb024360, 2022.

Shum, C. K., Woodworth, P. L., Andersen, O. B., Egbert, G. D., Francis, O., King, C., Klosko, S. M., Provost, C. L., Li, X., Molines, J.-M., Parke, M. E., Ray, R. D., Schlax, M. G., Stammer, D., Tierney, C. C., Vincent, P., and Wunsch, C. I.: Accuracy assessment of recent ocean tide models, Journal of Geophysical Research: Oceans, 102, 25 173–25 194, doi:10.1029/97JC00445, 1997.

Simon, B.: La Marée océanique cotière, vol. 1, Institut océanographique, URL `https://iho.int/iho_pubs/CB/C-33/C-33_maree_simon_fr.pdf`, 2007.

Simon, J. L., Bretagnon, P., Chapront, J., Chapront-Touzé, M., Francou, G., and Laskar, J.: Numerical expressions for precession formulae and mean elements for the Moon and the planets, Astronomy and Astrophysics, 282, 663–683, 1994.

Simon, K. M., James, T. S., Forbes, D. L., Telka, A. M., Dyke, A. S., and Henton, J. A.: A relative sea-level history for Arviat, Nunavut, and implications for Laurentide Ice Sheet thickness west of Hudson Bay, Quaternary Research (United States), 82, 185–197, doi:10.1016/j.yqres.2014.04.002, 2014.

Spiridonov, E. A.: Tidal Love numbers of degrees 2 and 3, Izvestiya - Atmospheric and Ocean Physics, 54, 911–931, doi:10.1134/S0001433818080133, 2018.

St. Laurent, L. C., Simmons, H. L., and Jayne, S. R.: Estimating tidally driven mixing in the deep ocean, Geophysical Research Letters, 29, 19–22, doi:10.1029/2002GL015633, 2002.

Stammer, D., Ray, R. D., Andersen, O. B., Arbic, B. K., Bosch, W., Carrère, L., Cheng, Y., Chinn, D. S., Dushaw, B. D., Egbert, G. D., Erofeeva, S. Y., Fok, H. S., Green, J. A. M., Griffiths, S., King, M. A., Lapin, V., Lemoine, F. G., Luthcke, S. B., Lyard, F., Morison, J., Müller, M., Padman, L., Richman, J. G., Shriver, J. F., Shum, C. K., Taguchi, E., and Yi, Y.: Accuracy assessment of global barotropic ocean tide models, Reviews of Geophysics, 52, 243–282, doi:10.1002/2014RG000450.Received, 2014.

Stein, R., Fahl, K., Gierz, P., and Frank Niessen, G. L.: Arctic Ocean sea ice cover during the penultimate glacial and the last interglacial, Nature Communications, 8, 373, doi:10.1038/s41467, 2017.

Stepanov, V. N. and Hughes, C. W.: Parameterization of ocean Self-Attraction and Loading in numerical models of the ocean circulation, Journal of Geophysical Research: Oceans, 109, doi:10.1029/2003JC002034, 2004.

Stevens, B., Giorgetta, M., Esch, M., Mauritsen, T., Crueger, T., Rast, S., Salzmann, M., Schmidt, H., Bader, J., Block, K., Brokopf, R., Fast, I., Kinne, S., Kornblueh, L., Lohmann, U., Pincus, R., Reichler, T., and Roeckner, E.: Atmospheric component of the MPI-M Earth System Model: ECHAM6, Journal of Advances in Modeling Earth Systems, 5, 146–172, doi:10.1002/jame.20015, 2013.

Street, R.: The dissipation of energy in the tides in connection with the acceleration of the Moon's mean motion, Proceedings of the Royal Society of London. Series A, Containing Papers of a Mathematical and Physical Character, 93, 348–359, doi:10.1098/rspa.1917.0023, 1917.

Sulzbach, R., Dobslaw, H., and Thomas, M.: High-resolution numerical modelling of barotropic global ocean tides for satellite gravimetry, Journal of Geophysical Research, Oceans, pp. 1–21, doi:10.1029/2020JC017097, 2021a.

Sulzbach, R., Dobslaw, H., and Thomas, M.: Mass variations induced by ocean tide oscillations (TiME21). V. 2.0., GFZ Data Services [Dataset], doi:10.5880/GFZ.1.3.2021.001, 2021b.

Sulzbach, R., Balidakis, K., Dobslaw, H., and Thomas, M.: TiME22: Periodic disturbances of the terrestrial gravity potential induced by oceanic and atmospheric tides, GFZ Data Services [Dataset], doi:10.5880/GFZ.1.3.2022.006, 2022a.

Sulzbach, R., Klemann, V., Dobslaw, H., and Thomas, M.: Global ocean tide model data during the last 21,000 years, GFZ Data Services [Dataset], doi:10.5880/GFZ.1.3.2022.005, 2022b.

Sulzbach, R., Wziontek, H., Hart-Davis, M. G., Dobslaw, H., Scherneck, H.-G., Van Camp, M., Omang, O. C. D., Antokoletz, E. D., Voigt, C., Dettmering, D., and Thomas, M.: Modeling gravimetric signatures of third-degree ocean tides and their detection in superconducting gravimeter records, Journal of Geodesy, 96, 35, doi:10.1007/s00190-022-01609-w, 2022c.

Sulzbach, R., Klemann, V., Knorr, G., Dobslaw, H., Dümpelmann, H., Lohmann, G., and Thomas, M.: Evolution of global ocean tide levels since the Last Glacial Maximum, Paleoceanography and Paleoclimatology, 38, doi:10.1029/2022PA004556, 2023.

Sun, Y., Knorr, G., Zhang, X., Tarasov, L., Barker, S., Werner, M., and Lohmann, G.: Ice sheet decline and rising atmospheric CO2 control AMOC sensitivity to deglacial meltwater discharge, Global and Planetary Change, 210, 103 755, doi:10.1016/j.gloplacha.2022.103755, 2022.

Taguchi, E., Stammer, D., and Zahel, W.: Inferring deep ocean tidal energy dissipation from the global high-resolution data-assimilative HAMTIDE model, Journal of Geophysical Research : Oceans, pp. 3909–3925, doi:10.1002/2013JC009563, 2014.

Tamura, Y., Sato, T., Ooe, M., and Ishiguro, M.: A procedure for tidal analysis with a Bayesian information criterion, Geophysical Journal International, 104, 507–516, doi:10.1111/j.1365-246X.1991.tb05697.x, 1991.

Tapley, B. D., Watkins, M. M., Flechtner, F., Reigber, C., Bettadpur, S., Rodell, M., Sasgen, I., Famiglietti, J. S., Landerer, F. W., Chambers, D. P., Reager, J. T., Gardner, A. S., Save, H., Ivins, E. R., Swenson, S. C., Boening, C., Dahle, C., Wiese, D. N., Dobslaw, H., Tamisiea, M. E., and Velicogna, I.: Contributions of GRACE to understanding climate change, Nature Climate Change, 9, 358–369, doi: 10.1038/s41558-019-0456-2, 2019.

Tarasov, L., Dyke, A. S., Neal, R. M., and Peltier, W. R.: A data-calibrated distribution of deglacial chronologies for the North American ice complex from glaciological modeling, Earth and Planetary Science Letters, 315–316, 30–40, doi:10.1016/j.epsl.2011.09.010, 2012.

Taylor, G. I.: Tidal friction in the Irish Sea, Philosophical Transactions of the Royal Society of London. Series A, 220, 1–33, doi:10.1098/rsta.1920.0001, 1920.

Thomas, M. and Sündermann, J.: Tides and tidal torques of the world ocean since the Last Glacial Maximum, Journal of Geophysical Research, 104, 3159–3183, doi:10.1029/1998JC900097, 1999.

Thomas, M., Sündermann, J., and Maier-Reimer, E.: Consideration of ocean tides in an OGCM and impacts on subseasonal to decadal polar motion excitation, Geophysical Research Letters, 28, 2457–2460, doi:10.1029/2000GL012234, 2001.

Thomson, W.: On the rigidity of the Earth, Philosophical Transactions of the Royal Society of London, 153, 573–582, URL `https://www.jstor.org/stable/108812`, 1863.

Thomson, W.: On gravitational oscillations of rotating water, Proceedings of the Royal Society, Edinburgh, 10, 92–100, doi:10.1017/S0370164600043467, 1879.

Thyng, K., Greene, C., Hetland, R., Zimmerle, H., and DiMarco, S.: True colors of oceanography: Guidelines for effective and accurate colormap selection, Oceanography, 29, 9–13, doi:10.5670/oceanog.2016.66, 2016.

Tushingham, A. M. and Peltier, W. R.: Validation of the ICE-3G Model of Würm-Wisconsin Deglaciation using a global data base of relative sea level histories, Journal of Geophysical Research: Solid Earth, 97, 3285–3304, doi:10.1029/91JB02176, 1992.

Tyler, R. H., Maus, S., and Lühr, H.: Satellite observations of magnetic fields due to ocean tidal flow, Science, 299, 239–241, doi:10.1126/science.1078074, 2003.

Uehara, K. and Saito, Y.: Tidal amplitude decreases in response to estuarine shrinkage: Tokyo Bay during the Holocene, Estuarine, Coastal Shelf Science, 225, 106 225, doi: 10.1016/j.ecss.2019.05.007, 2019.

Uehara, K., Scourse, J. D., Horsburgh, K. J., Lambeck, K., and Purcell, A. P.: Tidal evolution of the northwest European shelf seas from the Last Glacial Maximum to the present, Journal of Geophysical Research: Oceans, 111, 1–15, doi:10.1029/2006JC003531, 2006.

Unidata: Integrated Data Viewer (IDV) version 3.1 [software], Boulder, CO: UCAR/Unidata, doi:10.5065/D6RN35XM, 2012.

Vacchi, M., Engelhart, S. E., Nikitina, D., Ashe, E. L., Peltier, W. R., Roy, K., Kopp, R. E., and Horton, B. P.: Postglacial relative sea-level histories along the eastern Canadian coastline, Quaternary Science Reviews, 201, 124–146, doi:10.1016/j.quascirev.2018.09.043, 2018.

Van Camp, M., de Viron, O., Watlet, A., Meurers, B., Francis, O., and Caudron, C.: Geophysics from terrestrial time-variable gravity measurements, Reviews of Geophysics, 55, 938–992, doi:10.1002/2017RG000566, 2017.

Varshalovich, D. A., Moskalev, A. N., and Khersonskii, V. K.: Quantum Theory of Angular Momentum, WORLD SCIENTIFIC, doi:10.1142/0270, 1988.

Vasskog, K., Svendsen, J.-I., Mangerud, J., Agasøster, H. K., Svean, A., and Lunnan, E. M.: Evidence of early deglaciation (18 000 cal a bp) and a postglacial relative sea-level curve from southern Karmøy, south-west Norway, Journal of Quaternary Science, pp. 410–423, doi:10.1002/jqs.3109, 2019.

Velay-Vitow, J. and Peltier, W. R.: Out of the ice age: Megatides of the Arctic Ocean and the Bølling-Ållerød, Younger Dryas transition, Geophysical Research Letters, 47, 1–10, doi:10.1029/2020GL089870, 2020.

Velay-Vitow, J., Peltier, W. R., and Stuhne, G. R.: The tides of the glacial ocean and their possible connection to Heinrich event instabilities of the Laurentide Ice Sheet, Journal of Geophysical Research: Oceans, 125, 1–23, doi:10.1029/2019JC015444, 2020.

Voigt, C., Förste, C., Wziontek, H., Crossley, D., Meurers, B., Pálinkáš, V., Hinderer, J., Boy, J.-P., Barriot, J.-P., and Sun, H.: Report on the Data Base of the International Geodynamics and Earth Tide Service (IGETS), doi:10.2312/GFZ.b103-16087, URL `urn:nbn:de:kobv:b103-16087`, 2016.

Voigt, C., Sulzbach, R., Timmen, L., Dobslaw, H., Weise, A., Deng, Z., Stolarczuk, N., Pflug, H., Peters, H., Fietz, M., Thomas, M., Förste, C., and Flechtner, F.: A superconducting gravimeter on the island of Heligoland for the high-accuracy determination of regional ocean tide loading signals of the North Sea, Geophysical Journal International, doi:10.1093/gji/ggad147, 2023.

Wahr, J. M.: Body tides on an elliptical, rotating, elastic and oceanless earth, Geophys. J. R. Astron. Soc., 64, 677–703, doi:10.1111/j.1365-246X.1981.tb02690.x, 1981.

Wahr, J. M.: Deformation induced by polar motion, Journal of Geophysical Research: Solid Earth, 90, 9363–9368, doi:10.1029/JB090iB11p09363, 1985.

Wahr, J. M. and Sasao, T.: A diurnal resonance in the ocean tide and in the Earth's load response due to the resonant free 'core nutation', Geophys. J. R. Astron. Soc., 64, 747–765, doi:10.1111/j.1365-246X.1981.tb02693.x, 1980.

Wang, H., Xiang, L., Jia, L., Jiang, L., Wang, Z., Hu, B., and Gao, P.: Load Love numbers and Green's functions for elastic Earth models PREM, iasp91, ak135, and modified models with refined crustal structure from Crust 2.0, Computers and Geosciences, 49, 190–199, doi:10.1016/j.cageo.2012.06.022, 2012.

Wang, R.: Tidal response of the solid Earth, in: Tidal Phenomena, edited by Wilhelm, H., Zürn, W., and Wenzel, H.-G., pp. 27–57, Springer Berlin Heidelberg, doi:10.1007/BFb0011456, 1997.

Wang, X., Verlaan, M., Apecechea, M. I., and Lin, H. X.: Computation-efficient parameter estimation for a high-resolution global tide and surge model, Journal of Geophysical Research: Oceans, 126, 1–24, doi:10.1029/2020JC016917, 2021.

Ward, S. L., Neill, S. P., Scourse, J. D., Bradley, S. L., and Uehara, K.: Sensitivity of palaeotidal models of the northwest European shelf seas to glacial isostatic adjustment since the Last Glacial Maximum, Quaternary Science Reviews, 151, 198–211, doi:10.1016/j.quascirev.2016.08.034, 2016.

Weis, P.: Ocean Tides and the Earth's Rotation - Results of a High-Resolving Ocean Model forced by the Lunisolar Tidal Potential, 2006.

Weis, P., Thomas, M., and Sündermann, J.: Broad frequency tidal dynamics simulated by a high-resolution global ocean tide model forced by ephemerides, Journal of Geophysical Research: Oceans, 113, doi:10.1029/2007JC004556, 2008.

Wenzel, H.-G.: Analysis of Earth tide observations, in: Tidal Phenomena, pp. 59–75, Springer Berlin Heidelberg, doi:10.1007/BFb0011457, 1997a.

Wenzel, H.-G.: Tide-generating potential for the Earth, in: Tidal Phenomena, pp. 9–26, Springer Berlin Heidelberg, doi:10.1007/BFb0011455, 1997b.

Wessel, P., Luis, J. F., Uieda, L., Scharroo, R., Wobbe, F., Smith, W. H. F., and Tian, D.: The Generic Mapping Tools Version 6, Geochemistry, Geophysics, Geosystems, 20, 5556–5564, doi:10.1029/2019GC008515, 2019.

Wiese, D. N., Killett, B., Watkins, M. M., and Yuan, D. N.: Antarctic tides from GRACE satellite accelerations, Journal of Geophysical Research: Oceans, 121, 2874–2886, doi:10.1002/2015JC011488, 2016.

Wilmes, S., Schmittner, A., and Green, J. A. M.: Glacial ice sheet extent effects on modeled tidal mixing and the global overturning circulation, Paleoceanography and Paleoclimatology, 34, 1437–1454, doi:10.1029/2019PA003644, 2019.

Wilmes, S. B. and Green, J. A.: The evolution of tides and tidal dissipation over the past 21,000 years, Journal of Geophysical Research : Oceans, 119, 4083–4100, doi:10.1002/2013JC009605, 2014.

Woodworth, P. L.: The global distribution of the M1 ocean tide, Ocean Science, 15, 341–442, doi:10.5194/os-15-431-2019, 2019.

Woodworth, P. L., Hunter, J. R., Marcos, M., Caldwell, P., Menéndez, M., and Haigh, I.: Towards a global higher-frequency sea level dataset, Geoscience Data Journal, 3, 50–59, doi:10.1002/gdj3.42, 2017.

World Meteorological Organisation: Guide to meteorological instruments and methods of observation (WMO-No. 8), World Meteorological Organisation: Geneva, Switzerland, 2008.

Wunsch, C.: The long-period tides, Reviews of Geophysics, 5, 447, doi:10.1029/RG005i004p00447, 1967.

Wunsch, C.: Internal tides in the ocean, Reviews of Geophysics and Space Physics, 13, doi:10.1029/RG013i001p00167, 1975.

Wunsch, C.: Determining paleoceanographic circulations, with emphasis on the Last Glacial Maximum, Quaternary Science Reviews, 22, 371–385, doi:10.1016/S0277-3791(02)00177-4, 2003.

Wziontek, H., Sulzbach, R., Hart-Davis, M., Dobslaw, H., Scherneck, H.-G., Van Camp, M., Omang, O. C. D., Antokoletz, E. D., Voigt, C., Dettmering, D., and Thomas, M.: Data-unconstrained modeling and detection of 9 individual partial ocean tides of third-degree by terrestrial gravimetry, doi:10.5194/egusphere-egu22-8556, 2022.

Zahel, W.: Die Reproduktion gezeitenbedingter Bewegungsvorgänge im Weltozean mittels des hydrodynamisch-numerischen Verfahrens, 1970.

Zahel, W.: A global hydrodynamic-numerical 1-degree-model of the ocean-tides; the oscillation system of the M2-tide and its distribution of energy dissipation, Ann. Geophys., 33, 31–40, 1977.

Zahel, W.: The influence of solid Earth deformations on semidiurnal and diurnal ocean tides, in: Tidal friction and the Earth's rotation, pp. 98–124, Springer Verlag, Berlin-Heidelberg-New York, doi:10.1007/978-3-642-67097-8_9, 1978.

Zahel, W.: Mathematical modelling of global interaction between ocean tides and earth tides, Physics of the Earth and Planetary Interiors, 21, 202–217, doi:10.1016/0031-9201(80)90070-9, 1980.

Zahel, W.: Modeling ocean tides with and without assimilating data, Journal of Geophysical Research: Solid Earth, 96, 20 379– 20 391, doi:10.1029/91JB00424, 1991.

Zahel, W. and Müller, M.: The computation of the free barotropic oscillations of a global ocean model including friction and loading effects, Ocean Dynamics, 55, 137–161, doi:10.1007/s10236-005-0029-y, 2005.

Zaron, E. D.: Mapping the nonstationary internal tide with satellite altimetry, Journal of Geophysical Research: Oceans, 122, 539–554, doi:10.1002/2016JC012487, 2017.

Zaron, E. D. and Egbert, G. D.: Estimating open-ocean barotropic tidal dissipation: The Hawaiian Ridge, Journal of Physical Oceanography, 36, 1019–1035, doi:10.1175/JPO2878.1, 2006.

Zhang, X., Lohmann, G., Knorr, G., and Xu, X.: Different ocean states and transient characteristics in Last Glacial Maximum simulations and implications for deglaciation, Climate of the Past, 9, 2319–2333, doi:10.5194/cp-9-2319-2013, 2013.

Zhao, Z., Alford, M. H., Girton, J., Johnston, T. M., and Carter, G.: Internal tides around the Hawaiian Ridge estimated from multisatellite altimetry, Journal of Geophysical Research: Oceans, 116, 1–15, doi:10.1029/2011JC007045, 2011.

Zürn, W.: Earth tide observations and interpretation, in: Tidal Phenomena, pp. 77–94, Springer-Verlag, doi:10.1007/BFb0011458, 1997a.

Zürn, W.: The nearly-diurnal free wobble-resonance, in: Tidal Phenomena, pp. 95–109, Springer-Verlag, doi:10.1007/BFb0011459, 1997b.

Zweng, M. M., Reagan, J. R., Seidov, D., Boyer, T. P., Antonov, J. I., Locarnini, R. A., Garcia, H. E., Mishonov, A. V., Baranova, O. K., Weathers, K. W., Paver, C. R., and Smolyar, I. V.: World Ocean Atlas 2018, Volume 2: Salinity, World Ocean Atlas 2018, 2, 50, URL `https://www.ncei.noaa.gov/sites/default/files/2020-04/woa18_vol2.pdf`, 2018.

Eidesstattliche Erklärung

Hiermit versichere ich an Eides statt, die vorliegende Dissertation selbstständig und ohne unerlaubte Hilfe angefertigt zu haben.

Bei der Verfassung der Dissertation wurden keine anderen als die im Text aufgeführten Hilfsmittel verwendet.

Ein Promotionsverfahren zu einem früheren Zeitpunkt an einer anderen Hochschule oder bei einem anderen Fachbereich wurde nicht beantragt.

Ort, Datum

Roman Sulzbach

l

Acknowledgements

This thesis took advantage of the netCDF software developed by UCAR/Unidata (`http://doi.org/10.5065/D6H70CW6`). The presentation of scientific data in plots was achieved with help of the matplotlib (Hunter, 2007), cartopy (Met Office, 2010 - 2015), cmocean (Thyng et al., 2016) and numpy (Harris et al., 2020) libraries in an Anaconda environment (Anaconda, 2020). Flow charts and other figures within this work were created with Inkscape (Inkscape Project, 2020).

The presented FES14 (Lyard et al., 2006, 2021) ocean tide solutions were produced by Noveltis, Legos, and CLS and distributed by Aviso+, with support from CNES (`https://www.aviso.altimetry.fr/`). The empirical GOT ocean tide solutions in Figure 5.9 were provided by Richard Ray (personal communication, April 20, 2022). The tide gauge data presented in Figure 2.8 was provided by the Federal Maritime and Hydrographic Agency (BSH) Hamburg. The ocean normal modes presented in Figure 2.7 were provided by Prof. Dr. Malte Müller (personal communication, March 16, 2019). Figure 6.11 was provided by Dr. V. Klemann and H. Dümpelmann (personal communication, March 7, 2023).

I would like to thank my supervisor Prof. Dr. Maik Thomas and my scientific advisor Dr. Henryk Dobslaw for their supervision, fruitful discussions, the excellent working environment at the GFZ Potsdam, and the reliable support of my work.
I also would like to thank Petra Nerge for introducing me to the TiME source code, which was the fundament for the conducted research, and to Dr. Philipp Weis for providing the TiME software in the initial version and his helpful responses on several questions.

I would also like to thank Prof. Dr. Michael Schindelegger who agreed to be the reviewer for this thesis. His feedback to the conducted research and on several project meetings was greatly appreciated.

Further, I would like to express my ample thanks to the coauthors of the studies conducted for this thesis and within the framework of it. This especially but not exlcusively includes Hartmut Wziontek, Michael Hart-Davis, Kyriakos Balidakis, Linus Shihora, Pingping Huang, Volker Klemann, Christian Voigt, Christoph Dahle, Henryk Dobslaw, and Maik Thomas.

I would like to express my sincere thanks to the entire Section 1.3 at GFZ Potsdam that supported me during work for this thesis in every form possible, which includes scientific and other discussions, administrative help and a generally good working atmosphere.

I very much recognize the help of my proofreaders, Christian Cop, Martin Pospiech, and Jonathan Hahn, who helped to improve this thesis.

It is also important for me to acknowledge the share of my teachers, especially in science, at school, and university, as well as supervisors and colleagues at former stations of my education, in Bad Nauheim, Darmstadt, Bordeaux, and Mainz. It is largely thanks to the opportunities and trust I was given that it was possible to finish this thesis.

Also, I would like to acknowledge the essential role of old and newly-found friends in Darmstadt, Potsdam, and many other places, who supported me by lending an open ear and were a reliable address to find a recreation.

I want to express the most profound thanks to my family, who supported me for decades, encouraged me, and believed in my success in all situations.